Studies on the role of nano additives on the microstructure and Flux pinning in $Bi_2Sr_2(Ca_{0.86}Sr_{0.14})_{n-1}Cu_nO_{2n+4}$ superconductor composites

by

Pawan Kumar Verma

Registration Number: 17PHPH05

A thesis submitted for the degree of

Doctor of Philosophy

in

Physics

Under the supervision of

Prof. V. Seshu Bai

&

Prof. S. Srinath (co-supervisor)





School of Physics, University of Hyderabad Hyderabad – 500046, India May 2024 Dedicated to My Family **Declaration**

I, Pawan Kumar Verma, hereby declare that this thesis entitled "Studies on the role of

nano additives on the microstructure and Flux pinning in Bi₂Sr₂(Ca_{0.86}Sr_{0.14})_{n-}

 ${}_{1}Cu_{n}O_{2n+4}$ superconductor composites" submitted by me under the supervision of Prof.

V. Seshu Bai, Prof. S. Srinath (co-supervisor), School of Physics, University of Hyderabad,

Hyderabad, is a bonafide research work and also free from plagiarism. The work is original

and has not been submitted earlier as a whole or in part for the award of any

degree/diploma to this University or any other University / Institution.

Paman Verma

Pawan Kumar Verma

Regn. No.- 17PHPH05

Date: 17/05/2024

Place: Hyderabad

Certificate





This is to certify that the work described in this thesis entitled "Studies on the role of nano additives on the microstructure and Flux pinning in Bi₂Sr₂(Ca_{0.86}Sr_{0.14})_{n-1}Cu_nO_{2n+4} superconductor composites" has been carried out by Mr. Pawan Kumar Verma bearing Reg. No: 17PHPH05, in partial fulfilment of the requirements for the award of Doctor of Philosophy in the School of Physics, is a bonafide work carried out by him under our supervision and guidance. This thesis is free from plagiarism and has not been submitted earlier in part or in whole to this University or any other University/Institution for the award of any degree/diploma.

Further, the student has the following publications before the submission of the thesis for adjudication.

- 1]. **Pawan Kumar Verma**, A. Kaipamangalath, M. R. Varma and V. Seshu Bai, Non-reactive nano WO₃ inclusions to enhance flux pinning in Bi 2223 superconductor composites, *IEEE Transactions on Applied Superconductivity*, 34(1), 8000112 (2024),
- 2] **Pawan Kumar Verma,** B. V. Reddy, T. Rajasekharan, R. Revathy, M. R. Varma and V. Seshu Bai, Two-phase microstructure generated by reaction of nano WO₃ addition and its effect on flux pinning in Bi 2212 composites, **J Supercond Nov Magn 37, 1–14 (2024)**
- 3] Pawan K Verma, T. Rajasekharan, S.C. Das, K.P. Surendran and V. Seshu Bai, Effect of nano ZrO_2 addition on the properties of $Ca_{0.86}Sr_{0.14}CuO_2$ added Bi-2223 composites, **Journal of Physics: Conference Series 2545**, 012014 (2023)
- 4] P. Jeevan Kumar, Poly Rose, **Pawan Kumar Verma**, T. Rajasekharan and V. Seshu Bai, BSTO components using rapid prototyping and different gelcasiting systems, **Open Ceramics**, **17**, **100512** (2024).

Further, the student has passed the following course towards the fulfilment of course work required for Ph.D.

Course Code	Name of the Course	Credits	Pass/Fail
PY 801	Research Methodology	4	Pass
PY 802	Advanced Quantum Mechanics	4	Pass
PY 803	Advanced Experimental techniques	4	Pass
PY 804	Advanced Condensed Matter Physics	4	Pass

V. Seshu Bai

Prof. V. Seshu Bai

Supervisor School of Physics University of Hyderabad Hyderabad- 500046

Dr. V. Seshu Bai School of Physics University of Hyderabad

Day 2015/24 Prof. S. Srinath

Co-supervisor School of Physics University of Hyderabad Hyderabad- 500046

Dr. S. Srinath
Professor
School of Physics
UNIVERSITY OF HYDERABAD
Central University P.O.
Hyderabad-500 046.

Dean

School of Physics University of Hyderabad Hyderabad- 500046

DEAN School of Physics University of Hyderabad HYDERABAD - 500 046

Acknowledgements

I deem it a proud privilege and pleasure to express my sincere gratitude to my thesis advisor, **Prof. V. Seshu Bai**, School of Physics, University of Hyderabad, for her valuable guidance, support, encouragement, and independence given to me during my research. She was always passionate and enthusiastic about her research projects, was very open to new ideas, and showed me how exciting research can be. She has always been extremely generous with her time and knowledge, and I was inspired by her dedication to science. Her careful planning, coupled with a strong sense of duty, strictness, and warmth of love, enabled me in the successful completion of this thesis.

I am deeply grateful to **Prof. S. Srinath**, Professor at the School of Physics, University of Hyderabad, my thesis co-supervisor, and a member of the Doctoral Committee, for his valuable guidance, support, and concern during my Ph.D. His insistence on excellence, discipline, and sincerity always influenced me towards new research ideas. His care, motivation, and kindness will be remembered forever.

I would like to thank **Prof. K.C. James Raju**, who has been there as my Doctoral Committee member, for his discussions and suggestions throughout my research work.

I am grateful to Dr. T. Rajasekharan, for his invaluable scientific advice and discussions, which have significantly contributed to the depth and quality of this thesis work. His expertise and guidance were helpful in shaping the direction of this study.

I am thankful to Dr. Manoj Raama Varma, NIIST- Thiruvananthapuram, for his support, valuable suggestions and allowing me to use lab facilities including PPMS.

Further, I am grateful to the present Dean, School of Physics, Prof. K.C. James Raju and former Deans, Prof. Ashok Chatterjee, Prof. V. Seshu Bai and Prof. Bindu A. Bambah, for providing me with all the school level facilities.

I also thank all other faculty and the non-teaching staff of the School of Physics for their cooperation.

I thank the University of Hyderabad for the financial assistance during my Ph.D. course. I also acknowledge the Science and Engineering Research Board (SERB), Core Grant Project (CRG), and Advance Manufacturing Technologies (AMT) grant under the technology

development program of the Department of Science and Technology (DST), India, for funding my research work. I thank Institute of Eminence (IoE), university of Hyderabad for providing a travel grant to attend and present my research work at International Symposium on Superconductivity (ISS- 2022) in Japan.

I would like to express my heartfelt gratitude to my fellow lab mates Mr. B. Venkatesulu Reddy, P. Jeevan Kumar, Poly Rose, Akhil T., and Ms. Devaparna Bhattacharya. Their camaraderie, unwavering support, and collaborative spirit have been invaluable throughout the course of this research. I am fortunate to have had the opportunity to work alongside such talented individuals. Their friendship and encouragement have made this journey not only academically rewarding but also personally fulfilling.

I am thankful to all my seniors, Dr. Devendra K. Namburi, Dr. M. Ramudu, Dr. Sathish Kumar Ayila, Dr. P.M. Swaroop Raju and Dr. S.P.K. Naik, for their constant support and encouragement.

I am deeply grateful to my friends Aishwarya Bhatta, Dr. Najirul Islam, L.A. Longchar, Sushmita, Dr. Hemant Kumar Sharma, Dr. Sarthak, Dr. Pooja Saini, Vinod Rajpoot, Nitin, Rampyari, Dr. Dinesh Sahoo, Rohit, Aditi, Dr. Subroto Mondal, Pankaj, Manoj, Vedprakash, Prakash, Nidhi, Avik, Sridhar, Dr. K. Aswathi, Dr. R. Revathy, Chinnu, Aswathy V.S., Dr. Abhishek Jha who have been a constant source of encouragement and understanding throughout the journey of completing this thesis. Their unwavering support, even during the most challenging times, has been a source of strength. I appreciate the laughter, camaraderie, and shared experiences that have enriched my life beyond the confines of academia.

I owe my gratitude to my mother, Mrs. Bhagwati Devi, and father, Mr. Mohan Lal Verma, whose innumerable sacrifices, unconditional love, confidence, and support have driven me this far. I thank my brothers, Mr. Pramod and Mr. Preetam, and my sister, Ms. Babita, for their affection and wishes. I am thankful to all my family members and relatives for their support.

CONTENTS

Chapter 1: Introduction

1.1	Superconductor: Historical developments and	basic 1
	properties	
1.2	Type I and Type II superconductors	5
1.3	Applications of superconductors	7
1.4	Magnetization of type II superconductors	7
1.4.	1 Critical current density	8
1.4.	2 Pinning force density	9
1.5	Bi-Sr-Ca-Cu-O superconductors	10
1.5.	1 Bi ₂ Sr ₂ CuO ₆ crystal structure	10
1.5.	2 Bi ₂ Sr ₂ CaCu ₂ O _{8+δ} crystal structure	11
1.5.	3 Bi ₂ Sr ₂ Ca ₂ Cu ₃ O _{10+δ} crystal structure	11
1.6	YBCO and BSCCO comparison	12
1.7	Literature survey on BSCCO and the effect of	13
	secondary phase addition	
1.8	Motivation and aim of present work	23
1.9	Organization of the Thesis	23
Ref	erences	25

Chapter II: Synthesis and characterization

2.1 Introduction	34
2.2 Synthesis of precursor powders	34
2.2.1 Bi 2212 precursor powder synthesis	34
2.2.2 Bi 2223 precursor powder synthesis	34
2.2.3 (Ca,Sr)CuO phase preparation	34
2.3 Synthesis of nanoparticles	35
2.3.1 WO ₃ nanoparticles	35
2.3.2 Ca _{0.86} Sr _{0.14} CuO ₂ phase nanoparticles	35
2.4 Synthesis of BSCCO composites with nanoparticle	35
addition	
2.4.1 Bi 2212 composites with WO ₃ nanoparticles	35
2.4.2 Bi 2223 composites with WO ₃ nanoparticles	36
$2.4.3 \ Bi 2223+ 20mol Ca_{0.86}Sr_{0.14}CuO_2 phase with ZrO_2$	37
nanoparticles	
2.4.4 Bi 2223 composites with Ca _{0.86} Sr _{0.14} CuO ₂ nanoparticles	37
2.5 Characterization techniques	38
2.5.1 X-ray diffraction	38
2.5.2 Field Emission Scanning Electron Microscopy	39
2.5.3 Energy Dispersive X-ray Spectroscopy	40
2.5.4 Bulk density using Archimedes' principle	41
2.5.5 Vibrating sample magnetometer	42
2.6 Bean's critical state model and critical current density	43
2.7 Flux pinning	45
References	48

Chapter III

Effect of nano WO₃ addition on the structural, microstructural, and superconducting properties of Bi 2212 superconducting composites

3.1 Introduction	51
3.2 Experimental	53
3.2.1 Characterization of WO ₃ nanoparticles	53
3.2.2 Preparation of Bi 2212 composites	55
3.3 Results	55
3.3.1 XRD analysis of Bi 2212 composites	55
3.3.2 Microstructural analysis	57
3.3.3 Temperature dependence of magnetization	58
3.3.4 Field dependence of magnetization	59
3.3.5 Analysis of flux pinning force density	61
3.4 Conclusions	64
References	65

Chapter IV

Effect of adding non-reactive WO₃ nano inclusions to enhance flux pinning properties in Bi 2223 superconductor composites

4.1 Introduction	70
4.2 Experimental	72
4.2.1 Synthesis of precursor powders of Bi 2223	72
4.2.2 Composites of Bi 2223 with WO ₃ nanoparticle addition	73
4.2.3 Characterization of Bi 2223 samples with WO ₃ addition	73
4.3 Results and Discussion	74
4.3.1 X-ray diffraction studies	74
4.3.2 Microstructural studies	75
4.3.3 Density measurements	76
4.3.4 Magnetic measurements	77
4.3.5 Analysis of flux pinning force density	80
4.4 Conclusions	87
References	88

Chapter V

Effect of nano ZrO_2 addition on the flux pinning properties of $Ca_{0.86}Sr_{0.14}CuO_2$ phase added Bi 2223 composite

5.1 Introduction	93
5.2 Experimental	94
5.3 Results and Discussion	95
5.3.1 XRD analysis for the sample of BZ series	95
5.3.2 Microstructural analysis	97
5.3.3 Temperature dependence of magnetization	98
5.3.4 Field dependence of magnetization	99
5.3.5 Field dependence of critical current density	100
5.3.6 Analysis of flux pinning force density	101
5.4 Conclusions	105
References	106

Chapter VI

Enhanced superconducting properties of Bi 2223 composites at high concentration of non-reactive nano (Ca,Sr)CuO phase addition

6.1 Introduction	110
6.2 Experimental	112
6.3 Results and Discussion	113
6.3.1 Characterization of Ca _{0.86} Sr _{0.14} CuO ₂ phase particles	113
6.3.2 XRD analysis of composites	114
6.3.3 Microstructural analysis	115
6.3.4 Temperature dependence of magnetization	117
6.3.5 Critical current density and flux pinning force density	118
6.4 Conclusions	122
References	123

Chapter VII

Summary and conclusions

7.1 Problem addressed	126
7.2 Important findings	127
References	130

Chapter 1: Introduction

1.1 Superconductor: Historical developments and basic properties

A current that passes through a metal or an alloy dissipates due to resistive path. The resistance can be due to atomic vibrations or impurities in the material that scatter the electron path and subsequently dissipate the current. On cooling a material to lower temperatures, its electrical resistivity (ρ) decreases with temperature, the atomic vibration freezes till the resistivity reaches residual resistivity (ρ _o) at absolute Zero. The existing impurities in the materials, At temperatures zero Kelvin, primarily contribute to residual resistivity. The resistivity of any material can be given as

$$\rho = \rho_0 + \rho(T) \tag{1}$$

A *superconductor* is a material that ensures a resistance-less path to electrons by offering zero resistance. The first superconductor, in 1911, was discovered by Professor Heike Kamerlingh Onnes, who noticed that the electrical resistance of Mercury (Hg) abruptly vanishes at a temperature around 4.2 K [1]. After the liquefaction of Helium (He) gas at his Leiden laboratory in 1908, resistivity studies at such low temperatures became feasible.

He used superconductivity to describe the phenomenon when a material loses resistance below a particular temperature, called critical transition temperature. The critical transition temperature (T_c) is one of the three working conditions below which the material becomes superconducting. After discoevring superconductivity in Mercury (Hg) at 4.2 K, he determined the resistivity of other metals, such as Tin (Sn) and Lead (Pb), at lower temperatures and confirmed that they are also superconducting with T_c values of 3.7 K and 7.2 K, respectively [2].

The sole known characteristic property of superconductors was zero resistance till 1932. After 22 years of discovering superconductivity in 1933, Walter Meissner and Robert Ochsenfeld discovered that superconductors exhibit perfect diamagnetism when cooled below T_c [3]. In the superconducting state, a surface current is generated on the superconductor's surface to oppose the applied magnetic field, leading to the total expulsion of the magnetic field (B) from within the superconductor. This was called the Meissner effect. The critical field (H_c) is the field below which a superconductor continues to be in its superconducting state and is the second working condition.

So, the two basic properties of a superconductor are

- 1) Zero resistance
- 2) Meissner effect (B=0, inside)

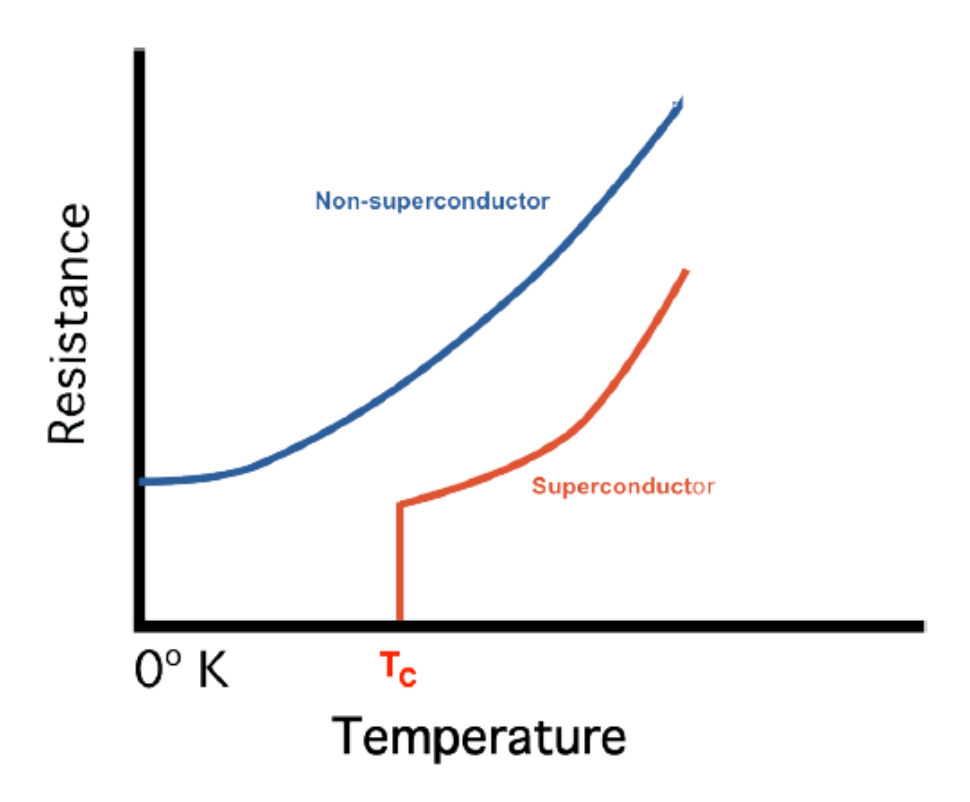


Figure 1.1: Temperature dependence of resistance for a non-superconducting and superconducting material.

The first model to explain superconductivity in materials is the two-fluid model proposed in the year 1934, by C. J. Gorter and H. Casimir [4]. According to this model, the electrons in a superconducting material are composed of normal and superconducting electrons. Below T_c, the fraction of normal electrons starts to decrease. This model was an ad-hoc model since it had no basis for the assumptions proposed.

The London brothers devised the London equations in 1935 to describe the electrodynamics of a superconductor in applied magnetic fields [5]. The two-fluid model's presumption quantifies the Meissner effect.

They also demonstrated that the magnetic field within the superconductor decays exponentially, and the distance from the superconductor's surface at which the magnetic field drops to 1/e times its value at the surface is known as London's penetration depth (λ_L). London's equations (2-3) are given below,

$$\frac{dJ}{dt} = -\frac{m}{n_s e^2} E \tag{2}$$

$$B(x) = B_a e^{-\frac{x}{\sqrt{\alpha}}} \tag{3}$$

where
$$\alpha = (\lambda_L)^2$$
 (4)

Where J= current density, m= mass of electron, n_s = superconducting electron density, E= electric field, B(x)= flux density of applied field at x distance from the surface, B_a = flux density of applied field at the surface,

In 1950, Lev Landau and Vitaly Lazarevich Ginzburg developed a new phenomenological (GL) theory for explaining superconductivity in materials [6]. The GL theory extends the earlier London theory by introducing a complex-valued order parameter (ψ), which accurately describes the behavior of the superconducting electron density (n_s).

In 1953, Alfred Brian Pippard modified London's theory and introduced a parameter called "Coherence Length (ξ)". Coherence length is the length over which the superconducting electron density n_s changes appreciably [7].

A study in 1957 by Alexei Alexeyevich Abrikosov discussed the mixed state in superconductors [8]. The vortex structure was foreseen using GL theory. His idea defined the Type-I and Type-II subcategories of superconductors. The ratio of penetration depth to coherence length, or the GL parameter ($\kappa = \lambda_L / \xi$), was described by him. Superconductors are categorized as Type-I or Type-II depending on the value of κ , whether κ is more than or less than 0.707, respectively.

John Bardeen, Leon Cooper, and John Robert Schrieffer (BCS) reported the first microscopic quantum theory of superconductivity in 1957 [9]. According to BCS theory, superconductivity arises from the interaction between two electrons of opposite spin (Cooper pair) and atomic vibrations (phonons).

A phonon mediates an interaction between electron pairs. The local lattice is distorted as a negatively charged electron passes through a lattice of the nuclei of positive ions. Around it, there is a higher density of positive charge. The Cooper pair is created when an additional electron, passing near the lattice, is drawn to this charge distortion. Therefore, by the phonon interaction, the electrons are indirectly drawn to one another and form a Cooper pair.

In simple terms, superconductivity is created by a Cooper pair having wave vectors of opposite sign, K^+ and K^- , but of the same magnitude, such that $K_{\text{net}} = 0$, which gives rise to the electron pair's infinite wavelength. This means that the lattice will not scatter the Cooper pair; thus, it does not experience any resistance as it passes through the material.

The formation of a coherent superposition of these Cooper pairs into a condensate state results in an energy gap in the excitation spectrum, which prevents electron scattering and contributes to the superconducting state or zero resistivity.

The superconducting band gap $\Delta(0)$ derived by BCS theory, is

$$\Delta(0) = 1.75 \text{ K}_{\text{B}} \text{T}_{\text{c}} \tag{5}$$

Where K_B = Boltzmann constant.

In 1962, British physicist Brian David Josephson predicted that a cooper pair (superconducting electrons) could cross an insulating barrier between two superconducting layers without losing momentum [10]. The insulating junction between two superconducting regions is called the Josephson junction. Later, this phenomenon was verified experimentally.

The significant discovery of high-temperature superconductivity came in 1986 when superconductivity was discovered in metallic oxide for the first time. Johannes Georg Bednorz and Karl Alexander Muller discovered superconductivity in the La-Ba-Cu-O system with T_c around 35 K [11]. The name "cuprates" was assigned to this group of superconductors that contain CuO₂ layers within their unit cells. It was the beginning of High T_c Superconductivity.

In the year after, 1987, Maw-Kuen Wu and Chu-Ching Wu found superconductivity in Y-Ba-Cu-O, having $T_c = 93$ K, above the boiling point of liquid nitrogen temperature [12].

Hiroshi Maeda and his colleagues at the National Research Institute for Metals in Japan subsequently identified superconductivity in the Bi-Sr-Ca-Cu-O compound (without any rare earth) in 1988, having T_c around 110 K [13]. The highest T_c (164 K), attained under the pressure of 30 GPa, is found in Hg-based superconductors [14].

In March 2001, Nagamatsu et al. discovered a new type of superconductor, MgB_2 , with a T_c = 39 K. MgB_2 is a layered, structured, conventional superconductor [15].

In 2008, Kamihara et al. observed superconductivity in LaFeAsO_{1-x}Fe_x with a T_c of 26 K [16]. Generally, the substances with strong magnetic moments were detrimental to superconductivity. However, the discovery of superconductors made of iron caught the scientific community by surprise. Fig. 1.2 displays the T_c and the year of superconductor discovery.

Newly discovered hydride superconductors (H₂S, LaH₁₀) exhibit superconductivity near room temperature under high pressure conditions [17,18].

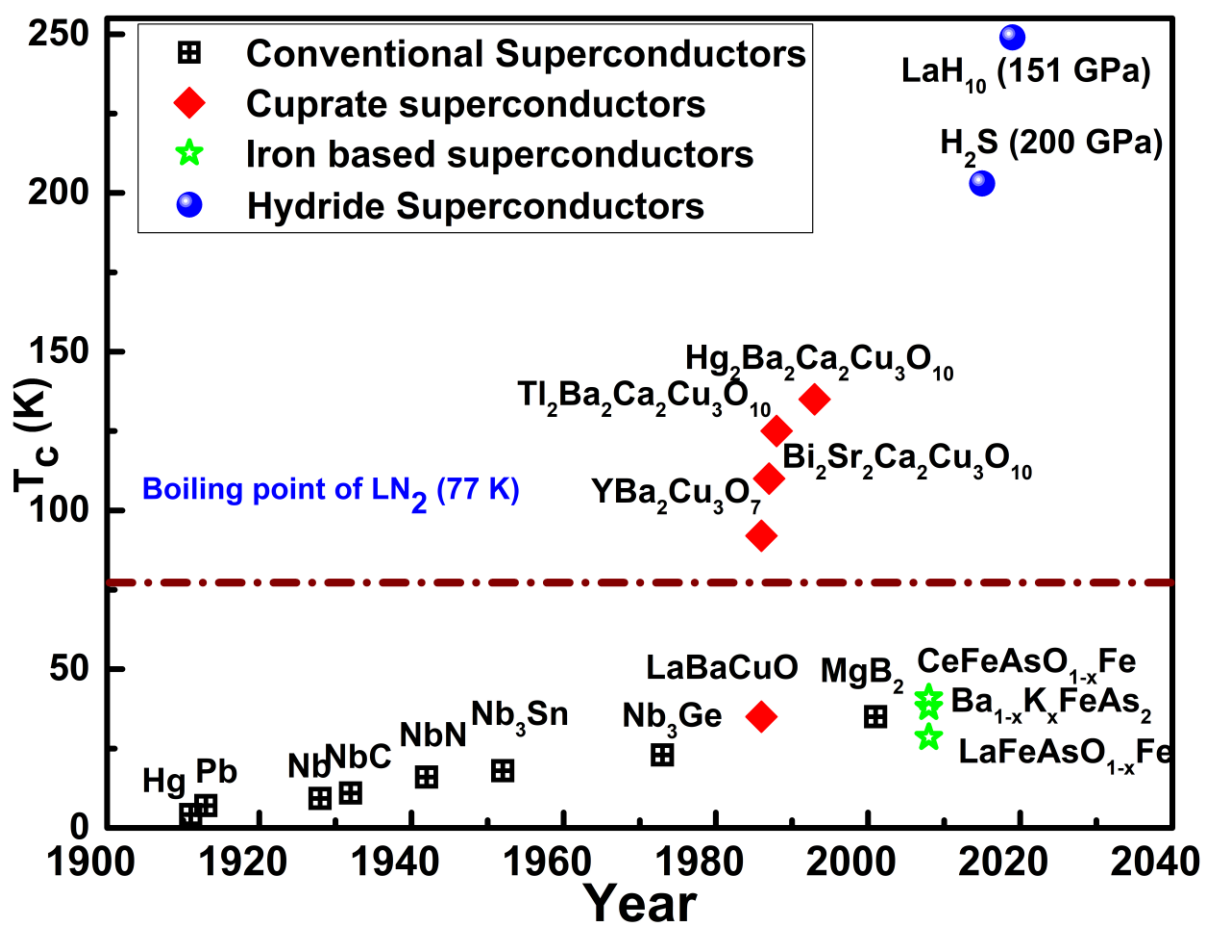


Figure 1.2: Critical temperature and discovering time for various superconductors [19].

The Critical temperature (T_c) is more intrinsic to a superconducting compound's chemical composition and structure. In contrast, the critical current density (J_c) and critical magnetic fields (H_c) are affected by microstructure and homogeneity. In searching for High T_c superconductors, Maeda et al. [13] discovered the Bi-Sr-Ca-Cu-O superconducting compound at the National Research Institute for Metals in Japan.

1.2 Type-I and Type-II superconductors

All type I superconductors completely expel the magnetic field, below a certain applied magnetic field known as the critical field (H_c). However, in the Type II category, when a superconductor is subjected to a magnetic field, the free energy diminishes, causing the generation of normal regions and superconducting regions in a hexagonal pattern. This state is called a mixed state or vortex state.

In the mixed state, the magnetic flux enters partially, in quantized units inside a superconductor, forming cylindrical domains called vortices. So, the superconducting material in a mixed state is a mixture of normal and superconducting regions.

In the Type II category, there are two critical magnetic fields, H_{c1} and H_{c2} . When the applied magnetic field is below H_{c1} , the material behaves as a perfect diamagnetic material. When the applied field exceeds H_{c1} , the material goes into a mixed state until it reaches H_{c2} . When the field is applied beyond H_{c1} , the superconducting material becomes normal. The critical fields (H_c , H_{c1} , and H_{c2}) are shown in Fig. 1.3.

Like H_c and T_c, a third critical parameter exists called critical current density (J_c). If the current density passing through a superconductor exceeds J_c, the superconductor will become normal. These three parameters define a critical surface for a superconductor. Within this surface, the material acts as a superconductor, but if any one of the three parameters exceeds its limit, the material becomes normal.

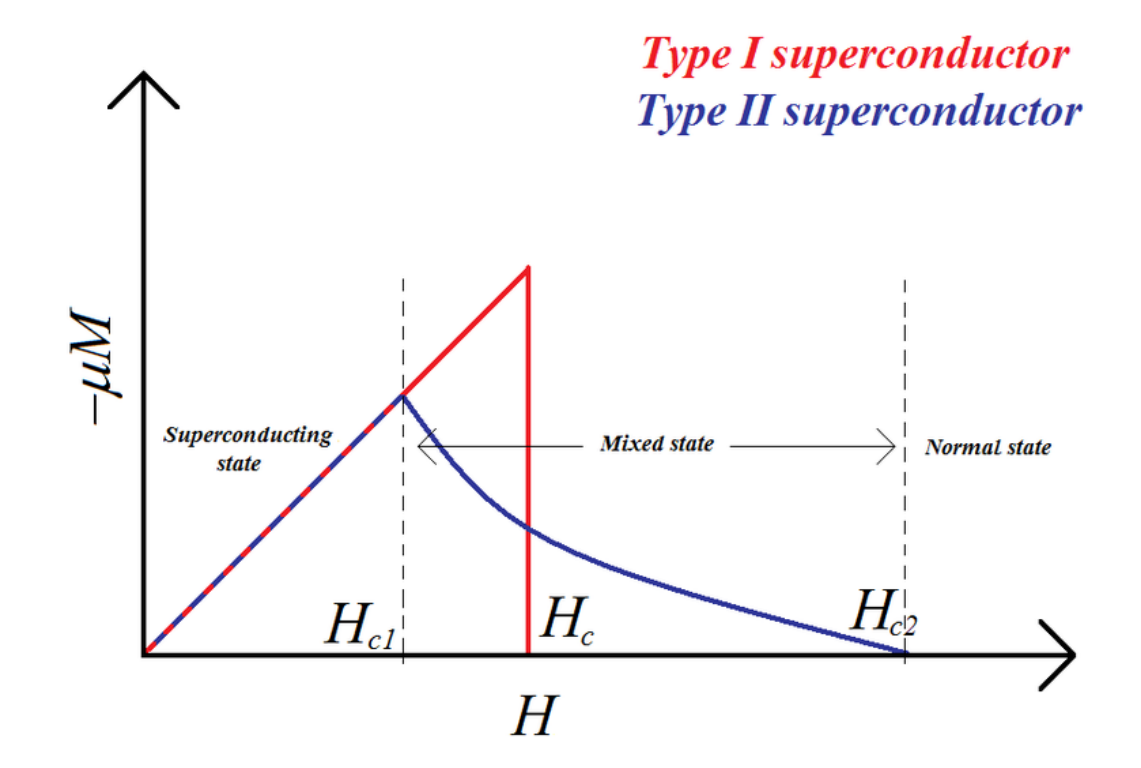


Figure 1.3: Magnetization curve for type I and type II superconductors showing various critical fields [20].

All elemental superconductors like Hg, Pb, Sn, etc., are type I superconductors, whereas all alloys like Nb₃Ge, MgB₂, YBa₂Cu₃O₇₋₈, BSCCO, Iron-based SmFeAsO_{1-x}F_x materials are type II superconductors.

1.3 Applications of Superconductors

Significant progress has been made in several fields because of the unique physical properties of superconductors. In many applications, superconducting materials can replace conventional materials and offer better performance. However, superconducting technology is often essential for achieving the necessary performance in various industries. Using superconducting components enables instruments and devices to be smaller and lighter than those made with conventional methods, which is especially important in areas like space applications.

The most common uses of superconductors are in power distribution (Cables, Transformers, Current leads, Fault current limiters, Motors), power generation and storage (Generators, Superconducting magnetic storage systems), magnets (Nuclear magnetic resonance (NMR), Magnetic resonance images (MRI), Fusion reactors, Particle accelerators, High field magnets), High field magnets for separation and shielding, Sensors, Magnetic levitation, and space applications [21].

1.4 Magnetization of type II superconductors:

The H_{c2} value for type II superconductors is very high, which makes them more useful for practical applications. All superconductors are diamagnetic when they are superconducting. Hence, a shielding current is generated on the surface in response to applying a field to expel that field. The shielding current will flow when the field is non-zero in type II superconductors. According to Maxwell's 4^{th} equation.

$$\nabla XB = \mu_0 J. \tag{6}$$

The magnetic moment induced by this shielding current is given by $m = \int M dV$, where M is the magnetization, magnetic moment (m) per unit volume, and dV is the volume element. A typical MH loop for a type II superconductor is shown in Fig. 4. For a type II superconductor, at low magnetic fields, the M-H curve follows the same path regardless of whether the magnetic field is being increased or decreased. However, as the magnetic field increases, vortices within the

superconductor start to interact and pin to defects in the material, leading to hysteresis and irreversible behavior. The field beyond which magnetization is reversible is known as an irreversible field (B_{irr}).

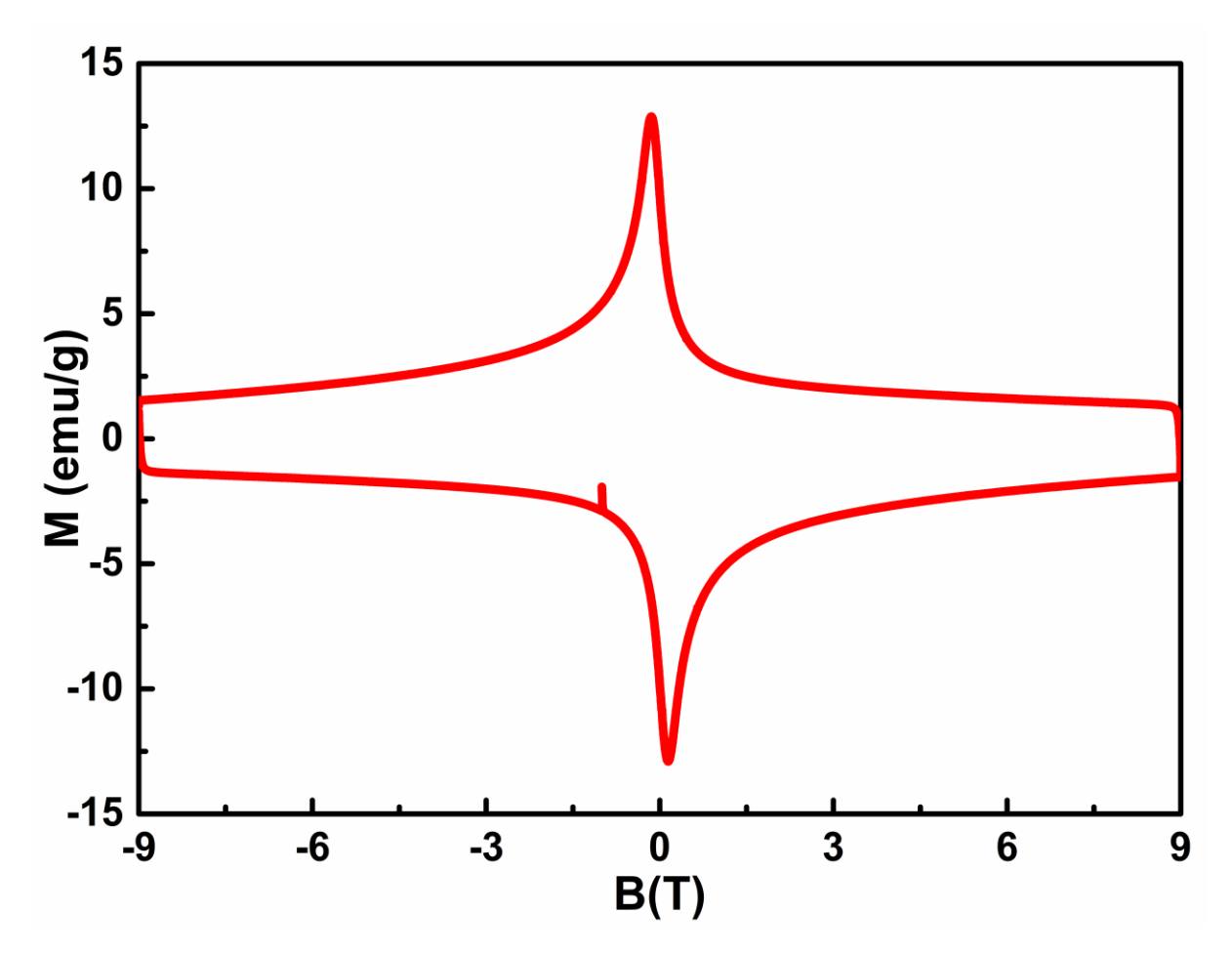


Figure 1.4: Typical MH loop for a BSCCO superconductor

1.4.1 Critical current density

Field dependence of magnetization data is used to determine the critical current density of a superconductor. Several models, like the Beans [22], Anderson and Kim model [23], compute critical current density from magnetization. The critical state model, or Bean's model [22], is the simplest and most widely used. The relation gives the critical current density for a sample with a rectangular cross-section.

$$J_c = \frac{20 \,\Delta M}{a(1-\frac{a}{3b})} \tag{7}$$

Where ΔM is the difference in magnetization, a, b are the sides of the rectangular section, with a < b.

As shown in the MH loop, the ΔM decreases with the field, which impacts the J_c at higher fields. The dissipation of J_c due to normal area is brought on by the field's penetration into the superconductor at the field above H_{c1} . This dissipation results from the action of the Lorentz force on the flux lines.

Due to Lorentz's force, fluxons move from their position in a direction perpendicular to the current flow. Flux pinning prevents the motion of vortices within the superconductor, which helps maintain constant J_c under varying magnetic fields.

1.4.2 Pinning force density:

Flux pinning force density (F_p) is defined as the force density required to pin flux lines at a particular point, and F_p is equal to and opposite to the Lorentz force and is given by

$$F_p = J_c X B \tag{8}$$

Local inhomogeneity caused by impurities, stacking faults, oxygen deficiency, grain boundaries, lattice substitution, and voids in the superconducting material can cause–pinning. These defects are called pinning centers. The intergranular coupling influences the critical current density in a superconductor. Weak pinning and breaking down of intergranular coupling at higher fields causes a sharp drop in J_c [24,25].

Superconducting material should be designed with intergranular coupling and exhibit enough mechanical strength for real-scale applications. Intergranular coupling can be improved by optimizing processing conditions, and strong pinning can be achieved by introducing submicron-sized pinning centers in the materials as the vortices get pinned to these inclusions. The strongest pinning is achieved when the size of the pinning centers is of the order of the coherence length of the Cooper pair. The density of pinning centers should be optimum, as at a high density of pinning centers, the superconducting fraction will reduce. Defects to improve flux pinning in the superconducting matrix can be introduced by different methods.

- a) Optimizing the conditions for heat and mechanical treatments to introduce lattice defects or to form fine-grained material with high surface defects.
- b) Exposing the superconducting material to heavy ion radiation will create columnar non-superconducting channels in linear defects.
- c) Secondary phases are added to the superconducting matrix to generate nanometer-size defects.

Among the three methods discussed above, the secondary phase addition method is widely used to tune the flux pinning in superconductors.

1.5 Bi-Sr-Ca-Cu-O Superconductors

copper (Bi-Sr-Ca-Cu-O/BSCCO) Bismuth strontium calcium oxide superconductors are a family of superconductors having generalized chemical first $Bi_2Sr_2Ca_{n-1}Cu_nO_{2n+4+\delta}$. BSCCO is the high-temperature superconductor without any rare earth element. BSCCO superconductors, after their discovery, gave a new direction to high-temperature superconductivity. BSCCO superconductors are one of the most studied superconductors.

There are three superconducting compounds in the BSCCO family: they are $Bi_2Sr_2CuO_{6+\delta}$ (n=1, denoted as $Bi\ 2201$) having T_c around 20 K, $Bi_2Sr_2CaCu_2O_{8+\delta}$ (n=2, denoted as $Bi\ 2212$) having T_c around 85 K and $Bi_2Sr_2Ca_2Cu_3O_{10+\delta}$ (n=3, denoted as $Bi\ 2223$) having T_c around 85 K. $Bi\ 2212$ and $Bi\ 2223$ have T_c above the boiling point of liquid nitrogen, that makes them more useful for various practical applications.

All cuprate superconductors have perovskite-layered crystal structure. BSCCO superconductors have a similar crystal structure; the only difference being the number of CuO₂ planes in the unit cell. There are four main building blocks of the crystal structure: (1) BiO plane, (2) SrO plane, (3) Ca plane, and (4) CuO₂ plane. The BiO and SrO planes work as the charge reservoir. The crystal structure of BSCCO superconductors can be seen as CuO₂ planes stacked with Ca planes and BiO planes sandwiched between SrO planes. For n>1, all members have CuO₂ planes separated by Ca atoms and covered by SrO planes in the *Z*-direction [26].

BSCCO superconductors exhibit multi-element complex phase diagrams and are highly sensitive to synthesis methods and processing conditions. The temperature range for single-phase formation, particularly for Bi 2223, is extremely narrow, making synthesis quite challenging [27].

1.5.1 Bi₂Sr₂CuO₆ crystal structure:

 $Bi_2Sr_2CuO_{6+\delta}(Bi\ 2201)$ superconductor has T_c around 20 K. It has one CuO_2 layer sandwiched between SrO plane and a BiO plane on each side of the crystal structure. Bi 2201 has an orthorhombic crystal structure with lattice parameters: a=5.36 Å, b=5.37 Å, and c=24.37 Å[28]. The crystal structure for Bi 2201 is shown in Fig. 1.5.

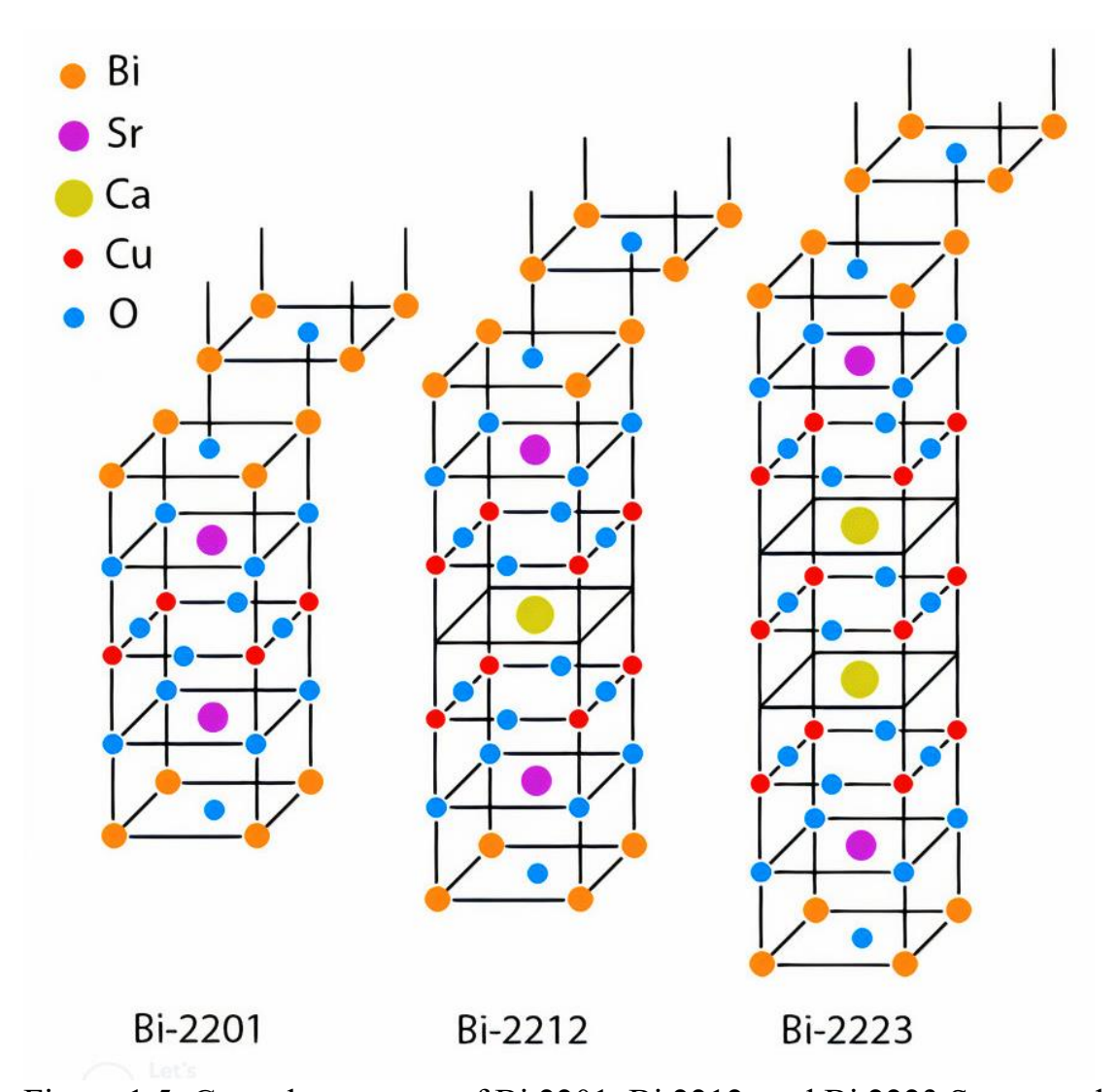


Figure 1.5: Crystal structures of Bi 2201, Bi 2212, and Bi 2223 Superconductors [29].

1.5.2 Bi₂Sr₂CaCu₂O_{8+ δ} crystal structure:

Bi₂Sr₂CaCu₂O_{8+ δ} (Bi 2212) has T_c around 85 K, and it is used for various applications. It has two CuO₂ planes separated by a Ca atom sandwiched between SrO plane and a BiO plane on both sides. The Bi 2212 has orthorhombic crystal structure with cell parameters: a=5.414 Å, b=5.418 Å, and c=30.89 Å [30]. The Crystal structure for the Bi 2212 superconductor is shown in Fig. 1.5.

1.5.3 Bi₂Sr₂Ca₂Cu₃O_{10+δ} crystal structure:

Bi₂Sr₂CaCu₂O_{10+ δ} (Bi 2223 has T_c around 110 K and is widely studied high-temperature superconductor. It has a similar crystal structure to Bi 2212; the differences are, one extra layer of CuO₂ plane and Ca atom in the unit cell. So, there are three CuO₂ layers separated by two Ca atoms, sandwiched between two SrO layers and then a BiO layer on both sides. The Bi 2223 has orthorhombic

crystal structure with lattice parameters: a= 5.39 Å, b= 5.41 Å, and c= 37.1 Å [31]. The Crystal structure for the Bi 2223 superconductor is shown in Fig. 1.5.

1.6 YBCO and BSCCO comparison

(Y/RE)Ba₂Cu₃O_{7-δ} (Y 123) superconductors have T_c of 92 K and exhibits a perovskite crystal structure similar to BSCCO. It is designed to have a microstructure that supports strong flux pinning, making it suitable for applications requiring high magnetic fields and high critical current densities. The flux pinning is attributed to Y₂BaCuO₅ (Y 211), a non-superconducting phase, found in the YBCO phase diagram. Around 30 vol% of one micron-sized Y 211 particles, distributed uniformly in the Y 123 matrix, are optimum for flux pinning. Y 211 particles create structural defects at the interfaces with the YBCO matrix that contribute to flux pinning [32].

Melt growth (MG) [33] and infiltration growth (IG) [34] are two processes used to fabricate YBCO superconductors with texture by cooling slowly through peritectic transformation temperature (T_p). The IG process is favored because it yields dense and homogeneous materials with better control over the microstructure and uniform distribution of Y 211 particles. However, for BSCCO superconductors, no similar process exists, and its phase formation is highly sensitive to temperature and atmospheric conditions maintained during processing.

Achieving biaxial texture is essential for enhancing J_c in YBCO and is crucial for the high performance of superconducting devices like wires and tapes [35]. HTSc wires/tapes are often fabricated using the powder-in-tube (PIT) method [36], where HTSc powder is filled into a metallic sheath, and is processed to form wires and then thermally treated. Control of processing parameters, such as temperature and deformation during wire drawing, are crucial for promoting biaxial texture. For YBCO, advanced methods such as pulsed laser deposition (PLD) and metalorganic chemical vapor deposition (MOCVD) are used to deposit thin films of YBCO on suitable substrates [37], which makes YBCO-coated conductors very costly as compared to BSCCO-tapes. Although BSCCO wires/tapes are economical, their utility has remained limited as they exhibit high flux creep. Much below the upper critical field (Bc₂) in HTSc, the rapid decrease in J_c on increasing the magnetic field and temperature is due to flux creep.

To arrest the flux creep in YBCO, defect generation by optimizing processing conditions and by secondary phase addition is explored and reported in the literature [38–40]. However, for BSCCO, although there are multiple reports of secondary phase addition, there has not been as firmly established success, unlike

in the case of YBCO. A detailed literature survey on the secondary phase addition to BSCCO superconductors is given below.

1.7 Literature Survey on BSCCO and the effect of secondary phase additions

After the discovery of BSCCO superconductors by Maeda et al., various research groups across the globe started to take an interest in BSCCO superconductors. Making single-phase Bi 2223 was still a challenge. Due to the narrow formation window for Bi 2223, Bi 2212, Bi 2201, and other secondary phases are also formed along with it.

Various groups reported that Pb substitution in place of Bi significantly increases the Bi 2223 phase. It was reported that the Pb substitution makes the reaction path advantageous for Bi 2223 phase formation and increases the thermodynamic stability of the Bi 2223 phase [41,42].

Bulk Bi 2223/Bi 2212 superconductors have drawn much interest because of their high T_c and superior superconducting properties. However, their practical uses have been constrained due to their low J_c and poor flux pinning properties. Researchers have investigated adding secondary phases to the matrix to improve performance. This literature review gives an overview of the research done to determine how adding secondary phases affected the bulk superconducting and flux pinning characteristics.

Various groups attempted Ga addition to Bi 2212 superconductors [43–45]. The consistent observation was the reduction in the Bi 2212 phase and Tc with increasing Ga content. Formation of the Ga-containing phase at a high content of Ga addition was also reported. Awana et al. [44] reported that the lattice parameter *c* contracts with Ga addition, indicating that Ga substitutes the Cu site. Dimmeso et al. [45] argued that the sample with the highest Ga content at low temperatures has better J_c due to effective flux pinning by the Ga-containing secondary phase, whereas Kazin et al. [43] claimed that the inclusion of Ga had no impact on the flux pinning properties of the Bi 2212 superconductor.

Amira et al. reported that Zn, in addition to Bi 2212 superconductor, deteriorates superconducting properties. Porosity increases, the T_c and Bi 2212 phase reduces, and Zn substitutes the Cu site [46]. The c parameter reduces, whereas Lovleena et al. argued that the a and b parameter increases, but there is no appreciable change in the c parameter [47]. Recently, Mandal et al. reported that the superconducting properties of Zn-doped Bi₂Sr₂CaCu_{1.85}Zn_{0.15}O_y samples are better than those of pure Bi 2212 superconductors. The decrease in T_c was consistent like others, but J_c, F_p, and irreversible field improved after Zn doping [48].

Superconducting properties of Bi 2212 superconductor are little affected by the addition of Ag; 30 vol. % Ag addition to Bi 2212 improves the hardness and fracture toughness, as reported by Singh et al. [49]. However, Madre et al. [50] reported that Ag addition is ineffective in improving mechanical properties. However, both reported that T_c and J_c do not increase much, and the melting onset decreases with Ag addition. Chen et al. [51] reported that texturing in 10 wt.% Ag added Bi 2212 samples is increased when melt processed in the high magnetic field.

Bi 2212 superconductors prepared using spark plasma sintering with potassium substitution are better than pure Bi 2212 superconductors. Due to similar ionic radii, K substitutes at the Ca site. Texturing and T_c improve with K substitution, and J_c and F_p increase. Bulk density is also improved for samples with low conc. of K substitution[52].

Yu et al. reported that Sb doesn't enter the Bi 2212 lattice site when doped at low concentration as the T_c remains constant with Sb content. Bi 2212 phase fraction reduces with the increase of Sb content. The formation of the monoclinic Bi₄Sr₄Ca₂SbO₄ phase was confirmed by TEM analysis [53].

A systematic work on the addition/substitution of RE (rare earth or Y) on Pb added (Bi, Pb)_{2.1}Sr₂Ca_{1.1}Cu_{2.1}(RE)_yO_{8+ δ} superconductors was reported by Biju et al. The following are the expected conclusions of their research.

- a) The RE substitute to the cationic atom (Bi/Sr/Ca/Cu) has an ionic radius nearly equal to the RE ion.
- b) At low concentrations of RE ion, the superconducting properties improve, but at higher concentrations, the formation of the secondary phase leads to deterioration of superconducting properties.
- c) The Bi 2212 phase formation is promoted within the solubility limit of RE ion to Bi 2212.

Bi_{1.7}Pb_{0.4}Sr₂Ca_{2.1}Nd_xCu_{2.1}O_{8+ δ} superconductor shows best properties when x=0.2-0.3, and when Nd concentration exceeds x= 0.3, the superconducting properties deteriorate. T_c, J_c, and F_p improve with Nd addition except for x= 0.5. No Nd containing the second phase was detected. Infield flux pinning properties were improved. It was reported that the Nd³⁺ ion is substituting to the Bi site due to their nearly equal radii [54]. Similar results were also reported for Bi_{1.6}Pb_{0.5}Sr_{2-x} Dy_xCa_{2.1} Cu_{2.1}O_{8+ δ}. For x= 0.2, the superconductor has the best performance. T_c, Δ T_c, and porosity increase with Dy content. For x= 0.5, the sample has poor performance. It was also reported that T_c and J_c don't depend strongly on the microstructure. Dy³⁺ ion substitutes to Sr site [55].

Y addition to Bi,Pb 2212 is also effective in enhancing T_c and J_c . For $Bi_{1.7}Pb_{0.4}Sr_{2.1}Ca_{2.1}Y_xCu_{2.1}O_{8+\delta}$ superconductor, Bi 2212 phase fraction decreases with increasing Y content. Y^{3+} ion can substitute at Ca/Sr site, depending on the concentration of Y. Microstructure and intergrain connection deteriorates with Y content, whereas porosity increases. Transport J_c improves at low conc. but decreases at high conc. of Y addition[56].

Ce addition to $Bi_{1.7}Pb_{0.4}Sr_{2.1}Ca_{1.1}Ce_xCu_{2.1}O_{8+\delta}$ is found to be effective when the Ce content is low (<0.2). Ce addition favors the Bi 2212 phase formation, T_c , and transport J_c increases till Ce < 0.2. Density and lattice parameter c decreases with Ce content. Ce is substituted to the Ca/Sr site. Ce addition provides nano defects that contribute to effective pinning [57]. Sotelo et al. reported that $Bi_2Sr_2Ca_1$ $xCe_xCu_2O8_{+\delta}$ (for x=0,0.01,0.05,0.1, and 0.25) superconductor's performance deteriorates after Ce addition. Although no Ce-containing secondary phase was formed, the T_c and flux pinning energy decreased with Ce content. The Irreversible field (B_{irr}) decreases, and the Irreversibility line (IL) shifts to lower fields [58].

Several groups report Yb addition to the Bi 2212 system. Sarun et al. reported that $Bi_{1.7}Pb_{0.4}Sr_{1.8}Yb_{0.2}Ca_{1.1}Cu_{2.1}O_{8+\delta}$ superconductor shows better properties than pure Bi 2212. Its T_c , J_c , texturing, and flux pinning improve after Yb substitution [59]. Similar results were also reported by Zhang et al. Additionally, they report that density is better for Yb-added $Bi_2Sr_{2-x}Yb_xCa_1Cu_2O_{8+\delta}$ samples. They attribute this improvement of superconducting properties to the normal point pinning provided by the nano defects due to Yb addition [60]. Sotelo et al. reported the adverse effect of Yb addition on $Bi_2Sr_2Ca_1Cu_{2-x}Yb_xO_{8+\delta}$. They reported that T_c and Flux pinning energy decreases with Yb content. The decrease in flux pinning energy is due to increased weak links among Bi 2212 grains after Yb addition [61].

MgO addition to Bi 2212 is found to improve superconducting properties to some extent. At low concentrations, the MgO particles are embedded in Bi 2212 grains, resulting in improved grain connectivity. No effect on T_c was observed, but ΔT_c and superconducting fraction decreased with MgO content [62].

When MgO particles were added to Bi 2212 by an optimized Nitrated method, Kazin et al. observed that the Mg_{1-x}Cu_xO particles were distributed uniformly throughout the material matrix. Smaller MgO additions resulted in the formation and even distribution of Mg_{1-x}Cu_xO_y particles in the size range of 0.2 to 0.4 microns in Bi 2212 grains. T_c did not alter in any way. They claimed that Mg_{1-x}Cu_xO_y particles help to pin the flux effectively, which improves the J_c-B characteristics. [63].

The effect of MgB₂ particles addition to Bi 2212 was reported by Vinod et al. They reported that at critical conc. of MgB₂, the J_c-B properties improved, and the irreversibility line shifted to higher field and temperature after MgB₂ addition. The layered grain growth got disturbed after MgB₂ addition. No effect on T_c and no presence of Mg containing secondary phase was reported [64].

Interfacial pinning is improved, and effective flux pinning is ensured throughout the material by a homogeneous dispersion of nanoparticles throughout the matrix. Only a few reports of nanoparticles adding to Bi 2212 superconductor are available. An interesting claim by Wei et al. suggests that nano MgO is compatible with Bi 2212 up to 20 mol. %. They also reported that no change in T_c and lattice parameters was observed after adding nano MgO. They added both (20 mol. %), micron and nano size MgO to Bi 2212; not much change in the magnetic hysteresis was observed for micron-sized MgO added Bi 2212 sample however, for nano MgO added Bi 2212 samples show larger hysteresis loops at 27 K, this was attributed to enhanced flux pinning by nano MgO addition [65].

Investigations are also conducted on the effects of adding noble metal (Ag, Au) nanoparticles to the Bi 2212 superconductor. Ag nanoparticle addition is found to improve intergranular coupling among the grains. An increase of nearly 60% in J_c is found for the Bi 2212 sample with 0.25 wt.% nano Ag addition. Bulk density and irreversible field also increase with Ag addition. Change in the thermodynamic properties due to Ag addition leads to the formation of highly crystallized grain boundaries of proper thickness that contribute to effective flux pinning. Analysis of flux pinning reveals that the nature of pinning changes to surface pinning after Ag addition [66]. However, no change in J_c was observed for nano-Au added Bi 2212 samples. Nano Au addition helps in the crystallization of the Bi 2212 phase. No appreciable change in the lattice parameters was observed. T_c and ΔT_c decrease with nano Au addition. A slight improvement in J_c for the Bi 2212 sample with the highest amount of nano Au is attributed to improved effective pinning by Au nanoparticles [67].

 M_xO_y (M= Al, Sn, W) nanoparticle addition to Bi 2212 is also reported. Nano Al_2O_3 addition is found to react with Bi 2212 to form an Al-containing secondary phase. T_c reduces after nano Al_2O_3 addition, but flux pinning improves [68]. Nano WO_3 addition to Bi 2212 has a negative effect. W enters the lattice or forms a secondary phase, suppressing the T_c or lowering the Bi 2212 phase content. The granular morphology of Bi 2212 grain is also affected after nano WO_3 addition. Transition width increases, whereas J_c decreases with nano WO_3 addition [69].

Table 1.1: Comparison of second phase addition to Bi 2212 reported in literature.

S. No.	Dopant	Results	Ref.	
1	Zn	T _c reduces with Zn. B _{irr} and F _p improve. Zero field J _c increases	[48]	
		from 12 kA/cm ² (pure Bi 2212) to 30 kA/cm ² at 5 K for Zn		
		added Bi 2212 sample. No effect on microstructure was		
		observed. J _c falls to zero at higher temperatures.		
2	Ag	T _c (Onset) increases after Ag addition. J _c improves slightly (2.2	[50]	
		kA/cm ² to 2.7 kA/cm ²) at 15 K for sample with Ag addition. Bi		
		2212 grain size also increases after Ag addition. No data on		
		higher temperatures		
3	K	T _c , J _c and F _p improve. Zero field J _c increases (40 kA/cm ² (pure	[52]	
		Bi 2212) to 125 kA/cm ²) at 4.2 K for K added Bi 2212 sample		
		but drops to zero at 6 T field. Texturing and Bi 2212 grain size		
		increases after K addition. No data on higher temperatures.		
4	MgB_2	T _c is unaffected, J _c improves at low conc. (till 0.1 wt.%) and	[64]	
		then decreases at 64 K. In field performance improves to 0.1		
		wt.% of MgB ₂ addition. Grain size decreases at higher conc.		
		No data on higher temperatures.		
5	Nano	T _c was constant, grain coupling improved after nano Ag	[66]	
	Ag	addition. Bulk density and grain size also improves after nano		
		Ag addition. Zero field J _c increases (almost double) but		
		becomes nearly equal at 1 T applied field at 4.2 K and the J _c		
_		for all samples nearly vanishes at 6 T.		
6	Nano	T _c decreases with nano WO ₃ . The J _c decreases with WO ₃	[69]	
	WO ₃	content and becomes zero around 2 T applied field at 10 K.		
7	CNT	T _c decreases after adding CNT. CNT added samples possess	[70]	
_		better pinning properties. No data on J _c .		
8	Nano	T _c , grain size, J _c and F _p improve with SiO ₂ content. Zero field	[71]	
	SiO ₂	J_c is better for samples with SiO_2 but the J_c vanishes around 3 T		
		applied field at 10 K. No data available at high temperatures.		

The effect of nano SnO_2 addition to Na substituted $Bi_2Sr_{2-x}(SnO_2)_xCaCu_{1.75}Na_{0.25}O_y$ superconductor is found to enhance Bi 2212 phase content when the SnO_2 content is low. Nano SnO_2 doesn't enter the lattice, but T_c and J_c decline with nano SnO_2 addition [72]. Imran et al. reported that T_c and ΔT_c for $Bi1_.6Pb_{0.4}Sr_2CaCu_2(SnO_2)_xO_y$ sample doesn't change when SnO_2 addition 2 wt.%. Flakiness for Bi 2212 grains increases with nano SnO_2 addition. Enhancement of flux pinning and J_c (for < 2wt.%) is attributed to nano SnO_2 addition [73].

Carbon nanotubes (CNT) addition to Bi 2212 superconductor was reported by Koblischka et al. CNT can be added to superconductors based on compatibility as an alternative to columnar defects. CNT addition causes the formation of secondary phases like (Sr,Ca)CuO, CuO, etc. These phases contribute to flux pinning if dispersed uniformly in the Bi 2212 matrix. A slight depression in T_c is

observed for the CNT-added sample, but the pinning properties are improved [70].

A recent study on Bi 2212 nanofibers doped with nano SiO₂ particles suggests that an appropriate amount of nano SiO₂ promotes Bi 2212 phase formation. T_c and Bi 2212 grain size increase with nano SiO₂ addition. Nano SiO₂ can enhance grain connectivity, morphology, grain orientation, and structure distortion, generating pining centers and contributing to effective pinning. The J_c improves with SiO₂ addition, 0.2 wt.% SiO₂ added Bi 2212 sample has the highest J_c (15 kA/cm² at 10 K). The flux pinning mechanism changes to surface pinning due to pinning centers generated by nano SiO₂ addition [71].

Although Bi 2212 is more stable than Bi 2223, elements of the added phase can go to the lattice and suppress the T_c or readily react with it to generate a secondary phase. The added phase may not be compatible with the microstructure as it can generate cracks or voids. The agglomerated secondary phase in the BSCCO matrix doesn't always facilitate flux pinning. The addition of a secondary phase, either nanometer- or micron-sized, to Bi 2223 has been reported in the literature to enhance several properties.

Bi 2223/ Ag is the most studied system. The effect of Ag addition to Bi 2223 superconductors has a mixed response, as reported by various researchers. Ag addition enhances the rate of Bi 2223 phase formation, and this rate strongly depends on the form of Ag additive. At higher conc. (> 25 wt.%) the Bi 2223 phase fraction reduces [74]. Ag addition doesn't improve superconducting properties and creates weak links [75]. Dou et al. reported that no effect of Ag addition on T_c, J_c, and lattice parameters was observed when processed in a partial Oxygen atmosphere. Still, superconducting properties deteriorated when processed in air [76]. Connectivity among grains improves with Ag addition. Bi 2223 phase fraction increases till 60 wt.% Ag addition. No effect of T_c was observed, as reported by Mastsuhita et al. [77]. Savvides et al. reported that T_c is constant, but J_c and flux pinning improves with 20-30 wt.% Ag addition to Bi 2223 superconductors [78]. Ag addition provides a plastic flow region that allows the relaxation of undesirable residual stress from the grain anisotropy of the superconductor, increasing the mechanical strength for Ag-added Bi 2223 samples. J_c improves with Ag addition (10-20 wt.%). No effect on T_c was observed [49].

 Ag_2O addition to Bi, Pb 2223 promotes degradation of the high T_c phase when sintered at high temperatures. Platelet-like grain size morphology corresponding to the Bi 2223 phase increases with Ag_2O addition. Ag peaks in the XRD pattern increase with Ag_2O content. No effect on T_c was reported [79].

Mishra et al. reported that Nb substitution to both (Bi, Cu) sites decreases Tc, but the decrease is much faster in the case of Cu site substitution. Nb substitution causes a reduction in the Bi 2223 phase and an increase in the Bi 2212 and Bi 2201 phase. Nb substitution on the Cu site has a more drastic effect than the Bi site [80]. Sozeri et al. reported that Nb addition enhances Bi 2223 phase formation till x = 0.1 in $Bi1.6Pb0.4Sr_2Ca_2Cu_3Nb_xO_y$ compound. The change in lattice parameters suggests that the Nb solubility is low (x<0.2). Nb substitutes the Bi site and improves coupling among grains T_c and J_c [81].

Various groups investigated the effect of adding metal oxides as secondary phases to Bi 2223 superconductor. Grivel et al. studied the impact of MnO and TiO₂ on Bi 2223 separately. The findings of both (MnO and TiO₂) addition are nearly similar, like decreases in T_c, formation of secondary phase, and for high conc. (7-10 wt.%)) of MnO/TiO₂ addition, the Bi 2223 phase formation was incomplete. Not much change in lattice parameters was reported [82,83].

ZnO (0- 50wt.%) addition to Bi 2223 was studied by Kozuka et al. XRD patterns show ZnO peaks, but no Zn-containing secondary phase was formed. The solid solution solubility of Zn is around 2 wt.% for 0-2 wt.% ZnO addition, the J_c is constant but decreases on further increasing ZnO content. Zn ion substitutes to Cu site. Lattice parameters change (increases, b and c decrease). T_c was unaffected by ZnO addition [84].

An interesting study on the reinforced MgO whiskers to Bi,Pb 2223 composites was reported by Yuan et al. T_c was immune till 20 vol.% MgO whisker addition. J_c decreases with MgO addition due to Bi,Pb 2223 matrix microstructural changes. An annealing for a longer duration can improve Bi 2223 microstructure by enhancing grain growth and eliminating grain boundaries. Repeated hot pressing improved J_c for Bi 2223, and MgO whiskers added Bi 2223 composites by densifying [85].

ZrO₂ addition to Bi,Pb 2223 causes decreases in T_c. The Bi 2223 phase fraction also reduces, whereas the Bi 2212 phase fraction increases with ZrO₂ content. ZrO₂ incorporates Bi 2223 without reacting at low concentration [86].

The effect of rare earth ion doping on Bi 2223 superconductors effectively enhances superconducting properties within their solubility limit. Bi_{1.8}Pb_{0.35}Sr_{1.9}Ca_{2.1}Cu₃Gd_xO_y superconductor surface morphology is degraded, and the grain size decreases after Gd addition. For x>0.3, secondary phases like Bi 2212 and Ca₂PbO₄ increased. Gd free sample has more extensive and uniform grains with better grain alignment. Grain connectivity worsens, and T_c and transport J c decrease with Gd addition. The reduction in superconducting

properties of Gd-added Bi 2223 superconductors is due to a lower fraction of the high T_c phase and changes in the electronic properties of grain boundaries caused by the presence of Gd ions [87].

At very low conc. Nd addition to Bi_{1.8}Pb_{0.35}Sr₂Ca_{2.1}Cu_{3.1}Nd_xO_y superconductor enhances self-field J_c and flux pinning strength. Pinning force maxima shifts to a higher field. For x>0.03 Nd, addition results in Bi 2212 and Ca2PbO4 formation. At high conc. of Nd addition, Bi 2212 is the major phase. No secondary phase containing Nd was reported. Nd substitutes to the Ca site [88]. Lee et al. reported that Bi 2223 phase disappeared around x= 0.1 for Bi_{1.84}Pb_{0.34}Sr_{1.91}(Ca_{1-x}Nd_x)_{2.03}Cu_{3.1}O_y superconductor. Lattice parameters change (a &b increases, c decreases), and T_c reduces with Nd content. The solubility limit of Nd in Bi 2223 is approximately x<0.015 [89].

XRD peaks corresponding to the Bi 2223 phase start diminishing with increasing Pr content to $Bi_{1.6}Pb_{0.4}Sr_2Ca_{2-x}Sm_xCu_3O_y$ superconductor, whereas Bi 2212 phase peaks increase. Lattice parameters were unchanged, but T_c decreases with Pr addition [90]. Kishore et al. reported similar results of Sm addition to $Bi_{1.7}Pb_{0.3}Sr_2Ca_{2-x}Pr_xCu_3O_y$; furthermore, they reported that the magnetic moment of R.E. ion doesn't play any role in suppressing the superconducting properties, Sm^{3+} ion provides electrons that causes a decrease in the hole conc. and deteriorates the superconducting properties. The solubility limit of Sm addition is around x=0.02, and Sm has lesser solubility than Pr [91].

The effect of Y substitution on Bi_{1.7}Pb_{0.3}Sr₂Ca_{2-x}Y_xCu₃O₁₀ superconductors is similar to that of all rare earths. Bi 2223 can react with Y at high temperatures and form Bi 2212. The Bi 2223 phase content decreases with Y addition. At high conc. In the Y addition, the formation of the Bi 2223 phase is not favored [92]. Sedky et al. reported that lattice parameter c decreases with increases in Y content. T_c and Bi 2223 phase decreases with Y content. Y has more solubility than other R.E. [93].

Kazin et al. reported a study on the interaction of $Sr_{1-x}Ca_xZrO_3$ to Bi 2223 superconductors. They added $(Bi,Pb)_2Sr_2Ca_2Cu_3O_y$ and $Sr_{1-x}Ca_xZrO_3$ in a 2:1 molar ratio. For x=0.2, the Bi 2223 phase remained unchanged. For higher values of x, the Bi 2223 phase increases with annealing time. Lattice parameter c decreases with increasing Ca content or c 0.0 a little effect on c 0.2 was observed [94].

Studies on the interaction of various nanoparticles to Bi 2223 are also reported. Jia et al. reported that nano ZrO₂ addition below 20 mol.% to Bi_{1.8}Pb_{0.4}Sr₂Ca₂Cu₃O_y improves J_c without affecting T_c. Above 20 mol.% nano

 ZrO_2 addition results in the decrease of J_c and broadening of ΔT_c . SEM analysis reveals that ZrO_2 dispersed homogeneously in the Bi 2223 matrix [95]. Similar results were also reported by Zouaoui et al. They reported that Bi 2223 sample with 0.1 wt.% nano ZrO_2 exhibits the best J_c and the highest H_{irr} . The activation energy and F_p improve with nano ZrO_2 addition. Sharp interface b/w nanosized ZrO_2 and Bi 2223 phase provide effective normal surface pinning [96].

Low conc. (0.2 wt.%) of nano Al₂O₃ addition to Bi_{1.6}Pb_{0.4}Sr_{1.9}Ca_{2.1}Cu₃O_y is effective in improving J_c. Al₂O₃ nanoparticles were found to be embedded in the Bi 2223 grains at low conc., but at higher conc. it agglomerates. Higher conc. of nano Al₂O₃ results in incomplete Bi 2223 phase formation. T_c decreases with Al₂O₃ addition [97].

Nano Ag addition is effective in enhancing superconducting properties. Skyorova et al. reported that adding Ag improves the connectivity among the grains, reduces weak links, and improves J_c . Samples with 15 wt.% nano Ag addition have almost three times J_c compared to pure Bi 2223 samples. Bi 2223 phase fraction, texturing, and T_c improve with nano-Ag addition [98]. Mawassi et al. reported that the Bi 2223 phase fraction decreases, whereas intensity for $Sr_{2.5}Bi_{0.5}Pb_3Ca_2CuO_y$ (non-superconducting) phase increases with nano-Ag addition. Bi 2223 platelet size also decreases with Ag addition. No change in lattice parameters and T_c was observed. The increase in ΔT_c is seen due to the formation of the secondary phase. Grain connectivity and J_c improve with nano-Ag addition [99].

The bulk density improves with nano SnO_2 addition to $Bi_{1.7-x}Pb_{0.3}Sn_xSr_2Ca_2Cu_3O_y$ superconductor. T_c decreases for Sn x>0.1 samples and shifts to lower temperatures. SnO_2 addition degrades the grain connectivity, Bi 2223 platelet size decreases, voids, and porosity increase. Overall, SnO_2 nanoparticles have a degradation effect on Bi 2223 [100].

A recent study on adding cubic-shaped modified TiO₂ nanoparticles to Bi 2223 found it to have a vital and destructive effect on the conductivity, orientation, and morphology of grains. Bi 2223 phase decreases with TiO₂ addition. TiO₂ nanoparticles prevent the growth of Bi 2223 grains, which reduces average grain size. T_c decreases, but J_c improves with nano TiO₂ addition [101].

The above literature brings out the efforts made to generate a microstructure of BSCCO with a suitable second phase, which can be introduced uniformly in sufficient amounts, without agglomeration in the superconducting matrix, and provide effective pinning of flux and enhance current densities at temperatures 30 K to 77 K.

Table 1.2: A comparison of various second phase addition to Bi 2223

S. No.	Dopant	Results	Ref.
1	Nb ₂ O ₃	Bi 2223 phase and T_c increase at low Nb content. At higher concentration, it agglomerates and causes deterioriation in transpot J_c at 50 K and 77 K. Microstructures and J_c are not given.	[81]
2	MgO	At higher of MgO content, Bi 2223 grain size and J_c reduce. MgO particles are found embeded in Bi 2223 grains without reaction. T_c remained constant but transition width Δ T_c increased with MgO addition. No data on higher temperatures	[102]
3	Nd ₂ O ₃	At Higher concentration,Nd addition leads to precipitation and reduces the Bi 2212 phase content present in Bi 2223. J_c and F_p improves with Nd addition (at low content). The Peak field in F_p shifts at higher fields after adding Nd. Only transport J_c at 77 K is given.	[88]
4	WO ₃	Bi 2223 phase fraction reduces with W content. J_c decreases with WO $_3$ content at 10- 25 K. No change in morphology of Bi 2223 grains. No data above 25 K.	[103]
5	Nano Ag	Bi 2223 phase conten and platelet size decrease with Ag addition. $T_{\rm c}$ was constant but Δ $T_{\rm c}$ increased with nano Ag addition. Grain connectivity and transport $J_{\rm c}$ improve with nano-Ag addition. No data on $J_{\rm c}$.	[99]
6	Nano MgO	Bi 2223 phase content and $T_{\rm c}$ reduces after nano MgO addition. Bi 2223 platelet size reduces after MgO addition. Voids size and number decreased with MgO addition, and resulted in better grain connectivity. $J_{\rm c}$ data is not given.	[104]
7	Nano Graphene	Bi 2223 phase content increases slightly at low conc. of nano graphene addition. $T_{\rm c}$ remained constant. Transport $J_{\rm c}$ improves for the sample with 1 wt.% nano graphene. The grain alignment improves after nano-graphene addition. No data on $J_{\rm c}$ at high temrpartures.	[105]
8	Nano ZrO ₂	$T_{\rm c}$ remained constant with nano ZrO $_2$ addition. Nano-sized Zr-containing precipitates were found embedded in Bi 2223 grains. $J_{\rm c}$ and $F_{\rm p}$ improve only till 0.2 wt.% of nano ZrO $_2$ addition and then decreases at 77 K.	[96]

Adding nanoparticles to the superconductor matrix is a viable way to improve the superconducting and flux pinning characteristics of bulk superconductors. When it comes to assessing how well nanoparticles can improve flux pinning and critical current density, factors such as size, concentration, dispersion, and interface quality are crucial. A basis for further research and improvement of bulk superconductors doped with nanoparticles, such as Bi 2212/Bi2223, is laid forth in the literature review, emphasizing the importance of nanoparticle addition. As shown in Tables 1.1 and 1.2, there is a lack of literature documenting

enhancements in superconducting properties at moderate temperatures (10 K - 77 K) and higher magnetic fields. Thus, there remains a quest for appropriate secondary phases to enhance superconducting properties in the temperature range of 10 K to 77 K, along with a method to incorporate them into the BSCCO matrix without inducing reactions and generate a 2-phase microstructure as Y-211 in Y-123.

1.8 Motivation and aim of present work

- A) Develop a methodology to add secondary phase particles to BSCCO superconductors without agglomeration.
- B) To understand why only low conc. of secondary phase addition is effective.
- C) Develop a process to avoid substitution of dopant to lattice.
- D) Generate an optimized microstructure like YBCO superconductors in BSCCO for better superconducting properties at higher fields.
- E) Study the effect of various nanoparticles addition on the structural, microstructural, and superconducting properties of BSCCO superconductors.

Present work adapts several methodologies to shine light on the problems discussed above and tries to find a solution. For this purpose, BSCCO superconductor with general formula $(Bi_1Pb)_2Sr_2(Ca_{0.86}Sr_{0.14})_{n-1}Cu_nO_y$ [106] is chosen. It is a well-studied system. For n= 2, it is $Bi_2Sr_2Ca_{0.86}Cu_2O_y$ and has T_c around 85 K, and for n= 5 and normalized to 3 Cu atoms per unit cell, it is $Bi_{1.2}Pb_{0.3}Sr_{1.54}Ca_{2.06}Cu_3O_y$ with T_c around 105 K and for n= ∞ , it is $Ca_{0.86}Sr_{0.14}CuO_2$ phase and it is non-superconducting.

This work focuses on investigating the effect of adding various nanoparticles (WO₃, ZrO₂, and Ca_{0.86}Sr_{0.14}CuO₂) on modifying the microstructure and influencing the superconducting properties of $(Bi,Pb)_2$ Sr₂ $(Ca_{0.86}Sr_{0.14})_{n-1}Cu_nO_y$ superconductors, at various temperatures and field regimes.

1.9 Organization of the thesis

The thesis is organized into six chapters. The first chapter of the thesis describes the basic properties of superconductors, historical background, and recent developments in the superconductivity area, a literature survey on the second phase addition to BSCCO superconductors, and the motivation for the present work. In the second chapter, various experimental techniques and theoretical models used are described.

In the third chapter, the synthesis of WO₃ nanoparticles and the effect of nano WO₃ addition on the microstructure and flux pinning properties of Bi 2212 are discussed in detail. The structural and superconducting properties are investigated

for various concentrations of nano WO₃ addition, and results are compared with pure Bi 2212 sample. Various techniques like XRD, FESEM, Edax, M-T, and M-H are used to study microstructural and flux pinning properties. The T_c decreases due to W substituting lattice and J_c, and flux pinning properties improve due to adequate flux pinning provided by WO₃ nanoparticles. Second phase (WSr₂CuO₆) phase particles generated by the reaction of WO₃ increase with WO₃ content and contribute to improving effective pinning in Bi 2212 composites.

The fourth chapter discusses the effect of WO₃ nanoparticle addition to Bi 2223 superconductors is also discussed in detail. The T_c remains constant (105 K) when nanoparticles are added to the processed Bi 2223 precursor powder, suggesting no lattice substitution. At low concentrations of nanoparticle addition, the superconducting properties are better than pure Bi 2223. WO₃ nanoparticles help improve J_c - B behavior at higher fields and temperatures. Microstructural analysis reveals that precipitates of W containing phase are present at the high concentration of WO₃ addition. WO₃ nanoparticles are effective in sustaining J_c and F_p at higher fields as revealed by flux pinning analysis.

The fifth chapter discusses the synthesis of Ca_{0.86}Sr_{0.14}CuO₂ phase powder by Nitrate synthesis. A composite with 20 mol.% Ca_{0.86}Sr_{0.14}CuO₂ addition to Bi 2223 powder was made, and the effect of ZrO₂ nanoparticles addition on this composite's microstructural and superconducting properties is discussed in detail. T_c was unaffected by the addition of ZrO₂ nanoparticles. At higher conc. of ZrO₂ nanoparticles addition, the Bi 2223 phase formation was inhibited, and the major phase was Bi 2212. Irreversible field increases after adding nanoparticles, suggesting these particles help enhance the flux pinning properties. ZrO₂ nanoparticles create defects in the Bi 2223 matrix that help improve J_c- B behavior, as revealed by microstructural analysis. Flux pinning analysis shows that surface defects generated by ZrO₂ nanoparticles are improving flux pinning properties at higher fields.

The Sixth chapter discusses the synthesis of (Ca,Sr)CuO₂ phase particles. To improve flux pinning properties, we added (Ca,Sr)CuO₂ particles to Bi 2223, by taking the analogy of Y 211 from YBCO phase diagram. Synthesis and characterization of (Ca,Sr)₂CuO₂ phase particles are discussed. The size of the (Ca,Sr)CuO₂ phase particles before adding them was around a few hundred nanometres. Microstructural analysis revealed that the (Ca,Sr)CuO₂ phase particles break into needle-shaped precipitates with dimensions around 40-80 nm. The concentration of these needled-shaped particles increases with the (Ca,Sr)CuO₂ phase content. XRD analysis revealed that the major phase is Bi 2223 and (Ca,Sr)CuO₂ phase peaks are also present. M-T curves suggest that

T_c(Onset) is consistent with (Ca,Sr)CuO₂ phase addition, suggesting no substitution to lattice, but the Meissner fraction is reduced. These nanometre sized needle-shaped precipitates are found to be distributed at grain boundaries without reacting with Bi 2223 grains. The superconducting properties improve with the Ca,Sr)CuO₂ phase content. Flux pinning analysis revealed that the flux pinning mechanism changes after adding (Ca,Sr)CuO₂ phase particles, and the pinning from needle-shaped particles is evident at moderate temperatures.

The seventh chapter summarizes the results obtained from various measurements and compares the impact of various nanoparticles introduced into Bi 2212, Bi 2223, and Ca_{0.86}Sr_{0.14}CuO₂ added Bi 2223 composites. It also summarizes various conclusions drawn from the research presented in the thesis.

References:

- [1] D. Van Delft, P. Kes, The discovery of superconductivity, Phys. Today. 63 (2010) 38–43. https://doi.org/10.1063/1.3490499.
- [2] A.C. Rose-Innes, E.H. Rhoderick, A.M. Goldman, Introduction to Superconductivity, Am. J. Phys. 38 (1970) 1048–1049. https://doi.org/10.1119/1.1976539.
- [3] W. Meissner, R. Ochsenfeld, Ein neuer Effekt bei Eintritt der Supraleitfahigkeit, Naturwissenschaften. 21 (1933) 787–788. https://doi.org/10.1007/BF01504252.
- [4] C.J. Gorter, H. Casimir, On supraconductivity I, Physica. 1 (1934) 306–320. https://doi.org/10.1016/S0031-8914(34)90037-9.
- [5] F. London and H. London, The electromagnetic equations of the supraconductor, Proc. R. Soc. London. Ser. A Math. Phys. Sci. 149 (1935) 71–88. https://doi.org/10.1098/rspa.1935.0048.
- [6] V.L. Ginzburg, L.D. Landau, On the Theory of Superconductivity, in: Supercond. Superfluidity, Springer Berlin Heidelberg, Berlin, Heidelberg, 1950: pp. 113–137. https://doi.org/10.1007/978-3-540-68008-6 4.
- [7] Alfred Brian Pippard and William Lawrence Bragg, An experimental and theoretical study of the relation between magnetic field and current in a superconductor, Proc. R. Soc. London. Ser. A. Math. Phys. Sci. 216 (1953) 547–568. https://doi.org/10.1098/rspa.1953.0040.
- [8] A.A. Abrikosov, Abrikosov, Type II Superconductivity, Sov-Phys JETP 5, 1174 (1957).pdf, Sov. Phys. JETP. 5 (1957) 1174.
- [9] J.R.S. J. Bardeen, L. N. Cooper, Theory of superconductivity, Theory Supercond. (2018) 1–332. https://doi.org/10.1201/9780429495700.
- [10] B.D. Josephson, Possible new effects in superconductive tunnelling, Phys. Lett. 1 (1962) 251–253. https://doi.org/10.1016/0031-9163(62)91369-0.
- [11] J.G. Bednorz, K.A. Muller, Possible high T_c superconductivity in the Ba?La?Cu?O system, Z. Phys. B Condens. Matter. 64 (1986) 189–193. https://doi.org/10.1007/BF01303701.

- [12] M.K. Wu, J.R. Ashburn, C.J. Torng, P.H. Hor, R.L. Meng, L. Gao, Z.J. Huang, Y.Q. Wang, C.W. Chu, Superconductivity at 93 K in a new mixed-phase Yb-Ba-Cu-O compound system at ambient pressure, Phys. Rev. Lett. 58 (1987) 908–910. https://doi.org/10.1103/PhysRevLett.58.908.
- [13] H. Maeda, Y. Tanaka, M. Fukutomi, T. Asano, A new High-T_c oxide superconductor without a rare earth element, Jpn. J. Appl. Phys. 27 (1988) L209–L210. https://doi.org/10.1143/JJAP.27.L209.
- [14] L. Gao, Y.Y. Xue, F. Chen, Q. Xiong, R.L. Meng, D. Ramirez, C.W. Chu, J.H. Eggert, H.K. Mao, Superconductivity up to 164 K in HgBa₂Ca_{m-1}Cu_mO_{2m+2+ δ} (m=1, 2, and 3) under quasihydrostatic pressures, Phys. Rev. B. 50 (1994) 4260–4263. https://doi.org/10.1103/PhysRevB.50.4260.
- [15] N. Jun, N. Norimasa, M. Takahiro, Z. Yuji, A. Jun, Superconductivity at 39 K in magnesium diboride, Nature. 410 (2001) 63–64.
- [16] Y. Kamihara, T. Watanabe, M. Hirano, H. Hosono, Iron-Based Layered Superconductor La[O_{1-x} F_x]FeAs (x=0.05-0.12) with $T_c=26$ K, J. Am. Chem. Soc. 130 (2008) 3296–3297. https://doi.org/10.1021/ja800073m.
- [17] A.P. Drozdov, M.I. Eremets, I.A. Troyan, V. Ksenofontov, S.I. Shylin, Conventional superconductivity at 203 kelvin at high pressures in the sulfur hydride system, Nature. 525 (2015) 73–76. https://doi.org/10.1038/nature14964.
- [18] A.P. Drozdov, P.P. Kong, V.S. Minkov, S.P. Besedin, M.A. Kuzovnikov, S. Mozaffari, L. Balicas, F.F. Balakirev, D.E. Graf, V.B. Prakapenka, E. Greenberg, D.A. Knyazev, M. Tkacz, M.I. Eremets, Superconductivity at 250 K in lanthanum hydride under high pressures, Nature. 569 (2019) 528–531. https://doi.org/10.1038/s41586-019-1201-8.
- [19] D. Duan, H. Yu, H. Xie, T. Cui, Ab Initio Approach and Its Impact on Superconductivity, J. Supercond. Nov. Magn. 32 (2019) 53–60. https://doi.org/10.1007/s10948-018-4900-8.
- [20] G. Mebratie Bogale, D. Atnafu Shiferaw, Iron-Based Superconductors, in: High Entropy Mater. Microstruct. Prop., IntechOpen, 2023: p. 38. https://doi.org/10.5772/intechopen.109045.
- [21] O. V. Kharissova, E.M. Kopnin, V. V. Maltsev, N.I. Leonyuk, L.M. León-Rossano, I.Y. Pinus, B.I. Kharisov, Recent advances on bismuth-based 2223 and 2212 superconductors: Synthesis, chemical properties, and principal applications, Crit. Rev. Solid State Mater. Sci. 39 (2014) 253–276. https://doi.org/10.1080/10408436.2013.836073.
- [22] C.P. Bean, Magnetization of hard superconductors, Phys. Rev. Lett. 8 (1962) 250–253. https://doi.org/10.1103/PhysRevLett.8.250.
- [23] V. Ambegaokar, B.I. Halperin, Voltage due to thermal noise in the dc Josephson effect, Phys. Rev. Lett. 22 (1969) 1364–1366. https://doi.org/10.1103/PhysRevLett.22.1364.
- [24] D. Dew-Hughes, Flux pinning mechanisms in type II superconductors, Philos. Mag. 30 (1974) 293–305. https://doi.org/10.1080/14786439808206556.
- [25] E.J. Kramer, Scaling laws for flux pinning in hard superconductors, J. Appl. Phys. 44 (1973) 1360–1370. https://doi.org/10.1063/1.1662353.

- [26] J.M. Tarascon, W.R. McKinnon, P. Barboux, D.M. Hwang, B.G. Bagley, L.H. Greene, G.W. Hull, Y. Lepage, N. Stoffel, M. Giroud, Preparation, structure, and properties of the superconducting compound series Bi₂Sr₂Ca_{n-1}Cu_nO_y with n=1,2, and 3, Phys. Rev. B. 38 (1988) 8885–8892. https://doi.org/10.1103/PhysRevB.38.8885.
- [27] P. Majewski, Materials aspects of the high-temperature superconductors in the system Bi₂O₃-SrO-CaO-CuO, J. Mater. Res. 15 (2000) 854–870. https://doi.org/10.1557/JMR.2000.0123.
- [28] S. Bhan, Y. Khan, B. Rothaemel, Effect of furnace atmosphere on the high-T_c Bi(Pb)-Sr-Ca-Cu-O superconductor, Supercond. Sci. Technol. 2 (1989) 265–268. https://doi.org/10.1088/0953-2048/2/5/003.
- [29] T. Jacobs, Unraveling the cuprate superconductor phase diagram intrinsic tunneling spectroscopy and electrical doping, 2016.
- [30] S.A. Sunshine, T. Siegrist, L.F. Schneemeyer, D.W. Murphy, R.J. Cava, B. Batlogg, R.B. van Dover, R.M. Fleming, S.H. Glarum, S. Nakahara, R. Farrow, J.J. Krajewski, S.M. Zahurak, J. V. Waszczak, J.H. Marshall, P. Marsh, L.W. Rupp, W.F. Peck, Structure and physical properties of single crystals of the 84-K superconductorBi_{2.2}Sr_{2.2}Ca_{0.8}Cu₂O_y, Phys. Rev. B. 38 (1988) 893–896.
- [31] H.W. Zandbergen, Y.K. Huang, M.J. V. Menken, J.N. Li, K. Kadowaki, A.A. Menovsky, G. van Tendeloo, S. Amelinckx, Electron microscopy on the $T_c = 110~K$ (midpoint) phase in the system Bi2O3–SrO–CaO–CuO, Nature. 332 (1988) 620–623. https://doi.org/10.1038/332620a0.
- [32] M. Muralidhar, M. Jirsa, N. Sakai, M. Murakami, Progress in melt-processed (Nd-Sm-Gd)Ba₂Cu₃O_y superconductors, Supercond. Sci. Technol. 16 (2003). https://doi.org/10.1088/0953-2048/16/1/201.
- [33] M. Murakami, S.I. Yoo, Comparative study of critical current densities and flux pinning among a flux-grown (formula presented) single crystal, melt-textured Nd-Ba-Cu-O, and Y-Ba-Cu-O bulks, Phys. Rev. B Condens. Matter Mater. Phys. 59 (1999) 1514–1527. https://doi.org/10.1103/PhysRevB.59.1514.
- [34] E.S. Reddy, T. Rajasekharan, Shape Forming Simultaneous with J_c Enhancement in REBa₂Cu₃O₇ Superconductors, J. Mater. Res. 13 (1998) 2472–2475. https://doi.org/10.1557/JMR.1998.0346.
- [35] S.S. Wang, K. Wu, K. Shi, Q. Liu, Z. Han, Development and evolution of biaxial texture of rolled nickel tapes by ion beam bombardment for high T_c coated conductors, Phys. C Supercond. Its Appl. 407 (2004) 95–102. https://doi.org/10.1016/j.physc.2004.04.026.
- [36] M.H. Pu, W.H. Song, B. Zhao, X.C. Wu, Y.P. Sun, J.J. Du, Enhanced flux pinning in (Bi, Pb)-2223/Ag tapes by slightly over-doped Pb, Supercond. Sci. Technol. 14 (2001) 299–304. https://doi.org/10.1088/0953-2048/14/6/301.
- [37] B.A. Albiss, I.M. Obaidat, Applications of YBCO-coated conductors: A focus on the chemical solution deposition method, J. Mater. Chem. 20 (2010) 1836–1845. https://doi.org/10.1039/b917294g.
- [38] P.M. Swarup Raju, N.D. Kumar, S.P. Kumar Naik, T. Rajasekharan, V. Seshubai, Introduction of Nano Ceria into Infiltration Growth Processed YBCO Superconducting

- Composites, J. Supercond. Nov. Magn. 27 (2014) 2277–2282. https://doi.org/10.1007/s10948-014-2592-2.
- [39] N. Devendra Kumar, T. Rajasekharan, R.C. Gundakaram, V. Seshubai, Extensive nanotwinning: Origin of high current density to high fields in preform-optimized infiltration-growth-processed YBa₂Cu₃O_{7-δ} superconductor, IEEE Trans. Appl. Supercond. 21 (2011) 3612–3620. https://doi.org/10.1109/TASC.2011.2168819.
- [40] S. Pavan Kumar Naik, V.S. Bai, Role of nano and micron-sized inclusions on the oxygen controlled preform optimized infiltration growth processed YBCO superconductors, J. Phys. Chem. Solids. 101 (2017) 65–73. https://doi.org/10.1016/j.jpcs.2016.10.008.
- [41] S. Ikeda, K. Aota, T. Hatano, K. Ogawa, A new mode of modulation observed in the Bi-Pb-Sr-Ca-Cu-O system, Jpn. J. Appl. Phys. 27 (1988) L2040–L2043. https://doi.org/10.1143/JJAP.27.L2040.
- [42] Y. Iwai, Y. Hoshi, H. Saito, M. Takata, Influence of the oxygen partial pressure on the solubility of PbO in the (Bi, Pb)₂Sr₂CaCu₂O_{8+y} superconducting oxides, Phys. C Supercond. Its Appl. 170 (1990) 319–324. https://doi.org/10.1016/0921-4534(90)90330-H.
- [43] P.E. Kazin, V. V. Poltavets, O.N. Poltavets, A.A. Kovalevsky, Y.D. Tretyakov, M. Jansen, Formation of Bi-2212 phase and phase assemblage in Ga-doped BSCCO system, Phys. C Supercond. Its Appl. 324 (1999) 30–38. https://doi.org/10.1016/S0921-4534(99)00444-X.
- [44] V.P.S. Awana, S.K. Agarwal, B. V. Kumaraswamy, B.P. Singh, A. V. Narlikar, Effect of 3d metallic dopants on superconductivity of the Bi ₂CaSr₂Cu₂O₈ system, Supercond. Sci. Technol. 5 (1992) 376–380. https://doi.org/10.1088/0953-2048/5/6/010.
- [45] L. Dimesso, I. Matsubara, T. Ogura, R. Funahashi, H. Yamashita, A. Tampieri, Preparation and characterization of the Ga doped Bi-Sr-Ca-Cu-O system, Phys. C Supercond. Its Appl. 227 (1994) 291–299. https://doi.org/10.1016/0921-4534(94)90084-1.
- [46] F. Bouaïcha, M. Mosbah, A. Amira, N. Boussouf, Effect of Zn doping in Bi (Pb) 2212 superconducting ceramics, 3039 (2006) 3036–3039. https://doi.org/10.1002/pssc.200567038.
- [47] Lovleena, I.K. Bidikin, A.L. Kholkin, B. Kumar, Structural changes in ab-plane of Zn doped Bi-2212 HTSC single crystals, Phys. C Supercond. 451 (2007) 44–48. https://doi.org/10.1016/j.physc.2006.10.003.
- [48] T. Sk, P. Mandal, D. Rakshit, A.K. Ghosh, Physica C: Superconductivity and its applications Drastic enhancement of magnetic critical current density in Zn doped, Phys. C Supercond. Its Appl. 603 (2022) 1354152. https://doi.org/10.1016/j.physc.2022.1354152.
- [49] J. Joo, J.P. Singh, T. Warzynski, A. Grow, R.B. Poeppel, Role of silver addition on mechanical and superconducting properties of high-Tc superconductors, Appl. Supercond. 2 (1994) 401–410. https://doi.org/10.1016/0964-1807(94)90087-6.
- [50] B. Özkurt, M.A. Madre, A. Sotelo, J.C. Diez, Effect of metallic Ag on the properties of Bi-2212 ceramic superconductors, J. Mater. Sci. Mater. Electron. 24 (2013) 3344—

- 3351. https://doi.org/10.1007/s10854-013-1253-8.
- [51] W.P. Chen, H. Maeda, P.X. Zhang, S. Awaji, K. Watanabe, M. Motokawa, Effect of Ag-doping on Texture Development of Bi 2212 Bulks in High Magnetic Field, J. Low Temp. Phys. 117 (1999) 771–775. https://doi.org/10.1023/a:1022509714964.
- [52] S. Zhang, C. Li, Q. Hao, X. Ma, T. Lu, P. Zhang, Optimization of Bi-2212 high temperature superconductors by potassium substitution, Supercond. Sci. Technol. 28 (2015). https://doi.org/10.1088/0953-2048/28/4/045014.
- [53] W.J. Yu, Z.Q. Mao, L. Yang, C.Y. Xu, M.L. Tian, L. Shi, G.E. Zhou, Y. Zhang, Characterization of the (Bi_{2-x}Sb_x)Sr₂CaCu₂O_y system, Phys. C Supercond. 244 (1995) 135–138. https://doi.org/10.1016/0921-4534(95)00031-3.
- [54] P.M. Sarun, A. Biju, P. Guruswamy, U. Syamaprasad, Enhanced Flux Pinning of an Nd-Added (Bi,Pb)-2212 Superconductor, J. Am. Ceram. Soc. 90 (2007) 3138–3141. https://doi.org/10.1111/j.1551-2916.2007.01896.x.
- [55] P.M. Sarun, S. Vinu, R. Shabna, A. Biju, U. Syamaprasad, Properties of superconducting, polycrystalline dysprosium-doped $Bi_{1.6}Pb_{0.5}Sr_{2-x}Dy_xCa_{1.1}Cu_{2.1}O_{8+\delta}$ (0 $\leq x \leq 0.5$), Mater. Res. Bull. 44 (2009) 1017–1021. https://doi.org/10.1016/j.materresbull.2008.11.013.
- [56] P.M. Sarun, R. Shabna, S. Vinu, A. Biju, U. Syamaprasad, Highly enhanced superconducting properties of Bi-2212 by Y and Pb co-doping, 404 (2009) 1602–1606. https://doi.org/10.1016/j.physb.2009.01.023.
- [57] A. Biju, P.M. Sarun, R.P. Aloysius, U. Syamaprasad, Comparison of superconducting properties of Ce added (Bi, Pb)-2212 with other rare earth additions, J. Alloys Compd. 433 (2007) 68–72. https://doi.org/10.1016/j.jallcom.2006.06.093.
- [58] B. Özçelik, C. Kaya, H. Gündoğmuş, A. Sotelo, M.A. Madre, Effect of Ce Substitution on the Magnetoresistivity and Flux Pinning Energy of the Bi₂Sr₂Ca_{1-x} Ce_x Cu₂O_{8+δ} Superconductors, J. Low Temp. Phys. 174 (2014) 136–147. https://doi.org/10.1007/s10909-013-0954-y.
- [59] P.M. Sarun, S. Vinu, R. Shabna, A. Biju, U. Syamaprasad, Microstructural and superconducting properties of Yb-substituted (Bi, Pb) -2212 superconductor sintered at different temperatures, 472 (2009) 13–17. https://doi.org/10.1016/j.jallcom.2008.04.103.
- [60] S. Zhang, C. Li, Q. Hao, T. Lu, P. Zhang, Influences of Yb substitution on the intergrain connections and flux pinning properties of Bi-2212 superconductors, Phys. C Supercond. Its Appl. 511 (2015) 26–32. https://doi.org/10.1016/j.physc.2015.02.004.
- [61] H. Gündoğmuş, B. Özçelik, A. Sotelo, M.A. Madre, Effect of Yb-substitution on thermally activated flux creep in the Bi₂Sr₂CaCu_{2-x}Yb_xO_y superconductors, J. Mater. Sci. Mater. Electron. 24 (2013) 2568–2575. https://doi.org/10.1007/s10854-013-1135-0.
- [62] K. Christova, A. Manov, J. Nyhus, U. Thisted, O. Herstad, S., Foss, K., Haugen, K. Fossheim, Bi₂Sr₂CaCu₂O_x bulk superconductor with MgO particles embedded, J. Alloys Compd. 340 (2002) 1–5. https://doi.org/10.1016/S0925-8388(01)02021-7.
- [63] P.E. Kazin, Y.D. Tretyakov, V. V. Lennikov, M. Jansen, Formation of the Bi₂Sr₂CaCu₂O_{8+δ} superconductor with Mg_{1-x}Cu_xO inclusions: The phases compatibility

- and the effect of the preparation route on the material microstructure and properties, J. Mater. Chem. 11 (2001) 168–172. https://doi.org/10.1039/b002795m.
- [64] K. Vinod, R.G.A. Kumar, A. Biju, P.M. Sarun, U. Syamaprasad, Flux pinning properties of magnesium diboride added (Bi,Pb)-2212 superconductors, J. Alloys Compd. 439 (2007) 2–5. https://doi.org/10.1016/j.jallcom.2006.08.066.
- [65] W. Wei, J. Schwartz, K.. Goretta, U. Balachandran, A. Bhargava, Effects of nanosize MgO additions to bulk Bi_{2.1}Sr_{1.7}CaCu₂O_x, Phys. C Supercond. 298 (1998) 279–288. https://doi.org/10.1016/S0921-4534(97)01889-3.
- [66] S. Zhang, C. Li, Q. Hao, J. Feng, T. Lu, P. Zhang, Optimized Intergrain Connection and Transport Properties of Bi-2212 High-Temperature Superconductors by Ag Nanoparticles Inclusions, J. Supercond. Nov. Magn. 28 (2015) 1729–1736. https://doi.org/10.1007/s10948-015-2981-1.
- [67] U. ÖZTORNACI, B. ÖZKURT, The effect of nano-sized metallic Au addition on structural and magnetic properties of Bi_{1.8}Sr₂Au_xCa_{1.1}Cu_{2.1}O_y (Bi-2212) ceramics, Ceram. Int. 43 (2017) 4545–4550. https://doi.org/10.1016/j.ceramint.2016.12.109.
- [68] K.C. Goretta, V.R. Todt, D.J. Miller, M.T. Lanagan, Y.L. Chen, U. Balachandran, J. Guo, J.A. Lewis, Engineered flux-pinning centers in Bi₂Sr₂CaCu₂O_x and TIBa₂Ca₂Cu₃O_x superconductors, J. Electron. Mater. 24 (1995) 1961–1966. https://doi.org/10.1007/BF02653017.
- [69] B. Özkurt, The influence of WO₃ nano-particle addition on the structural and mechanical properties of Bi_{1.8}Sr₂Ca_{1.1}Cu_{2.1}O_y ceramics, J. Mater. Sci. Mater. Electron. 24 (2013) 4233–4239. https://doi.org/10.1007/s10854-013-1390-0.
- [70] S.L. Huang, M.R. Koblischka, K. Fossheim, T.W. Ebbesen, T.H. Johansen, Microstructure and flux distribution in both pure and carbon-nanotube-embedded Bi₂Sr₂CaCu₂O_{8+δ} superconductors, Phys. C Supercond. Its Appl. 311 (1999) 172–186. https://doi.org/10.1016/S0921-4534(98)00609-1.
- [71] L.P. Qiu, Y.R. Zhang, S.L. Gao, Q.H. Zheng, T.T. Zhang, G.T. Cheng, S. ze Cao, W.P. Hang, S. Ramakrishna, Y.Z. Long, Fabrication and magnetic properties of SiO₂ nanoparticles-doped BSCCO superconducting nanofibers by solution blow spinning, Phys. C Supercond. Its Appl. 608 (2023) 1354251. https://doi.org/10.1016/j.physc.2023.1354251.
- [72] M.E. Aytekin, B. Özkurt, The Influence of Nano-Sized SnO₂ Doping on Physical and Magnetic Properties of the Bi₂Sr_{2-x}(SnO₂)_xCa₁Cu_{1.75}Na_{0.25}O_y Superconductors, J. Supercond. Nov. Magn. 33 (2020) 965–970. https://doi.org/10.1007/s10948-019-05336-w.
- [73] M.D. Aliff-Imran, M. Nur-Afrina, M.J. Masnita, M.H.H. Jumali, R. Abd-Shukor, Nano-tin(IV) oxide addition effects on the transport and AC susceptibility parameters of Bi_{1.6}Pb_{0.4}Sr₂CaCu₂O₈ superconductor, J. Mater. Sci. Mater. Electron. 33 (2022) 13947–13955. https://doi.org/10.1007/s10854-022-08325-3.
- [74] A. Sobha, R.P. Aloysius, P. Guruswamy, K.G.K. Warrier, U. Syamaprasad, Phase evolution in Ag, Ag₂O and AgNO₃ added (Bi,Pb)-2223 superconductor, Phys. C Supercond. Its Appl. 307 (1998) 277–283. https://doi.org/10.1016/S0921-4534(98)00411-0.

- [75] D.W. Johnson, D.A. Fleming, Influence of silver and excess copper on the formation and properties of 2223 (Bi, Pb)-Sr-Ca-Cu-0 superconductor, J. Mater. Res. 6 (1991) 455–458. https://doi.org/10.1557/JMR.1991.0455.
- [76] S.X. Dou, K.H. Song, H.K. Liu, C.C. Sorrell, M.H. Apperley, A.J. Gouch, N. Savvides, D.W. Hensley, The interaction of Ag with Bi-Pb-Sr-Ca-Cu-O superconductor, Phys. C Supercond. Its Appl. 160 (1989) 533–540. https://doi.org/10.1016/0921-4534(89)90431-0.
- [77] T. Matsushita, A. Suzuki, T. Kishida, M. Okuda, H. Naito, The effect of Ag on the superconductivity of Bi_{2-x}Pb _xSr₂Ca₂Cu₃O_y superconductors prepared by an optimum thermal procedure, Supercond. Sci. Technol. 7 (1994) 222–226. https://doi.org/10.1088/0953-2048/7/4/007.
- [78] N. Savvides, A. Katsaros, S.X. Dou, Critical current density and flux pinning in silver/superconductor composites and tapes, Phys. C Supercond. 179 (1991) 361–368. https://doi.org/10.1016/0921-4534(91)92183-C.
- [79] Y.D. Chiu, T.S. Lei, C.H. Kao, Effects of sintering temperature on the superconducting and microstructural properties of Bi_{1.7}Pb_{0.4}Sr_{1.6}Ca_{2.4}Cu_{3.6}O_Y/Ag₂O composites, J. Mater. Sci. 29 (1994) 2678–2682. https://doi.org/10.1007/BF00356817.
- [80] D.R. Mishra, P.L. Upadhyay, R.G. Sharma, Superconductivity of Nb-substituted Bi-2223 superconductor, Phys. C Supercond. 304 (1998) 293–306. https://doi.org/10.1016/S0921-4534(98)00257-3.
- [81] H. Sözeri, N. Ghazanfari, H. Özkan, A. Kilic, Enhancement in the high-T_c phase of BSCCO superconductors by Nb addition, Supercond. Sci. Technol. 20 (2007) 522–528. https://doi.org/10.1088/0953-2048/20/6/007.
- [82] J.C. Grivel, A. Jeremie, R. Flukiger, The influence of TiO₂ additions on the formation and the superconducting properties of the (Bi,Pb)₂Sr₂Ca ₂Cu₃O_{10-y} phase, Supercond. Sci. Technol. 8 (1995) 41–47. https://doi.org/10.1088/0953-2048/8/1/007.
- [83] J.C. Grivel, R. Flükiger, Effects of mno additions on the formation of the (Bi, Pb)₂Sr₂Ca₂Cu₃O_{10-y} phase, Supercond. Sci. Technol. 8 (1995) 751–754. https://doi.org/10.1088/0953-2048/8/10/002.
- [84] T. Kozuka, H. Ogawa, A. Kan, A. Suzumura, Influence of ZnO doping on superconductivity and crystal structure of (Bi, Pb)-2223 superconductor, J. Eur. Ceram. Soc. 21 (2001) 1913–1917. https://doi.org/10.1016/S0955-2219(01)00142-X.
- [85] Y.S. Yuan, M.S. Wong, S.S. Wang, Superconducting properties of MgO-whisker reinforced BPSCCO composite, Phys. C Supercond. Its Appl. 250 (1995) 247–255. https://doi.org/10.1016/0921-4534(95)00330-4.
- [86] H. Azhan, F. Fariesha, S. Khalida, Effect of heat treatments and Zr doped on superconducting properties of Bi_{1.6}Pb_{0.4}Sr₂Ca₂Cu₃O_δ ceramics, J. Supercond. Nov. Magn. 24 (2011) 265–270. https://doi.org/10.1007/s10948-010-1011-6.
- [87] C. Terzioglu, H. Aydin, O. Ozturk, E. Bekiroglu, I. Belenli, The influence of Gd addition on microstructure and transport properties of Bi-2223, Phys. B Condens. Matter. 403 (2008) 3354–3359. https://doi.org/10.1016/j.physb.2008.04.033.
- [88] R.P. Aloysius, P. Guruswamy, U. Syamaprasad, Enhanced flux pinning in (Bi, Pb)-2223 superconductor by Nd addition, Supercond. Sci. Technol. 18 (2005) 427–431.

- https://doi.org/10.1088/0953-2048/18/4/009.
- [89] M.S. Lee, K.Y. Song, Effect of Nd substitution for the Ca site in the 110 K phase of (Bi,Pb)-Sr-Ca-Cu-O superconductors, Supercond. Sci. Technol. 15 (2002) 851–854. https://doi.org/10.1088/0953-2048/15/6/301.
- [90] R. Singh, A. Gupta, S.K. Agarwal, D.P. Singh, A. V Narlikar, Superconductivity in Prdoped, Supercond. Sci. Technol. 11 (1998) 311–314. https://doi.org/10.1088/0953-2048/11/3/010.
- [91] K. Nanda Kishore, M. Muralidhar, V. Hari Babu, O. Peña, M. Sergent, F. Bénière, Effect of rare-earth Sm³⁺ substitution on the superconducting properties of the Bi_{1.7}Pb_{0.3}Sr₂Ca_{2-x}Sm_xCu₃O_y system, Phys. C Supercond. Its Appl. 204 (1993) 299–304. https://doi.org/10.1016/0921-4534(93)91012-K.
- [92] L. Bonoldi, G.L. Calestani, M.G. Francesconi, G. Salsi, M. Sparpaglione, L. Zini, Structural stability of bismuth-based superconductors under heterovalent substitution, Phys. C Supercond. Its Appl. 241 (1995) 37–44. https://doi.org/10.1016/0921-4534(94)02364-6.
- [93] A. Sedky, The impact of Y substitution on the 110 K high Tc phase in a Bi (Pb):2223 superconductor, J. Phys. Chem. Solids. 70 (2009) 483–488. https://doi.org/10.1016/j.jpcs.2008.12.006.
- [94] P.E. Kazin, M. V Makarova, M. Jansen, T. Adelsberger, Y.D. Tretyakov, Interaction of Bi(Pb)-2223/2212 ceramics with, Supercond. Sci. Technol. 10 (1997) 616–620. https://doi.org/10.1088/0953-2048/10/8/016.
- [95] Z.Y. Jia, H. Tang, Z.Q. Yang, Y.T. Xing, Y.Z. Wang, G.W. Qiao, Effects of nano-ZrO₂ particles on the superconductivity of Pb-doped BSCCO, Phys. C Supercond. Its Appl. 337 (2000) 130–132. https://doi.org/10.1016/S0921-4534(00)00072-1.
- [96] M. Zouaoui, A. Ghattas, M. Annabi, F. Ben Azzouz, M. Ben Salem, Effect of nano-size ZrO₂ addition on the flux pinning properties of (Bi, Pb)-2223 superconductor, Supercond. Sci. Technol. 21 (2008). https://doi.org/10.1088/0953-2048/21/12/125005.
- [97] M. Annabi, A. M'chirgui, F. Ben Azzouz, M. Zouaoui, M. Ben Salem, Addition of nanometer Al₂O₃ during the final processing of (Bi,Pb)-2223 superconductors, Phys. C Supercond. Its Appl. 405 (2004) 25–33. https://doi.org/10.1016/j.physc.2004.01.012.
- [98] D. Sýkorová, V. Jakeš, O. Smrčková, Bi-based superconductors with nanosized silver dopant, Phys. Status Solidi C. 3 (2006) 3027–3030. https://doi.org/10.1002/pssc.200567033.
- [99] R. Mawassi, S. Marhaba, M. Roumié, R. Awad, M. Korek, I. Hassan, Improvement of superconducting parameters of Bi_{1.8}Pb_{0.4}Sr₂Ca₂Cu₃O_{10+δ} added with nano-Ag, J. Supercond. Nov. Magn. 27 (2014) 1131–1142. https://doi.org/10.1007/s10948-013-2408-9.
- [100] Ş. Yavuz, Ö. Bilgili, K. Kocabaş, Effects of superconducting parameters of SnO₂ nanoparticles addition on (Bi, Pb)-2223 phase, J. Mater. Sci. Mater. Electron. 27 (2016) 4526–4533. https://doi.org/10.1007/s10854-016-4327-6.
- [101] H. Fallah-Arani, A. Sedghi, S. Baghshahi, F. shahbaz tehrani, R.S. Moakhar, N. Riahi-Noori, N.J. Nodoushan, Bi-2223 superconductor ceramics added with cubic-shaped TiO₂ nanoparticles: Structural, microstructural, magnetic, and vortex pinning studies,

- J. Alloys Compd. 900 (2022) 163201. https://doi.org/10.1016/j.jallcom.2021.163201.
- [102] E. Guilmeau, B. Andrzejewski, J.G. Noudem, The effect of MgO addition on the formation and the superconducting properties of the Bi2223 phase, Phys. C Supercond. Its Appl. 387 (2003) 382–390. https://doi.org/10.1016/S0921-4534(02)02360-2.
- [103] N. Türk, H. Gündoğmuş, M. Akyol, Z.D. Yakıncı, A. Ekicibil, B. Özçelik, Effect of tungsten (W) substitution on the physical properties of Bi-(2223) superconductors, J. Supercond. Nov. Magn. 27 (2014) 711–716. https://doi.org/10.1007/s10948-013-2351-9.
- [104] T. Çördük, Ö. Bilgili, K. Kocabaş, Investigation of effects of MgO nanoparticles addition on the superconducting properties of Bi-2223 superconductors, J. Mater. Sci. Mater. Electron. 28 (2017) 14689–14695. https://doi.org/10.1007/s10854-017-7336-1.
- [105] S.N. Abdullah, M.M.A. Kechik, A.N. Kamarudin, Z.A. Talib, H. Baqiah, C.S. Kien, L.K. Pah, M.K. Abdul Karim, M.K. Shabdin, A.H. Shaari, A. Hashim, N.E. Suhaimi, M. Miryala, Microstructure and Superconducting Properties of Bi-2223 Synthesized via Co-Precipitation Method: Effects of Graphene Nanoparticle Addition, Nanomaterials. 13 (2023). https://doi.org/10.3390/nano13152197.
- [106] V.S. Bai, S. Ravi, T. Rajasekharan, R. Gopalan, On the composition of 110 K superconductor in a (Bi,Pb)-Sr-Ca-Cu-O system, J. Appl. Phys. 70 (1991) 4378–4382. https://doi.org/10.1063/1.349119.

Chapter 2: Synthesis and characterization

2.1 Introduction

In this chapter, the synthesis of Bi 2212, Bi 2223, and Ca_{0.86}Sr_{0.14}CuO₂ phase powders by nitrate method [1] is discussed in detail. Synthesis of WO₃ and Ca_{0.86}Sr_{0.14}CuO₂ phase nanoparticles is described. A complete stepwise flow chart for sample preparation of Bi 2212 and Bi 2223 composites is given. Analysis of magnetic hysteresis loops of high-temperature superconductors is presented. Determination of critical current density using Bean's extended critical state model is discussed. Hughes' model and Klein's model describing the dominant flux pinning mechanism in superconductors are presented.

2.2 Synthesis of precursor powders

2.2.1 Bi 2212 precursor powder synthesis:

Bi 2212 precursor powder was synthesized using high-purity Bi₂O₃, SrCO₃, CaCO₃, and CuO powders. These powders were weighed out in stoichiometric ratios of 2:2.14:0.86:2 of the metal atoms, respectively, and were dissolved one by one in concentrated nitric acid and mixed under continuous stirring. The solution was heated while stirring at 80 °C till it was converted to a blue color solid. The solid was ground into a fine powder and calcined at 500 °C. The calcined powder was ground again and annealed thrice at 800 °C, with intermediate grinding to get Bi 2212 precursor powder.

2.2.2 Bi 2223 precursor powder synthesis:

Bi 2223 precursor powder was synthesized by nitrate method using high purity Bi₂O₃, Pb(NO₃)₂, SrCO₃, CaCO₃, CuO. The powders weighed out in a stoichiometric ratio of 1.2:0.3:2.06:1.54:3, were dissolved individually in concentrated nitric acid, except Pb(NO₃)₂, and were mixed continuously using a stirrer, to which a requisite amount of Pb(NO₃)₂ dissolved in distilled water was added. The solution was continuously heated and stirred for drying. The dried solid was ground and calcined at 500 °C. The resultant powder thus obtained was annealed thrice at 800 °C, for 24 hours each, with intermediate grindings.

2.2.3 (Ca,Sr)CuO phase preparation

The Ca_{0.86}Sr_{0.14}CuO₂, phase (in (Ca,Sr)CuO system, also referred to as infinity phase or I-phase) powder was also prepared by nitrate method discussed above

except that the final calcination was done at 900 °C twice for 24 hours each with one intermediate grinding.

2.3 Synthesis of nanoparticles

2.3.1 WO₃ nanoparticles

WO₃ nanoparticles were synthesized by a simple reaction of Tungsten (W) metal powder with H₂O₂ [2]. First, Tungsten metal powder was dispersed in a precooled distilled water solution and Hydrogen peroxide (MERCK, 30%). W and H₂O₂ react to give a solution of light-yellow color with suspended WO₃ nanoparticles. The solution was kept at 273 K for several hours using an ice bath to control the exothermic reaction. It was then vacuum-dried to obtain WO₃ nanoparticles. The detailed characterization of WO₃ nanoparticles is given in Chapter 3.

2.3.2 Ca_{0.86}Sr_{0.14}CuO₂ phase nanoparticles

Ca_{0.86}Sr_{0.14}CuO₂ phase nanoparticles were prepared by the citrate sol-gel combustion method discussed elsewhere [3]. Firstly, the metal carbonates/oxides are dissolved in conc. nitric acid to get a clear solution. To this solution, an aqueous solution of citric acid is added in the desired proportion (1 gram of citric acid to 1 gram of metal ion). A firing agent, ethylene glycol/ sugar, was added in the requisite proportion. The pH of the solution was adjusted to above 7. The gel underwent stirring and heating until it began to swell. Eventually, spontaneous combustion took place, transforming the gel into flakes. These flakes were gathered and ground into powder. The ground powder was calcined twice at 500 °C with one intermediate grinding to get Ca_{0.86}Sr_{0.14}CuO₂ phase nanoparticles.

2.4 Synthesis of BSCCO composites with nanoparticle addition

BSCCO Composite Systems Studied

- a) Bi 2212 with WO₃ nanoparticles
- b) Bi 2223 with WO₃ nanoparticles
- c) Bi $2223 + Ca_{0.86}Sr_{0.14}CuO_2$ with ZrO_2 nanoparticles
- d) Bi 2223 with Ca_{0.86}Sr_{0.14}CuO₂ nanoparticles

2.4.1 Bi 2212 composites with WO₃ nanoparticles

For Bi 2212 composites, WO₃ nanoparticles were added to the Bi 2212 precursor powder in different concentrations using a sol-casting technique [4]. Sol-casting method was used to add nanoparticles uniformly without agglomeration into the BSCCO matrix phase. WO₃ nanoparticle added Bi 2212 powder is dried, de-

bindered, and pressed at 12 ton pressure using a hydraulic press. The pellets were sintered twice at 830 °C for 24 hours after partially melting at 870 °C, with one intermediate pressing. Repeated pressing and sintering are required for the densification of Bi 2212 ceramics. A stepwise flow chart for sample preparation is given in Fig. 2.1.

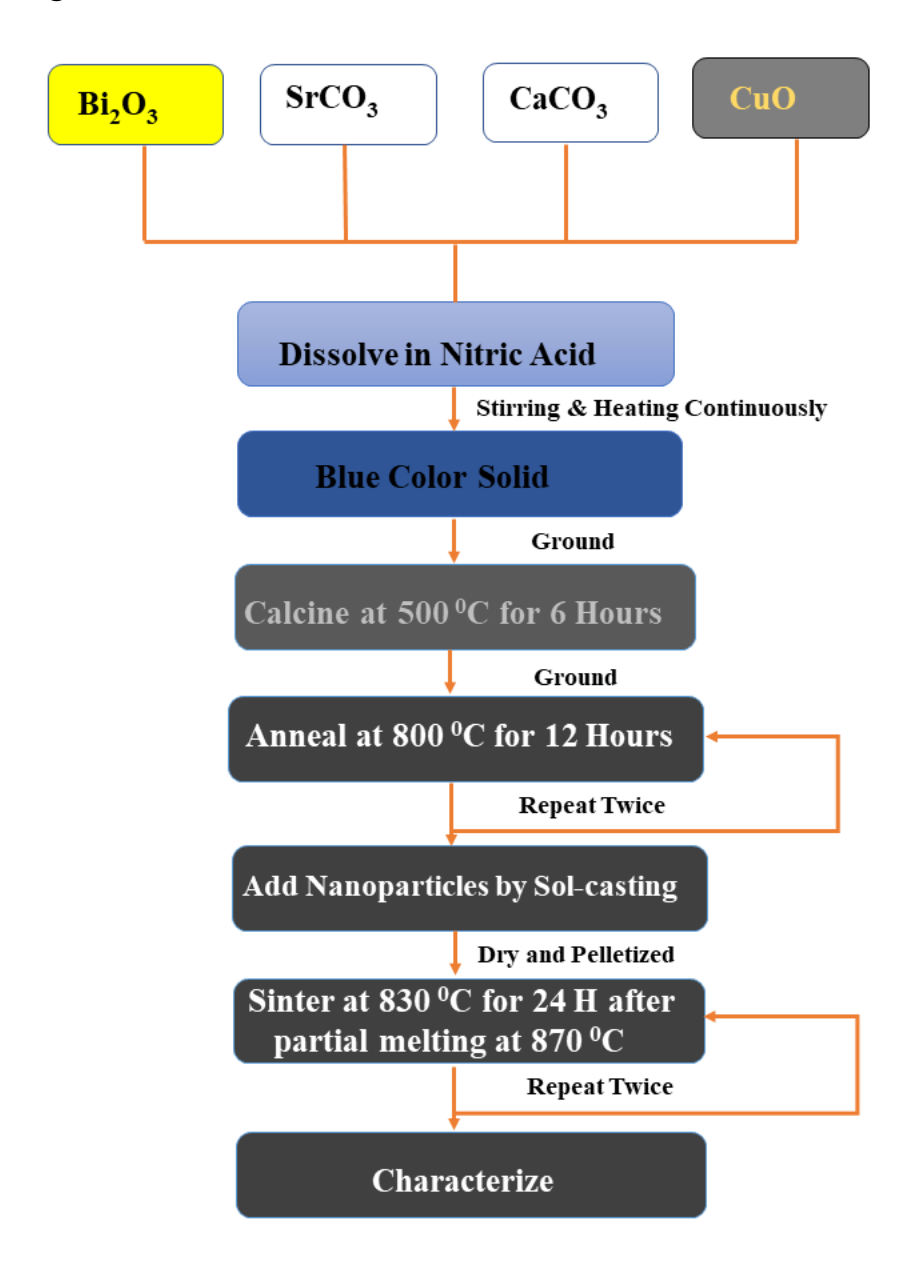


Figure 2.1: Stepwise flow chart for Bi 2212 sample preparation.

2.4.2 Bi 2223 composites with WO₃ nanoparticles

For Bi 2223 composites, the precursor powder is first pelletized and sintered once at 845 °C for 48 hours. Subsequently, the sintered pellet is pulverized. Then, nanoparticles are added to the processed and ground powder at different concentrations using the sol-casting technique. Then, the nanoparticle-added Bi 2223 powder is dried, de-binder, and pelletized at 12-ton pressure using a

hydraulic press. The pellet is sintered twice at 845 °C with one intermediate pressing. A similar method is used for making all the Bi 2223 composites. A stepwise flow chart for sample preparation is given in Fig. 2.2.

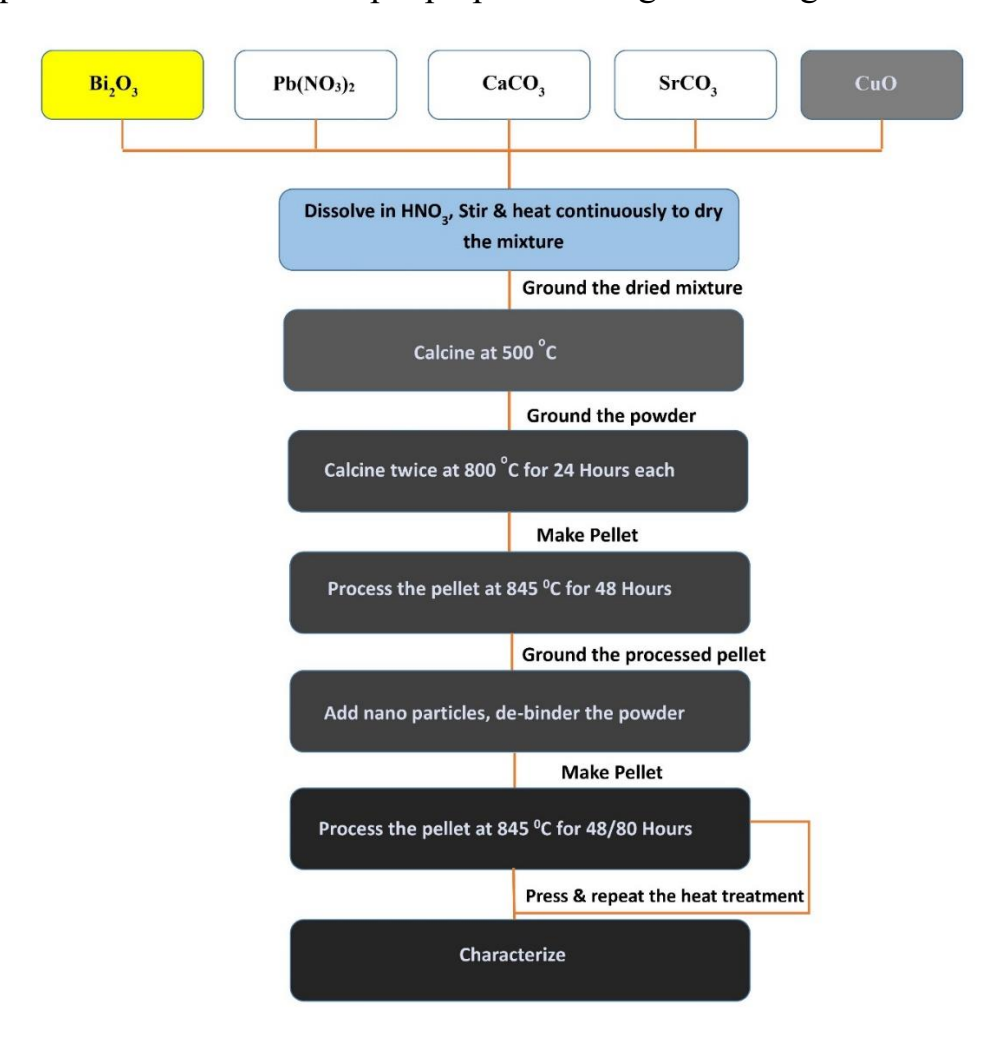


Figure 2.2: Stepwise flow chart for Bi 2223 composites preparation.

2.4.3 Bi 2223 + 20 mol $Ca_{0.86}Sr_{0.14}CuO_2$ phase with ZrO_2 nanoparticles

20 mol Ca_{0.86}Sr_{0.14}CuO₂ phase precursor powder and 100 mol of Bi 2223 precursor powder were mixed and tumbled for several hours. The mixed powder was pelletized and sintered once at 845 °C for 48 hours. The sintered pellet was ground to powder form. ZrO₂ nanoparticles of 200 nm size were bought from Saint Gobin and were added to the ground powder in various concentrations by sol-casting technique. Then, the nanoparticle-added powder was dried, debindered, and pelletized again. The resulting pellets were sintered twice at 845°C, with an intermediate pressing.

2.4.4 Bi 2223 composites with Ca_{0.86}Sr_{0.14}CuO₂ nanoparticles

Various amounts of Ca_{0.86}Sr_{0.14}CuO₂ nanoparticles (0- 50 mol) were added to 100 mol of Bi 2223 by sol-casting technique. Then, the Ca_{0.86}Sr_{0.14}CuO₂ phase

nanoparticle-added Bi 2223 powder was dried, de-bindered, and pelletized. The resulting pellets were sintered twice at 845°C, with one intermediate pressing.

2.5 Characterization techniques

Samples were cut into several pieces for characterization after final sintering using different techniques. The top surface was used for structural analysis using the X-ray diffraction technique.

2.5.1 X-ray Diffraction:

In 1912, Max von Laue recognized crystalline materials as 3-dimensional diffraction gratings for X-rays with a wavelength (λ) correlating to the distance between atoms. W. L. Bragg explained X-ray diffraction by conceptualizing the crystal as a collection of evenly spaced parallel planes known as Bragg's planes. The crystal structure of a material can be revealed through the X-ray diffraction technique, which nowadays serves as a quick primary tool for identifying the phases of crystalline substances.

The X-ray diffraction technique relies on the principle of constructive interference of monochromatic X-rays as they interact with the material being studied [5,6]. The incoming X-rays engage with the electrons surrounding the atoms within the material, and the X-ray reflection occurs at specific angles of incidence. According to Bragg, if the path difference of X-rays is 2d Sin θ , constructive interference occurs when Bragg's condition is fulfilled.

$$2d Sin\theta = n \lambda$$
 Bragg's Law (1)

Here, n is an integer, and d is the interplanar distance.

Intensity of diffraction is governed by the equation,

$$I = |F|^2 p \left(\frac{1 + \cos^2 2\theta}{\sin^2 \theta \cos \theta} \right) \tag{2}$$

I is the relative intensity, F and P are the structure factor, and multiplicity factor, respectively, and θ is the Bragg angle. Despite fulfilling Bragg's law, no diffraction lines are detected in the XRD pattern due to the crystallographic planes having a zero-structure factor. The pictorial representation of the X-ray diffractometer is shown in Fig. 2.3. The violet color lines represent the planes of the atoms located in the reciprocal lattice, where the interplanar distance (d_{hkl}) is indicated by Miller indices (h k l). The X-ray beam passes through a collimator and filter before reaching the sample. A detector measures the intensity at an angle 2θ relative to the sample's plane. When the incident angle equals the angle of reflection, the reflected beams are considered to be in phase, and the path difference corresponds to an integer multiple of wavelengths. Therefore, the

intensities are plotted with respect to 20. A Panalytical X'Pert 3 diffractometer with Cu-K α radiation of wavelength ~1.54 Å was used to take XRD patterns to study all the samples in the present work.

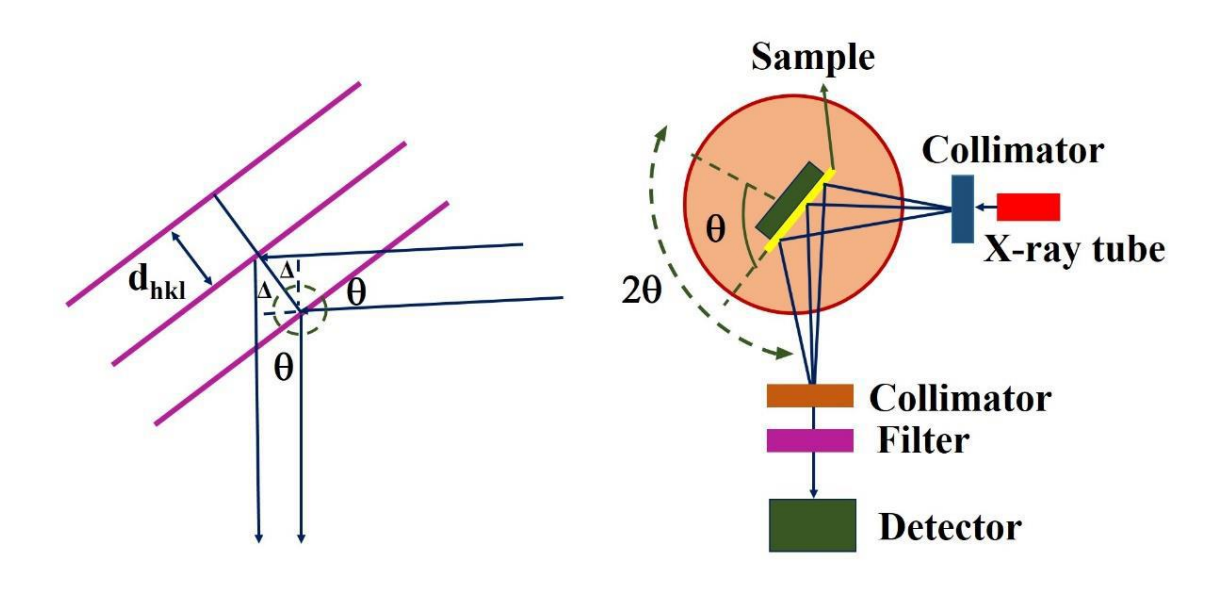


Figure 2.3: Schematic representation of X-ray diffractometer

The sample holder is affixed to the goniometer and remains stationary without undergoing rotation around the θ axis in θ –2 θ diffractometers. The X-ray tube is fixed to a movable arm on the goniometer, ensuring fully automated operation and data acquisition. The samples were fixed on a standard sample holder, and the XRD data was recorded at room temperature. Scanning of the samples was done within the 2 θ range of 10° to 90°, with a scanning step size of 0.017°. All samples, in theory, provide all conceivable orientations of the crystal lattice, and the goniometer enables varied angles of incidence for the detector to capture the intensity of the diffracted beam from the sample. Highscore software was used for Rietveld refinement for phase analysis.

2.5.2 Field Emission Scanning Electron Microscopy:

A field emission scanning electron microscope (FESEM) is used to study the microstructural and morphological properties of a material. A high-intensity electron beam is allowed to be bombarded on the sample surface. The electron beam is concentrated on a small spot on the sample, and it systematically scans the sample surface, creating a high-resolution, two-dimensional image.

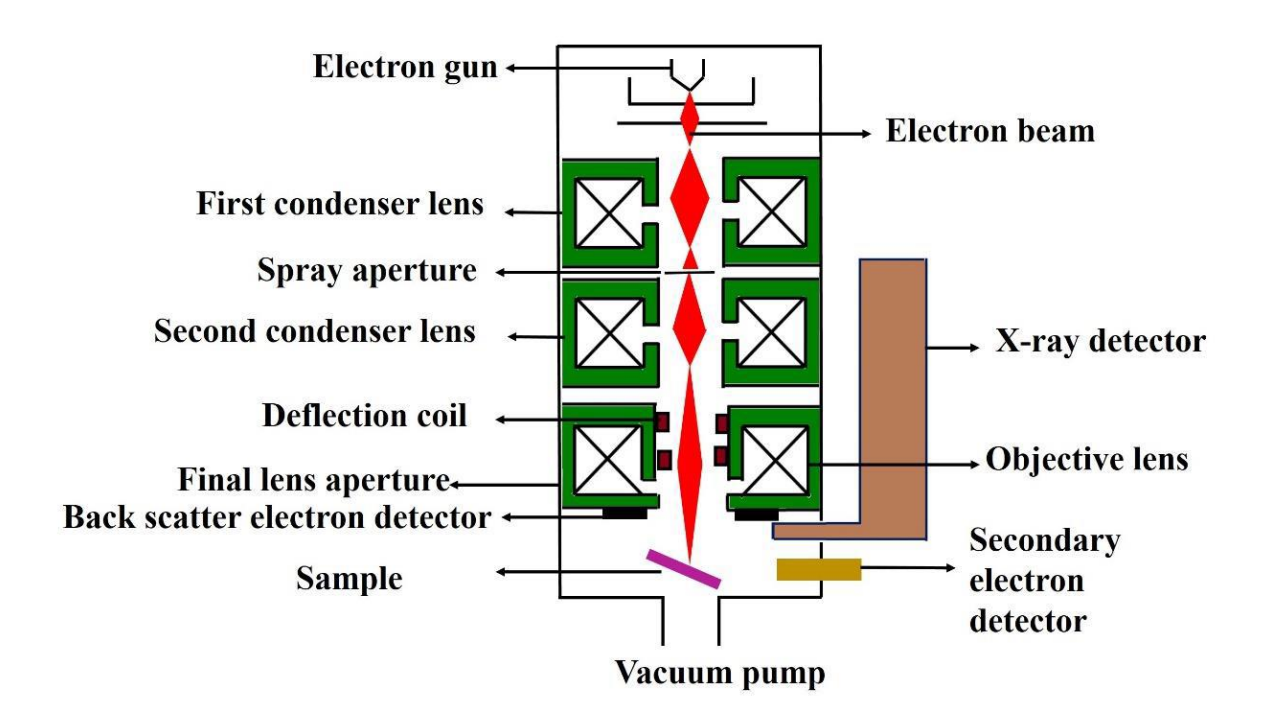


Figure 2.4: Pictorial representation of Field Emission Scanning Electron Microscope

The fundamental process involves the interaction of the primary electron beam with the sample, resulting in the production of secondary electrons (SE), backscattered electrons (BSE), characteristic X-rays, cathodoluminescence (CL), and heat. BSE and SE give the microstructural details of the sample. Secondary electrons (SE) offer information about the topography and morphology, while backscattered electrons (BSE) supply contrast within the composition to identify multiphases present in the samples. The FESEM resolution ranges from 10 nm to 200 nm. Non-conductive specimens may accumulate a charge under the electron beam, leading to image artifacts. To address this, insulating samples require an electrically conductive coating, such as gold, carbon, or another metal or alloy prior to observation under FESEM. A pictorial representation is given in Fig. 2.4.

The main components include the electron source, electron gun, sample stage, detector, display devices, and essential elements like power supply, vacuum system, cooling system, vibration-free floor, ambient magnetic and electric fields, etc. The specimen's surface was coated with gold for conductivity in this study. The analysis of microstructures in the prepared samples was conducted using the (Model Ultra 55, Carl-Zeiss make) field emission scanning electron microscope along with Energy dispersive spectrometry.

2.5.3 Energy Dispersive X-ray Spectroscopy (EDS):

To determine the composition of various phases present in the microstructural studies of the samples, each phase was chosen individually and examined using

EDS. It is also referred to commonly as energy dispersive analysis of X-rays (EDAX). Various techniques, including point scan, area scan, line scan, and wavelength mapping on the sample, were employed to estimate the relative quantities of different elements present in each phase. EDS is an analytical method used in FESEM to quantitatively and qualitatively determine the elemental composition of different phases in the studied materials. EDS detectors with a beryllium window can identify all elements A atomic numbers (Z) greater than oxygen at concentrations above 0.1%. Additionally, "windowless" EDS detectors can detect oxygen, nitrogen, and carbon at concentrations greater than 1.0%. EDS displays the spatial distribution of elements as dot maps or line profiles, with a spatial resolution of one micron.

As the electron beam scans the sample, it produces X-rays emitted by the atoms. X-rays are produced when high-energy radiation ionizes an atom, leading to the removal of an inner shell electron. An electron residing in a higher energy outer shell fills the now vacant inner shell to restore the ionized atom to its ground state. In this process, energy is released, equivalent to the potential energy difference between the two shells. This surplus energy, specific to each atomic transition, is emitted by the atom either as an X-ray photon or is self-absorbed and emitted as an Auger electron. The energy of each X-ray is distinctive to the atom from which it originates. The EDS system captures these X-rays, organizes them by energy, and presents the number of X-ray photons relative to their energy.

The qualitative EDS spectrum can be captured through either photography or plotting. This data can subsequently be analyzed to generate either an elemental area analysis, portrayed as a dot map, or a linear elemental analysis, represented as a line scan. These analyses illustrate the distribution of a specific element on the sample's surface. The EDS data can be contrasted with established standard substances or computer-simulated theoretical standards to provide either a thorough "quantitative" or a "semi-quantitative" assessment. The position of peaks on the energy spectrum decides the identification of elements.

The intensities of the peaks differ due to variations in the probability of each transition occurring, and the detector's efficiency is influenced by energy. The EDS spectrum exhibits peak width as a consequence of energy dispersion being a statistical occurrence; not every photon generates the same number of electronhole pairs, and there is thermal noise resulting from the amplification process.

2.5.4 Bulk Density using Archimedes' principle:

Archimedes' principle allows precise determination of the density of any irregularly shaped sample. In this method, the sample's weight is measured both in the air and within a liquid medium of known density. The liquid can be water,

glycerol, or ethanol, based on the nature of the material used. The following relation is used to calculate the density of the material.

$$\rho_{\text{sample}} = \frac{W \text{ air}}{W \text{ air-} W \text{ liquid}} \times \rho_{\text{liquid}}$$
 (3)

 W_{air} and W_{liquid} is the weight of the sample in air and in a liquid medium, respectively, and ρ liquid is the density of liquid medium.

We also used Archimedes' principle to assess the density and porosity content in our BSCCO samples, which are ceramic nature. The weight of the sample is measured in air and glycerol media (density 1.26 g/cm³), using a weighing balance (Mettler AE 240) with 0.02 mg accuracy. The density of Bi 2212 [7] and Bi 2223 [8] from the literature is 6 and 6.4 g/cc respectively.

2.5.5 Vibrating Sample Magnetometer (VSM) facility

The basic working principle of Vibrating Sample Magnetometer (VSM) is Faraday's law of magnetic induction. The instantaneous magnetization of a sample is found with high accuracy by using VSM [9]. Faraday's law states that a varying magnetic field induces an electromotive force (emf). VSM is a device designed to measure the magnetic moment of a sample by vertically oscillating it in a uniform magnetic field. The sample is positioned at the midpoint of two fixed inductive pick-up coils, linked in series and wound in opposite directions. This configuration ensures that the system detects only the non-uniform flux variations caused by the vibration of the sample [10].

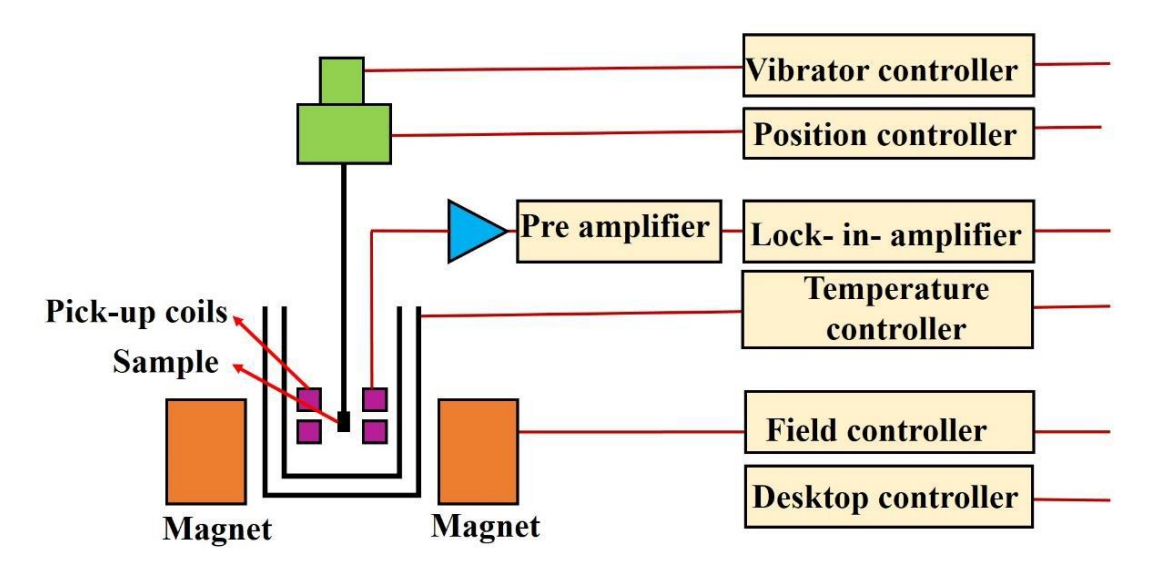


Figure 2.5: Schematic diagram of Vibrating Sample Magnetometer

The magnetic dipole moment surrounding the sample generates a stray field (or demagnetization field), which varies with the sample's vertical movement over

time. The alterations in this stray field are transmitted to the pick-up coils. The movement of the sample induces an electric field in the pick-up coils due to the changes in magnetic flux. The measured induced current is proportional to magnetization of the sample and the magnetization depends on the magnetic field's strength. The induced emf is measured and amplified by a lock-in amplifier which is controlled and monitored by a software program, and the magnetic moment is calculated.

In our current research, we have used a Vibrating Sample Magnetometer (VSM) integrated with the Physical Property Measurement System (PPMS, Dynacool, Quantum Design, USA). The PPMS system is composed of a cryostat assembly, Controlled area network (CAN) module bay, pump cabinet, and a computer. Within the cryostat assembly, there is a superconducting magnet (made of NbTi wire), a sample chamber, a pulse tube assembly, gas valves, and electronic circuits. The VSM is equipped with a linear motor for sample vibration, and a coil set puck is employed to detect the response in the pick-up coil. Automation and control are managed through the utilization of Multivu software. The sample is placed after attaching to the sample holder and positioned at the center of the gradiometer pick-up coils. The VSM motor module guides the precise position and amplitude of oscillation. Additionally, the VSM detection module can identify both in-phase and quadrature-phase signals derived from the encoder and the amplified voltage from the pick-up coils. These signals are subsequently transmitted to the CAN bus of the VSM application connected to a PC. M-T curves were recorded by cooling the sample in the temperature range of 120 K to 20 K at a 5 mT applied field, in the present work, using VSM on PPMS.

M-H loops were obtained at temperatures of 5 K, 10 K, 15 K, 20 K, and 30 K up to a 9 T applied field and at 50 K and 77 K up to a 5 T applied field for various samples examined.

2.6 Bean's critical state model and Critical current density (Jc) calculation

In superconductors, J_c is estimated from field-dependent magnetization using Bean's critical state model [11]. This model elucidates any change in the magnetic flux and current density within a superconductor, as the field changes. The basic assumption of this model is that either the current density is zero or equal to J_c inside a superconductor, and it is independent of the local internal field.

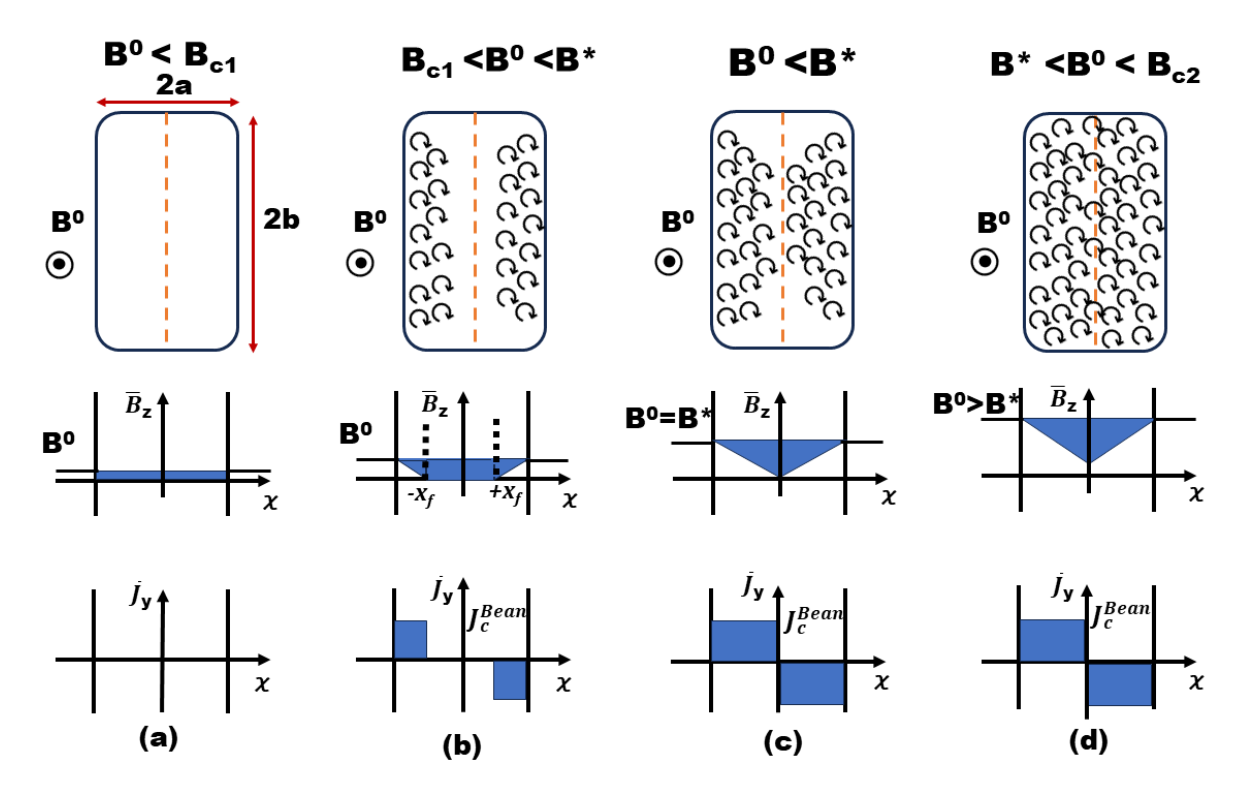


Figure 2.6: Initial magnetization of superconducting specimen (Bean's Model) [11]

Consider a rectangular specimen having width 'a' and length 'b'. From Maxwell's equation, the relationship between the internal field (B) and current density (J).

$$\nabla XB = \mu_0 J(B) \tag{4}$$

The supercurrents flow where the internal magnetic field is zero. Bean's model assumes a constant J_c, independent of an applied field inside a superconductor.

At the critical state, $J \rightarrow J_c$ and

$$\nabla XB = \mu_0 J_c \tag{5}$$

where J_c is critical current density in Am^{-2} and $B = \mu_0 H_i$ is the magnetic induction in Tesla, and μ_0 is the absolute permeability.

The local magnetization $M_i = H_i$ - H, H is the applied field. The total magnetization M can be obtained by averaging M_i across the cross-sectional area of the sample. Consider the magnetization in two stages,

- 1) 0<H<H*
- 2) H*< H

Here, H^* is the value of the internal field when it reaches the center of the sample. The magnetization curve M(H), for an infinite slab is given as

$$M(H) = -H + \frac{H^2}{2I_c a} \quad \text{for } \theta < H < H^*$$
 (6)

$$M(H) = -\frac{J_c}{2} \qquad \text{for } H^* < H \qquad (7)$$

The reverse curve for an applied maximum field (H_m) is given by

$$M(H) = -\frac{J_c}{2} + H_m - H - \frac{(H_m - H)^2}{4I_c a}$$
 for H_m -2 H *< H < H_m (8)

$$M(H) = -\frac{J_c}{2}$$
 for $-H_m - H^* < H_m < 2H^*$ (9)

When $H_m > 2H^*$, J_c and M are related for a superconducting slab of thickness 2a by,

$$M(H^+) - M(H^-) = J_c a$$
 (10)

Therefore, for a given field H, J_c can be determined by measuring the width of the M-H hysteresis loop.

For the orthorhombic shaped sample,

$$M(H^+) - M(H^-) = J_c b (1 - \frac{b}{3a})$$
 (11)

here, a and b are the dimensions of the sample cross-section with $a \ge b$.

The critical current densities (J_c) of the samples were determined following extended Bean's critical state model [11,12], and using the relation

$$J_c = 20 \frac{\Delta M}{d} \tag{12}$$

here $\Delta M = \mathrm{M}^+$ - M^- (in emu/cc), $d = b(1 - \frac{b}{3a})$; $a \ge b$ are the dimensions of the cross-section of the sample (in cm). M^+ and M^- represent the average magnetization with respect to increasing and decreasing fields respectively,

2.7 Flux pinning

When a superconductor enters a mixed state, it simultaneously accommodates normal and superconducting regions. In this state, a superconductor permits flux lines in a lattice arrangement to penetrate it, and this array of flux lines is referred to as the Abrikosov lattice. In a superconductor, minimizing the free energy occurs when the cores of vortices overlap with defects like dislocations, precipitates, and atomic-scale vacancies. These defects possess distinct properties compared to the rest of the medium (which is superconducting), resulting in reduced superconducting condensation energy. Vortices can be pinned by point,

line, surface, and three-dimensional pinning locations. The spatial arrangement of defects also influences the shape of a pinned vortex because a flux line, which would be straight in a homogeneous material, may curve to align with various pinning centers to minimize its energy [13].

Flux pinning in superconductors refers to the ability of a superconductor to pin magnetic flux lines within its interior, preventing them from moving freely. In the absence of pinning, the flux line lattice is uniform; however, introducing pinning leads to a flux gradient when the applied magnetic field is raised or lowered. This results in a higher vortex density near the superconductor's surface, where vortices originate and move into the bulk. This gradient induces bulk magnetization currents, shielding the superconductor against the applied magnetic field. Pinning centers can be introduced intentionally by doping the material, exposing it to ionizing radiation, diminishing the grain size to enhance the surface area of grain boundaries, and incorporating second phase precipitates [14].

Flux pinning is essential in superconductors for many practical applications, improving their stability and overall performance. By constraining the movement of flux lines, flux pinning enables superconductors to sustain their superconducting state even when exposed to external magnetic fields or experiencing changes in operating conditions. This is crucial in applications like superconducting magnets, where maintaining a stable and controlled magnetic field is essential. Researchers frequently investigate diverse methods to augment flux pinning in superconductors, including introducing artificial defects to enhance their practical effectiveness. A detailed literature survey on introducing artificial defects to BSCCO superconductors is presented in section 1.7 of Chapter 1.

Several models have been presented to comprehend the flux pinning mechanism present in a superconductor. Based on their experimental observations, Klein et al. [8] developed a model that gives a qualitative explanation of the pinning mechanism present in a superconductor. The scaling field used for this model is the peak field, corresponding to the maximum value of flux pinning force density ($F_p = J_c X B$). There are three kinds of pinning (δk , Normal point, and normal surface pinning). Here δk pinning arises from the difference in the average resistivity due to composition fluctuation, non-uniform distribution of dislocation, and martensitic transformation. Normal point pinning arises from the distribution of non-superconducting pinning centers of very small size, comparable to coherence length (ξ), like nanoparticles. In contrast, surface pinning occurs due to defects at the pinning centers, which are bigger, like grain boundaries and non-superconducting secondary phases. F_p/F_p max vs. B/B_p is plotted along with the theoretical equations for δk , Normal point, and normal surface pinning to find the pinning mechanism present in a superconductor. The

theoretical equations for δk , Normal point, and normal surface pinning are given as [15,16]

For δk Pinning,

$$F_p/F_{p max} = f(b) = 3h^2(1 - \frac{2h}{3})$$
 (13)

For normal point Pinning,

$$F_p/F_{p max} = f(b) = \frac{9}{4}h(1 - \frac{h}{3})^2$$
 (14)

For normal surface pinning

$$F_p/F_{p max} = f(b) = \frac{25}{16}h^{1/2}(1 - \frac{h}{5})^2$$
 (15)

Agreement of experimental data with any of the theoretical curves suggests the kind of pinning operative in the sample at the given temperature and field regime.

Dew Hughes [17] proposed a quantitative model to explain the pinning mechanism present in a superconductor. Irreversible field (B_{irr}) is used as scaling field. He proposed an equation to describe the pinning mechanism present in a superconductor,

$$\frac{F_p}{F_p \max} = f(b) = A * \left(\frac{B}{B_{irr}}\right)^p * \left(1 - \frac{B}{B_{irr}}\right)^q \tag{16}$$

Here A is a numerical constant, p and q are fitting parameters. Information on the pinning mechanism is provided by p and q. Fitting the experimental curve to equation 16, one can determine the values of p, and q which describe the pinning mechanism present in the samples. The values for p and q for different pinning mechanisms are given in Table 2.1.

Dew Hughes' model for pinning describes well the observations of conventional type I superconductors. But for type II superconductors, the values for p and q differ from the ideal values due to the presence of different sized pinning centers contributing to various pinning mechanisms simultaneously.

Table 2.1: The type of pinning mechanism corresponding to values of fitting parameters p and q.

Type of	p	q	
Point pins	Core Pinning	1	2
	δk Pinning	2	1
Surface pins	Core Pinning	1/2	2
	δk Pinning	3/2	1
Volume pins	Core Pinning	0	2
	δk Pinning	1	1

Core pinning or δl pinning arises from the variation of mean free path of superconducting electrons due to non-superconducting secondary phase precipitates in the superconducting matrix. δk pinning is caused by small difference in G-L parameter (κ) that can occur due to non-uniform distribution of dislocations, the local difference in the composition, or the oxygen valency in the unit cell.

The pinning centers are further classified based on their sizes as point, surface, and volume pins.

Point pinning is observed when defects such as precipitates, dislocations or variations in oxygen valency are extremely small, typically of the order of nanometer size. The size of point pins is smaller than the spacing between flux lines (d) in all directions. Surface pins have two dimensions larger than d, whereas volume pins have all dimensions larger than d [18].

In the case of superconductors with second-phase addition, different mechanisms may be valid in different fields and temperature regimes, or a combination of them may be simultaneously operative, which makes the analysis complex. More details are discussed in Chapters 3 to 6 regarding the applicability of different models to different composites studied.

References

P.E. Kazin, Y.D. Tretyakov, V. V. Lennikov, M. Jansen, Formation of the Bi₂Sr₂CaCu₂O_{8+δ} superconductor with Mg_{1-x}Cu_xO inclusions: The phases compatibility and the effect of the preparation route on the material microstructure and properties, J. Mater. Chem. 11 (2001) 168–172. https://doi.org/10.1039/b002795m.

- [2] A. Enferadi-Kerenkan, A.S. Ello, T.O. Do, Synthesis, Organo-Functionalization, and Catalytic Properties of Tungsten Oxide Nanoparticles As Heterogeneous Catalyst for Oxidative Cleavage of Oleic Acid As a Model Fatty Acid into Diacids, Ind. Eng. Chem. Res. 56 (2017) 10639–10647. https://doi.org/10.1021/acs.iecr.7b03001.
- [3] R.S. Liu, W.N. Wang, C.T. Chang, P.T. Wu, Synthesis and characterization of high-T_c superconducting oxides by the modified citrate gel process, Jpn. J. Appl. Phys. 28 (1989) L2155–L2157. https://doi.org/10.1143/JJAP.28.L2155.
- [4] P.M.S. Raju, V. Seshubai, T. Rajasekharan, A generic process to introduce nanoparticles into powder preforms and its application to Infiltration Growth processing of REBa₂Cu₃O₇ superconductor, Mater. Chem. Phys. 161 (2015) 59–64. https://doi.org/10.1016/j.matchemphys.2015.05.004.
- [5] A.W. Hull, A NEW METHOD OF CHEMICAL ANALYSIS., J. Am. Chem. Soc. 41 (1919) 1168–1175. https://doi.org/10.1021/ja02229a003.
- [6] M. Eckert, Max von Laue and the discovery of X-ray diffraction in 1912, Ann. Phys. 524 (2012). https://doi.org/10.1002/andp.201200724.
- [7] K. Christova, A. Manov, J. Nyhus, U. Thisted, O. Herstad, S.E. Foss, K.N. Haugen, K. Fossheim, Bi₂Sr₂CaCu₂O_x bulk superconductor with MgO particles embedded, J. Alloys Compd. 340 (2002) 1–5. https://doi.org/10.1016/S0925-8388(01)02021-7.
- [8] V. Rouessac, J. Wang, J. Provost, G. Desgardin, Processing and superconducting properties of highly textured Bi(Pb)-2223 ceramics by sinter-forging, Phys. C Supercond. 268 (1996) 225–232. https://doi.org/10.1016/0921-4534(96)00423-6.
- [9] S. Foner, Versatile and Sensitive Vibrating Sample Magnetometer, 557 (2004) 548–557.
- [10] S. Foner, The vibrating sample magnetometer: Experiences of a volunteer (invited), J. Appl. Phys. 79 (1996) 4740–4745. https://doi.org/10.1063/1.361657.
- [11] C.P. Bean, Magnetization of hard superconductors, Phys. Rev. Lett. 8 (1962) 250–253. https://doi.org/10.1103/PhysRevLett.8.250.
- [12] C.P. BEAN, Magnetization of High-Field Superconductors, Rev. Mod. Phys. 36 (1964) 31–39. https://doi.org/10.1103/RevModPhys.36.31.
- [13] T. Matsushita, Flux Pinning in Superconductors, 1st ed., Springer Berlin Heidelberg, Berlin, Heidelberg, 207AD. https://doi.org/10.1007/978-3-540-44515-9.
- [14] R. Wördenweber, Engineering of superconductors and superconducting devices using artificial pinning sites, Phys. Sci. Rev. 2 (2019) 1–20. https://doi.org/10.1515/psr-2017-8000.
- [15] L. Civale, M.W. McElfresh, A.D. Marwick, F. Holtzberg, C. Feild, J.R. Thompson, D.K. Christen, Scaling of the hysteretic magnetic behavior in YBa₂Cu₃O₇ single crystals, Phys. Rev. B. 43 (1991) 13732–13735. https://doi.org/10.1103/PhysRevB.43.13732.
- [16] T. Goto, K. Inagaki, K. Watanabe, Critical current density in filamentary (Nd, Sm, Eu, Gd)-Ba-Cu-O superconductors prepared by a solution spinning method, Phys. C Supercond. Its Appl. 330 (2000) 51–57. https://doi.org/10.1016/S0921-4534(99)00608-5.

- [17] D. Dew-Hughes, Flux pinning mechanisms in type II superconductors, Philos. Mag. 30 (1974) 293–305. https://doi.org/10.1080/14786439808206556.
- [18] R. Ma, Y. Ma, W. Song, X. Zhu, S. Liu, J. Du, Y. Sun, C. Li, P. Ji, Y. Feng, P. Zhang, Imperfection of flux pinning classification based on the pinning center size, Phys. C Supercond. 411 (2004) 77–82. https://doi.org/10.1016/j.physc.2004.06.009.

Chapter 3

Effect of WO₃ nanoparticle addition on the structural, microstructural, and superconducting properties of Bi 2212 superconducting composites

3.1 Introduction

Bi 2212 is the well-studied high-temperature superconductor (HTSc) and is mostly preferred for making superconducting wires/tapes due to its high critical density (J_c) at 4.2 K [1]. High porosity, larger anisotropy, and poor intergrain connections are the common factors that limit the practical use of HTSc materials [2]. Repeated pressing and sintering at optimized temperatures are found to gain higher density [3] and show better performance in bulk or tapes.

Higher T_c is an advantage for HTSc compared to conventional superconductors. However, for real applications, their performance significantly deteriorates even with the application of a small field. The motion of flux lines causes J_c to drop drastically; this phenomenon is referred to as flux creep [4,5]. Introducing defects of sizes comparable to the coherence length (a few nm) of the superconductor creates pinning centres, and subsequently improves superconducting properties, especially J_c .

Lattice defects like stacking faults[6,7], dislocations [8], twin boundaries [9], etc., can pin the flux lines but are not easy to control as they depend on the processing conditions of superconductors. On the other hand, nanometer-sized pinning centers introduced by second-phase additions, if they can be controlled, can help in improving the physical properties of superconductors.

To improve the flux pinning properties of BSCCO superconductors, various studies of adding nano-sized secondary phases are reported. Nano MgO addition to Bi 2212 bulk and superconductor tapes are reported by various research groups [10–12]. When compared to the undoped sample, MgO addition enhanced flux pinning and also increased the irreversible field (B_{irr}) at 27 K [10].

Zhang et al. reported that the thermodynamic properties of Bi 2212 superconductors changed after adding Ag nanoparticles; the intergrain coupling improved, and J_c increased. Average 5 nm sized Ag nanoparticles were found to be embedded in the Bi 2212 matrix, improving J_c (to 4 kA/cm² till 6 T) at 4.2 K.

The dominant pinning mechanism was found to be surface pinning due to the formation of highly crystalline grain boundaries by nano-Ag addition [13].

Nano ZrO_2 particle addition to Bi 2212 superconductor tape caused the formation of $(Ca,Sr)ZrO_3$ precipitates of smaller size that are reported to be effective pinning centres that caused enhancement in flux pinning. However, J_c decreased with nano ZrO_2 addition at high fields, and the J_c for the sample without ZrO_2 addition was better or comparable at all fields [14].

Berdan Ozkurt reported that adding nano WO₃ (40 nm) to Bi_{1.8}Sr₂W_xCa_{1.1}Cu_{2.1}O_y, x=0, 0.05, 0.1, and 0.25 ceramics by solid-state synthesis route had negative effects. T_c , J_c , and connectivity among grains decreased with W content [15].

A detailed literature survey on the secondary phase addition is given in the first chapter, section 1.7.

From the information reported and presented above, it is observed that a secondary phase addition to BSCCO superconductors doesn't always improve their superconducting properties, especially under higher applied fields. Therefore, it is necessary to identify suitable pinning centers and develop methods to evenly distribute them within the superconducting matrix and not cause any reactions. Investigating the impact of various defects introduced through doping or formed during processing is essential. These defects can effectively act as flux pinning centers across different field strengths. Such research would be valuable in the creation of superconducting composites with microstructures capable of achieving higher J_c , sustained even under high applied fields.

In this direction, we have investigated the effect of uniformly distributed WO₃ nanoparticles, added by a sol-casting [16] process, into the Bi 2212 matrix. For the current study, we added WO₃ nanoparticles in the size range of 2 -12 nm to Bi 2212 powder. Superconducting samples with different amounts of WO₃ nanoparticle addition were processed at temperatures close to the melting point of Bi 2212 to facilitate a reaction and were characterized using various techniques. The critical current densities and flux pinning observed in samples with varying WO₃ content are analysed in the light of their microstructural details, as discussed below.

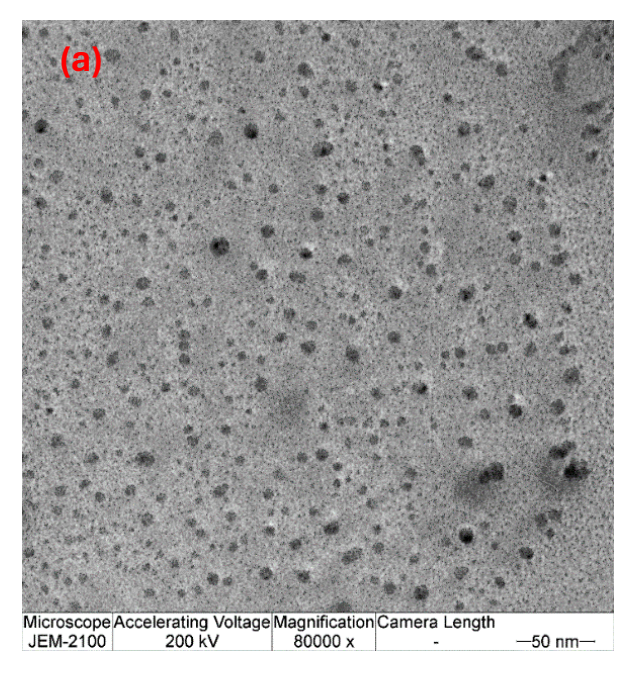
3.2 Experimental

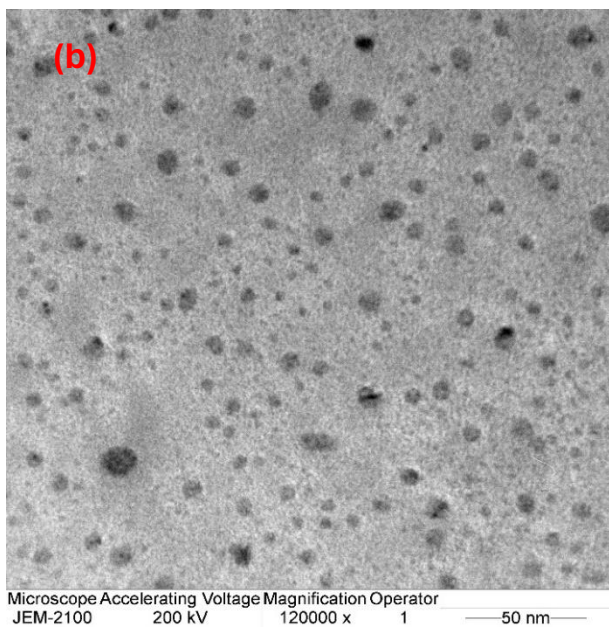
In the present work, Bi 2212 composites having Bi₂Sr_{2.14}Ca_{0.86}Cu₂O_y composition [17–19] were synthesized, chosen from a superconducting Bi₂Sr₂(Ca_{0.86}Sr_{0.14})_{n-1}Cu_nO_y series with varying concentration of WO₃ nanoparticles. The stoichiometric powders were prepared by nitrate route [20,21]. For this, high-purity Bi₂O₃, SrCO₃, CaCO₃, and CuO were weighed out in stoichiometric ratios of the metal atoms, to synthesize the composition Bi₂Sr_{2.14}Ca_{0.86}Cu₂O_y, and were dissolved individually in concentrated Nitric acid and were mixed under continuous stirring. The solution was heated while stirring till it was converted to a blue color solid which was ground into a fine powder and calcined at 500 °C. The calcined powder was ground again and annealed thrice at 800 °C, with intermediate grinding to get precursor powder of Bi 2212. A stepwise flow chart of sample preparation for Bi 2212 composites is given in Chapter 2, Fig. 2.1.

3.2.1 Characterization of WO₃ nanoparticles

Synthesis of WO₃ nanoparticles is discussed in detail in Chapter 2, section 2.4.2.

WO₃ nanoparticles thus obtained were added in different mass ratios to the fine powders of Bi 2212 using a dispersive sol-casting method [16] that enables their uniform distribution in the matrix. In the Sol-casting process, a powder mix of the Bi 2212 matrix phase and the WO₃ nanoparticles are suspended in a liquid medium consisting of a dispersant (Darvan 821), monomer (Methylacrylamlide), and cross-linker (N, N' methylene bisacrylamide) [19].





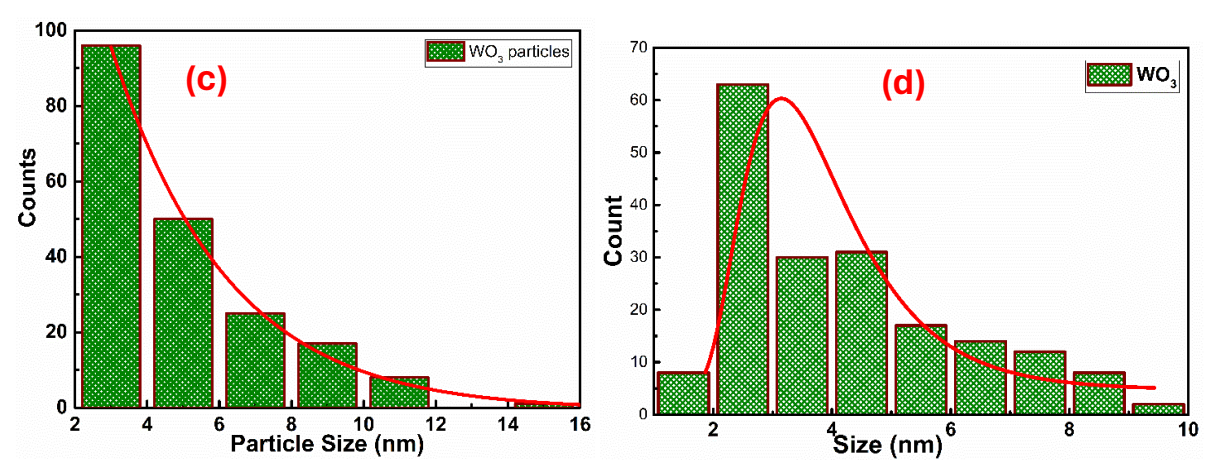


Figure 3.1 (a&b): TEM images showing WO₃ nanoparticles dispersed in a liquid medium, (c&d) Histogram shows that most particles are in the 2-6 nm range.

The resultant free-flowing slurry is tumbled for several hours and is polymerized by adding initiator (Ammonium persulphate) and catalyst (N-N-N'-N'-Tetramethylethylenediamine) and then is dried. The dried powders were debindered by heating to 800° C. This process prevents agglomeration of WO₃ nanoparticles in the Bi 2212 matrix.

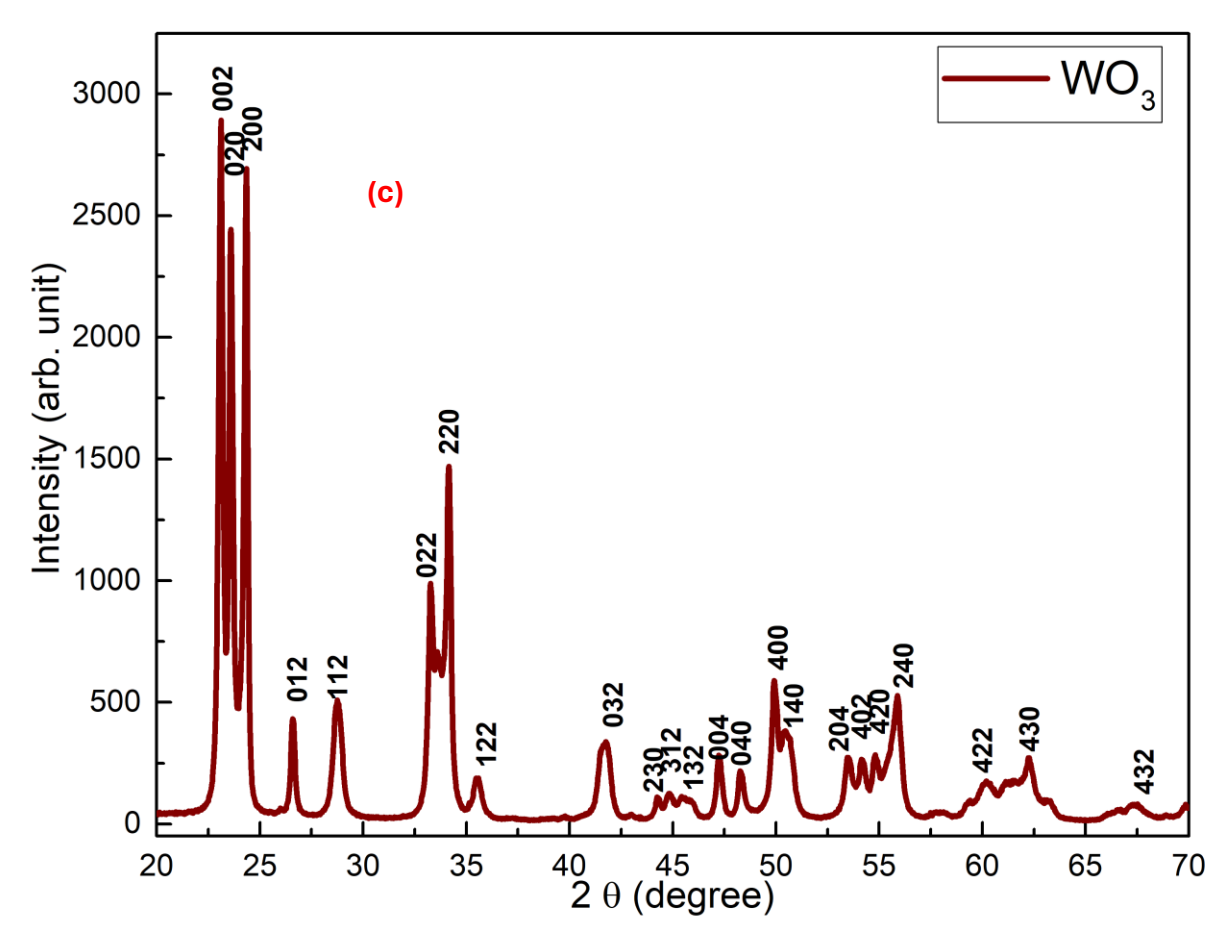


Figure 3.2: Indexed XRD pattern for WO₃ nanoparticles having orthorhombic structure.

Particle size distribution of WO₃ nanoparticles was done using Image J software. Fig. 3.1 shows two TEM micrographs and their corresponding histogram for particle size distribution. As can be seen, particles are in the 2-12 nm range, and most are in the 2-6 nm range. Analysis of the XRD pattern confirms the formation of WO₃ with an orthorhombic structure. The lattice parameters are a = 7.320(9) Å, b = 7.704(9) Å, and c = 7.535(6) Å. The indexed XRD pattern of WO₃ particles is shown in Fig. 3.2.

3.2.2 Preparation of Bi 2212 composites:

Pellets having dimensions, 20 mm diameter and 5 mm height were made using a uniaxial hydraulic press at 12-Ton pressure. Then the pellets were melted partially by annealing at 870 °C for 30 minutes and then were sintered at 830 °C for 24 hours to obtain Bi 2212 composites with uniformally distributed WO₃ nanoparticles. The resultant samples were subjected to a second stage of pressing and sintering (referred to as press-sintering) for densification. Bi 2212 composites thus synthesized with different amounts of nano WO₃ were coded as follows: Pure Bi 2212 sample with no WO₃ addition as WB 0, and with 0.1, 1, and 5 wt. % nano WO₃ addition as WB 1, WB 2, and WB 3, respectively.

All the samples were characterized for phase formation by analyzing their X-ray diffraction patterns recorded (on Malvern Panalytical diffractometer) using Cu K_{α} radiation. Magnetic field (H) dependence of Magnetization (M) was recorded using PPMS (Quantum Design, Dynacool) at various Temperatures (T). The onset temperatures T_c (onset) of superconducting transitions were measured from M-T curves recorded for each sample, and the critical current density (J_c) was calculated at varying magnetic fields from the M-H loops recorded at various temperatures.

3.3 Results

3.3.1 XRD Analysis of Bi 2212 Composites

Indexed X-ray diffraction (XRD) patterns for all the Bi 2212 composite samples are given in Fig. 3.3. Major peaks among all the peaks in the XRD patterns could be indexed to Bi 2212 phase as the main phase. X'pert Highscore Plus software was used for phase identification and lattice parameter analysis.

Minute amounts of the low T_c phase $Bi_2Sr_2CuO_6$ (Bi 2201) and traces of other oxide phases are indicated in Fig. 3.3.

For sample, WB 2 having 1 wt.% or more of nano WO₃ addition, the formation of a second phase was detected, which could be indexed to the WSr₂CaO₆ compound. The diffraction peaks observed at 2 θ values, 18.83, 36.48, 44.2, and 55.04, represent the presence of this phase. Using Highscore software, it was estimated that the amount of WSr₂CaO₆ phase increased from 6.6% for sample WB 2 to ~ 20 % in sample WB 3 with 5 wt.% of WO₃ addition.

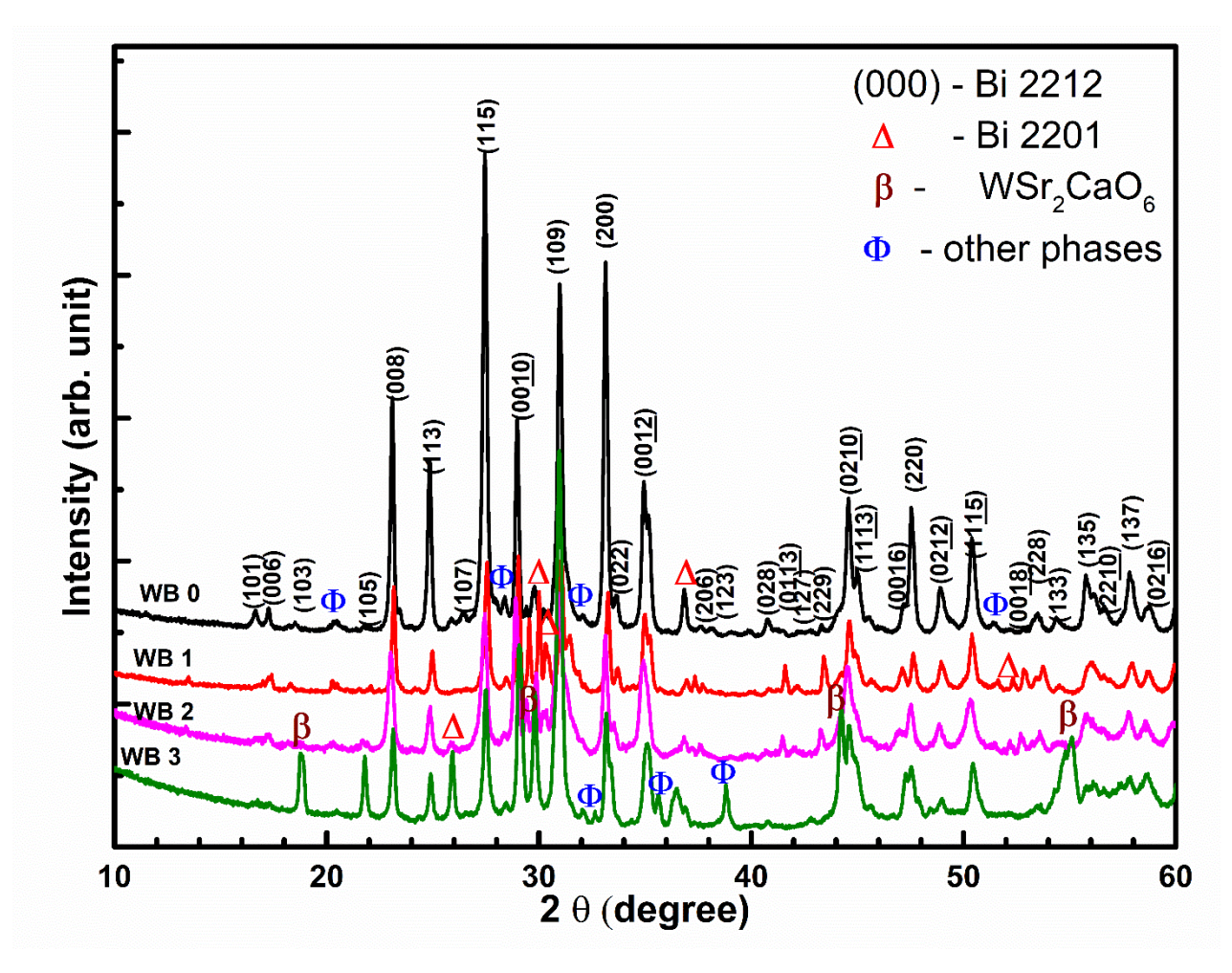


Figure 3.3: Indexed XRD patterns for all the Bi 2212 samples with nano WO₃ addition showing Bi 2212 as the main phase present. Minor amounts of Bi 2201 (marked Δ) and other oxide phases (marked Φ) are seen. At higher concentrations of WO₃, the formation of the WSr₂CaO₆ (marked β) phase was observed.

The amount of the WSr₂CaO₆ phase has increased with the rise in WO₃ content, confirming that nano WO₃ reacted with matrix phase elements during the heating process to form this phase. A slight shift in the lattice parameters was also observed with nano WO₃ addition, compared to sample WB 0, which suggests that a small amount of W enters the unit cell, probably substituting for Cu, due to their comparable ionic radii [22]. Lattice parameters and the phases present in all the samples are given in Table 3.1.

Table 3.1: Lattice parameters and phase identification for all Bi 2212 samples with nano WO₃ addition

Sample	Lattice parameters of 2212 phase			Traces of Minority phases present	Other impurity phases
	a (Å)	b (Å)	c (Å)		
WB 0	5.405(6)	5.407(7)	30.817(7)	Bi 2201 (△), Bi-Sr-O and Sr-	-
				Сu-O (Ф)	
WB 1	5.411(6)	5.418(4)	30.905(1)	Bi 2201 (△), Bi-Sr-O (Φ)	-
WB 2	5.414(7)	5.415(8)	30.916(6)	Bi 2201 (△), Bi-Sr-O (Φ)	WSr ₂ CaO ₆ (β) 6.6%
WB 3	5.414(5)	5.414(2)	30.855(5)	Bi 2201 (Δ)	WSr ₂ CaO ₆ (β) 20.8%

3.3.2 Microstructural analysis

Fig. 3.4 shows the FESEM images of microstructures of fractured surfaces in all the samples. All samples have closely packed platelet-like grains. In samples with addition of nano WO₃ (mostly of size 2-6 nm), spherical particles (20-80 nm size) of a second phase have formed and are found located systematically at the platelet boundaries.

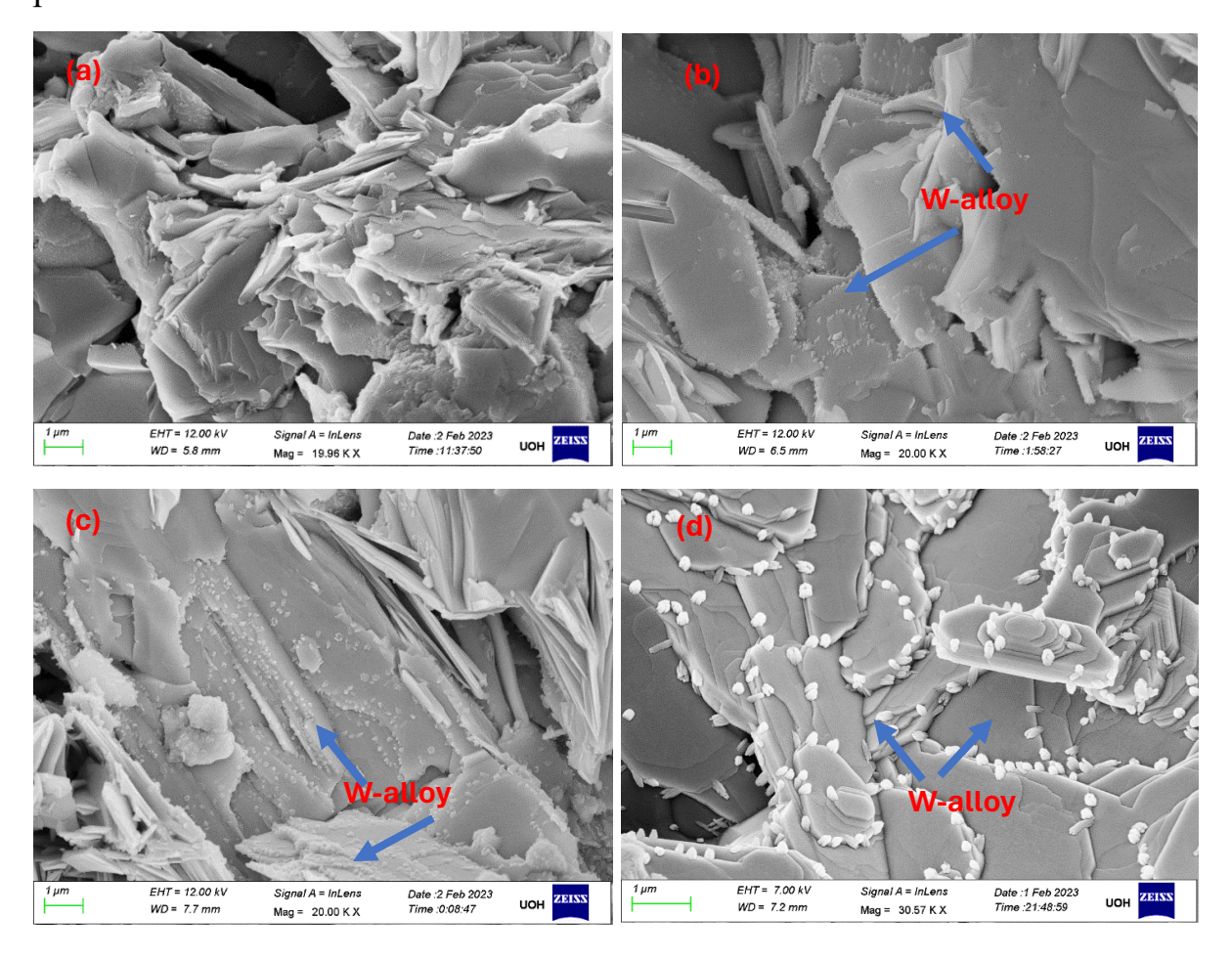


Figure 3.4 (a-d): FESEM micrographs of fractured surfaces of all Bi 2212 samples with nano WO₃ addition; W-containing phase observed are marked for samples WB 1, WB 2, and WB 3.

The number density of spherical particles was observed to increase with increasing WO₃ content. Energy dispersive X-ray (EDAX) analysis in the region of the particles in WB 2 and WB 3 showed a composition containing W-Sr-Ca-O phase. It was difficult to assess the exact composition of the particles due to their small size. Combining the results from XRD analysis, we identify the particles to be of WSr₂CaO₆ phase. Interestingly, the nano WO₃ particles have reacted locally with the elements of the matrix phase and formed a two-phase microstructure akin to Y 123 with Y 211 precipitates [9,23–26]. We believe that the uniform distribution of second-phase WSr₂CaO₆ particles in Bi 2212, observed in Fig. 3.4, is a result of the local reaction of uniformly distributed WO₃ nanoparticles in the Bi 2212 matrix without agglomeration, which was possible due to sol-casting process used in the present work. The fact that the number density of these secondary phase defects/precipitates can be controlled by varying the nano WO₃ content is significant in optimizing microstructures for better superconducting properties like in YBCO superconductors.

3.3.3 Temperature dependence of Magnetization

Fig. 3.5 shows the temperature dependence of magnetization (M) recorded for all Bi 2212 samples with WO₃ nanoparticles addition, at 5 mT applied field, in the temperature range 20-120 K. The occurrence of diamagnetic transition in the range 80-90 K confirms the formation of Bi 2212 as the majority phase in all the samples. For the sample WB 0, with no nano WO₃ addition, T_c (Onset) is around 90 K while 5 wt% nano WO₃ added sample exhibits the lowest T_c (Onset) of around 80.5 K. We observe that the T_c (onset) reduced from 90 to 80 K with nano WO₃ addition and that the superconducting fraction decreased gradually. This supports the possible substitution of W in the unit cells of Bi 2212, possibly at the Cu site, as discussed in XRD analysis. Change of T_c owing to the substitution of certain ions of comparable radii into the lattice is widely reported [27–31]. In the present system, the decrease in T_c is marginal and hence would affect the properties only close to T_c .

The transition widths (ΔT_c) were calculated, using the definition $\Delta T_c = T_c$ 90% - T_c 10% [32], from the normalized M-T curves shown in Fig. 3.5 and are given in Table 3.2. Here, T_c 10% and T_c 90% are the temperatures at which the diamagnetic signal strength falls to 10 % and 90 %, respectively, of the total drop across the transition. Samples WB 1 and WB 2 have relatively lower transition widths, ΔT_c .

Transition widths in the range 20 to 40 K are reported for Bi 2212 superconductors, for instance, with Yb substitutions [33] and Au addition [34].

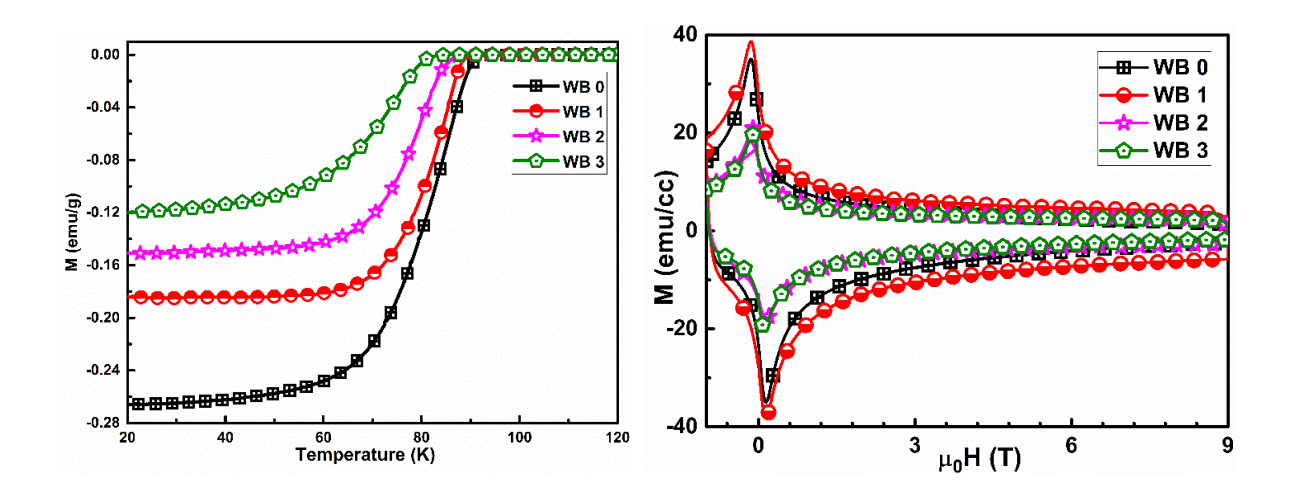


Fig. 3.5: Temperature dependence of magnetization for all Bi 2212 samples with nano WO₃ addition, showing an increased shift in the onset of diamagnetic transition to low temperatures with an increase in WO₃ content.

Fig. 3.6: Field dependence of magnetization for Bi 2212 samples with nano WO₃ addition at 5 K, showing all the samples have $J_c > 0$, till 9 T applied field

Table 3.2: Transition temperatures and transition widths for Bi 2212 samples with nano WO₃ addition

S. No.	Sample	$T_c(\mathbf{K})$	$\Delta T_c(\mathbf{K})$
1	WB 0	90	23.2
2	WB 1	88.2	16.5
3	WB 2	85	18.2
4	WB 3	80.5	29.2

3.3.4 Field dependence of Magnetization

Magnetic hysteresis (M-H) loops are recorded in all composites at different temperatures (5 K, 15 K, 50 K, and 77 K). MH loops recorded at 5 K for all the samples is shown in Fig. 3.6. The hysteresis in M (opening of an M-H loop) is proportional J_c . At 5 K, M-H loops for all the samples are open till 9 T, indicating that all the samples support non-zero J_c up to the highest applied fields and hence have an irreversibility field B_{irr} of above 9 T.

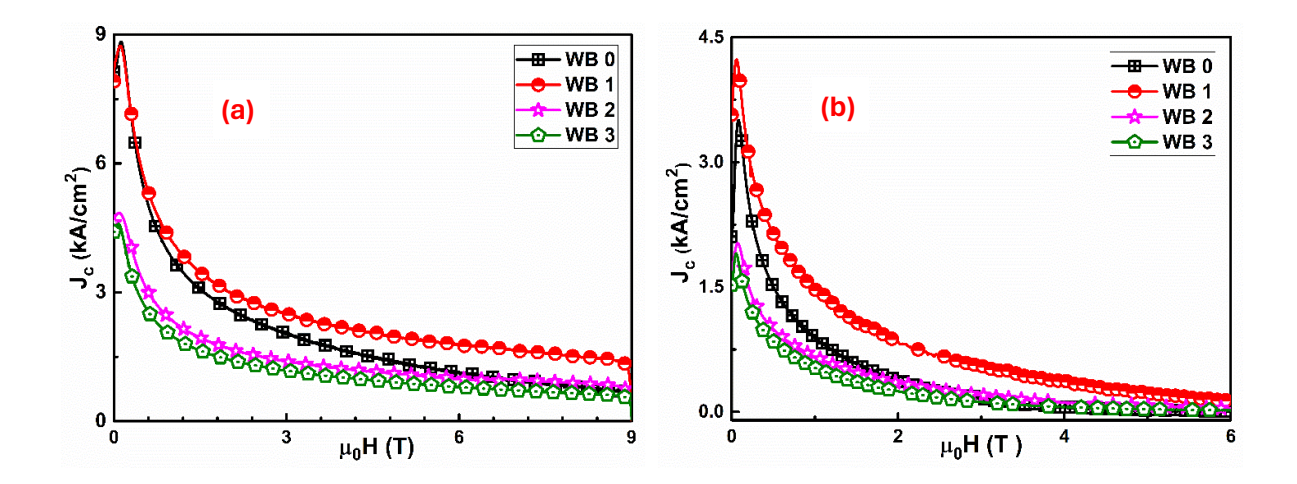
The field dependence of J_c for all composites estimated using the extended critical state model [35] is shown in Figs. 3.7 (a & b) at 5 K and 15 K. At 5 K,

samples WB 0 and WB 1 have nearly the same J_c values at lower fields, but at higher fields, the J_c for sample WB 0 decreases rapidly compared to the sample with 0.1 wt.% WO₃ nanoparticles addition. At 15 K, the sample WB 1 exhibits substantial enhancement in J_c and has the highest value among all the samples in the entire field range.

It can also be seen from Fig. 3.7 (c) that the fall in J_c with T is much more rapid in WB 0 with no nano WO₃ addition. J_c for sample WB1, with 0.1 wt.% WO₃ is higher than for WB 0, in the temperature range of 10 K to 50 K. For WB 1 sample $J_c(0)$ value has increased by 60 % at 15 K and by 35% at 50 K, with respect to those of WB 0. This suggests that the pinning centres generated by low concentrations of nano WO₃ addition are effective in the intermediate temperature range. All samples were superconducting up to 77 K.

Here, we bring in an analogy to the YBa₂Cu₃O_{7- δ} superconductor (called YBCO or Y 123) system in which distribution of around 30 mol % of non-superconducting Y 211 particles in Y 123 matrix leads to substantial enhancement of J_c [36,37]. This is attributed to flux pinning caused by fine secondary defects like stacking faults generated at the interface of the particles with the matrix phase. The secondary defects are of size comparable to the coherence length of HTSCs, as observed from spectroscopic investigations [9,25,38].

From this, we infer optimum levels of defect density generated by the W-alloy phase (WSr₂CaO₆) particles present in the Bi 2212 matrix in WB 1 sample, which appears to have provided effective flux pinning retaining higher J_c as observed in Fig. 3.7(b) to higher fields. The $J_c(0)$ values, (i.e. J_c at zero field) are given in Table 3.3 for all the samples at different temperatures.



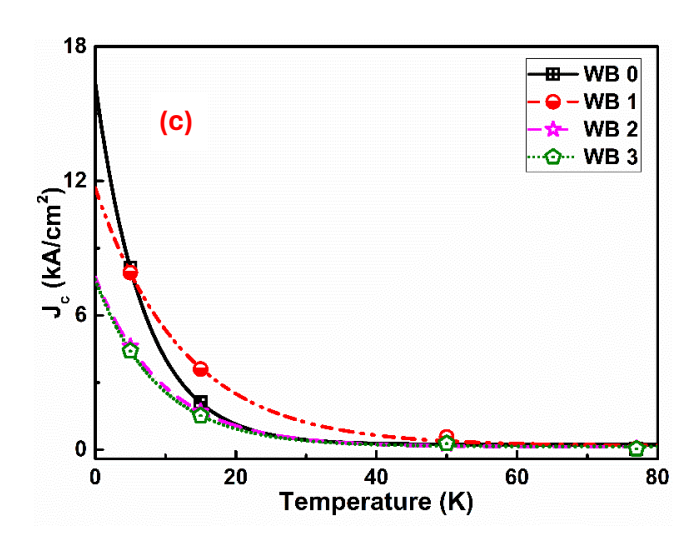


Fig. 3.7: Field dependence of J_c at a) 5 K and b) 15 K, respectively; c) T dependence of zero field J_c in the range 5 K to 77 K, for all the samples of Bi 2212 series with nano WO₃ addition

3.3.5 Analysis of Flux Pinning Force Density (F_p)

For an in-depth understanding of flux pinning occurring in Bi 2212 composite samples, the flux pinning force density (F_p) is calculated using the relation, $F_p = J_c x B$ and is analysed using the scaling laws.

The F_p vs B curves at 5 K, 15 K, and 50 K are shown in Figs. 3.8 (a-c). At 5 K, F_p monotonically increases with the applied field for all the samples with WO₃ addition, while it reaches a maximum at about 5 T for WB 0. This shows that flux lines remain pinned till the 9 T applied field in the composites, suggesting suppression of flux creep, compared to WB 0, even at low temperatures. The F_p has the highest value for WB 1 when compared to other samples at all temperatures. The $F_{p max}$ values for all the samples are given in Table 3.3.

Table 3.3: B* (T) at 15 and 50 K, J_c (0) and $F_{p max}$ at 5, 15, and 50 K for the Bi 2212 samples with varying nano WO₃ addition

Sample	15 K	50 K	5 K		15	K	50 K	
	B*	B *	$J_{c}\left(\theta\right)$	F _{p max}	$J_{c}\left(\theta\right)$	F _{p max}	$J_{c}\left(\theta\right)$	F _{p max}
	(T)	(T)	A/cm ²	N/cm ³	A/cm ²	N/cm ³	A/cm ²	N/cm ³
WB 0	6.37	0.20	8124.5	870.7	2109.2	113.9	421	1.22
WB 1	8.35	0.32	7908.1	1566.4	3602.5	218.1	570.5	2.1
WB 2	8.55	0.24	4617.7	914.8	1697.3	90.8	260.8	0.77
WB 3	7.0	0.14	4408.1	662.8	1524	68.4	282.8	0.35

At higher temperatures like 15 K and 50 K, the $F_{p max}$ (the peak value of F_p in the F_p vs ($B = \mu_o H$) curves) shifts to lower fields for all the samples, due to flux creep that is known to be predominant in BSCCO superconductors compared to YBCO [39,40] superconductors and it increases with rise in temperature. However, for WB 1 sample, $F_{p max}$ occurs at higher fields at all temperatures, compared to all other samples. This suggests that at low concentrations of WO₃, effective flux pinning is achieved to higher fields. The full width at half maximum (FWHM) of F_p vs B curves is a measure of the range of fields in which pinning is effective and is found to be 5.45 T at 15 K for WB 1, while it is 2.9 T for WB 0, as can be seen from Fig. 3.8(b). The fact that the peak widths of F_p vs. B curves for WB 1 sample are larger till 50 K confirms the effective field range of flux pinning to have been enhanced by the defects generated by adding 0.1 wt.% nano WO₃ to Bi 2212.

Studies on the pinning mechanism in BSCCO samples in literature, propose normal surface pinning at grain boundaries (δl pinning) to be dominant [41,42] while substitutional defects and the presence of low T_c superconducting phases, if any, would cause δT_c pinning [43]. In the present set of composites, we find that pinning from the defects generated by the reaction of nano WO₃ is also effective, in addition to the structural defects at platelet/grain boundaries, leading to additional surface pinning in composites over a broader field range compared to that of WB 0, as seen in Figs. 3.8 (a-c). Small amounts of Bi 2201 phase (with a T_c of 10 K) present become normal and contribute marginally to flux pinning at all temperatures above 10 K.

To understand the nature of pinning present in our samples, we plotted the normalized pinning force $(f = F_p/F_{p max})$ vs. $h (=B/B_p)$ along with the theoretical curve for Normal surface pinning mechanism as discussed in the literature [13,44–46]. For this, the field is normalized to peak field B_p (i.e., the field at F_p max) such that $h = B/B_p = \mu_0 H/\mu_0 H_p$.

The scaling laws in terms of h [13,41,42,44–47] for δk pinning, normal point pinning, and surface pinning are given by equations (13-15) given in Chapter 2 and are indicated by the continuous curves in Figs. 3.8(d & e).

It can be seen from Figs. 8 (d -e), that the experimental curves are in the vicinity of the theoretical curve for normal surface pinning at 15 K and 50 K. The deviation from theoretical curve at fields well above B_p is attributed to the presence of additional pinning mechanisms that are operative at higher fields. At 5 K, the maximum in F_p is not reached even up to 9 T for the composites; hence, further analysis in terms of scaling laws was not considered at this temperature.

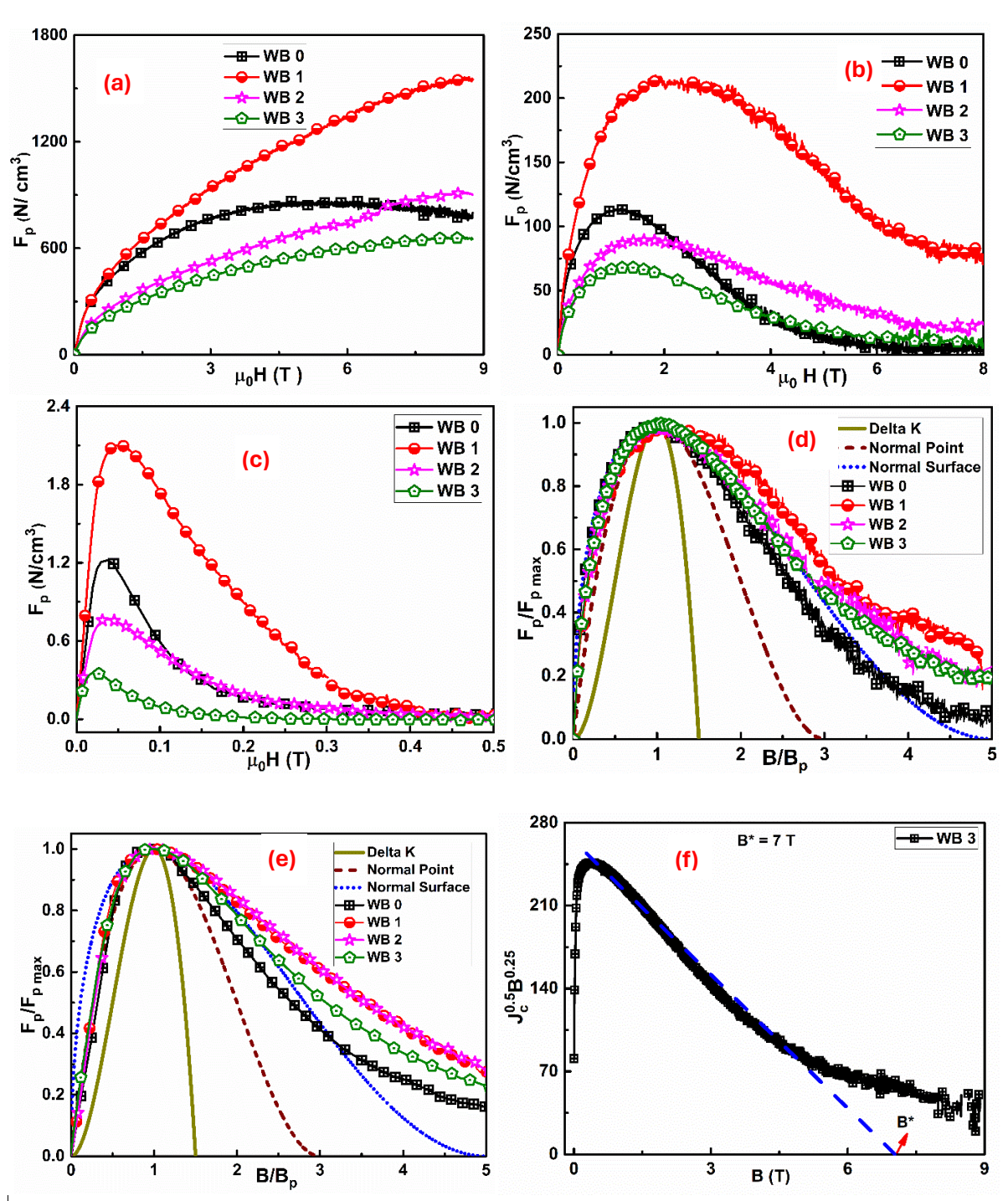


Fig. 3.8 (a-c): Field dependence of Pinning force density at 5, 15, and 50 K respectively, (d, e) f vs. B/B_p curves along with theoretical curve at 15 and 50 K respectively for all the Bi 2212 samples with nano WO₃ addition, (f) B^* estimation, shown typically, for sample WB 3 at 15 K, using Kramer's approach.

From Kramer's approach, we determined B^* , the characteristic field beyond which the rigidity of the flux line lattice (FLL) effectively vanishes, and B^* is $< B_{c2}$ in HTSc due to flux creep. B^* was obtained by linear extrapolation to zero of the low- J_c segment of the Kramer curve [48] in which $J_c^{1/2}B^{1/4}$ is plotted

vs. field B. This approach of obtaining B^* is reported by [13,49,50]. Fig. 3.8(f) shows a typical plot for sample WB 3 from which B^* is determined. B^* values at 15 and 50 K are shown in Table 3.3.

Lower transition widths indicative of better grain connectivity would also play a role in the superior superconducting properties observed for samples WB 1 and WB 2. Since Sample WB 0 has no nano WO₃ addition, there is an inadequacy of pinning centres to provide effective pinning at higher fields and this explains the rapid fall in J_c in WB 0 at higher fields.

According to reports based on computer simulations of the interactions between pinning centres and flux lines, at high defect densities, the mobility of the flux lines increases such that the flux lines can jump freely from one defect to another without being pinned [51,52]. This might be the cause of why the presence of secondary phases is effective only at low concentrations, and the superconducting properties start to degrade at higher concentrations.

Flux pinning from various sources/ mechanisms can thus simultaneously exist to different extents in high T_c superconductors and can be effective at different field and temperature regimes. However, separating the contributions from these sources to quantitatively flux pinning is a complex problem.

3.4 Conclusions

To mimic the two-phase microstructure of the YBCO system which enhances flux pinning and improves J_c subsequently, we have studied the effect of WO₃ nanoparticles addition on the superconducting properties of Bi₂Sr_{2.14}Ca_{0.86}Cu₂O_y superconductor. Through sol-casting process, WO₃ nanoparticles were uniformly distributed into the Bi 2212 matrix, which, on heating to 870 °C for a short duration, generated nearly spherical particles (20-80 nm) of WSr₂CaO₆ phase as a second phase. These particles are seen to be well dispersed along the Bi 2212 platelet boundaries, as observed in FESEM images of fractured samples.

The number density of second-phase precipitates generated increased with the nano WO₃ content, confirming their formation was caused by the local reaction of WO₃ nanoparticles with the matrix phase. M-H loops recorded show B_{irr} to be above 9 T at 5 K in the composites with nano WO₃ addition, which is higher compared to pure Bi 2212 sample having B_{irr} around 5 T. Addition of nano WO₃ in low concentrations (0.1 wt.%) is found to enhance the superconducting properties of Bi 2212 in a broad range of fields at intermediate temperatures of 10 K to 50 K. The better superconducting properties in composite with nano WO₃ addition are attributed to the effective flux pinning caused by the secondary defects created at the interface of the WSr₂CaO₆ particles with the Bi 2212 matrix.

As the concentration of nano WO₃ increased, the zero-field J_c decreased, indicating a reduction in the superconducting phase fraction. Analysis of pinning force density using scaling laws suggests that multiple pinning mechanisms can be operative at different field and temperature regimes. Our results show that controlling the two-phase microstructure can sustain effective flux pinning across a wide range of magnetic fields.

The current study shows that the sol-casting method is more effective than the conventional solid-state synthesis method for introducing suitable nanoparticles uniformly, without agglomeration, in the Bi 2212 matrix. The J_c value diminished to zero around 5 T applied field at 4.2 K, when the WO₃ nanoparticles were added by the solid-state synthesis method as reported [15] whereas, for WO₃ nanoparticles added by sol-casting method, as in sample WB 1, the J_c falls nearly 4 times the $J_c(0)$ value but is sustained to 2 kA/cm² at 5 K till 9 T applied field. Previous studies in the literature suggest that the addition of nano-sized Ag to Bi 2212 led to the fall of J_c approximately 100 times the $J_c(0)$ value, even at 4.2 K at 6 T applied field [13]. Nanosized Al precipitates added to Bi 2212 similarly resulted in the deterioration of J_c at an applied field of 5 T at 4.2 K [53]. At 10 K, in nano SiO₂ added Bi 2212 samples, the J_c diminishes around 3 T applied field [54]. Hence, in comparison to existing literature, WO₃ nanoparticles are a better candidate as pinning centres to pin the flux lines at higher applied fields and in the 10 K- 50 K temperature range.

The fact that the present Bi 2212 composites possess a two-phase microstructure, as in the YBCO system, with controllable second-phase particle density. This study presents an opportunity to design controllable microstructures in BSCCO superconductors by locally reacting suitable nanoparticles, thus enhancing flux pinning.

References

- [1] F. Kametani, J. Jiang, M. Matras, D. Abraimov, E.E. Hellstrom, D.C. Larbalestier, Comparison of growth texture in round Bi 2212 and flat Bi 2223 wires and its relation to high critical current density development, Sci. Rep. 5 (2015) 1–9. https://doi.org/10.1038/srep08285.
- [2] L.N. Bulaevskii, L.L. Daemen, M.P. Maley, J.Y. Coulter, Limits to the critical current in high- T_c superconducting tapes, Phys. Rev. B. 48 (1993) 13798–13816. https://doi.org/10.1103/PhysRevB.48.13798.
- [3] R.R. Kumar, R.P. Aloysius, R.J. Bose, P. Guruswamy, U. Syamaprasad, Preparation of dense, high J_c Bi-2223 superconductors by multistage cold pressing, Supercond. Sci. Technol. 18 (2005) 689–693. https://doi.org/10.1088/0953-2048/18/5/018.

- [4] N. Chikumoto, M. Konczykowski, N. Motohira, A.P. Malozemoff, Flux-creep crossover and relaxation over surface barriers in Bi₂Sr₂CaCu₂O₈ crystals, Phys. Rev. Lett. 69 (1992) 1260–1263. https://doi.org/10.1103/PhysRevLett.69.1260.
- [5] A.N. Lykov, Magnetic flux creep in HTSC and Anderson-Kim theory (Review Article), Low Temp. Phys. 40 (2014) 773–795. https://doi.org/10.1063/1.4896968.
- [6] Y. Yamada, K. Takahashi, H. Kobayashi, M. Konishi, T. Watanabe, A. Ibi, T. Muroga, S. Miyata, T. Kato, T. Hirayama, Y. Shiohara, Epitaxial nanostructure and defects effective for pinning in Y(RE)Ba₂Cu₃O_{7-x} coated conductors, Appl. Phys. Lett. 87 (2005) 1–3. https://doi.org/10.1063/1.2061874.
- [7] S. Eley, A. Glatz, R. Willa, Challenges and transformative opportunities in superconductor vortex physics, J. Appl. Phys. 130 (2021). https://doi.org/10.1063/5.0055611.
- [8] D. Shi, J.G. Chen, U. Welp, M.S. Boley, A. Zangvil, Lattice defects and flux pinning in crystallized metal-oxide glasses in the Bi-Sr-Ca-Cu-O system, Appl. Phys. Lett. 55 (1989) 1354–1356. https://doi.org/10.1063/1.101896.
- [9] N. Devendra Kumar, T. Rajasekharan, R.C. Gundakaram, V. Seshubai, Extensive nanotwinning: Origin of high current density to high fields in preform-optimized infiltration-growth-processed YBa₂Cu₃O_{7-δ} superconductor, IEEE Trans. Appl. Supercond. 21 (2011) 3612–3620. https://doi.org/10.1109/TASC.2011.2168819.
- [10] W. Wei, J. Schwartz, K.. Goretta, U. Balachandran, A. Bhargava, Effects of nanosize MgO additions to bulk Bi_{2.1}Sr_{1.7}CaCu₂O_x, Phys. C Supercond. 298 (1998) 279–288. https://doi.org/10.1016/S0921-4534(97)01889-3.
- [11] K. Christova, A. Manov, J. Nyhus, U. Thisted, O. Herstad, S., Foss, K., Haugen, K. Fossheim, Bi₂Sr₂CaCu₂O_x bulk superconductor with MgO particles embedded, J. Alloys Compd. 340 (2002) 1–5. https://doi.org/10.1016/S0925-8388(01)02021-7.
- [12] I.E. Agranovski, A.Y. Ilyushechkin, I.S. Altman, T.E. Bostrom, M. Choi, Methods of introduction of MgO nanoparticles into Bi-2212/Ag tapes, Phys. C Supercond. Its Appl. 434 (2006) 115–120. https://doi.org/10.1016/j.physc.2005.12.005.
- [13] S. Zhang, C. Li, Q. Hao, J. Feng, T. Lu, P. Zhang, Optimized Intergrain Connection and Transport Properties of Bi-2212 High-Temperature Superconductors by Ag Nanoparticles Inclusions, J. Supercond. Nov. Magn. 28 (2015) 1729–1736. https://doi.org/10.1007/s10948-015-2981-1.
- [14] C. Li, S. Zhang, L. Gao, Q. Hao, L. Bai, P. Zhang, Doping effects of ZrO₂ nanoparticles on the superconducting properties of Bi-2212 tapes, J. Mater. Sci. Mater. Electron. 26 (2015) 3583–3588. https://doi.org/10.1007/s10854-015-2872-z.
- [15] B. Özkurt, The influence of WO3 nano-particle addition on the structural and mechanical properties of Bi_{1.8}Sr₂Ca_{1.1}Cu_{2.1}O_y ceramics, J. Mater. Sci. Mater. Electron. 24 (2013) 4233–4239. https://doi.org/10.1007/s10854-013-1390-0.
- [16] P.M.S. Raju, V. Seshubai, T. Rajasekharan, A generic process to introduce nanoparticles into powder preforms and its application to Infiltration Growth processing of REBa₂Cu₃O₇ superconductor, Mater. Chem. Phys. 161 (2015) 59–64. https://doi.org/10.1016/j.matchemphys.2015.05.004.
- [17] S. Ravi, V. Seshu Bai, AC susceptibility study in the 85 K phase of the Bi-Sr-Ca-Cu-O

- system, Phys. C Supercond. Its Appl. 230 (1994) 51–60. https://doi.org/10.1016/0921-4534(94)90445-6.
- [18] S. Ravi, V. Seshu Bai, Excess conductivity studies in pure and Ag doped 85 K phase in Bi-Sr-Ca-Cu-O system, Solid State Commun. 83 (1992) 117–121. https://doi.org/10.1016/0038-1098(92)90887-F.
- [19] P.K. Verma, T. Rajasekharan, S.C. Das, K.P. Surendran, V. Seshu Bai, Effect of nano ZrO₂ addition on the properties of Ca_{0.86}Sr_{0.14}CuO₂ added Bi 2223 composites, J. Phys. Conf. Ser. 2545 (2023) 012014. https://doi.org/10.1088/1742-6596/2545/1/012014.
- [20] V.Seshu Bai, S. Ravi, T. Rajasekharan, R. Gopalan, On the composition of 110 K superconductor in a (Bi,Pb)-Sr-Ca-Cu-O system, J. Appl. Phys. 70 (1991) 4378–4382. https://doi.org/10.1063/1.349119.
- [21] D. -X. Chen, A. Hernando, F. Conde, J. Ramírez, J.M. González-Calbet, M. Vallet, Lower critical field and surface barrier in sintered Bi₂Sr₂CaCu ₂O_{8+δ} superconductor, J. Appl. Phys. 75 (1994) 2578–2583. https://doi.org/10.1063/1.356232.
- [22] R.D. Shannon, Revised effective ionic radii and systematic studies of interatomic distances in halides and chalcogenides, Acta Crystallogr. Sect. A. 32 (1976) 751–767. https://doi.org/10.1107/S0567739476001551.
- [23] M. Thoma, Y. Shi, T. Dennis, J. Durrell, D. Cardwell, Effect of Y-211 particle size on the growth of single grain Y-Ba-Cu-O bulk superconductors, J. Cryst. Growth. 412 (2015) 31–39. https://doi.org/10.1016/j.jcrysgro.2014.11.037.
- [24] M. Murakami, Processing of bulk YBaCuO, Supercond. Sci. Technol. 5 (1992) 185–203. https://doi.org/10.1088/0953-2048/5/4/001.
- [25] N. Devendra Kumar, T. Rajasekharan, K. Muraleedharan, A. Banerjee, V. Seshubai, Unprecedented current density to high fields in YBa₂Cu₃O_{7-δ} superconductor through nano-defects generated by preform optimization in infiltration growth process, Supercond. Sci. Technol. 23 (2010) 105020. https://doi.org/10.1088/0953-2048/23/10/105020.
- [26] S. Pavan Kumar Naik, N. Devendra Kumar, P. Missak Swarup Raju, T. Rajasekharan, V. Seshubai, Effect of infiltration temperature on the properties of infiltration growth processed YBCO superconductor, Phys. C Supercond. Its Appl. 487 (2013) 72–76. https://doi.org/10.1016/j.physc.2013.01.008.
- [27] Lovleena, I.K. Bidikin, A.L. Kholkin, B. Kumar, Structural changes in ab-plane of Zn doped Bi-2212 HTSC single crystals, Phys. C Supercond. 451 (2007) 44–48. https://doi.org/10.1016/j.physc.2006.10.003.
- [28] K.C. Goretta, V.R. Todt, D.J. Miller, M.T. Lanagan, Y.L. Chen, U. Balachandran, J. Guo, J.A. Lewis, Engineered flux-pinning centers in Bi₂Sr₂CaCu₂O_x and TIBa₂Ca₂Cu₃O_x superconductors, J. Electron. Mater. 24 (1995) 1961–1966. https://doi.org/10.1007/BF02653017.
- [29] P.E. Kazin, V. V. Poltavets, O.N. Poltavets, A.A. Kovalevsky, Y.D. Tretyakov, M. Jansen, Formation of Bi-2212 phase and phase assemblage in Ga-doped BSCCO system, Phys. C Supercond. Its Appl. 324 (1999) 30–38. https://doi.org/10.1016/S0921-4534(99)00444-X.
- [30] V.P.S. Awana, S.K. Agarwal, B. V. Kumaraswamy, B.P. Singh, A. V. Narlikar, Effect of

- 3d metallic dopants on superconductivity of the Bi ₂CaSr₂Cu₂O₈ system, Supercond. Sci. Technol. 5 (1992) 376–380. https://doi.org/10.1088/0953-2048/5/6/010.
- [31] P.M. Sarun, R. Shabna, S. Vinu, A. Biju, U. Syamaprasad, Highly enhanced superconducting properties of Bi-2212 by Y and Pb co-doping, 404 (2009) 1602–1606. https://doi.org/10.1016/j.physb.2009.01.023.
- [32] M.H. Gharahcheshmeh, E. Galstyan, A. Xu, J. Kukunuru, R. Katta, Y. Zhang, G. Majkic, X.-F. Li, V. Selvamanickam, Superconducting transition width (ΔT_c) characteristics of 25 mol% Zr-added (Gd, Y)Ba₂ Cu₃O_{7- δ} superconductor tapes with high in-field critical current density at 30 K, Supercond. Sci. Technol. 30 (2017) 015016. https://doi.org/10.1088/0953-2048/30/1/015016.
- [33] H. Gündoğmuş, B. Özçelik, A. Sotelo, M.A. Madre, Effect of Yb-substitution on thermally activated flux creep in the Bi₂Sr₂Ca₁Cu_{2-x}Yb_xO _y superconductors, J. Mater. Sci. Mater. Electron. 24 (2013) 2568–2575. https://doi.org/10.1007/s10854-013-1135-0.
- [34] U. ÖZTORNACI, B. ÖZKURT, The effect of nano-sized metallic Au addition on structural and magnetic properties of Bi_{1.8}Sr₂ Au_xCa_{1.1}Cu_{2.1}O_y (Bi-2212) ceramics, Ceram. Int. 43 (2017) 4545–4550. https://doi.org/10.1016/j.ceramint.2016.12.109.
- [35] C.P. Bean, Magnetization of hard superconductors, Phys. Rev. Lett. 8 (1962) 250–253. https://doi.org/10.1103/PhysRevLett.8.250.
- [36] N. Devendra Kumar, T. Rajasekharan, K. Muraleedharan, A. Banerjee, V. Seshu bai, Unprecedented current density to high fields in YBa₂Cu₃O_{7-δ} superconductor through nano-defects generated by preform optimization in infiltration growth process, Supercond. Sci. Technol. 23 (2010) 105020. https://doi.org/10.1088/0953-2048/23/10/105020.
- [37] N. Devendra Kumar, P. Missak Swarup Raju, S. Pavan Kumar Naik, T. Rajasekharan, V. Seshu bai, Effect of preform compaction pressure on the final microstructures and superconducting properties of YBa₂Cu₃O_{7-δ} superconductors fabricated by directionally solidified Preform optimized infiltration growth process, J. Low Temp. Phys. 174 (2014) 113–127. https://doi.org/10.1007/s10909-013-0955-x.
- [38] M. Muralidhar, M. Jirsa, N. Sakai, M. Murakami, Progress in melt-processed (Nd-Sm-Gd)Ba₂Cu₃O_y superconductors, Supercond. Sci. Technol. 16 (2003). https://doi.org/10.1088/0953-2048/16/1/201.
- [39] D.E. Lacey, J.A. Wilson, Low-field flux-creep measurements on YBCO and BSCCO, Supercond. Sci. Technol. 5 (1992) 724–731. https://doi.org/10.1088/0953-2048/5/12/005.
- [40] H. Salamati, P. Kameli, AC susceptibility study of YBCO thin film and BSCCO bulk superconductors, J. Magn. Mater. 278 (2004) 237–243. https://doi.org/10.1016/j.jmmm.2003.12.1311.
- [41] D. Sharma, R. Kumar, V.P.S. Awana, DC and AC susceptibility study of sol-gel synthesized Bi₂Sr₂CaCu₂O_{8+δ} superconductor, Ceram. Int. 39 (2013) 1143–1152. https://doi.org/10.1016/j.ceramint.2012.07.038.
- [42] M. Zouaoui, A. Ghattas, M. Annabi, F. Ben Azzouz, M. Ben Salem, Effect of nano-size ZrO₂ addition on the flux pinning properties of (Bi, Pb)-2223 superconductor,

- Supercond. Sci. Technol. 21 (2008). https://doi.org/10.1088/0953-2048/21/12/125005.
- [43] M.R. Koblischka, Nanoengineering of flux pinning sites in high-T_c superconductors, Tsinghua Sci. Technol. 8 (2003) 280–291.
- [44] L. Klein, E.R. Yacoby, Y. Yeshurun, A. Erb, G. Müller-Vogt, V. Breit, H. Wühl, Peak effect and scaling of irreversible properties in untwinned Y-Ba-Cu-O crystals, Phys. Rev. B. 49 (1994) 4403–4406. https://doi.org/10.1103/PhysRevB.49.4403.
- [45] T. Goto, K. Inagaki, K. Watanabe, Critical current density in filamentary (Nd, Sm, Eu, Gd)-Ba-Cu-O superconductors prepared by a solution spinning method, Phys. C Supercond. Its Appl. 330 (2000) 51–57. https://doi.org/10.1016/S0921-4534(99)00608-5.
- [46] M. Murakami, S.I. Yoo, Comparative study of critical current densities and flux pinning among a flux-grown (formula presented) single crystal, melt-textured Nd-Ba-Cu-O, and Y-Ba-Cu-O bulks, Phys. Rev. B Condens. Matter Mater. Phys. 59 (1999) 1514–1527. https://doi.org/10.1103/PhysRevB.59.1514.
- [47] S. Vinu, P.M. Sarun, R. Shabna, A. Biju, U. Syamaprasad, Enhancement of flux pinning and Anderson-Dew-Hughes pinning analysis in Bi_{1.6}Pb_{0.5}Sr_{2-x} Tb_xCa_{1.1}Cu_{2.1}O_{8+δ} superconductor, J. Alloys Compd. 477 (2009) 13–16. https://doi.org/10.1016/j.jallcom.2008.10.033.
- [48] E.J. Kramer, Scaling laws for flux pinning in hard superconductors, J. Appl. Phys. 44 (1973) 1360–1370. https://doi.org/10.1063/1.1662353.
- [49] R.A. Rose, S.B. Ota, P.A.J. de Groot, B. Jayaram, Scaling of the vortex pinning force in Bi₂Sr₂CaCu₂O_{8+y}, Phys. C Supercond. Its Appl. 170 (1990) 51–55. https://doi.org/10.1016/0921-4534(90)90227-6.
- [50] A. Leveratto, A.A. Armenio, A. Traverso, G. De Marzi, G. Celentano, A. Malagoli, Transport current and magnetization of Bi-2212 wires above liquid Helium temperature for cryogen-free applications, Sci. Rep. 11 (2021) 1–9. https://doi.org/10.1038/s41598-021-91222-2.
- [51] A.E. Koshelev, I.A. Sadovskyy, C.L. Phillips, A. Glatz, Optimization of vortex pinning by nanoparticles using simulations of the time-dependent Ginzburg-Landau model, Phys. Rev. B. 93 (2016) 1–5. https://doi.org/10.1103/PhysRevB.93.060508.
- [52] L. Civale, Vortex pinning and creep in high-temperature superconductors with columnar defects, Supercond. Sci. Technol. 10 (1997) A11–A28. https://doi.org/10.1088/0953-2048/10/7A/003.
- [53] S. Zhang, M. Liang, C. Li, Q. Hao, J. Feng, P. Zhang, Enhanced flux pinning properties in Bi-2212 high temperature superconductors with nano-sized precipitates, Mater. Lett. 157 (2015) 197–200. https://doi.org/10.1016/j.matlet.2015.05.096.
- [54] L.P. Qiu, Y.R. Zhang, S.L. Gao, Q.H. Zheng, T.T. Zhang, G.T. Cheng, S. ze Cao, W.P. Hang, S. Ramakrishna, Y.Z. Long, Fabrication and magnetic properties of SiO₂ nanoparticles-doped BSCCO superconducting nanofibers by solution blow spinning, Phys. C Supercond. Its Appl. 608 (2023) 1354251. https://doi.org/10.1016/j.physc.2023.1354251.

Chapter 4

Effect of adding non-reactive WO₃ nano inclusions to enhance flux pinning properties in Bi 2223 superconductor composites

4.1 Introduction

Over the years, extensive research in the realm of high-temperature superconductors (HTSc) has resulted in the development of convenient and economically feasible methods for producing lengthy wires or tapes using Bi-based superconductors owing to their micaceous nature compared to RE-123 and Tl-based copper oxide systems [1]. Recent advancements in HTSc materials have created opportunities for practical applications in several areas including electrical power devices [2,3] magnetic shields [4], and fault current limiters [5].

Though Silver clad Bi 2212 superconducting wires are commercially available [6]. Their practical application is limited to temperatures below 30 K, despite the T_c being 85 K, because of the predominant flux creep phenomenon. This flux creep results in swift decrease in the J_c [7].

Realizing tapes of Bi 2223 phase (with higher T_c of 110 K) for practical application at higher temperatures and fields, several factors to be addressed, like phase formation, stability, suitable microstructure, and suppression of flux creep to enhance J_c (B, T). Intergrowth of lower T_c phases and the formation of uncontrolled second phases is often reported in Bi 2223; the amounts of coexisting phases are sensitive to initial composition, and the methods of synthesis and heat treatment followed [1].

In the mixed state of superconductors, the Lorentz force causes the flux lines to move from their pinned position, leading to energy dissipation and an exponential decrease in J_c. To overcome this, microscopic non-superconducting precipitates or defects are introduced in the superconducting matrix to pin these flux lines [8]. The size, shape, and number density of these precipitates play a significant role in deciding the extent of flux pinning. Optimal flux pinning occurs when the dimensions of precipitates are comparable to the size of the coherence length of the superconductor, which is a few nanometers [9].

Lattice defects [10], grain boundaries [11], and twin boundaries [12] that form during the processing of superconducting materials and secondary phases that form during synthesis or are added externally are known to contribute to flux

pinning and suppress the rapid fall in J_c(B, T), thus improving superconducting properties.

Various studies on the addition of secondary phases to Bi 2223 are reported in literature like Nd and Tb Co-doping [13], Zn addition[14], Nd addition [15] Nb addition [16]. A detailed literature review on secondary phase addition to Bi 2223 is given in chapter 1, section 1.6.

Using solid-state reaction, the addition of WO₃ to Bi 2223 is reported [17] to have resulted in the substitution of W at the Cu site and improved J_c at lower concentrations, at 10 K. ZnO addition to Bi 2223 was found to lower the melting temperature of the Bi 2223 phase, whereas T_c (onset) remained the same [18].

Among the studies on the effect of nanoparticles as flux pinning centers, graphene nanoparticles were found to reduce T_c (onset). The addition of nanographene led to an increase of high T_c phase content, and when compared all the samples, the sample with 1 wt.% nano graphene addition had higher J_c [19].

Jia et al. found that T_c was constant on adding nano ZrO_2 to $Bi_{1.8}Pb_{0.4}Sr_2Ca_{2.2}Cu_3O_{10+y}$ superconductors and that nano ZrO_2 provides effective flux pinning and enhances J_c at 5 K [20]. The addition of Al_2O_3 nanoparticles to Bi 2223 (up to 0.2 wt.%) has increased J_c at low concentrations, whereas J_c deteriorates at higher concentrations due to a decrease in Bi 2223 phase content and agglomeration of Al-rich phase particles [21].

However, the majority of studies on the effect of pinning centers on the superconducting properties of bulk Bi 2223 superconductors are at temperatures below 30 K, and there is limited information on the flux pinning mechanism that contributes to enhanced superconducting properties at higher fields and temperatures.

The microstructure and superconducting properties in BSCCO superconductors exhibit an intrinsic connection, with the microstructure being influenced by the sintering time and temperature [22]. Limited literature exists that establishes a direct correlation between improving the microstructure through the introduction of a secondary phase and the subsequent enhancement of superconducting properties in BSCCO superconductors. Larger BSCCO grains may exhibit higher J_c values at lower fields, while smaller grains display superior J_c-B behavior due to enhanced flux pinning by their smaller size and the presence of non-superconducting grain boundaries [23]

The recent advent of cryogens/refrigerants available for operation at 50 K makes it attractive to look for designing a microstructure of the Bi 2223 phase that enhances flux pinning and enables applications at moderate temperatures. According to existing literature, adding secondary phase precipitates can reduce

 J_c if it agglomerates and obstructs the supercurrent flow or if it reduces the superconducting phase content or lowers the T_c when it substitutes to the lattice site. This indicates the possibility of improving the superconducting properties at higher temperatures and fields by incorporating non-reactive, non-superconducting precipitates of nanometer size while retaining a significant amount of the superconducting phase and maintaining T_c around 110 K of the Bi 2223 superconductor.

In this direction, we have envisaged introducing WO₃ nanoparticles dispersed uniformly into Bi 2223 bulk without reaction and studying the flux pinning behavior at various temperatures and field ranges.

We have added WO₃ nanoparticles to Bi_{1.2}Pb_{0.3}Sr_{1.54}Ca_{2.06}Cu₃O_y (Bi 2223 phase) and studied their effect on the superconducting properties of Bi 2223. This composition was derived from a systematic work done on a series, with the general formula Bi₂Sr₂(Ca_{0.86}Sr_{0.14})_{n-1}Cu_nO_y, where the Bi 2223 phase was stabilized at n=5 and normalized to 3 Cu atoms per unit cell [24]. In the present work, WO₃ nanoparticles were added to once processed Bi 2223 phase, which was powdered after one sintering at 845 °C, with the idea of distributing the nanoparticles into the matrix phase without reaction. This is in contrast to adding them along with raw/precursor materials used to synthesize Bi 2223, as reported in the literature [17]. We have added WO₃ nanoparticles by a Sol-casting technique [25] developed by our group for the homogenous distribution of the nanoparticles in the matrix phase. This process is different from those reported in the literature [20,21,26] and it prevents nanoparticle agglomeration in the matrix.

The temperature and field dependences of magnetic properties of the Bi 2223 composites thus obtained are determined from M-H loops recorded from 10 K to 77 K and up to 9 T applied magnetic fields. The nature of flux pinning is studied and the limiting fields (B* and B_{irr}) for flux pinning at different field regimes are estimated using scaling laws.

4.2 Experimental

4.2.1 Synthesis of precursor powders of Bi 2223

The Bi 2223 phase precursor powder was synthesized by metal nitrate decomposition method using high purity Bi₂O₃ (Alfa Aesar, 99.975%), Pb(NO₃)₂ (Sigma, >99%), SrCO₃ (Sigma, >99%), CuO (Merck, >99%), CaCO₃ (Sigma, >99. The powders weighed out in stoichiometric ratio were dissolved individually in conc. Nitric acid and were mixed using stirrer, to which a requisite amount of

Pb(NO₃)₂ dissolved in distilled water was added. The solution was dried, and the resultant powder was calcined at 500 °C. The calcined powder was annealed twice for 24 hours each at 800 °C with one intermediate grinding and is used as precursor powder of Bi 2223.

4.2.2 Composites of Bi 2223 with WO₃ nanoparticle addition

Bi_{1.2}Pb_{0.3}Sr_{1.54}Ca_{2.06}Cu₃O_y with the addition of WO₃ nanoparticles (x= 0, 0.1, 0.5, and 5) wt.%, referred to as BW series, were investigated. The samples of the BW series with different amounts of WO₃ nanoparticle addition were coded as follows; the sample without nano WO₃ addition is BW 0; those with 0.1, 0.5, and 5 wt.% nano WO₃ addition to Bi 2223 phase are BW 1, BW 2, and BW 3, respectively. Synthesis and characterization of WO₃ nanoparticles are given in Chapter 2 and Chapter 3, respectively.

The composites of the BW series were synthesized as discussed below. The annealed precursor powders of Bi-2223 were pelletized using a hydraulic press under a pressure of 12 tons and sintered at 845 °C for 48 Hours. The sintered pellet was ground to fine powder, to which WO₃ nanoparticles were added by solcasting technique [25], debindered, and pelletized again. This technique [25] ensures uniform distribution of nanoparticles in the matrix phase, through polymerization using organic binders, which are subsequently removed by burnout. Final sintering was done at 845 °C for 48 hours, which was repeated with one intermediate pressing. Repeated pressing and sintering (press-sintering) process is known to enhance the density of BSCCO samples and improve superconducting properties [24,27]. The stepwise flow chart with details of Bi 2223 composite preparation is given in Fig. 2.2 of Chapter 2.

4.2.3 Characterization of Bi 2223 samples with WO₃ addition

All samples of BW series prepared are characterized by analyzing XRD patterns to confirm phase formation and determine lattice parameters using X'Pert Highscore plus software. Microstructures and composition are examined on cracked samples to observe the morphology and orientation of the grains using Field Emission Scanning Electron Microscope (FESEM) with energy dispersive analysis x-ray spectroscopy (EDAX). The temperature and field dependence of the magnetization of the samples are measured using a Physical property measurement system. The density of the samples was determined using Archimedes' principle to assess the levels of porosity and its role on the superconducting properties. For the density measurement, the weights of the

samples were measured in an air and liquid (glycerin) medium using a Mettler balance with 0.02 mg accuracy. All results are discussed in detail below.

4.3 Results & Discussion

4.3.1 X-ray diffraction studies

Fig. 4.1 shows the indexed X-ray diffraction patterns for all the samples of the BW series. All the diffraction peaks in the XRD pattern could be indexed to Bi 2223 as the main phase with minor amounts of Bi 2212 and Bi 2201 phases, which are estimated using Highscore plus software.

All the samples exhibit Bi 2223 as the majority phase with Orthorhombic structure. The diffraction peak at Bragg angle $2\theta = 23.5^{\circ}$ observed in BW 1 and BW 2 (with 0.1 and 0.5 wt.% nano WO₃, respectively) is representative of WO₃. Phase analysis indicated Sample BW 3 with 5 wt.% addition of nano WO₃ to have traces of a W-containing phase. The absence of secondary phases containing W in samples with lower concentrations of nano WO₃ addition suggests that WO₃ has not reacted with the elements of the Bi 2223 phase or that such phases are too minor in quantity to be detected. The absence of the Bragg peak at $2\theta = 23.5^{\circ}$ and the appearance of a low-intensity peak pertaining to the WSrCaO₆ phase at around $2\theta = 30.7^{\circ}$ in sample BW 3 (with 5 wt.% nano WO₃) suggests that at higher concentrations, nano WO₃ reacts with elements of the matrix phase forming traces of W-containing phase. It has also suppressed the formation of lower T_c phases.

Table 4.1: Lattice parameters and phase content for nano WO₃ added Bi 2223 samples.

S. No.	Sample	Lattice parameters (Å)				Phase content (%)			
		a	b	c	Bi 2223	Bi 2212	Bi 2201	W phase	
		- 440(-)	7.004(0)	2= 0= 6(0)	0.7.0	4.4	2.2		
1	BW 0	5.413(7)	5.381(3)	37.076(8)	95.3	1.4	3.2	-	
2	BW 1	5.414(2)	5.407(6)	37.093(3)	99	1	-	-	
3	BW 2	5.415(0)	5.401(0)	37.097(1)	97.8	1.8	0.4	-	
4	BW 3	5.412(9)	5.404(7)	37.075(0)	99.5	0.3	-	0.2	

An enhancement in the intensities of 00l lines for all the samples shows that all the samples are textured along the c-axis. Table 4.1 shows the details of lattice parameters and phase content in all the samples of BW series.

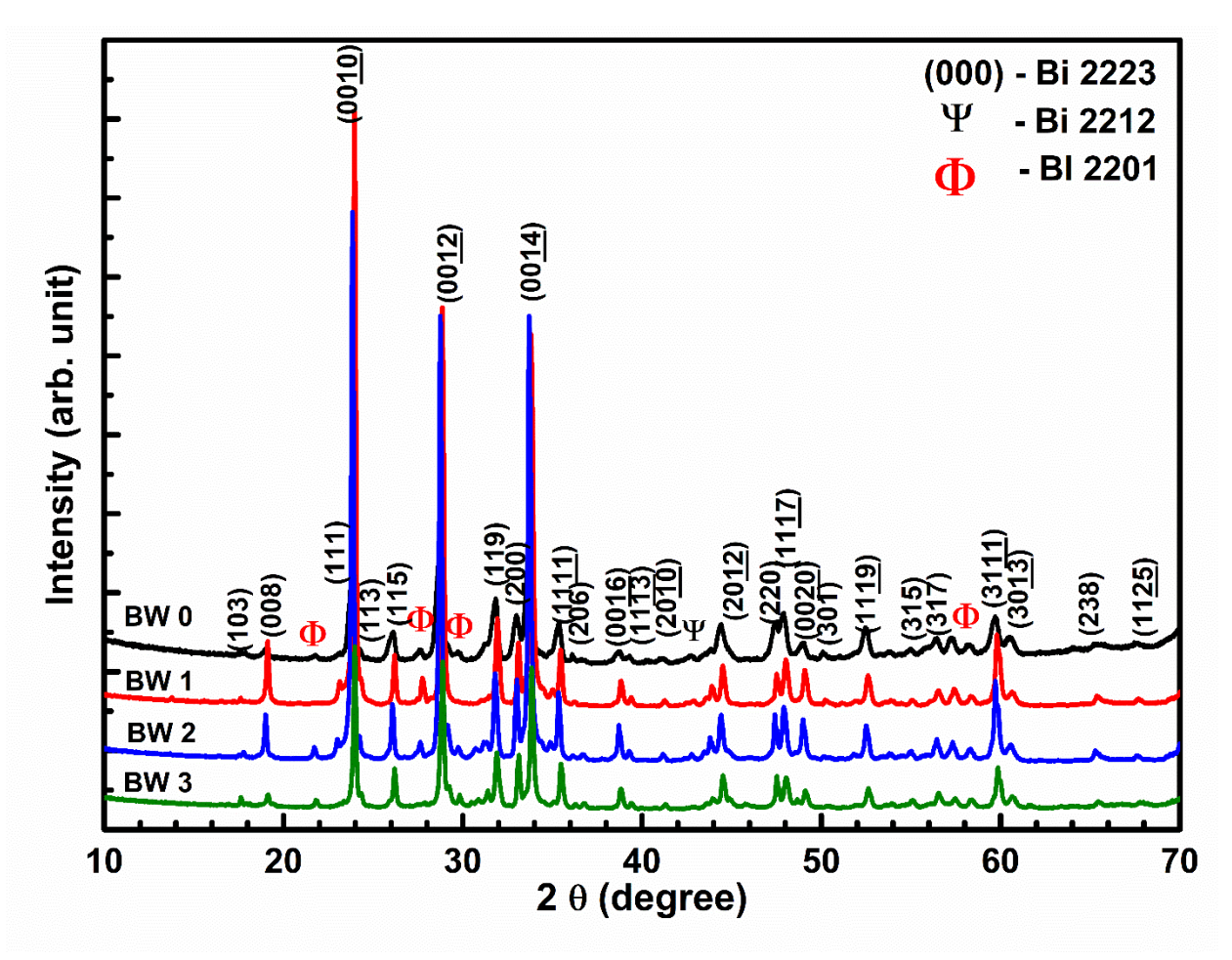
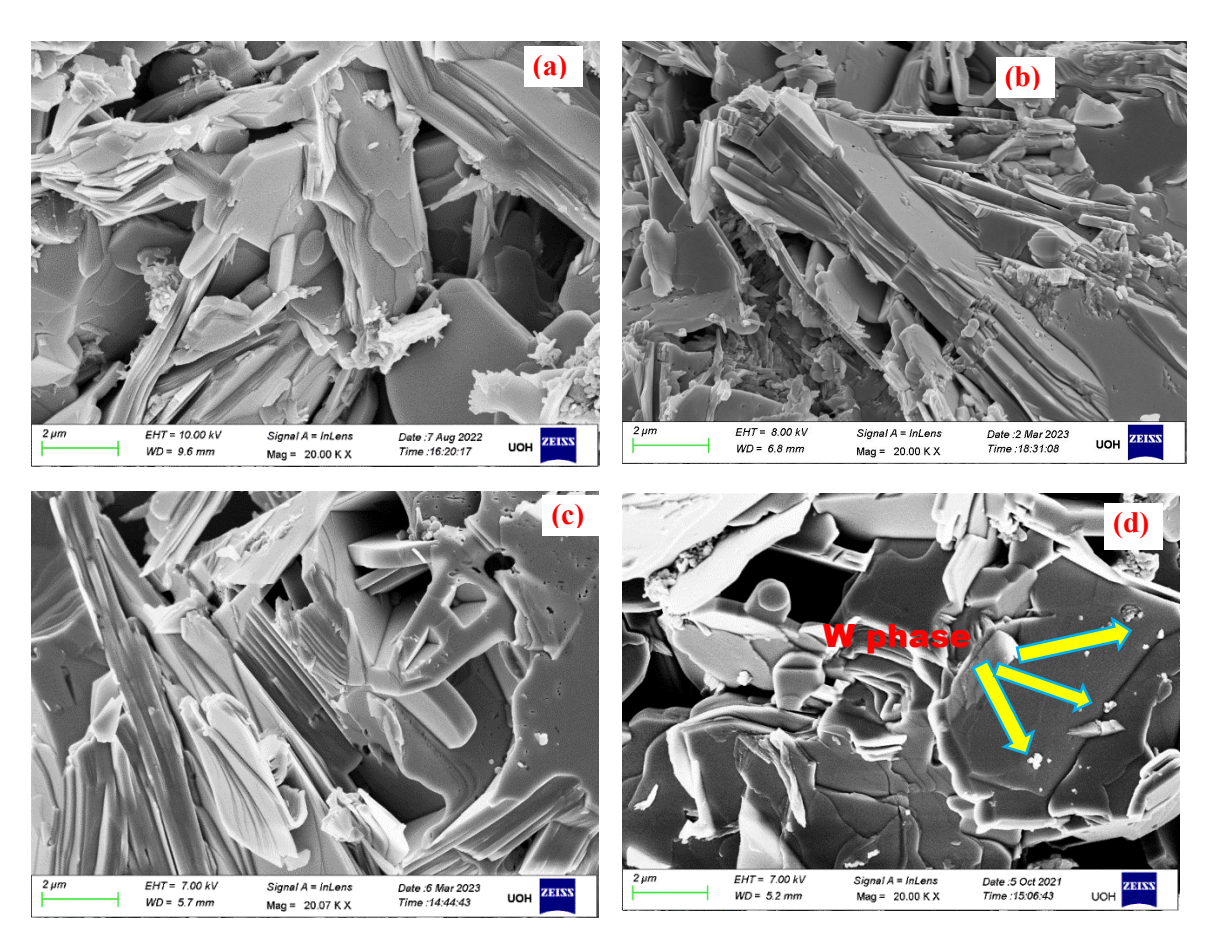


Figure 4.1: Indexed XRD patterns of all the Bi- 2223 samples with WO₃ nanoparticle addition.

4.3.2 Microstructural studies

Fig. 4.2 shows the FESEM micrographs of the fractured surfaces of the samples. Large Bi 2223 grains in the form of stacks of platelet-like grains can be seen. Large platelet-like morphology is typical of press-sintered BSCCO superconductors [15,21,27,28]. WO₃ nanoparticle addition has not affected the large micaceous platelet-like morphology of the matrix Bi 2223 phase. Sample BW 3 with 5 wt.% nano WO₃ has shown traces of a W-containing phase (See Fig. 4.2 (d)). Due to minor amounts of this phase, the exact composition could not be determined. However, from the Bragg peak seen at $2\theta = 30.7^{\circ}$ in XRD, we identify this phase possibly to be WSrCaO₆. Because of similar morphology and presence in very low amounts, the distinct lower T_c phases (Bi 2212 and Bi 2201) couldn't be individually distinguished. The composition for Bi 2223 and W containing phase is given in Table 4.1(a).



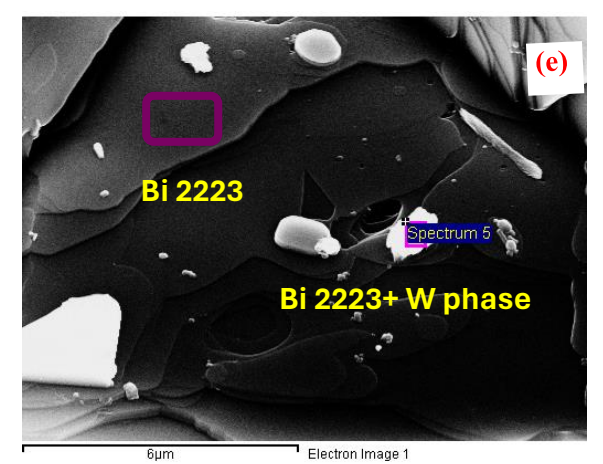


Table 4.1(a): Composition estimates from Edax analysis for Bi 2223 and W containing phase

Element	Bi 2223	Bi 2223 + W
	Atomic %	Atomic %
Bi	7.46	5.79
Pb	1.21	-
Sr	7.22	7.92
Ca	7.91	7.35
Cu	11.26	8.45
W	-	2.96
0	64.95	67.52

Figure 4.2 (a-d): FESEM micrograph recorded in fractured surfaces of Bi 2223 samples with WO₃ nanoparticles addition (0. 0.1, 0.5 and 5 wt.%), W containing phases are marked for sample BW 3, (e) Bi 2223 along with W phase are marked and their composition are given in Table 4.1(a).

4.3.3 Density measurements

We have assessed the density of the samples as it is known that voids and porosity that may be present in the HTSc due to their ceramic nature would provide hinderance to the current flow and can be a source to reduce the current densities.

The theoretical density for Bi 2223 having composition $Bi_{1.6}Pb_{0.4}Sr_2Ca_2Cu_3O_{10+\delta}$ is 6 g/cc from the literature [15,21,27]. The theoretical density for the BW 0 composition is estimated from XRD data to be 5.39 g/cc. The measured density (g/cc) and relative density (%) with respect to theoretical density of bulk pellets are given in Table 4.2. We note that sample BW 2 has a lower density compared to other samples.

4.3.4 Magnetic Measurements

Temperature dependence of magnetization (M-T) for all Bi 2223 composites is shown in Fig. 4.3. The data were collected while cooling the samples from 120 K to 20 K in 5 mT applied field. All samples show a sharp diamagnetic transition, corresponding to the Bi 2223 phase with T_c (onset) of around 105 K. The T_c (onset) is not much affected by WO₃ nanoparticle addition, contrary to the observations reported in the literature [17]. This suggests that W has not replaced any atoms in the unit cells of the Bi 2223 matrix. Adding WO₃ nanoparticles to once-processed Bi 2223 powder has reduced the possibility of reaction and formation of substantial amounts of secondary phases. This also suggests that WO₃ remains distributed as nanoparticles in the Bi 2223 matrix, which is not observable in FESEM images.

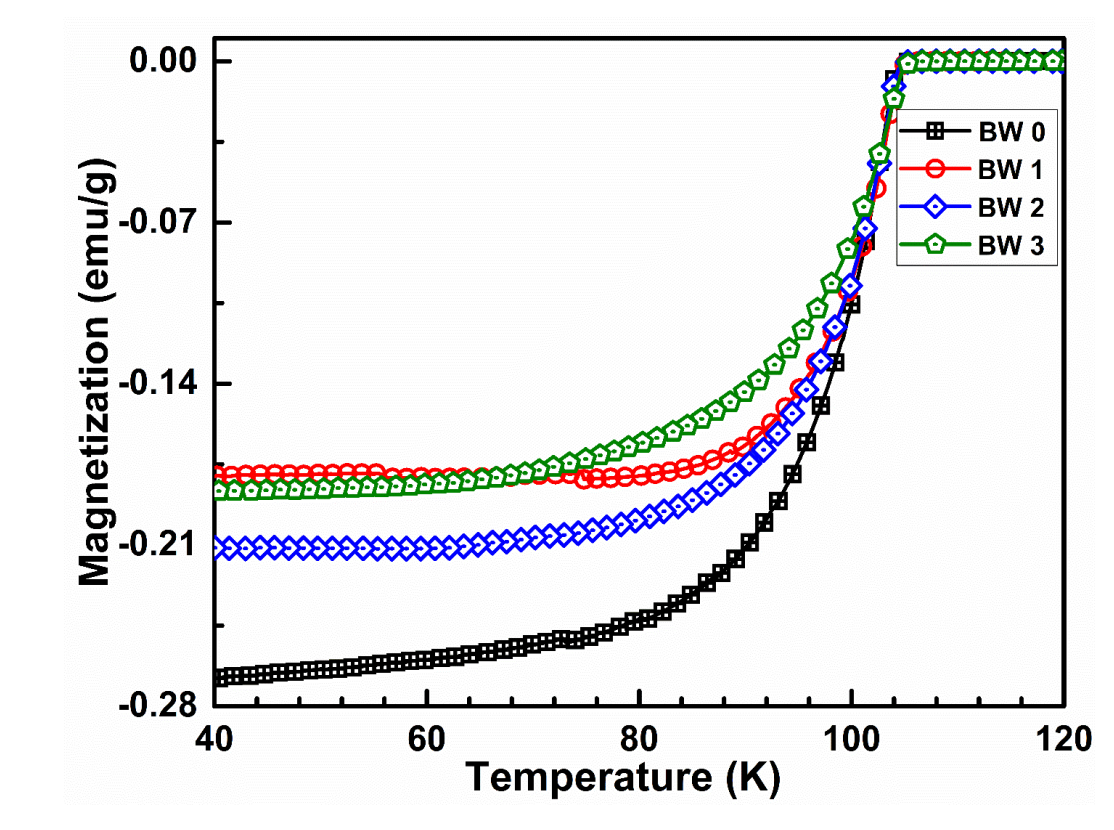


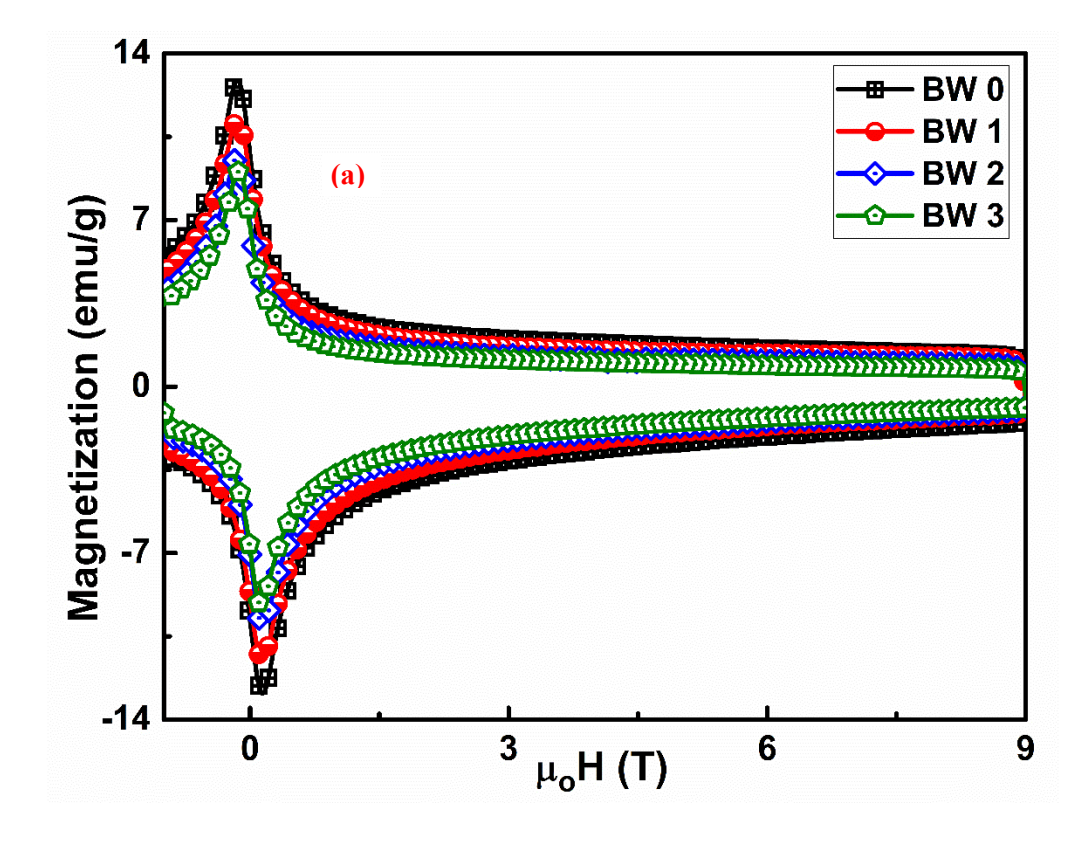
Figure 4.3: Temperature dependence of magnetization for all Bi 2223 samples with nano WO₃ addition recorded at a DC field of 5 mT.

The transition widths (ΔT_c) are measured as the difference in the temperatures at 90% and 10% of the diamagnetic signal across the superconducting transition. The transition width for sample BW 3 is found to be the highest, while it is the lowest for sample BW 1 as seen from Table 4.2. The transition width is a measure of homogeneity in the properties of grains and the grain connectivity [29].

Table 4.2 – Onset temperature of Diamagnetic transition (T_c), the transition width (ΔT_c), the measured density, and relative density for all the samples of the BW series.

Sample	$T_c(\mathbf{K})$	ΔT_c (K)	Density (g/cc)	Relative density (%)
BW 0	104.7	19.3	4.95	91.8
BW 1	104.9	12.6	4.86	90.2
BW 2	104.4	18.3	4.28	79.3
BW 3	104.9	24.9	4.78	88.5

Field dependence of magnetization was studied by recording M-H loops to high fields at different temperatures 10 K, 30 K, 50 K, and 77 K. For all the samples, the M-H loops at 10 K are open till 9 Tesla applied field as shown in Fig. 4.4 (a) indicating that the irreversibility fields (B_{irr}) are well above 9 T at 10 K.



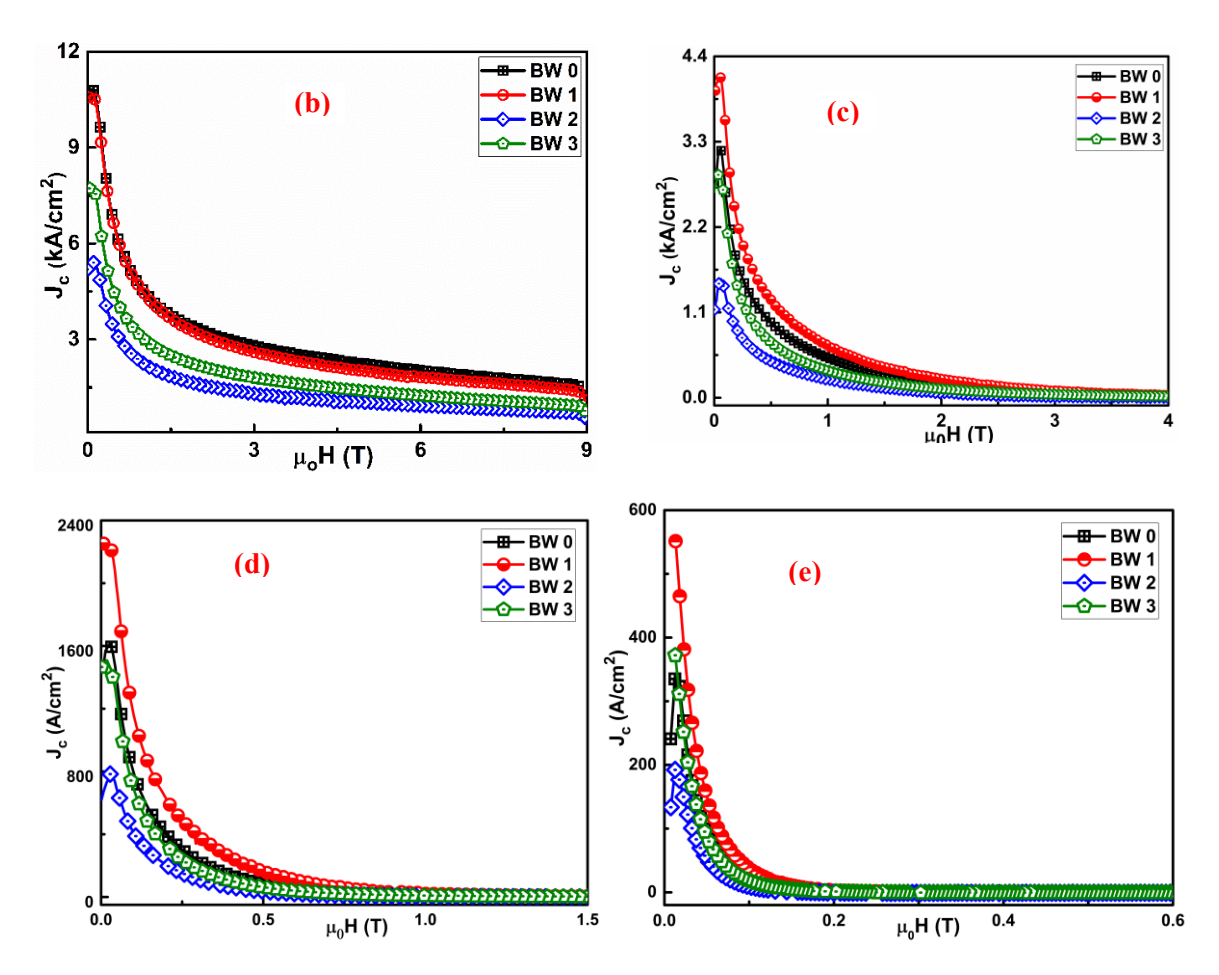


Figure 4.4 (a): M- H loops recorded at 10 K, (b) - (e) Magnetic field dependence of J_c at 10 K, 30 K, 50 K, and 77 K and for all Bi 2223 samples with varying nano WO₃ content.

The critical current density for all the samples was calculated from the corresponding M- H loops, using Bean's critical state model [30], discussed in section 2.6 of chapter 2.

Figs. 4.4(b) & (e) show the field dependence of J_c determined at 10 K - 77 K, respectively. Fig. 4.4 shows that J_c decreases with the applied field, as is observed in oxide superconductors, but all the present samples have finite J_c values till 9 T at 10 K. The rapid decrease in J_c on increasing the magnetic field and temperature is due to flux creep known to occur much below the upper critical field B_{c2} in HTSc [31], [32].

It can be seen from Fig. 4.4(b) that the J_c value for the BW 0 and BW 1 samples are nearly equal at 10 K, but at higher temperatures like 30 K, the J_c value for the sample BW 1, with 0.1 wt.% nano WO₃ exceeded that of other samples at zero field $(J_c(0))$ as well as at finite fields $(J_c(B))$. The small peak observed in J_c curves near zero field is akin to the low field peak observed by

Sinoussi et al. close to H_{cl} due to the pinning of vortices that are few in number and have long-range interaction [33].

We see from Fig. 4.4 that the $J_c(B)$ curve for the sample BW 2 is lower than those for others. We examine the data in light of the bulk densities of the samples given in Table 4.2. The sample BW 0 has the highest density of around 4.95 g/cm³. The density is relatively low for BW 2 among all the samples, suggesting that the lower J_c values correlate to higher porosity that limits the size of the diamagnetic current loops in this sample. A similar dependence of J_c on density was observed in Bi 2212 tapes [7] and Bi 2223 bulk samples [21,27].

4.3.5 Analysis of Flux Pinning Force density (F_p)

Field and temperature dependence of current densities are known to be governed by the microstructural features of HTSc samples. The flux line lattice generated by the application of magnetic field interacts with the defects/inhomogeneities in the material which causes pinning of the flux lines to the defect sites, which act as pinning centers. The nature and extent of the contribution of the defects to the pinning force depends on their size relative to the coherence length (ξ) of the material and the defect density [34,35].

Intrinsic pinning due to weak coupling across Cu-O layers along the c-axis of copper oxide-based superconductors is dominant in defect-free YBCO single crystals and thin films [36]. On the other hand, flux pinning can be caused by multiple types of defects associated with non-superconducting second-phase additions [37], chemical substitutions at atomic sites in the unit cells [38], twin planes [39] or the presence of superconducting lower T_c phases [40] in the case of HTSc, in general. These can be present in HTSc when they are synthesized in the form of either single crystals, thin films, textured, or polycrystalline specimens. Flux pinning would enhance the critical current densities $J_c(B)$ by working against flux creep and will occur in a specific field range where pinning is effective [21].

Scaling models proposed by Dew Hughes define several pairs of parameters that would describe the dominant pinning mechanism in the superconductors to arise from point pins, surface pins, or volume pins [41]. On the other hand, Kramer's model considers the elasticity of the flux line lattice that undergoes shear beyond a characteristic field [42]. Applying scaling laws to the measured pinning force densities helps to identify the nature of the pinning mechanisms associated with the defects.

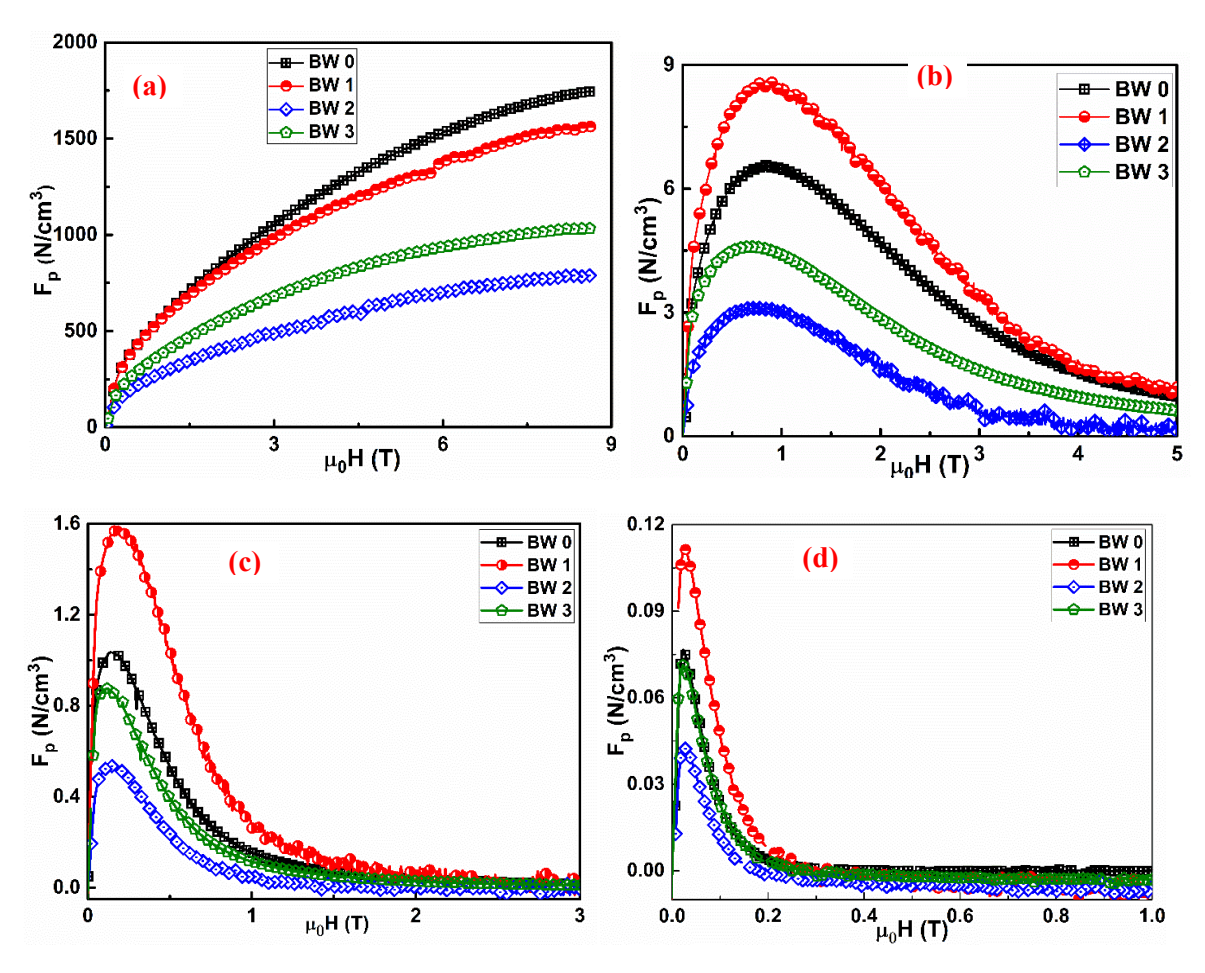


Figure 4.5 (a-d): Flux pinning force density variation with the applied field at 10, 30, 50, and 77 K, respectively, for the BW- series samples of Bi 2223 with nano WO₃ addition

An analysis of flux pinning force curves generated as a function of the applied field has been carried out to gain insight into the dominant flux pinning mechanism in the present set of samples. The flux pinning force density (F_p) is given by, $F_p = J_c x B$, where B is the applied field. F_p vs. B curves, which represent field dependence of flux pinning force density, for all the samples studied in this work, are shown in Fig. 4.5 at temperatures 10 K, 30 K, 50 K, and 77 K.

It can be seen from Fig. 4.5 (a) that the flux pinning force density increases monotonically with an increase in the field up to 9 Tesla, the maximum field applied at 10 K for all the samples. At higher temperatures, F_p exhibits a maximum ($F_{p max}$) at a field, B_p corresponding to the peak in F_p -B curves. The magnitude of $F_{p max}$ differs from sample to sample, while B_p , the peak position on the field axis, is observed to be in a small field range for all the samples at a given temperature. At 10 K, $F_{p max}$ has not been reached for samples up to the 9T field. The rapid reduction in the magnitudes of $F_{p max}$ and B_p with an increase in temperature is due to flux creep, which is known to be dominant in BSCCO superconductors, compared to (Y, RE)BCO systems, due to larger interlayer spacing [43].

The critical current densities $(J_c(0))$ at zero field and finite fields $(J_c(B))$, maximum pinning force $F_{p max}$, and the full width at half maximum (FWHM) of the pinning force density peaks (shown in Fig. 4.5), are compared in Table 4.3 at different temperatures studied. FWHM is a measure of the wide field range in which pinning is effective.

Table 4.3 (a & b): Comparison of $J_c(0)$, $J_c(B)$, $F_{p max}$, and FWHM at different temperatures for all the Bi-2223 sample series with WO₃ addition.

Sample		10 K		30 K				
	$J_c(0)$	$J_c(5T)$	$F_{p max}$	$J_c(0)$	$J_c(1T)$	$F_{p max}$	FWHM	
	(A/cm^2)	(A/cm^2)	(N/cm^3)	(A/cm^2)	(A/cm^2)	(N/cm^3)	(T)	
BW 0	10825	2260	1745	3215	515	65.7	2.57	
BW 1	10600	2040	1570	4160	700	86.1	2.54	
BW 2	5390	1040	792	1545	260	31.4	2.03	
BW 3	7765	1465	1033	2885	350	46.1	2.32	

Sample		50 K			77 K	
	$J_c(0)$	$F_{p max}$	FWHM	$J_c(0)$	F _{p max}	FWHM
	(A/cm^2)	(N/cm^3)	(T)	(A/cm^2)	(N/cm^3)	(T)
BW 0	1615	10.35	0.48	336	0.77	0.064
BW 1	2270	15.88	0.58	552	1.11	0.068
BW 2	785	5.42	0.43	194	0.43	0.065
BW 3	1505	8.75	0.44	373	0.71	0.068

Fig. 4.5 and the data in Table 4.3 indicate that Sample BW 1 with 0.1 wt.% nano WO₃ addition exhibits a larger pinning force compared to other samples at 30 K, 50 K, and 77 K at all fields, which suggests that pinning due to WO₃ addition is effective at low concentrations of nano WO₃ Addition.

As the field increases, F_p is expected to decrease to zero at the upper critical field B_{c2} , which is observed in conventional superconductors. But, in HTSC, it is the irreversibility field B_{irr} ($<< B_{c2}$), at which F_p is found to vanish due to flux creep [44]. Unpinned flux motion occurs in the region between B_{irr} and B_{c2} .

One looks at scaling laws applicable to the observed flux pinning curves to investigate the mechanism. For this purpose, curves of normalized pinning force density $(f = F_p/F_{p max})$ vs normalized field $(b = B/B_{irr})$ are analyzed in the light of various mechanisms that include pinning due to spatial variations in mean free path (δl pinning) or in Ginzburg-Landau parameter k (δk or δT_c pinning) [40].

The initial task in this direction is to determine B_{irr} , representing the limiting field at which the pinning force becomes zero. However, since more than one type of pinning mechanism might exist simultaneously in HTSc due to various types of defects that may be present, the pinning force curves due to different mechanisms would overlap, and the measured curves are a superposition of all such contributions.

Hence, it is more complex to identify the scaling laws if more than one pinning mechanism is involved, as the limiting field for each mechanism is then different. In the present set of samples, one expects, in addition to pinning due to inherent structural defects at grain boundaries (that contribute to surface pinning), pinning due to the addition of nano-WO₃ particles to the Bi 2223 phase to be present. Traces of lower T_c phases could also contribute to a small extent. Hence, we followed the approach given below to determine the characteristic fields B^* and B_{irr} that represent the limiting fields for the pinning mechanisms at low and high fields.

To identify the dominant contribution to the measured pinning force curves, we plotted the variation of normalized $f = F_p/F_{p,max}$ as a function of h ($h = B/B_p = \mu_o H/\mu_o H_p = H/H_p$), where B_p is the field at which F_p is maximum, for all the samples along with the scaling law function for surface pinning mechanism.

The normalized pinning force from ΔK , normal point and normal surface pinning mechanism are given by [45,46].

We show $F_p/F_{p,max}$ vs H/H_p curves, along with the curves of the theoretical model represented by equation (13-15) given in Chapter 2, in Fig. 4.6 (a) at 30 K. Scaling laws cannot be applied to the data at 10 K since the peak in F_p is not observed even up to 9 T, the maximum applied field.

The proximity of the experimental data to the theoretical surface pinning curve in Fig. 4.6 (a-c) suggests the dominant mechanism to be associated with normal surface pinning sites at platelet/grain boundaries.

The deviation from the theoretical curve for surface pinning at fields above the respective peak fields (B_p) suggests additional pinning due to other mechanisms to be effective at higher fields, which would vanish at B_{irr} , as discussed later.

To determine B^* , the characteristic field equivalent to the irreversibility field for the low field pinning mechanism, we use the scaling law defined by Kramer [42] for surface pins and plot $J_c^{0.5}B^{0.25}$ vs B. A typical plot for BW 1 is shown in Fig. 4.6(d), from which B^* is determined to be 5 T at 30 K. B^* values

represent the limiting field for pinning at low fields, and the B^* values thus obtained are presented in Table 4.4 for all the samples.

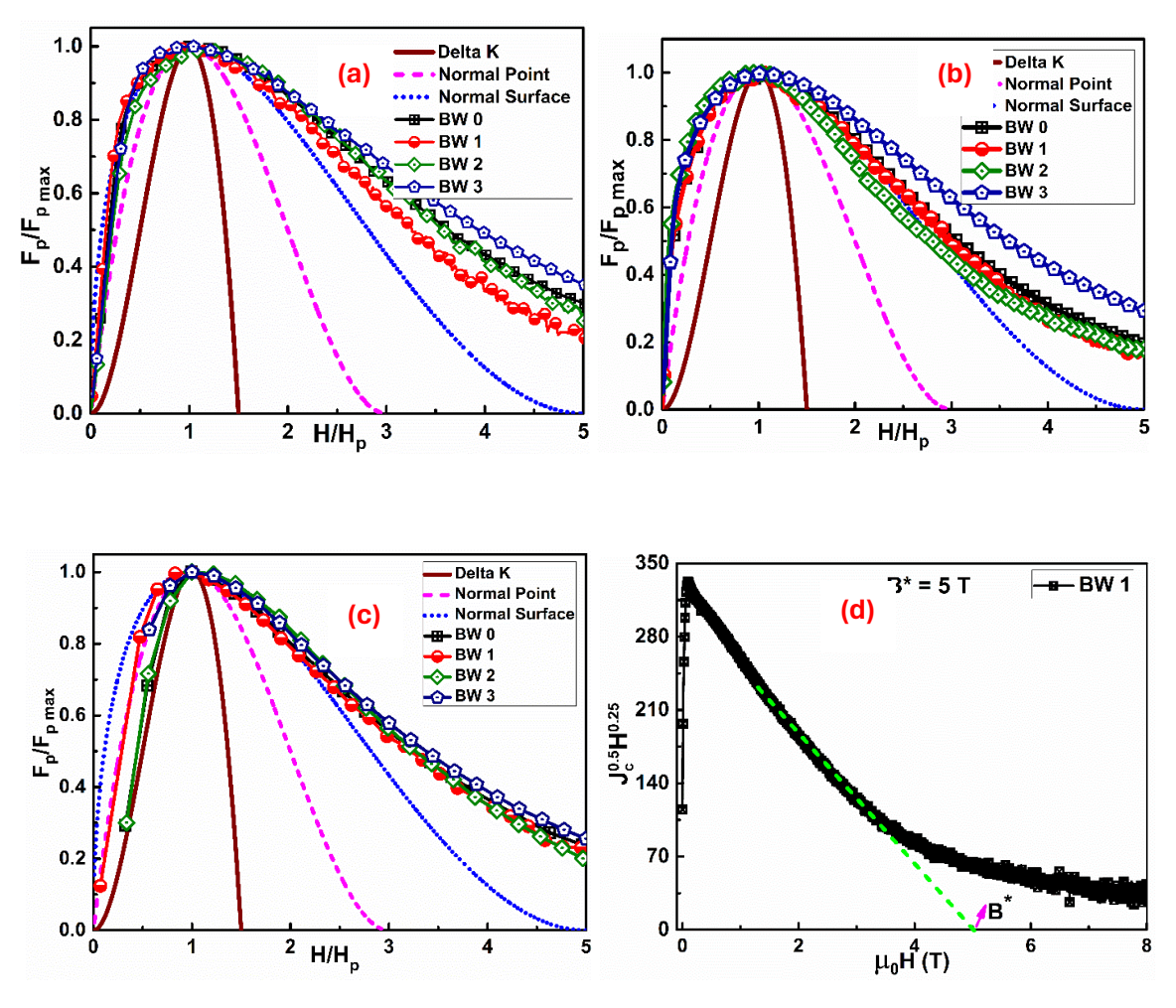


Figure 4.6 (a-c): $F_p/F_{p \text{ max}}$ vs H/H_p curves for all the BW samples at 30 K, 50 K, and 77 K along with theoretical pinning curve, (b) Estimation of B^* for BW 1 sample at 30 K, from Kramer's approach,

The irreversibility field B_{irr} of the materials can be determined, in general, from the closure of the M-H loops at high fields. However, the M-H loops of all the samples are open till 9 T field at 10 K; hence, the B_{irr} value could not be determined at 10 K from the closure of M-H loops. This is also reflected in F_p vs. B curves, as it does not exhibit a peak up to 9 T, as seen in Fig. 4.5 (a).

It is important to note that the pinning force is finite beyond B^* for all the samples, as seen from the tail region of the curves, at high fields in Fig. 4.6(b). This region is manifested by a rapid reduction in J_c (as well as F_p) due to flux creep, which is known to occur in HTSc, and this fall can, in turn, get slower/suppressed if another pinning mechanism becomes operative at high fields.

From an examination of the curves in Fig. 4.6(a) at fields above B_p , it is evident, from the gradual deviation from the theoretical curve for surface pinning, that the contribution to F_p increases with an increase in WO₃ content to 5 wt.% from 0.1 wt.% at 30 K and 50 K.

Irreversible field (B_{irr}) is an important parameter, especially for HTSc, as it determines the upper limit of a superconductor's current-carrying capability [47]. As reported in the BSCCO system, defects introduced into the superconducting matrix can raise B_{irr} to higher fields [15],[47], [48], [49],[50].

Irreversible field (B_{irr}) is the limiting field that defines the pinned vortex state. Above B_{irr} , flux lines are not pinned, and F_p vanishes. In literature, there are numerous criteria to determine B_{irr} , for instance, as the field where J_c reaches some minimum proposed value like 10 A/cm² [51], 100 A/cm² [52], or 1000 A/cm² [53] or the field at which a superconductor becomes resistance-less at a particular temperature [48,50]. We follow a different approach to determine B_{irr} by analyzing the exponential decay in F_p with field. In other words, to determine the magnitude of B_{irr} that represents the effective field at which the pinning mechanism at high fields vanishes, resulting in overall J_c to become zero, the tail region of the F_p vs B curves (beyond B_p) is analyzed in terms of an exponential decay function given below.

$$F_p(B) = C + D * Exp(-\frac{B}{B_x})$$
(2)

Here C, D, and B_x are the fit parameters. Equation 2 is solved for B, setting $F_p(B)=0$ to get $B_{irr}(T)$, where F_p vanishes at 30, 50, and 77 K, and are presented in Table 4.4.

The B_{irr} values thus determined are scaled to a function given by equation 3,

$$B_{irr}(T) = B_{irr}(0) * (1-(T/T_c))^m,$$
(3)

from which B_{irr} values of the samples are estimated at 10 K and are also presented in Table 4.4. B_{irr} (0), the value of B_{irr} at zero temperature, and m, the fitting parameter at different temperatures, are given in Table 4.4. The fit parameter m can have values from 1.5- 5.5, based on the anisotropy of the superconducting system [54,55]. Values close to 3 are reported for m in Bi 2223 bulk and tapes [56].

Table 4.4: $B^*(T)$, $B_{irr}(T)$, $B_{irr}(0)$, and m values for all the Bi 2223 samples with nano WO₃ addition

G1-	$B^*(T)$ $B_{irr}(T)$					$B_{irr}(0)$	m		
Sample	30 K	50 K	77 K	10 K	30 K	50 K	77 K		
BW 0	4.5	1.0	0.17	16.96	6.85	2.02	0.38	24.9	3.8
BW 1	5	1.19	0.17	32.36	11.11	2.70	0.29	50.9	4.5
BW 2	4.2	0.86	0.15	12.64	5.48	1.82	0.19	18.0	3.5
BW 3	4	1.01	0.32	35.60	9.77	1.97	0.26	61.7	5.5

Fig. 4.7 shows the variation of B_{irr} (T) for all the samples, which indicates that B_{irr} shifts to higher fields in the WO₃ doped samples, except in sample BW 2 of higher porosity as evidenced by lower density. The shift of B_{irr} to higher fields is indicative of flux pinning sustained to higher fields.

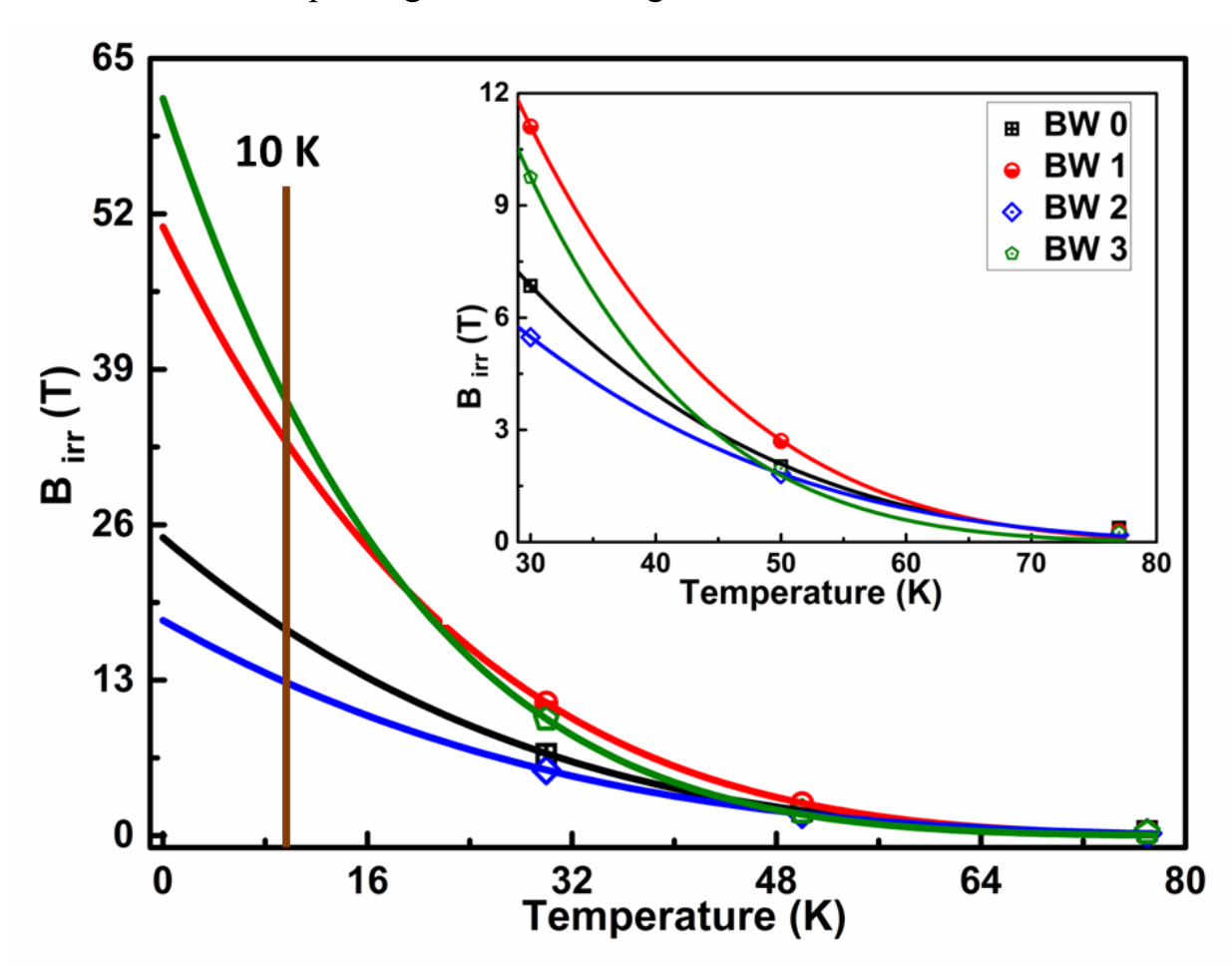


Figure 4.7: B_{irr} values at various temperatures for all Bi 2223 samples with nano WO₃ addition, inset: B_{irr} vs T, magnified above 30 K.

There is no experimental evidence as to why superconducting properties improve at deficient concentrations of a second phase addition, as is observed in BW 1 sample in the present study. Some theoretical studies [34,35] suggest that a high density of pinning centers would allow flux lines to jump from one pinning center to another, causing deterioration of J_c . Senoussi et al. [33] argued that there are two types of vortex lattice interactions: long-range at low fields where fewer flux lines exist and short-range at higher fields with higher flux lines. It seems possible that in different field regimes, the defects that cause effective pinning coupled with the energy of vortex lattice can accordingly be different, leading to more than one pinning mechanism to exist simultaneously, as is observed in the present composites.

4.4 Conclusion

In this study, we studied the effect of WO₃ nanoparticle addition on the superconducting properties of Bi_{1.2}Pb_{0.3}Sr_{1.54}Ca_{2.06}Cu₃O_y superconductor composites. M-T curves show that T_c (onset) nearly unchanged at 105 K, main phase is Bi 2223, indicating nano WO₃ has not reacted with the elements of Bi 2223 matrix phase, especially at low concentrations. We have used the sol-casting method of adding WO₃ nanoparticles to enable uniform distribution of nanoparticles in the Bi 2223 matrix. WO₃ nanoparticle addition to already once processed Bi 2223 powder, rather than adding them along with the ingredients mixed and processed to form Bi 2223, has prevented W substitution to lattice sites in the unit cells of the matrix phase.

FESEM micrograph reveals the presence of packed dense grains having platelike morphology. A critical current density of 11 kA/cm² is obtained in the sample BW 1 having 0.1 wt.% WO₃ nanoparticles addition to Bi 2223 phase at 10 K and zero field. Variation in J_c occurring at higher temperatures and fields is analyzed to assess the origin of flux pinning in various field regimes. The observed pinning force density F_p (B, T) is attributed to two different mechanisms. An analysis in the light of scaling laws suggests normal surface pinning due to interfacial defects associated with grain/platelet boundaries to be the dominant mechanism at low fields. The addition of WO₃ nanoparticles has suppressed the swift decrease in J_c due to flux creep at higher fields. The limiting fields B^* and B_{irr} where pinning due to different mechanisms vanishes, are estimated from a detailed analysis of normalized F_p . B_{irr} values calculated from the study of F_p vs field curves above the peak field B_p show a shift towards higher fields in WO₃-containing samples, except for BW 2 of lower density. Identification of flux pinning mechanisms operative at different field regimes presented here would be important for designing superconductor composites with enhanced properties. In summary, the addition of low concentrations (0.1 wt.%) of WO₃ nanoparticles without reaction with the matrix phase led to enhanced flux pinning sustained to fields above B_p up to higher temperatures.

References

- [1] D. Uglietti, A review of commercial high temperature superconducting materials for large magnets: from wires and tapes to cables and conductors, Supercond. Sci. Technol. 32 (2019) 053001. https://doi.org/10.1088/1361-6668/ab06a2.
- [2] D. Larbalestier, A. Gurevich, D.M. Feldmann, A. Polyanskii, High-Tc superconducting materials for electric power applications, Nature. 414 (2001) 368–377. https://doi.org/10.1038/35104654.
- [3] J.R. Hull, Applications of high-temperature superconductors in power technology, Reports Prog. Phys. 66 (2003) 1865–1886. https://doi.org/10.1088/0034-4885/66/11/R01.
- [4] H. Ohta, A. Koike, K. Hoshino, H. Kotaka, E. Sudoh, K. Kato, H. Takahara, Y. Uchikawa, K. Shinada, M. Takahata, Y. Yamada, T. Matsui, Neuromagnetic Squid Measurements in A Helmet-Type Superconducting Magnetic Shield of Bscco, IEEE Trans. Appl. Supercond. 3 (1993) 1953–1956. https://doi.org/10.1109/77.233577.
- [5] M. Chen, W. Paul, M. Lakner, L. Donzel, M. Hoidis, P. Unternaehrer, R. Weder, M. Mendik, 6.4 MVA resitive fault current limiter based on Bi-2212 superconductor, Phys. C Supercond. Its Appl. 372–376 (2002) 1657–1663. https://doi.org/10.1016/S0921-4534(02)01096-1.
- [6] J. Jiang, G. Bradford, S.I. Hossain, M.D. Brown, J. Cooper, E. Miller, Y. Huang, H. Miao, J.A. Parrell, M. White, A. Hunt, S. Sengupta, R. Revur, T. Shen, F. Kametani, U.P. Trociewitz, E.E. Hellstrom, D.C. Larbalestier, High-performance Bi-2212 round wires made with recent powders, IEEE Trans. Appl. Supercond. 29 (2019). https://doi.org/10.1109/TASC.2019.2895197.
- [7] A. Leveratto, A.A. Armenio, A. Traverso, G. De Marzi, G. Celentano, A. Malagoli, Transport current and magnetization of Bi-2212 wires above liquid Helium temperature for cryogen-free applications, Sci. Rep. 11 (2021) 1–9. https://doi.org/10.1038/s41598-021-91222-2.
- [8] V. Ortalan, M. Herrera, M.W. Rupich, N.D. Browning, Three dimensional analyses of flux pinning centers in Dy-doped YBa₂Cu₃O_{7-x} coated superconductors by STEM tomography, Phys. C Supercond. Its Appl. 469 (2009) 2052–2059. https://doi.org/10.1016/j.physc.2009.08.012.
- [9] W.K. Kwok, U. Welp, A. Glatz, A.E. Koshelev, K.J. Kihlstrom, G.W. Crabtree, Vortices in high-performance high-temperature superconductors, Reports Prog. Phys. 79 (2016). https://doi.org/10.1088/0034-4885/79/11/116501.
- [10] V.F. Shamray, A.B. Mikhailova, A. V. Mitin, Crystal structure and superconductivity of Bi-2223, Crystallogr. Reports. 54 (2009) 584–590. https://doi.org/10.1134/S1063774509040075.
- [11] S. Zhang, C. Li, Q. Hao, J. Feng, T. Lu, P. Zhang, Optimized Intergrain Connection and Transport Properties of Bi-2212 High-Temperature Superconductors by Ag

- Nanoparticles Inclusions, J. Supercond. Nov. Magn. 28 (2015) 1729–1736. https://doi.org/10.1007/s10948-015-2981-1.
- [12] N.D. Kumar, T. Rajasekharan, K. Muraleedharan, A. Banerjee, V. Seshubai, Unprecedented current density to high fields in YBa₂Cu₃O_{7-δ} superconductor through nano-defects generated by preform optimization in infiltration growth process, Supercond. Sci. Technol. 23 (2010). https://doi.org/10.1088/0953-2048/23/10/105020.
- [13] M.M.A. Sekkina, H.A. El-Daly, K.M. Elsabawy, Terbium-neodymium co-doping in Bi sites on the BPSCCO bismuth cuprate superconductor, Supercond. Sci. Technol. 17 (2004) 93–97. https://doi.org/10.1088/0953-2048/17/1/016.
- [14] R.B. Saxena, R. GIRI, V.P.S. Awana, H.K. Singh, M.A. Ansari, B. V. Kumaraswamy, A. Gupta, R. Nigam, K.P. Singh, H. Kishan, O.N. Srivastava, Impact of Zn substitution on phase formation and superconductivity of $Bi_{1.6}Pb_{0.4}Sr_2Ca_2Cu_{3-x}Z_xO_{10-\delta}$ with x=0.0, 0.015, 0.03, 0.06, 0.09 and 0.12, Mod. Phys. Lett. B. 19 (2005) 771–778. https://doi.org/10.1142/S0217984905008785.
- [15] R.P. Aloysius, P. Guruswamy, U. Syamaprasad, Enhanced flux pinning in (Bi, Pb)-2223 superconductor by Nd addition, Supercond. Sci. Technol. 18 (2005) 427–431. https://doi.org/10.1088/0953-2048/18/4/009.
- [16] H. Sözeri, N. Ghazanfari, H. Özkan, A. Kilic, Enhancement in the high-T_c phase of BSCCO superconductors by Nb addition, Supercond. Sci. Technol. 20 (2007) 522–528. https://doi.org/10.1088/0953-2048/20/6/007.
- [17] N. Türk, H. Gündoğmuş, M. Akyol, Z.D. Yakıncı, A. Ekicibil, B. Özçelik, Effect of tungsten (W) substitution on the physical properties of Bi-(2223) superconductors, J. Supercond. Nov. Magn. 27 (2014) 711–716. https://doi.org/10.1007/s10948-013-2351-9.
- [18] T. Kozuka, H. Ogawa, A. Kan, A. Suzumura, Influence of ZnO doping on superconductivity and crystal structure of (Bi, Pb)-2223 superconductor, J. Eur. Ceram. Soc. 21 (2001) 1913–1917. https://doi.org/10.1016/S0955-2219(01)00142-X.
- [19] S.N. Abdullah, M.M.A. Kechik, A.N. Kamarudin, Z.A. Talib, H. Baqiah, C.S. Kien, L.K. Pah, M.K. Abdul Karim, M.K. Shabdin, A.H. Shaari, A. Hashim, N.E. Suhaimi, M. Miryala, Microstructure and Superconducting Properties of Bi-2223 Synthesized via Co-Precipitation Method: Effects of Graphene Nanoparticle Addition, Nanomaterials. 13 (2023). https://doi.org/10.3390/nano13152197.
- [20] Z.Y. Jia, H. Tang, Z.Q. Yang, Y.T. Xing, Y.Z. Wang, G.W. Qiao, Effects of nano-ZrO₂ particles on the superconductivity of Pb-doped BSCCO, Phys. C Supercond. Its Appl. 337 (2000) 130–132. https://doi.org/10.1016/S0921-4534(00)00072-1.
- [21] A. Ghattas, M. Annabi, M. Zouaoui, F. Ben Azzouz, M. Ben Salem, Flux pinning by Al-based nano particles embedded in polycrystalline (Bi,Pb)-2223 superconductors, Phys. C Supercond. Its Appl. 468 (2008) 31–38. https://doi.org/10.1016/j.physc.2007.10.006.
- [22] H. Fallah-Arani, S. Baghshahi, A. Sedghi, D. Stornaiuolo, F. Tafuri, D. Massarotti, N. Riahi-Noori, The influence of heat treatment on the microstructure, flux pinning and magnetic properties of bulk BSCCO samples prepared by sol-gel route, Ceram. Int. 44 (2018) 5209–5218. https://doi.org/10.1016/j.ceramint.2017.12.128.

- [23] P.M. Sarun, S. Vinu, R. Shabna, A. Biju, U. Syamaprasad, Microstructural and superconducting properties of Yb-substituted (Bi, Pb) -2212 superconductor sintered at different temperatures, 472 (2009) 13–17. https://doi.org/10.1016/j.jallcom.2008.04.103.
- [24] V.Seshu Bai, S. Ravi, T. Rajasekharan, R. Gopalan, On the composition of 110 K superconductor in a (Bi,Pb)-Sr-Ca-Cu-O system, J. Appl. Phys. 70 (1991) 4378–4382. https://doi.org/10.1063/1.349119.
- [25] P.M.S. Raju, V. Seshubai, T. Rajasekharan, A generic process to introduce nanoparticles into powder preforms and its application to Infiltration Growth processing of REBa₂Cu₃O₇ superconductor, Mater. Chem. Phys. 161 (2015) 59–64. https://doi.org/10.1016/j.matchemphys.2015.05.004.
- [26] M. Zouaoui, L. Bessais, M. Ben Salem, Thermally activated dissipation and pinning mechanisms in a Bi2223 superconductor with the addition of nanosized ZrO₂ particles, Supercond. Sci. Technol. 23 (2010) 095013. https://doi.org/10.1088/0953-2048/23/9/095013.
- [27] R.R. Kumar, R.P. Aloysius, R.J. Bose, P. Guruswamy, U. Syamaprasad, Preparation of dense, high JC Bi-2223 superconductors by multistage cold pressing, Supercond. Sci. Technol. 18 (2005) 689–693. https://doi.org/10.1088/0953-2048/18/5/018.
- [28] N. Darsono, D.H. Yoon, K. Raju, Effects of the Sintering Conditions on the Structural Phase Evolution and T_c of Bi_{1.6}Pb_{0.4}Sr₂Ca₂Cu₃O₇ Prepared Using the Citrate sol–gel Method, J. Supercond. Nov. Magn. 29 (2016) 1491–1497. https://doi.org/10.1007/s10948-016-3459-5.
- [29] M.H. Gharahcheshmeh, E. Galstyan, A. Xu, J. Kukunuru, R. Katta, Y. Zhang, G. Majkic, X.-F. Li, V. Selvamanickam, Superconducting transition width (ΔT_c) characteristics of 25 mol% Zr-added (Gd, Y)Ba₂Cu₃O_{7-δ} superconductor tapes with high in-field critical current density at 30 K, Supercond. Sci. Technol. 30 (2017) 015016. https://doi.org/10.1088/0953-2048/30/1/015016.
- [30] C.P. Bean, Magnetization of hard superconductors, Phys. Rev. Lett. 8 (1962) 250–253. https://doi.org/10.1103/PhysRevLett.8.250.
- [31] M.R. Beasley, R. Labusch, W.W. Webb, Flux creep in type-II superconductors, Phys. Rev. 181 (1969) 682–700. https://doi.org/10.1103/PhysRev.181.682.
- [32] R.G. Mints, I. Papiashvili, Flux creep in type-II superconductors: The self-organized criticality approach, Phys. Rev. B Condens. Matter Mater. Phys. 71 (2005) 1–7. https://doi.org/10.1103/PhysRevB.71.174509.
- [33] S. Senoussi, C. Aguillon, P. Manuel, The origin of the low field peak in the hysteresis cycle of high-T_c oxides and the influence of magnetic pinnings, Phys. C Supercond. Its Appl. 175 (1991) 202–214. https://doi.org/10.1016/0921-4534(91)90254-V.
- [34] A.E. Koshelev, I.A. Sadovskyy, C.L. Phillips, A. Glatz, Optimization of vortex pinning by nanoparticles using simulations of the time-dependent Ginzburg-Landau model, Phys. Rev. B. 93 (2016) 1–5. https://doi.org/10.1103/PhysRevB.93.060508.
- [35] A. Glatz, I.A. Sadovskyy, U. Welp, W.K. Kwok, G.W. Crabtree, The Quest for High Critical Current in Applied High-Temperature Superconductors, J. Supercond. Nov. Magn. 33 (2020) 127–141. https://doi.org/10.1007/s10948-019-05255-w.

- [36] T. Nishizaki, T. Aomine, I. Fujii, K. Yamamoto, S. Yoshii, T. Terashima, Y. Bando, Transport critical currents and flux pinning mechanisms in single-crystalline thin films of YBa₂Cu₃O_{7-δ}, Phys. C Supercond. Its Appl. 181 (1991) 223–232. https://doi.org/10.1016/0921-4534(91)90104-7.
- [37] C. Xu, A. Hu, N. Sakai, M. Izumi, I. Hirabayashi, Flux pinning properties and superconductivity of Gd-123 superconductor with addition of nanosized SnO₂/ZrO₂ particles, Phys. C Supercond. Its Appl. 445–448 (2006) 357–360. https://doi.org/10.1016/j.physc.2006.04.082.
- [38] M. Daeumling, J.M. Seuntjens, D.C. Larbalestier, Oxygen-defect flux pinning, anomalous magnetization and intra-grain granularity in YBa₂Cu₃O_{7-δ}, Nature. 346 (1990) 332–335. https://doi.org/10.1038/346332a0.
- [39] N. Devendra Kumar, T. Rajasekharan, R.C. Gundakaram, V. Seshubai, Extensive nanotwinning: Origin of high current density to high fields in preform-optimized infiltration-growth-processed YBa₂Cu₃O_{7-δ} superconductor, IEEE Trans. Appl. Supercond. 21 (2011) 3612–3620. https://doi.org/10.1109/TASC.2011.2168819.
- [40] M. Koblischka, A. van Dalen, T. Higuchi, S. Yoo, M. Murakami, Analysis of pinning in superconductors, Phys. Rev. B Condens. Matter Mater. Phys. 58 (1998) 2863–2867. https://doi.org/10.1103/PhysRevB.58.2863.
- [41] D. Dew-Hughes, Flux pinning mechanisms in type II superconductors, Philos. Mag. 30 (1974) 293–305. https://doi.org/10.1080/14786439808206556.
- [42] E.J. Kramer, Scaling laws for flux pinning in hard superconductors, J. Appl. Phys. 44 (1973) 1360–1370. https://doi.org/10.1063/1.1662353.
- [43] T.P. Sheahen, Introduction to High-Temperature Superconductivity, in: Springer US, Boston, MA, 2002. https://doi.org/10.1007/b115100.
- [44] L. Civale, M.W. McElfresh, A.D. Marwick, F. Holtzberg, C. Feild, J.R. Thompson, D.K. Christen, Scaling of the hysteretic magnetic behavior in YBa₂Cu₃O₇ single crystals, Phys. Rev. B. 43 (1991) 13732–13735. https://doi.org/10.1103/PhysRevB.43.13732.
- [45] L. Klein, E.R. Yacoby, Y. Yeshurun, A. Erb, G. Müller-Vogt, V. Breit, H. Wühl, Peak effect and scaling of irreversible properties in untwinned Y-Ba-Cu-O crystals, Phys. Rev. B. 49 (1994) 4403–4406. https://doi.org/10.1103/PhysRevB.49.4403.
- [46] T. Goto, K. Inagaki, K. Watanabe, Critical current density in filamentary (Nd, Sm, Eu, Gd)-Ba-Cu-O superconductors prepared by a solution spinning method, Phys. C Supercond. Its Appl. 330 (2000) 51–57. https://doi.org/10.1016/S0921-4534(99)00608-5.
- [47] Q. Li, M. Suenaga, T. Kaneko, K. Sato, C. Simmon, Collapse of irreversible field of superconducting Bi₂Sr₂Ca₂Cu₃O_{10+δ}/Ag tapes with columnar defects, Appl. Phys. Lett. 71 (1997) 1561–1563. https://doi.org/10.1063/1.119965.
- [48] W.D. Huang, W.H. Song, Z. Cui, B. Zhao, M.H. Pu, X.C. Wu, T. Hu, Y.P. Sun, J.J. Du, Enhancement of flux pinning in (Bi, Pb)-2223/Ag tapes doped with MgO nanorods, Supercond. Sci. Technol. 13 (2000) 1499–1504. https://doi.org/10.1088/0953-2048/13/10/316.
- [49] A.T. Pham, D.T. Tran, D.B. Tran, L.T. Tai, N.K. Man, N.T.M. Hong, T.M. Le, D.

- Pham, W.N. Kang, D.H. Tran, Unraveling the Scaling Characteristics of Flux Pinning Forces in Bi_{1.6}Pb_{0.4}Sr₂Ca_{2-x}Na_xCu₃O_{10+δ} Superconductors, J. Electron. Mater. 50 (2021) 1444–1451. https://doi.org/10.1007/s11664-020-08676-9.
- [50] M.H. Pu, W.H. Song, B. Zhao, X.C. Wu, T. Hu, Y.P. Sun, J.J. Du, Enhanced flux pinning in (Bi, Pb)-2223/Ag tapes by slight Pr substitution, Supercond. Sci. Technol. 14 (2001) 305–310. https://doi.org/10.1088/0953-2048/14/6/302.
- [51] Y. Mawatari, H. Yamasaki, S. Kosaka, M. Umeda, Critical current properties and vortex-glass-liquid transition in Ag-sheathed Bi-2223 tapes, Cryogenics (Guildf). 35 (1995) 161–167. https://doi.org/10.1016/0011-2275(95)93989-D.
- [52] J. ichi Shimoyama, K. Kitazawa, K. Shimizu, S. Ueda, S. Horii, N. Chikumoto, K. Kishio, Generic guiding law between irreversibility field and anisotropy Chemical control of critical current of high temperature superconductors, J. Low Temp. Phys. 131 (2003) 1043–1052. https://doi.org/10.1023/A:1023440824299.
- [53] S.Y. Shan Yu, Y.O. Yuichi Okuda, E.T.-M. Eiji Takayama-Muromachi, Critical Current Densities and Irreversibility Fields in Pb-Doped and Pb-Free Bi₂Sr₂Ca₂Cu₃ O_y Superconductors, Jpn. J. Appl. Phys. 35 (1996) 2619. https://doi.org/10.1143/JJAP.35.2619.
- [54] Y.C. Kim, J.R. Thompson, D.K. Christen, Y.R. Sun, M. Paranthaman, E.D. Specht, Surface barriers, irreversibility line, and pancake vortices in an aligned HgBa₂Ca₂Cu₃O₈ superconductor, Phys. Rev. B. 52 (1995) 4438–4445. https://doi.org/10.1103/PhysRevB.52.4438.
- [55] M. Baenitz, G. Fuchs, K.A. Nenkov, A. Attenberger, C. Ecker, K. Kajikawa, E. V Antipov, H.R. Khan, A uniform description of irreversibility lines for various high-T, Phys. C Supercond. Its Appl. 355 (2001) 299–306.
- [56] J. Sosnowski, M. Rabara, K. Demachi, K. Miya, The influence of the pinning centres' form on the I V characteristics of the high- T_c superconductors, Supercond. Sci. Technol. 13 (2000) 558–566. https://doi.org/10.1088/0953-2048/13/5/326.

Chapter 5

Effect of nano ZrO₂ addition on the flux pinning properties of Ca_{0.86}Sr_{0.14}CuO₂ phase added Bi 2223 composite

5.1 Introduction

Artificial pinning centers are added to the BSCCO superconducting matrix to control the flux flow at higher magnetic fields. Efforts to add a secondary phase as artificial pinning centers to the Bi 2223 superconductor have been reported, but the outcomes do not consistently align with the intended results.

From the last two chapters, we find that nanoparticles are helpful in improving superconducting properties at very low concentrations. Similar reports of adding secondary phases to Bi 2223 are also present, where the secondary phase is effective in low concentrations [1-3].

Adding oxide nanoparticles to Bi 2223 superconductors improves J_c and pinning force density (F_p). Introducing 20 nm sized MgO nanoparticles to Bi 2223 superconductors has significantly enhanced T_c and transport J_c . Furthermore, the addition of nano MgO has resulted in improvements in the Bi 2223 phase fraction and its flux pinning capabilities, and it is also reported that MgO exhibits chemical inertness towards Bi 2223 and is uniformly distributed among the Bi 2223 grains [2].

Many reports of nano ZrO_2 addition to Bi 2223 are available in the literature. Jia et al. found that ZrO_2 addition to Pb added Bi 2223 improved intragranular J_c and flux pinning properties at higher fields and did not impact the T_c till the ZrO_2 concentration was less than 30 mol % [3]. The addition of nano ZrO_2 to Bi 2223 superconductor improved flux pinning properties, the activation energy(U_{eff} (H, T)) of vortex flow motion, and J_c and F_p behavior. This was attributed to the nanometer-sized Zr-rich phase contributing to extrinsic pinning centers. The sharp interface between the Zr-rich phase particles and the Bi 2223 phase provided effective normal surface pinning centers. Notably, no effects were observed on the T_c or the morphology of the Bi 2223 phase [4,5].

 $(Bi,Pb)_2Sr_2(Ca_{0.86}Sr_{0.14})_{n-1}Cu_nO_y$ for n=5, defines Bi 2223, and for n= infinity, it is $Ca_{0.86}Sr_{0.14}CuO_2$ compound [6,7]. We have synthesized $Ca_{0.86}Sr_{0.14}CuO_2$ phase and added 20 mol of it to 100 mol of Bi 2223 superconductors to form a composite. Nano ZrO_2 in various concentrations (0.5, 1, and 10 wt.%) was added to the composite to see their combined effect on the flux pinning and other superconducting properties at various temperatures and fields. The effect of

adding both the secondary phases ((Ca,Sr)CuO₂ and nano ZrO₂) is discussed in detail in the present study.

5.2 Experimental techniques

The powders (Bi_{1.2}Pb_{0.3}Sr_{1.54}Ca_{2.06}Cu₃O_y and Ca_{0.86}Sr_{0.14}CuO₂) were prepared by metal nitrate decomposition method [8–10] using high-quality Bi₂O₃, Pb(NO₃)₂, SrCO₃, CaCO₃, and CuO powders. To get Bi_{1.2}Pb_{0.3}Sr_{1.54}Ca_{2.06}Cu₃O_y powder, the powders in the stoichiometric ratio were initially dissolved in conc. Nitric acid one by one, the resulting solution was dried and calcined at 500 °C for a few hours. The calcined powder was ground and annealed at 800 °C twice for 24 hours, each with one intermediate grinding.

Similarly, Ca_{0.86}Sr_{0.14}CuO₂ powder was also prepared by nitrate method, but the annealing was done at 900 °C. Bi_{1.2}Pb_{0.3}Sr_{1.54}Ca_{2.06}Cu₃O_y (Bi 2223) and Ca_{0.86}Sr_{0.14}CuO₂ mixed powders were tumbled for 8 hours before being pelletized. The pellet was processed for 48 hours at 845 °C to form the composite. The processed pellet was ground to powder, and ZrO₂ nanoparticles were then added in different amounts using a sol-casting process, [11] to enable uniform distribution of nanoparticles in the composite.

After adding ZrO₂ nanoparticles, the powder was de-bindered, pressed into the pellet (20 mm in diameter and 5-6 mm in height), and sintered twice at 845 °C for 48 hours with one intermediate pressing. Repeated pressing and sintering is required to densify the Bi 2223 superconductors, as reported in the literature [12,13]. Pressing at an optimized pressure is necessary for better grain connectivity and improved superconducting properties [14,15].

For reference, a pure Bi 2223 superconducting sample, and a composite without nano ZrO₂ are also prepared using the method as mentioned above. Table 5.1 gives the details of all the samples. After final processing, the pellets were cut for characterization.

Table 5.1 : Initial composition and Transition temperatures for a	all the sampl	les
--	---------------	-----

Sample Code	Initial composition	Tc (Onset), K
BZ 0	Pure Bi 2223	104.5
BZ 1	(Bi 2223+ Ca _{0.86} Sr _{0.14} CuO ₂) composite (100:20 mol)	105
BZ 2	(Bi 2223+ Ca _{0.86} Sr _{0.14} CuO ₂) composite (100:20 mol)	104.2
	with 0.5 wt.% nano ZrO ₂	
BZ 3	(Bi 2223+ Ca _{0.86} Sr _{0.14} CuO ₂) composite (100:20 mol)	104.5
	with 1 wt.% nano ZrO ₂	
BZ 4	(Bi 2223+ Ca _{0.86} Sr _{0.14} CuO ₂) composite (100:20 mol)	77
	with 10 wt.% nano ZrO ₂	

5.3 Results and Discussion

XRD analysis confirmed the phase formation of the (Ca,Sr)CuO₂ phase. The (Ca,Sr)CuO₂ system is complex and can exist in many phases. This phase is also sensitive to pressure, atmosphere, and synthesis temperature [16–18]. The indexed XRD pattern for the (Ca,Sr)CuO₂ phase, synthesized at 900 °C, is shown in Fig. 5.1. In addition to the (Ca,Sr)CuO₂ phase, a few peaks corresponding to CuO, and various other oxide phases can also be observed.

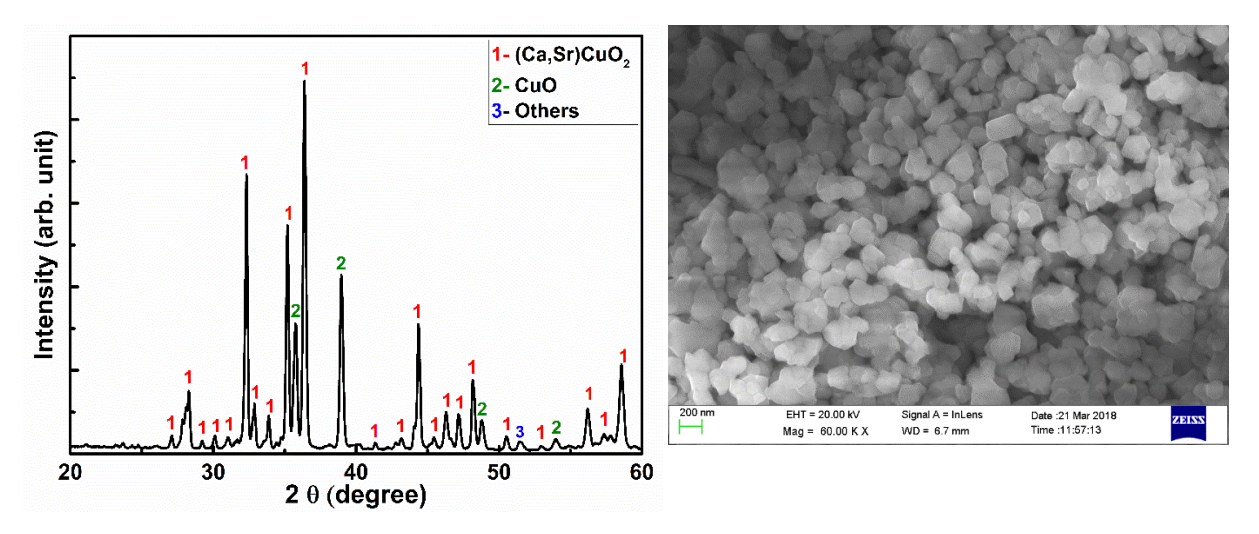


Figure 5.1 (a): Indexed XRD pattern for (Ca,Sr)CuO₂ phase, showing the presence of CuO and other phases, (b) FESEM micrograph for ZrO₂ particles showing particles are in 50-200 nm range in size.

ZrO₂ nanoparticles (Saint Gobain) were added to (Ca,Sr)CuO₂ added Bi 2223 composites. A FESEM micrograph for ZrO₂ nanoparticles is shown in Fig. 5.1(b). The particles ZrO₂ nanoparticles were found to be in the 50- 200 nm range before adding. The ZrO₂ nanoparticles were well dispersed in water using a high-power ultrasonicator and added to the gelling medium.

5.3.1 XRD analysis for samples of BZ series

Indexed XRD patterns for samples BZ 0- BZ 4 are shown in Fig. 5.2. Samples BZ 0 is nearly single phase Bi 2223. Most of the peaks for samples BZ 1- BZ 3 are indexed to the Bi 2223 phase; low-intensity peaks corresponding to Bi 2212, Bi 2201, and other phases are also present. Peaks corresponding to (Ca,Sr)CuO₂ are marked (δ). The majority of peaks for sample BZ 4 are indexed to the Bi 2212 phase, suggesting Bi 2212 is the major phase and higher conc. of nano ZrO₂ addition restricts the formation of the Bi 2223 phase. XRD analysis suggests that all the samples are crystalline, with Bi 2223 being the major phase in samples BZ 0 to BZ 3, whereas the major phase in sample BZ 4 is the Bi 2212 phase. Strontium Zirconate (SrZrO₃) phase peaks around 2θ position of 30.78 and 54.74 are also marked as others. A systematic increase in the intensity of the SrZrO₃

phase peak at 30.78 degree with increasing ZrO₂ content suggests that nano ZrO₂ particles react with (Ca,Sr)CuO₂ and form the SrZrO₃ phase. In literature, there are reports where a low concentration of nanoparticle addition to Bi 2223 leads to the formation of secondary phases [19,20], and a high concentration of nanoparticle addition causes incomplete Bi 2223 phase formation [21,22]. The lattice parameters for Bi 2223 phase for samples BZ 0- BZ 3 are given in Table 5.2.

Table 5.2: Lattice parameters of Bi 2223 phase for samples BZ 0- BZ 3

Sample	Lattice parameters of Bi 2223 phase					
	a (Å)	b (Å)	c (Å)			
BZ 0	5.413(7)	5.381(3)	37.076(8)			
BZ 1	5.409(7)	5.398(9)	37.078(2)			
BZ 2	5.404(2)	5.403(2)	37.046(2)			
BZ 3	5.403(9)	5.407(4)	37.051(4)			

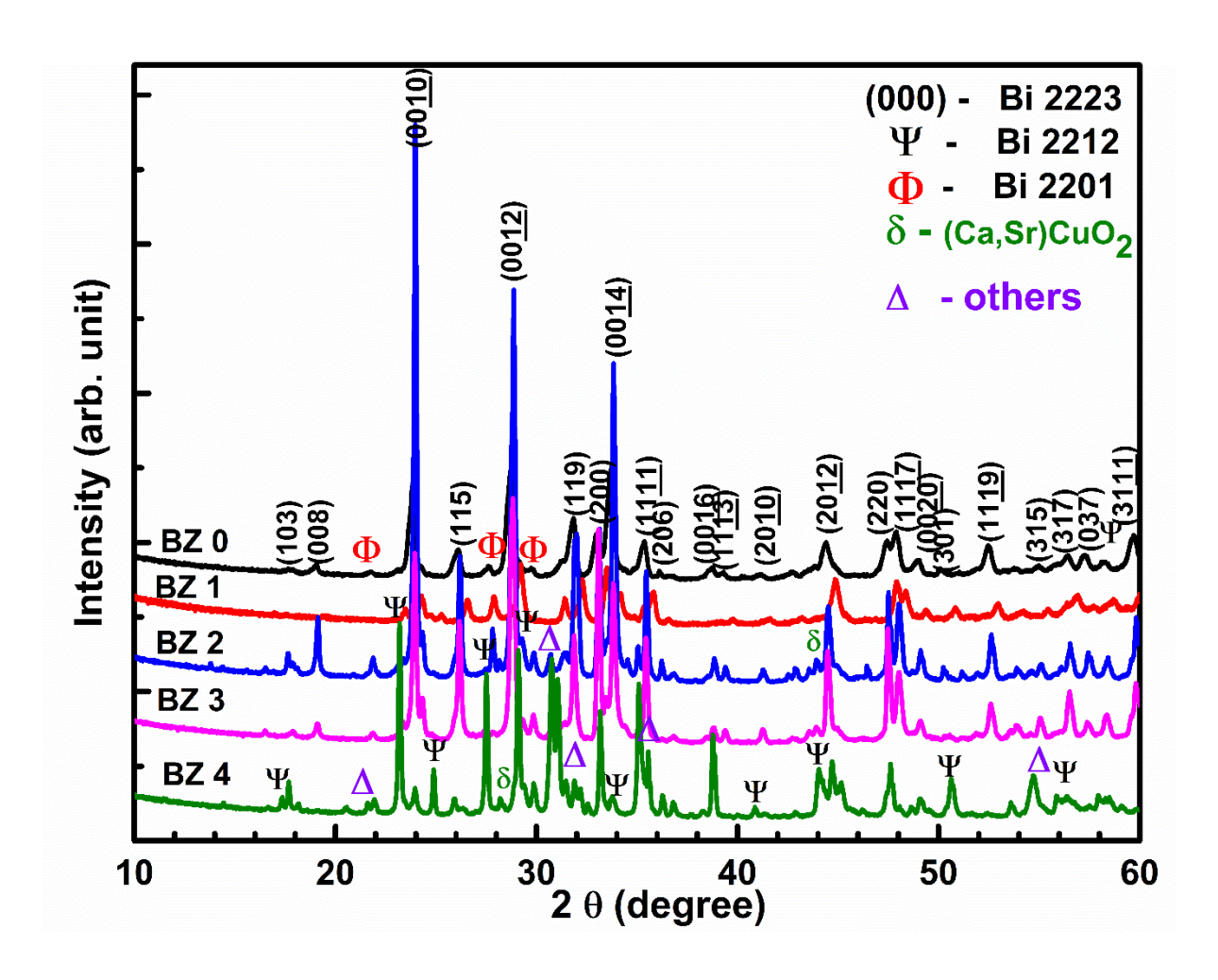
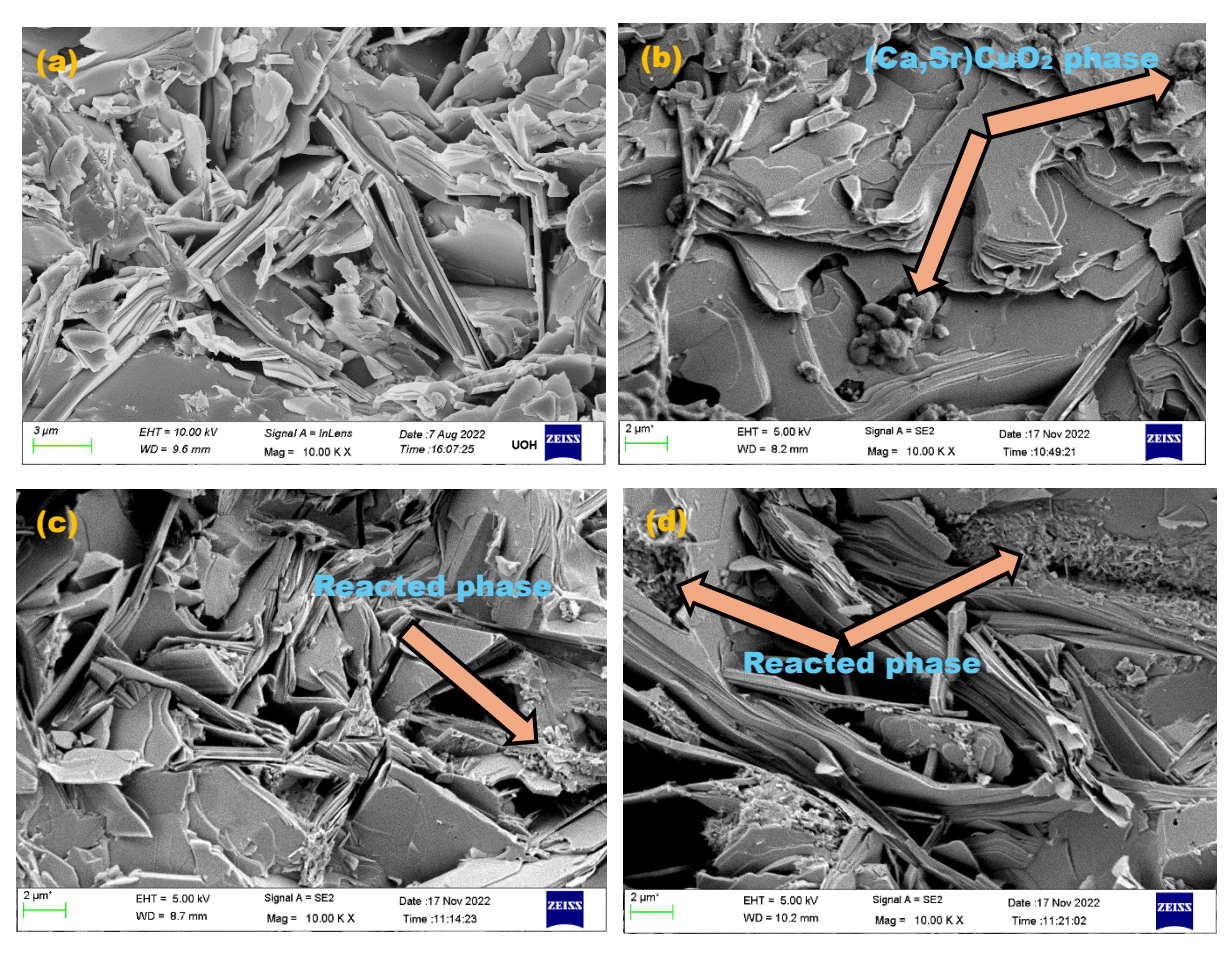


Figure 5.2: Indexed XRD patterns for all samples showing Bi 2212 as the major phase for sample BZ 4 and Bi 2223 for other samples.

5.3.2 Microstructural analysis

Fig. 5.3 shows the FESEM micrograph for all samples. Randomly oriented large and dense platelets like grains corresponding to Bi 2223 are present for samples BZ 0 – BZ 3. The smaller grains corresponding to the Bi 2212 phase are present for sample BZ 4. (Ca,Sr)CuO₂ phase particles, spherical in size are distinctly seen for sample BZ 1 in Fig. 5.3(f), and the composition of these particles is confirmed EDAX analysis. These particles are a few microns in size, uniformly dispersed, and lying intact among Bi 2223 grains. Nano ZrO₂ added samples have a reacted phase present among the grains and this reacted phase increases with increasing ZrO₂ concentration. This phase formed due to the reaction of ZrO₂ and (Ca,Sr)CuO₂ phase is also verified by XRD analysis (SrZrO₃). Sample BZ 4 has the highest amount of this reacted phase among Bi 2212 grains. At higher conc. of nano ZrO₂ addition, the increased amount of this reacted phase inhibited the formation of the Bi 2223 phase for sample BZ 4. Similar microstructures for sintered BSCCO ceramics are reported in the literature [23–28].



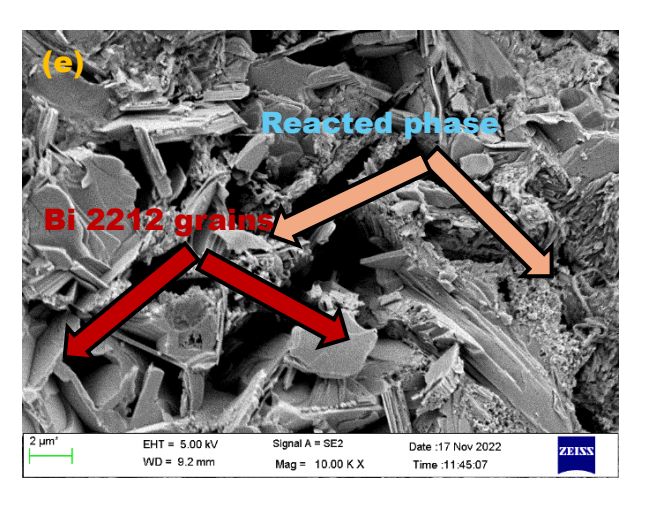




Figure 5.3 (a-e): FESEM micrograph for BZ 0- BZ 4 showing Bi 2223 and Bi 2212 grains, (Ca,Sr)CuO₂, and Reacted phases, (f) FESEM micrograph for sample BZ 1 showing (Ca,Sr)CuO₂ phase particles among Bi 2223 grains.

5.3.3 Temperature dependence of magnetization

To assess the superconducting transition temperature, the temperature dependence of magnetization was measured at 5 mT applied field in the temperature range 120 K- 20 K and shown in Fig. 5.4. A sharp diamagnetic transition around 105 K for samples BZ 0 – BZ 3 suggests that the main phase present is Bi 2223. In contrast, for sample BZ 4, a transition around 80 K indicates that Bi 2212 is the major phase. Among all the samples, sample BZ 1 has the sharpest transition. Also, the lower transition width for sample BZ 1 suggests that it has better grain connectivity and superconducting properties. The decrease in the Meissner fraction can be seen after adding secondary phases. The secondary phase addition didn't cause any change in the T_c for sample BZ 0- BZ 3 unlike reported in the literature [25–27,29], this suggests that the added secondary phases are not substituted to the lattice. From XRD, microstructure, and MT analysis, it is confirmed that sample BZ 4 has Bi 2212 as the main phase, so sample BZ 4 is not included for comparison of remaining superconducting properties. The T_c (Onset) values for all samples are given in Table 5.1.

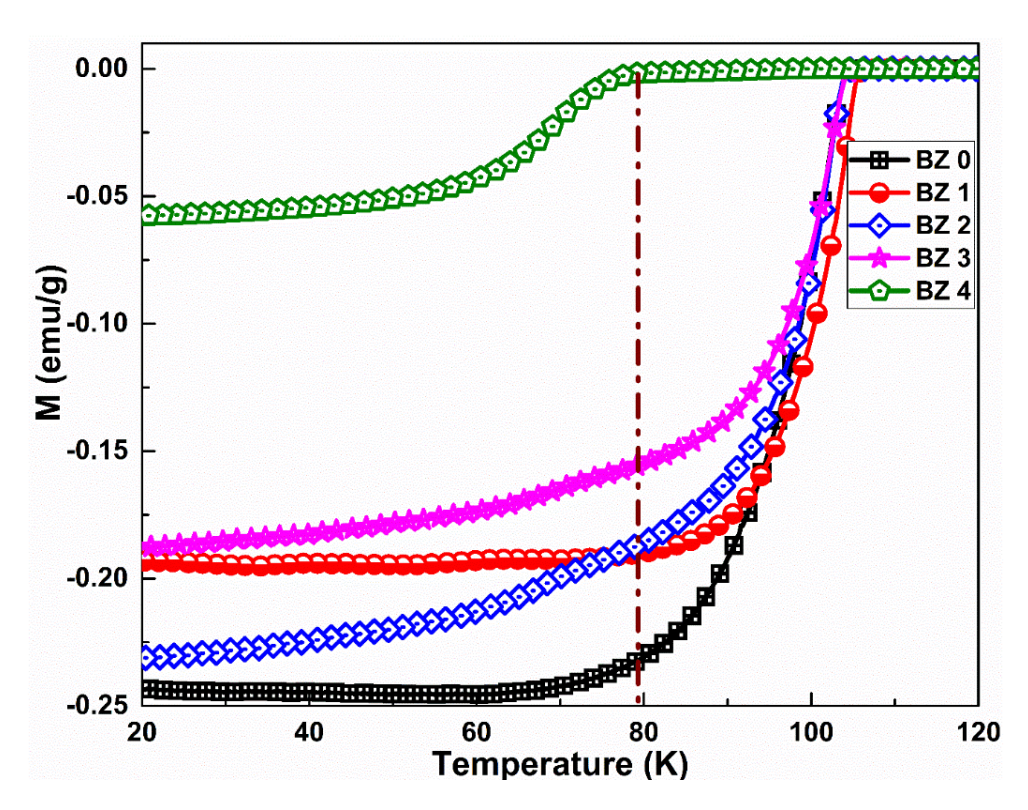


Figure 5.4: Temperature dependence of magnetization for all composites showing a sharp diamagnetic transition around 105 K for samples BZ 0- BZ 3 and around 80 K for sample BZ 4.

5.3.4 Field dependence of magnetization

MH loops were recorded for all the samples at various temperatures. Fig. 5.5 shows the MH loops at 10 K and 20 K for samples BZ 0- BZ 3. The MH loops for all samples are open till 9 T. The opening of an MH loop is an indirect measure of J_c . So, at low temperatures (10 K and 20 K) the opening of MH loops suggests that all samples have finite J_c till 9 T field.

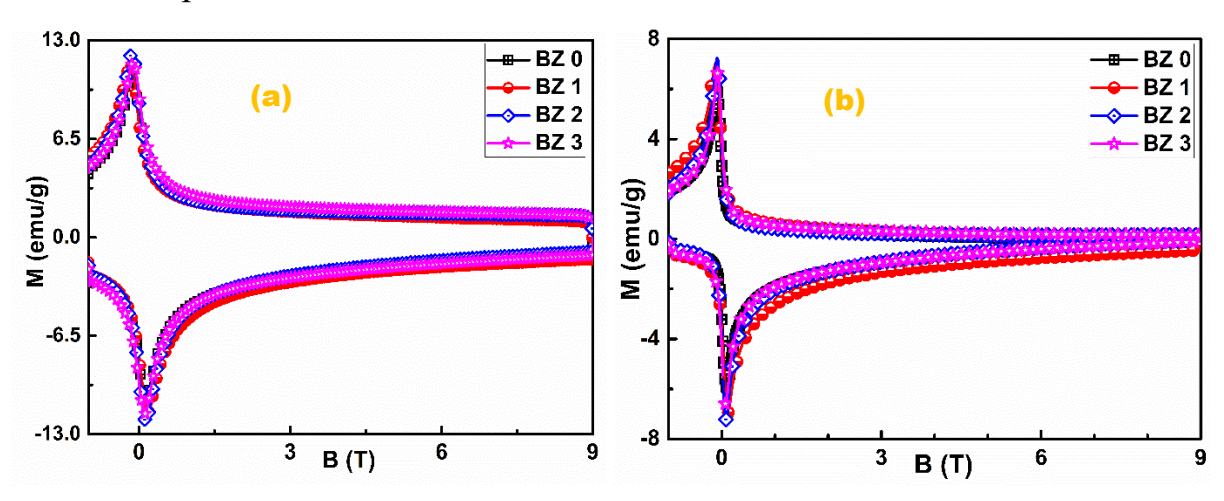


Figure 5.5(a-d): Field dependence of Magnetization for samples BZ 0- BZ 3 at 10 K and 20 K.

5.3.5 Field dependence of critical current density

Critical current densities were measured from the recorded MH loops at various temperatures using Bean's critical state model [30].

The field dependence of J_c for samples BZ 0 - BZ 3, at 10 K, 20 K, 30 K, and 50 K is shown in Fig. 5.6(a-d). At 10 K and 20 K, all samples have non-zero J_c values till 9 T applied field, and sample BZ 1 has better J_c -B behaviour among all the samples. Similar J_c- B behaviour was also observed for sample BZ 1 at higher temperatures. The better J_c -B behaviour for sample BZ 1 is attributed to the (Ca, Sr)CuO₂ phase particles distributed among Bi 2223 grains without reaction, contributing to effective flux pinning centers.

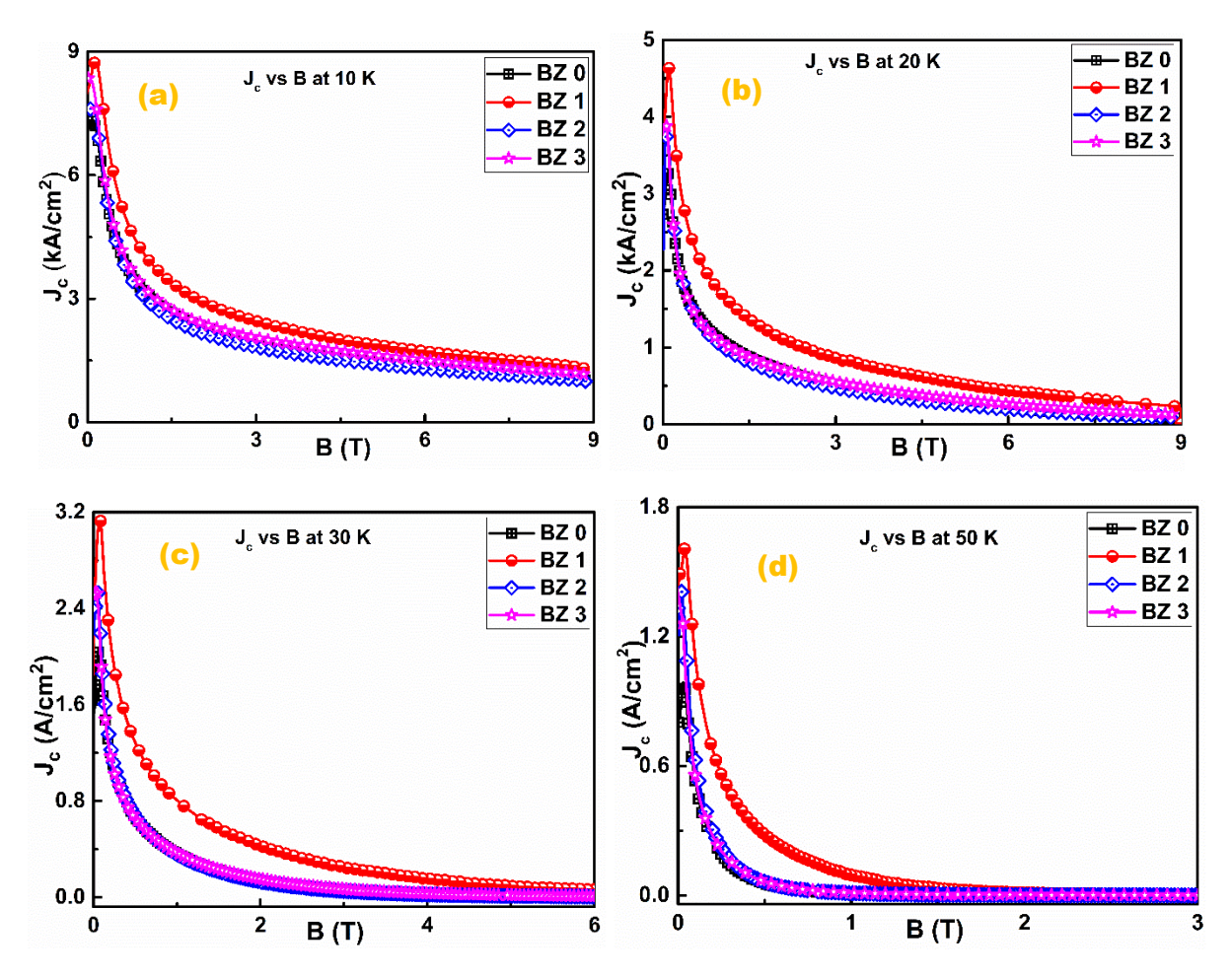


Figure 5.6(a-d): Field dependence of J_c at 10, 20, 30, and 50 K for samples BZ 0 – BZ 3.

Samples BZ 0, BZ 2, and BZ 3 have similar J- B behaviour. Sample BZ 0 lacks pinning centres whereas sample BZ 2- BZ 3 has a reacted phase that reduces Bi 2223 phase content, this suggests that pinning centres of optimum density provide flux pinning.

5.3.6 Analysis of Flux Pinning Force Density (F_p)

Flux pinning force density ($F_p = J_c X B$) is plotted with respect to the field and shown in Fig. 5.7. F_p determines the performance of a superconductor in an applied magnetic field. At 10 K, the F_p increases with the field applied, due to low flux creep at low temperatures, the available pinning centers in the form of defects like grain boundaries, precipitates, etc., present in each sample can pin the flux lines. For 20 K, F_p increases with the field and subsequently decreases after a maximum, all samples have broad maxima suggesting better F_p - B behaviour at 20 K till a certain field. At 30 K, sample BZ 1 has maxima around 2 T, whereas all other samples have maxima around 1 T, this shows that sample BZ 1 has better flux pinning behaviour at higher fields (till 2 T). At 50 K, the F_p maxima shifts towards lower fields due to high flux creep near T_c .

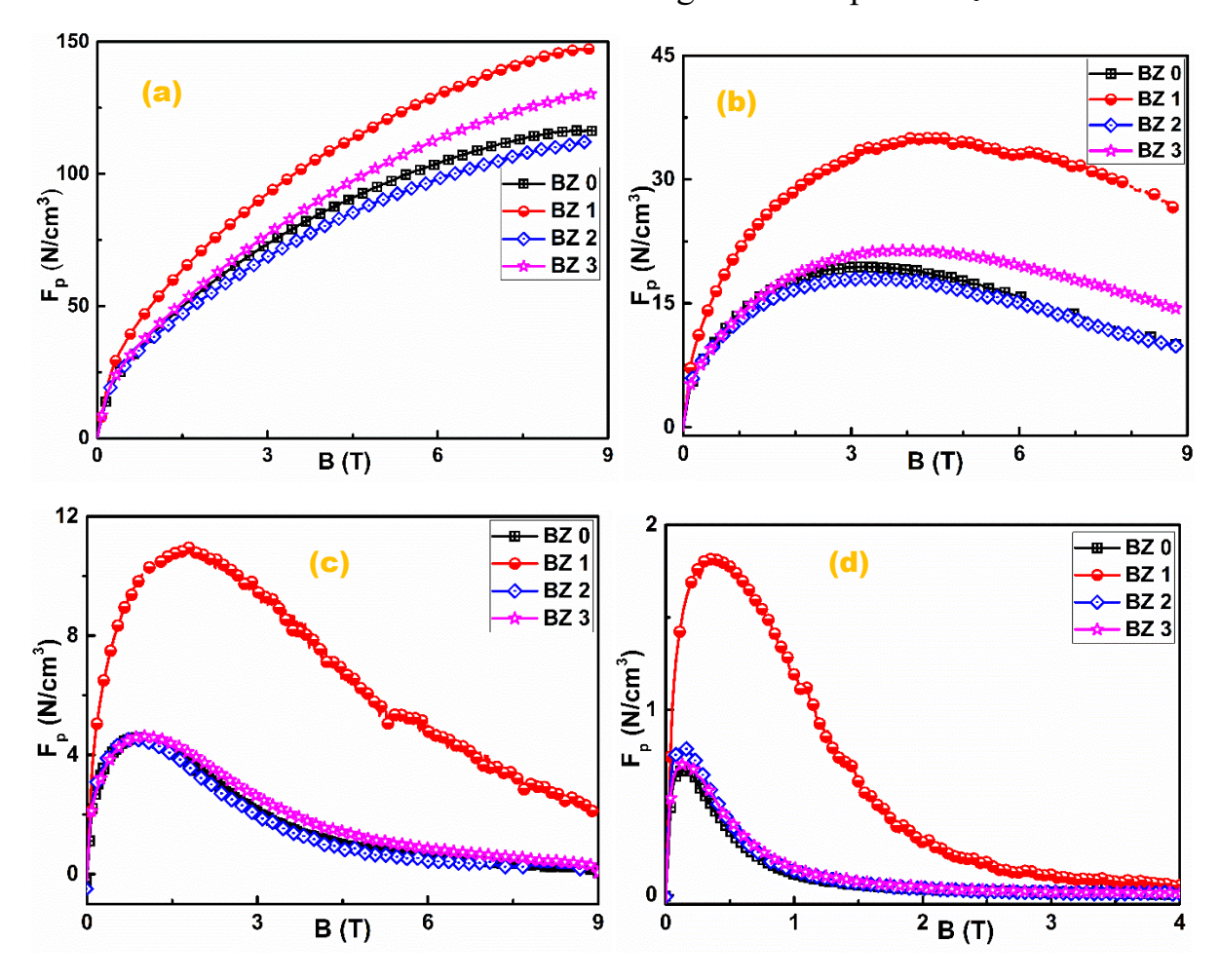


Figure 5.7(a-d): Field dependence of F_p at 10 K, 20 K, 30 K, and 50 K for samples BZ 0- BZ 3.

To control high flux creep, adequate pinning centers must be introduced into the superconducting matrix without causing any disturbances to it. At all temperatures, especially at higher temperatures, the in-field pinning behaviour for sample BZ 1 is better among all the samples and this is due to (Ca,Sr)CuO₂ phase particles. These particles work as efficient pinning centers and are distributed among Bi 2223 grains without reacting or without forming a secondary phase for sample BZ 1.To examine the dominant nature of pinning present in our samples, we have used the Kramer-Hughes model [31,32] and a model developed by Klein et al. [33] Both models give similar information about the pinning mechanism present in our samples.

To understand a qualitative picture of the pinning mechanism, present in the samples, we have plotted the $f(F_p/F_{p \text{ max}})$ vs. h (B/B_p) curve along with the theoretical plots of normal point, normal surface, and δk pinning as given by Kelin's model, here $F_{p \text{ max}}$ is the maximum pinning force and B_p is the field corresponding to $F_{p \text{ max}}$.

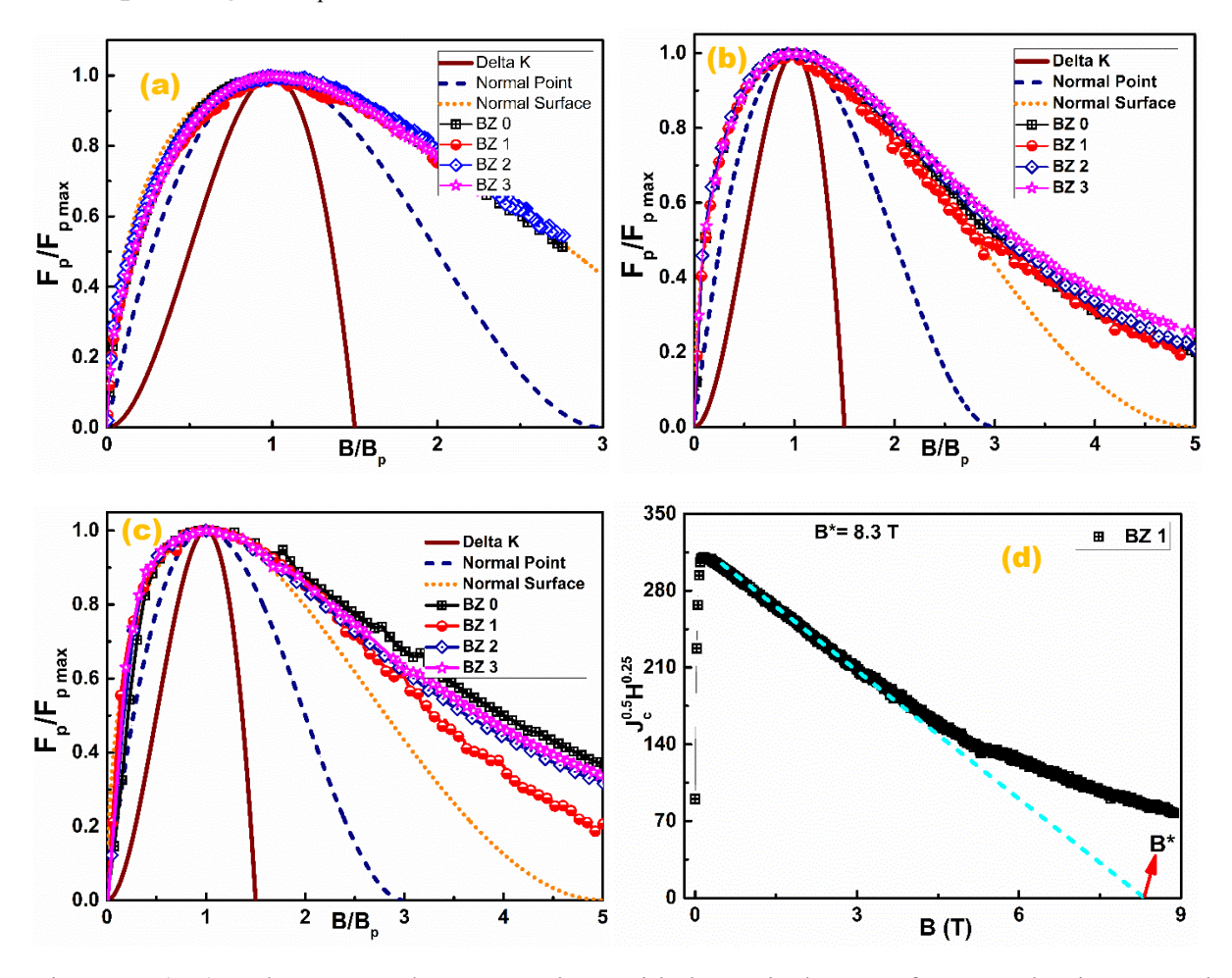


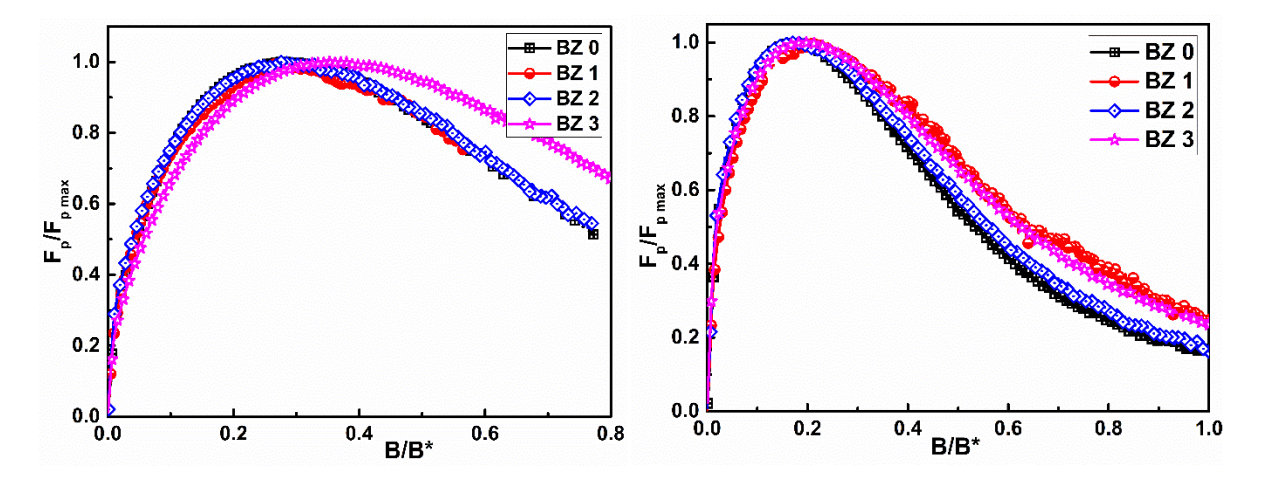
Figure 5.8(a-c): $F_p/F_{p\,max}$ vs B/B_p curves along with theoretical curves for normal point, normal surface, and δk pinning for samples BZ 0 – BZ 3 at 20 K, 30 K, and 50 K, (d) A typical B* determination using Kramer's criteria for sample BZ 1 at 20 K.

The theoretical equations for normal point, normal surface, and δk pinning can be found elsewhere [9,34]. The f vs. h plots at 20 K, 30 K, and 50 K are given in Fig. 5.8 (a-c). At 20 K, where the flux creep is low, all samples show the presence of similar pinning behaviour, i.e., surface pinning, and it matches exactly with the theoretical curve for the surface pinning mechanism.

At 30 K, all samples have similar (Surface) pinning mechanisms but at higher field, the f vs h plots deviated from the theoretical surface pinning mechanism. After crossing this field, the experimental curves deviate due to presence of another pinning mechanism. Similar deviations in the experimental curves from the theoretical curve are also reported by [35,36]. At 50 K, the f vs. h curves deviate from the theoretical curve for the surface pinning mechanism after maxima. After maxima, the f vs. h curves for all samples can be seen, unlike at 20 and 30 K. The f vs h curve for sample BZ 1 is in the nearest vicinity of the theoretical surface pinning curve, suggesting that the (Ca,Sr)CuO₂ phase particles are helpful in retaining the flux pinning at higher fields and higher temperatures.

Using Kramer- Hughes model, we have plotted $f(F_p/F_{p \text{ max}})$ versus $b(B/B^*)$ and fitted the data to Hughe's equation given in Chapter 2, equation 16, for analyzing the dominant flux pinning present in our samples.

Here, B* is the characteristic field responsible for vanishing one pinning mechanism, and it is determined using Kramer's criteria [32], whereas A, p, and q are the fitting parameters. A typical B* determination plot for sample BZ 1 at 20 K is shown in Fig. 5.8(d). According to the Hughes model, the values for the pair of fitting parameters (p, q) describe the nature of the flux pinning mechanism present. Such as if p = 1/2, and q = 2, then the pinning mechanism present is surface pinning or if p = 1 and q = 2, then the pinning mechanism present is point pinning. Fig. 5.9 shows the f vs. b curves for all samples. A typical Hughes fit at 20 K for sample BZ 1 is also given in Fig 5.9 (d).



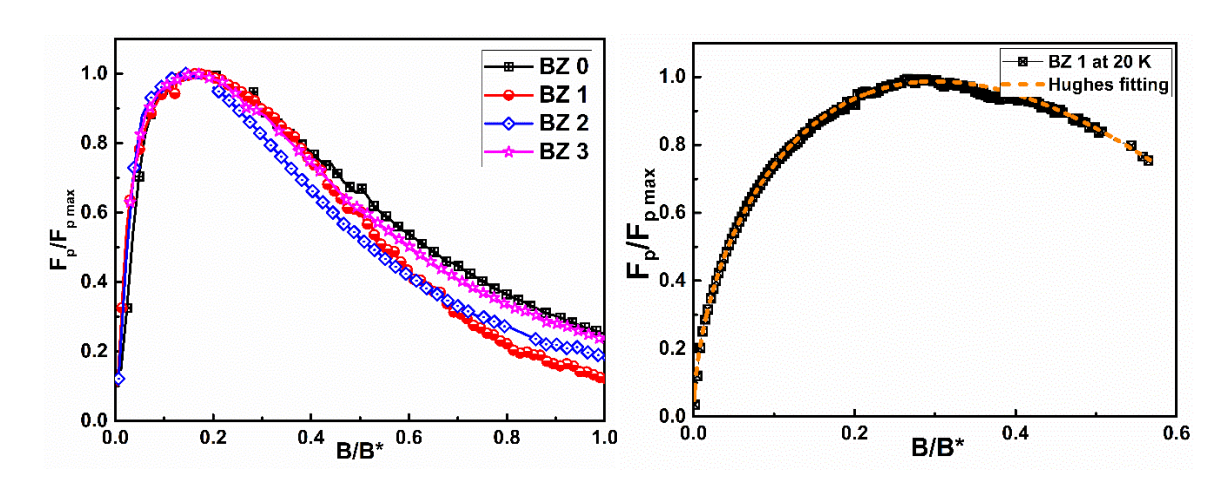


Figure 5.9(a-c): $F_p/F_{p \; max}$ vs B/B^* curves for samples BZ 0-BZ 3 at 20 K, 30 K, and 50 K, (d) Hughes fitting of experimental data at 20 K for sample BZ 1

Table 5.3: B*(T) and fitting parameters for Hughes equation at 20 K, 30 K, and 50 K.

Sample	20 K			30 K			50 K					
	B *, T	A	p	q	B*, T	A	p	q	B*, T	A	p	q
BZ 0	11.4	2.90	0.54	1.21	5.3	2.78	0.39	1.79	0.81	2.34	0.35	1.29
BZ 1	15.5	3.08	0.56	1.31	8.3	2.25	0.34	1.20	2.2	2.76	0.39	1.74
BZ 2	11.4	2.56	0.48	1.07	4.9	2.49	0.35	1.58	0.94	2.48	0.33	1.75
BZ 3	11	2.34	0.50	0.77	5.2	2.26	0.33	1.27	0.93	1.85	0.24	1.05

B*(T) and fitting parameters (A, p, and q) for samples BZ 0- BZ 3 at 20 K, 30 K, and 50 K are given in Table 5.3. Sample BZ 1 has the highest B*(T) values at all the temperatures. The fitting parameter values are close to those of the surface pinning mechanism(p, q). When several pinning mechanisms coexists in a superconductor, the p and q values deviate from the ideal values. In HTSc, multiple defects of various sizes are present, and these defects contribute to different pinning mechanisms simultaneously and cause deviation in the ideal values of fitting parameters. For the Bi 2223 system, the deviation in p, q values than ideal values (p=0.5, q=2) for surface pinning, suggests the existence of more than one pinning mechanism are also reported [37,38].

Defects are responsible for flux pinning in a superconductor; these defects could be of various types, dimensions, or vacancies, such as point defects, grain boundaries, slip dislocation, precipitates, and secondary phases. So, these different types of defects actively participate in pinning the flux lines at different temperatures and fields [39]. Several scaling laws were proposed for various superconducting systems like MgB₂ [40] and other systems [39]. However, for a

complex system like BSCCO, where various defects are present and contribute collectively to flux pinning, there is still an ongoing quest to address these defects to identify the coexisting flux pinning mechanism.

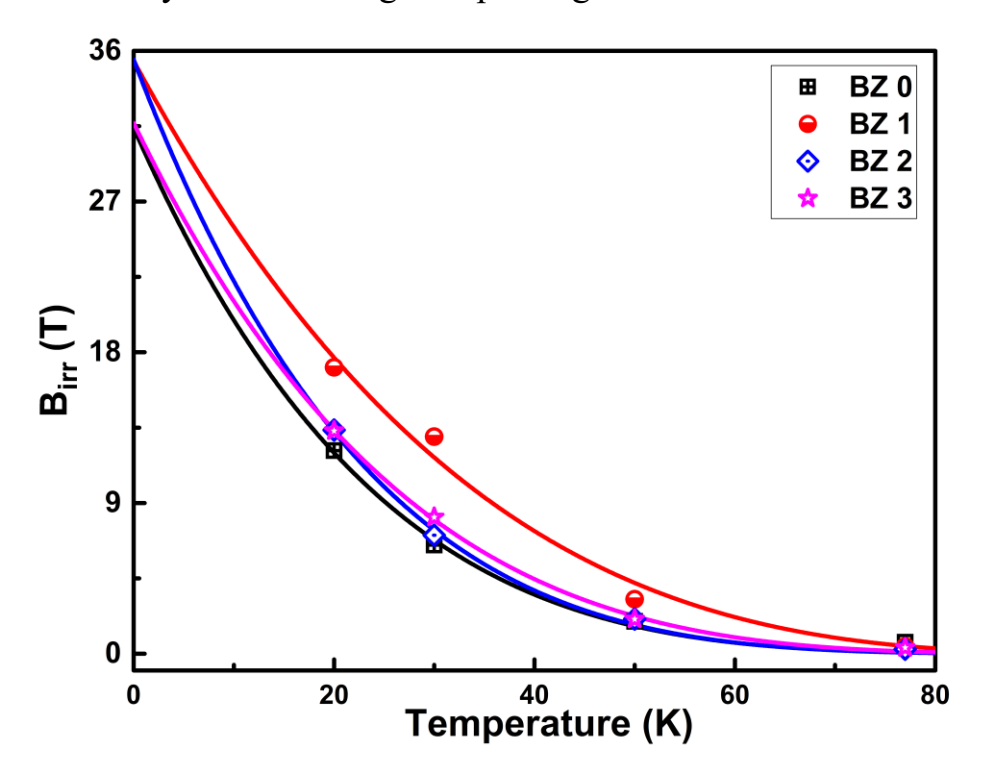


Figure 5.10: Temperature dependence of B_{irr} for samples BZ 0- BZ 3

The irreversible field (B_{irr}) was estimated by fitting the Fp vs B curves into an exponential equation, as explained in Chapter 4. Sample BZ 1 exhibits the highest B_{irr} values, BZ 2 and BZ 3 samples also have better B_{irr} values than that of sample BZ 0. This can be attributed to additional pinning centers introduced by the (Ca,Sr)CuO2 or the reacted phase. The temperature dependence of the irreversible field is shown in Fig. 5.10.

5.4 Conclusions

20 mol (Ca,Sr)CuO₂ phase added Bi 2223 composites (20:100 mol) with varying amounts of nano ZrO₂ addition were synthesized and characterized using various techniques. XRD Analysis showed that the main phase for samples except BZ 4 was the high T_c phase (Bi 2223). Larger amounts of nano ZrO₂ addition for Sample BZ 4 suppressed the formation of high T_c phase. Microstructural analysis revealed large platelet-like grains of Bi 2223 in samples BZ 0 to BZ 3. Addition of 20 mol of (Ca,Sr)CuO₂ phase particles enhanced J_c up to an applied field of 9 T at 20 K, for sample BZ 1. Interestingly, (Ca,Sr)CuO₂ formed as non-reacted spherical particles among Bi 2223 grains, leading to enhanced flux pinning at

high magnetic fields. The distribution of non-reacted (Ca,Sr)CuO₂ particles in the Bi 2223 matrix for BZ 1 sample created a two-phase microstructure similar to that of Y 123 with Y 211 precipitates. The effective increase in J_c was achieved by creating a high density of small-sized structural defects formed at the interface between the second-phase particles and the matrix, facilitating effective pinning. The addition of ZrO₂ nanoparticles to the above composite is found to react with the (Ca,Sr)CuO₂ particles, forming SrZrO₃ as an impurity phase. This decreased the superconducting phase fraction and lowered the J_c(0) compared to BZ 1 but enhanced the field range in which flux pinning was effective in samples with ZrO₂ addition. Pinning force density was analysed in terms of scaling models and it was found that surface pinning is the dominant pinning mechanism at low fields. Examination of the data, fit the Hughes model, suggests that sample BZ 3 has better-pinning properties at fields close to B* compared to samples with lower ZrO₂ content. This is attributed to flux pinning caused by the defect density created by the reaction products after nano ZrO₂ addition. Pinning from different mechanisms is thus observed to be operative at different field regimes. Birr increased after (Ca,Sr)CuO2 and nano ZrO2 addition. It will be of interest to optimize the microstructures in textured BSCCO tapes on similar lines, with a larger superconducting fraction retained, for achieving enhanced performance.

References

- [1] R.B. Saxena, R. Giri, V.P.S. Awana, H.K. Singh, M.A. Ansari, B. V. Kumaraswamy, A. Gupta, R. Nigam, K.P. Singh, H. Kishan, O.N. Srivastava, Impact of Zn substitution on phase formation and superconductivity of $Bi_{1.6}Pb_{0.4}Sr_2Ca_2Cu_{3-x}Zn_xO_{10-\delta}$ with $x=0.0,\,0.015,\,0.03,\,0.06,\,0.09$ and 0.12, Mod. Phys. Lett. B. 19 (2005) 771–778. https://doi.org/10.1142/S0217984905008785.
- [2] N.A.A. Yahya, R. Abd-Shukor, Effect of different nanosized MgO on the transport critical current density of Bi_{1.6}Pb_{0.4}Sr₂Ca₂Cu₃O₁₀ superconductor, J. Supercond. Nov. Magn. 27 (2014) 329–335. https://doi.org/10.1007/s10948-013-2302-5.
- [3] Z.Y. Jia, H. Tang, Z.Q. Yang, Y.T. Xing, Y.Z. Wang, G.W. Qiao, Effects of nano-ZrO₂ particles on the superconductivity of Pb-doped BSCCO, Phys. C Supercond. Its Appl. 337 (2000) 130–132. https://doi.org/10.1016/S0921-4534(00)00072-1.
- [4] M. Zouaoui, L. Bessais, M. Ben Salem, Thermally activated dissipation and pinning mechanisms in a Bi 2223 superconductor with the addition of nanosized ZrO₂ particles, Supercond. Sci. Technol. 23 (2010) 095013. https://doi.org/10.1088/0953-2048/23/9/095013.
- [5] M. Zouaoui, A. Ghattas, M. Annabi, F. Ben Azzouz, M. Ben Salem, Effect of nanosize ZrO₂ addition on the flux pinning properties of (Bi, Pb)-2223 superconductor, Supercond. Sci. Technol. 21 (2008). https://doi.org/10.1088/0953-2048/21/12/125005.
- [6] V. Seshu Bai, S. Ravi, T. Rajasekharan, R. Gopalan, On the composition of 110 K superconductor in a (Bi,Pb)-Sr-Ca-Cu-O system, J. Appl. Phys. 70 (1991) 4378–4382. https://doi.org/10.1063/1.349119.

- [7] S. Ravi, V. Seshu Bai, Fluctuation induced excess conductivity in the Bi_{1.2}Pb_{0.3}Sr_{1.5}Ca₂Cu₃O_y compound, Phys. C Supercond. 182 (1991) 345–350. https://doi.org/10.1016/0921-4534(91)90533-5.
- [8] D. -X. Chen, A. Hernando, F. Conde, J. Ramírez, J.M. González-Calbet, M. Vallet, Lower critical field and surface barrier in sintered Bi₂Sr₂CaCu₂O_{8+δ} superconductor, J. Appl. Phys. 75 (1994) 2578–2583. https://doi.org/10.1063/1.356232.
- [9] P.K. Verma, T. Rajasekharan, S.C. Das, K.P. Surendran, V. Seshu Bai, Effect of nano ZrO₂ addition on the properties of Ca_{0.86}Sr_{0.14}CuO₂ added Bi 2223 composites, J. Phys. Conf. Ser. 2545 (2023) 012014. https://doi.org/10.1088/1742-6596/2545/1/012014.
- [10] S. Ravi, V. Seshu Bai, Fluctuation induced excess conductivity in the Bi_{1.2}Pb_{0.3}Sr_{1.5}Ca₂Cu₃O_y compound, Phys. C Supercond. 182 (1991) 345–350. https://doi.org/10.1016/0921-4534(91)90533-5.
- [11] P.M.S. Raju, V. Seshubai, T. Rajasekharan, A generic process to introduce nanoparticles into powder preforms and its application to Infiltration Growth processing of REBa₂Cu₃O₇ superconductor, Mater. Chem. Phys. 161 (2015) 59–64. https://doi.org/10.1016/j.matchemphys.2015.05.004.
- [12] R.R. Kumar, R.P. Aloysius, R.J. Bose, P. Guruswamy, U. Syamaprasad, Preparation of dense, high J_c Bi-2223 superconductors by multistage cold pressing, Supercond. Sci. Technol. 18 (2005) 689–693. https://doi.org/10.1088/0953-2048/18/5/018.
- [13] V.Seshu Bai, S. Ravi, T. Rajasekharan, R. Gopalan, On the composition of 110 K superconductor in a (Bi,Pb)-Sr-Ca-Cu-O system, J. Appl. Phys. 70 (1991) 4378–4382. https://doi.org/10.1063/1.349119.
- [14] K. Habanjar, A. Najem, A.M. Abdel-Gaber, R. Awad, Effect of pelletization pressure on the physical and mechanical properties of (Bi, Pb)-2223 superconductors, Phys. Scr. 95 (2020) 065702. https://doi.org/10.1088/1402-4896/ab7f46.
- N. Devendra Kumar, P. Missak Swarup Raju, S. Pavan Kumar Naik, T. Rajasekharan, V. Seshubai, Effect of preform compaction pressure on the final microstructures and superconducting properties of YBa₂Cu₃O_{7-δ} superconductors fabricated by directionally solidified Preform optimized infiltration growth process, J. Low Temp. Phys. 174 (2014) 113–127. https://doi.org/10.1007/s10909-013-0955-x.
- [16] M. Kato, I. Nagai, Y. Koike, Low-temperature synthesis of Sr_{12-x}Ca _xCuO₂ from hydroxide precursor, Solid State Ionics. 108 (1998) 275–281.
- [17] R.S. Roth, C.J. Rawn, J.J. Ritter, B.P. Burton, Phase Equilibria of the System SrO-CaO-CuO, J. Am. Ceram. Soc. 72 (1989) 1545–1549. https://doi.org/10.1111/j.1151-2916.1989.tb07704.x.
- [18] T. Siegrist, S.M. Zahurak, D.W. Murphy, R.S. Roth, The parent structure of the layered high-temperature superconductors, Nature. 334 (1988) 231–232. https://doi.org/10.1038/334231a0.
- [19] R. Mawassi, S. Marhaba, M. Roumié, R. Awad, M. Korek, I. Hassan, Improvement of superconducting parameters of Bi_{1.8}Pb _{0.4}Sr₂Ca₂Cu₃O_{10+δ} added with nano-Ag, J. Supercond. Nov. Magn. 27 (2014) 1131–1142. https://doi.org/10.1007/s10948-013-2408-9.
- [20] W.D. Huang, W.H. Song, Z. Cui, B. Zhao, M.H. Pu, X.C. Wu, T. Hu, Y.P. Sun, J.J.

- Du, Enhancement of flux pinning in (Bi, Pb)-2223/Ag tapes doped with MgO nanorods, Supercond. Sci. Technol. 13 (2000) 1499–1504. https://doi.org/10.1088/0953-2048/13/10/316.
- [21] Y.C. Guo, Y. Tanaka, T. Kuroda, S.X. Dou, Z.Q. Yang, Addition of nanometer SiC in the silver-sheathed Bi2223 superconducting tapes, Phys. C Supercond. Its Appl. 311 (1999) 65–74. https://doi.org/10.1016/S0921-4534(98)00625-X.
- [22] G. Yildirim, Beginning point of metal to insulator transition for Bi-2223 superconducting matrix doped with Eu nanoparticles, J. Alloys Compd. 578 (2013) 526–535. https://doi.org/10.1016/j.jallcom.2013.07.016.
- [23] E. Guilmeau, B. Andrzejewski, J.G. Noudem, The effect of MgO addition on the formation and the superconducting properties of the Bi 2223 phase, Phys. C Supercond. Its Appl. 387 (2003) 382–390. https://doi.org/10.1016/S0921-4534(02)02360-2.
- [24] M. Roumié, S. Marhaba, R. Awad, M. Kork, I. Hassan, R. Mawassi, Effect of Fe₂O₃ nano-oxide addition on the superconducting properties of the (Bi,Pb)-2223 phase, J. Supercond. Nov. Magn. 27 (2014) 143–153. https://doi.org/10.1007/s10948-013-2288-z.
- [25] Ş. Yavuz, Ö. Bilgili, K. Kocabaş, Effects of superconducting parameters of SnO₂ nanoparticles addition on (Bi, Pb)-2223 phase, J. Mater. Sci. Mater. Electron. 27 (2016) 4526–4533. https://doi.org/10.1007/s10854-016-4327-6.
- [26] M. Annabi, A. M'chirgui, F. Ben Azzouz, M. Zouaoui, M. Ben Salem, Addition of nanometer Al₂O₃ during the final processing of (Bi,Pb)-2223 superconductors, Phys. C Supercond. Its Appl. 405 (2004) 25–33. https://doi.org/10.1016/j.physc.2004.01.012.
- [27] N. Türk, H. Gündoğmuş, M. Akyol, Z.D. Yakıncı, A. Ekicibil, B. Özçelik, Effect of tungsten (W) substitution on the physical properties of Bi-(2223) superconductors, J. Supercond. Nov. Magn. 27 (2014) 711–716. https://doi.org/10.1007/s10948-013-2351-9.
- [28] Y.D. Chiu, T.S. Lei, C.H. Kao, Effects of sintering temperature on the superconducting and microstructural properties of Bi_{1.7}Pb_{0.4}Sr_{1.6}Ca_{2.4}Cu_{3.6}O_Y/Ag₂O composites, J. Mater. Sci. 29 (1994) 2678–2682. https://doi.org/10.1007/BF00356817.
- [29] S.N. Abdullah, M.M.A. Kechik, A.N. Kamarudin, Z.A. Talib, H. Baqiah, C.S. Kien, L.K. Pah, M.K. Abdul Karim, M.K. Shabdin, A.H. Shaari, A. Hashim, N.E. Suhaimi, M. Miryala, Microstructure and Superconducting Properties of Bi-2223 Synthesized via Co-Precipitation Method: Effects of Graphene Nanoparticle Addition, Nanomaterials. 13 (2023). https://doi.org/10.3390/nano13152197.
- [30] C.P. Bean, Magnetization of hard superconductors, Phys. Rev. Lett. 8 (1962) 250–253. https://doi.org/10.1103/PhysRevLett.8.250.
- [31] D. Dew-Hughes, Flux pinning mechanisms in type II superconductors, Philos. Mag. 30 (1974) 293–305. https://doi.org/10.1080/14786439808206556.
- [32] E.J. Kramer, Scaling laws for flux pinning in hard superconductors, J. Appl. Phys. 44 (1973) 1360–1370. https://doi.org/10.1063/1.1662353.
- [33] L. Klein, E.R. Yacoby, Y. Yeshurun, A. Erb, G. Müller-Vogt, V. Breit, H. Wühl, Peak effect and scaling of irreversible properties in untwinned Y-Ba-Cu-O crystals, Phys.

- Rev. B. 49 (1994) 4403–4406. https://doi.org/10.1103/PhysRevB.49.4403.
- [34] T. Goto, K. Inagaki, K. Watanabe, Critical current density in filamentary (Nd, Sm, Eu, Gd)-Ba-Cu-O superconductors prepared by a solution spinning method, Phys. C Supercond. Its Appl. 330 (2000) 51–57. https://doi.org/10.1016/S0921-4534(99)00608-5.
- [35] H. Fallah-Arani, S. Baghshahi, A. Sedghi, N. Riahi-Noori, Enhancement in the performance of BSCCO (Bi-2223) superconductor with functionalized TiO₂ nanorod additive, Ceram. Int. 45 (2019) 21878–21886. https://doi.org/10.1016/j.ceramint.2019.07.198.
- [36] L.P. Qiu, Y.R. Zhang, S.L. Gao, Q.H. Zheng, T.T. Zhang, G.T. Cheng, S. ze Cao, W.P. Hang, S. Ramakrishna, Y.Z. Long, Fabrication and magnetic properties of SiO₂ nanoparticles-doped BSCCO superconducting nanofibers by solution blow spinning, Phys. C Supercond. Its Appl. 608 (2023) 1354251. https://doi.org/10.1016/j.physc.2023.1354251.
- [37] M.A. Ali, S.S. Banerjee, Coexistence of different pinning mechanisms in Bi-2223 superconductor and its implications for using the material for high current applications, J. Appl. Phys. 131 (2022). https://doi.org/10.1063/5.0093741.
- [38] A.T. Pham, D.T. Tran, D.B. Tran, L.T. Tai, N.K. Man, N.T.M. Hong, T.M. Le, D. Pham, W.N. Kang, D.H. Tran, Unraveling the Scaling Characteristics of Flux Pinning Forces in Bi_{1.6}Pb_{0.4}Sr₂Ca_{2-x}Na_xCu₃O_{10+δ} Superconductors, J. Electron. Mater. 50 (2021) 1444–1451. https://doi.org/10.1007/s11664-020-08676-9.
- [39] E.F. Talantsev, New Scaling Laws for Pinning Force Density in Superconductors, Condens. Matter. 7 (2022) 74. https://doi.org/10.3390/condmat7040074.
- [40] M. Eisterer, Calculation of the volume pinning force in MgB₂ superconductors, Phys. Rev. B Condens. Matter Mater. Phys. 77 (2008) 2–6. https://doi.org/10.1103/PhysRevB.77.144524.

Chapter 6

Enhanced superconducting properties of Bi 2223 composites at high concentration of non-reactive nano (Ca,Sr)CuO phase addition

6.1 Introduction

The sensitivity of Bi₂Sr₂Ca_{n-1}Cu_nO_y (BSCCO) superconductors to increased temperature and high magnetic fields, which result in thermally assisted flux flow (TAFF) and the consequent performance reduction, significantly limits their practical applications. Control and suppression of TAFF are required to improve the performance of BSCCO superconductors at moderate to high magnetic fields [1]. The most effective way to control TAFF is by generating defects of the size of coherence length in the Bi 2223 matrix by various methods. The best approach is to incorporate nanoparticles into the BSCCO superconducting matrix. However, optimizing nanoparticles' composition, size, shape, and concentration to enhance the superconducting performance of superconductors is still a challenge [2].

Increasing critical current density and improving flux pinning by optimizing the microstructural features through nanoparticle addition to the BSCCO matrix is an open problem [3].

Various studies of secondary phase addition aimed at improving the properties of Bi 2223 superconductors are reported in the literature [4–12]. However, the added secondary phases are effective in pinning flux only at very low concentrations. At higher concentrations, the secondary phase either agglomerates or reacts with matrix and substantially reduces the Bi 2223 phase amount, which causes deterioration in superconducting properties. Only a few studies are reported where an added secondary phase at higher concentrations is found to be effective in causing observable improvement in critical current density (J_c) like ZrO₂ [9] and MgO [13] addition to Bi 2223.

From our previous work, discussed in chapters 3 and 4, we found that WO3 nanoparticle addition is effective at low concentrations, both in Bi 2212 [2] and Bi 2223 [6], and shows better J_c -B behavior at 0.1 wt.% addition. However, higher concentrations of WO₃ resulted in a W-containing phase, followed by deterioration in superconducting properties. We also found that the addition of $Ca_{0.86}Sr_{0.14}CuO_2$ phase to Bi 2223 composites (20:100 mol) [14] had shown improved $J_c(B)$ performance, with the spherical-shaped $Ca_{0.86}Sr_{0.14}CuO_2$ phase

particles (1-2 μ m size) distributed among Bi 2223 grains without reaction. These observations inspired us to study the effect of submicron-sized Ca_{0.86}Sr_{0.14}CuO₂ phase particle addition, in varying quantities, to Bi 2223 to generate a two-phase microstructure with an aim to enhance the superconducting properties of the composite.

We recall here that the two-phase microstructure of YBCO superconductors, where uniform distribution of about one micron-sized non-superconducting Y₂BaCuO₅ (Y 211) particles by about 30 vol%, in superconducting YBa₂Cu₃O₇ (Y 123) matrix, results in significant improvement in its superconducting properties [15,16].

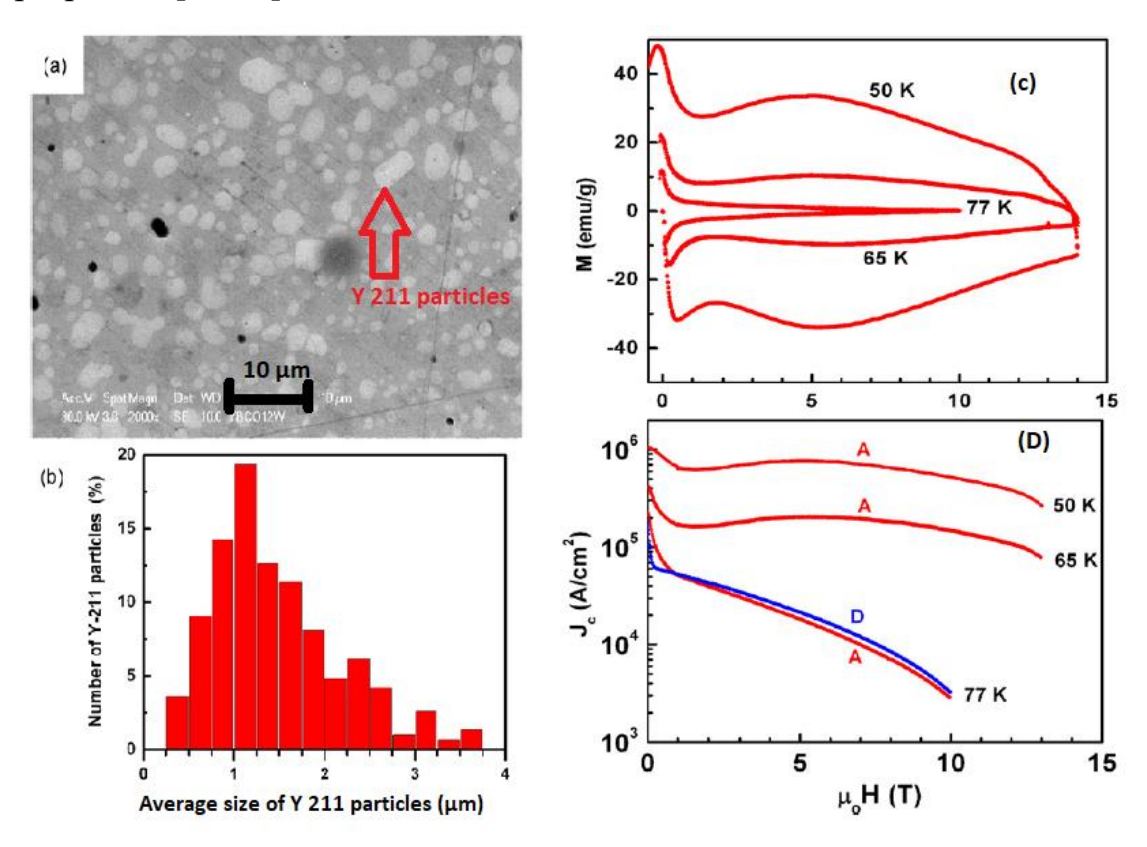


Figure 6.1(a): SEM micrograph showing the distribution of Y 211 particles in YBCO matrix, (b) Histogram showing the size distribution of Y 211 particles in the range 1-4 μ m and most particles are around 1 μ m, (c) MH loops at various temperatures, (d) Field dependence of J_c at various temperatures. This figure is reprinted from [15].

As can be seen, from Fig. 6.1, the J_c is sustained to be high (>100 kA/cm²) above up to 14 applied field in YBCO samples at temperatures lower than 65 K. Significant rise in J_c is known to be due to the flux pinning caused by the defects associated with non-reacting Y 211 inclusions of micron size in the Y 123 matrix.

For the BSCCO superconductor, such a second phase option that remains non-reactive and provides substantial pinning of flux at 77 K is still being sought.

The properties of BSCCO superconductors are significantly influenced by the microstructural modifications which in turn are influenced by the processing conditions like sintering time and temperature [19]. In literature, only a few reports are available where improved microstructure and better superconducting properties due to secondary phase addition are discussed. There have been recent attempts reported to obtain similar two-phase microstructures in BSCCO systems, by optimization of process conditions, with an aim to improve flux pinning and critical current densities at moderate temperatures and fields [2,6].

The secondary phase Y 211 introduced into Y 123 matrix by 30 vol%, for effective flux pinning, belongs to the phase diagram of the YBCO system. In the case of BSCCO system, no systematic study is reported on identifying a non-reacting second phase that belongs to BSCCO phase diagram. In the present work, taking analogy from the YBCO composite, we have chosen to incorporate submicron particles of Ca_{0.86}Sr_{0.14}CuO₂ phase, derived from the BSCCO phase diagram [20]. BSCCO composites thus obtained are investigated for their superconducting properties.

Bi_{1.2}Pb_{0.3}Sr_{1.54}Ca_{2.06}Cu₃O_y is a well-studied Bi 2223 system, derived from (Bi,Pb)₂Sr₂(Ca_{0.86}Sr_{0.14})_{n-1}Cu_nO_y general formula, for n= 5 and normalized to 3 Cu atoms per unit cell [21]. As n tends to infinity in the general formula, one gets the Ca_{0.86}Sr_{0.14}CuO₂ compound, referred to here, as the infinity phase and is part of the BSCCO phase diagram. Ca_{0.86}Sr_{0.14}CuO₂ phase is regarded as a stable parent structure of A₂B₂Ca_{n-1}Cu_nO_y type superconductors like (Bi, Hg, Th based) [22], and it coexists with Bi 2223 in the phase diagram [21]. A series of compounds are synthesized by adding various concentrations (0-50 mol) of nano (Ca,Sr)CuO phase to 100 mol of Bi 2223, and investigated the changes in their microstructural and superconducting properties. Method of sol-casting [5] was used to obtain a uniform distribution of nanoparticles in the matrix.

6.2 Experimental

Bi 2223 powder was prepared using the metal nitrate decomposition method [22] using high-quality Bi₂O₃ (Alfa Aesar, 99.975%), SrCO₃ (Sigma, >99%), CaCO₃ (Sigma, >99%), CuO (Merck, >99%), and Pb(NO₃)₂ (Sigma, >99%), powders. The Bi 2223 powder was calcined at 800 °C twice with one intermediate grinding. Ca_{0.86}Sr_{0.14}CuO₂ phase nanoparticles were prepared by the citrate route, discussed in section 2.3.2 of chapter 2 [17,18]. Ca_{0.86}Sr_{0.14}CuO₂ phase nanoparticles were

calcined twice at 500 °C. Bi 2223 and Ca_{0.86}Sr_{0.14}CuO₂ powders were mixed in various proportions using the sol-casting technique [19,20]. Sol-casting enabled the homogenous distribution of Ca_{0.86}Sr_{0.14}CuO₂ phase particles into the Bi 2223 matrix without agglomeration. This technique is based on the polymerization of slurry-containing ceramic powders (Bi 2223 and (Ca,Sr)CuO phase) after tumbling for several hours. The slurry was allowed to polymerize; binders were removed by heating to 800 °C for 24 hours, and the Bi 2223 composite powder with Ca_{0.86}Sr_{0.14}CuO₂ phase addition was pelletized and sintered twice at 845 °C with one intermediate pressing. Repeated pressing and sintering are useful for densification. The details of compositions of Bi 2223 with Ca_{0.86}Sr_{0.14}CuO₂ addition are given in Table 6.1.

6.3 Results and Discussions:

6.3.1 Characterization of Ca_{0.86}Sr_{0.14}CuO₂ phase particles

The phase formation of $Ca_{0.86}Sr_{0.14}CuO_2$ phase formation was confirmed by XRD analysis, and microstructure analysis revealed that particles are in the submicron range. Fig. 6.2(a) shows the indexed XRD pattern for $Ca_{1.9}Sr_{0.1}CuO_3$ phase. A few peaks around 2 θ positions 35.6, 38, and 53.4 corresponding to the CuO phase are also present. $Ca_{1.9}Sr_{0.1}CuO_3$ phase after annealing can be balanced using the equation given below.

$$2(Ca_{0.86}Sr_{0.14}CuO_2)$$
 \approx $Ca_{1.9}Sr_{0.1}CuO_3 + CuO_3$

The FESEM micrograph in Fig. 6.2(b) suggests that (Ca,Sr)CuO phase particles are in the submicron range.

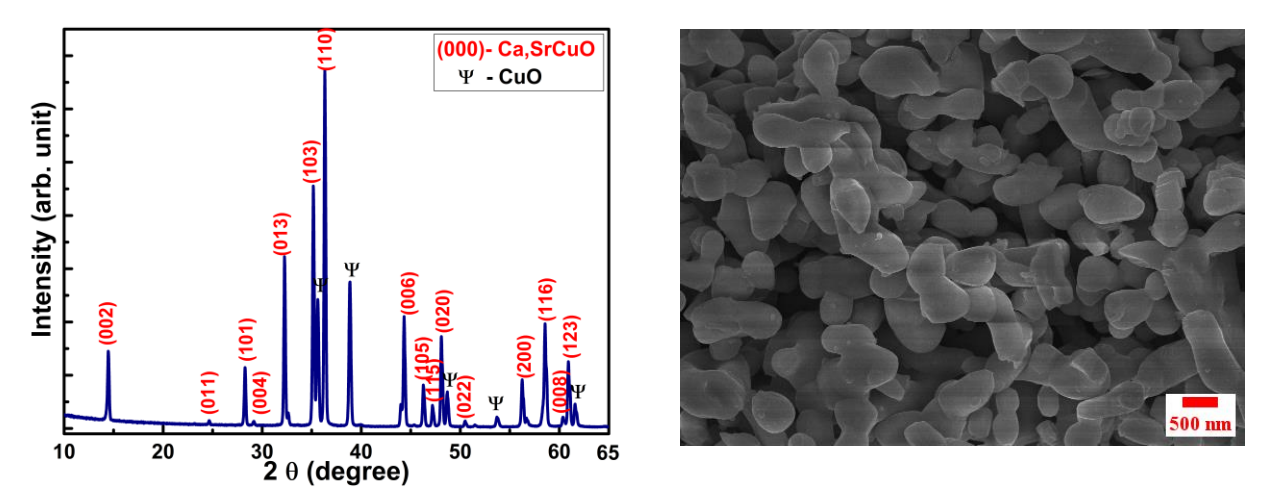


Figure 6.2(a): Indexed XRD patterns for (Ca,Sr)CuO phase along with few peaks

corresponding to CuO phase, (b) FESEM micrograph for (Ca,Sr)CuO phase, showing particles are in the submicron range.

6.3.2 XRD analysis of composites

The indexed XRD patterns shown in Fig. 6.3, suggest that for all the samples, majority of the peaks could be indexed to Bi 2223 phase, which is present with (Ca,Sr)CuO phase and traces of Bi 2212 phase. The sample NI 0 is nearly single phase Bi 2223. Low-intensity XRD lines at 2θ positions ~ 27.8 and 29.7 degrees correspond to the Bi 2212 phase in sample NI 0- NI 2. XRD lines of substantial intensity at around 36.3, 44, 56.2, 58.5, and 61 degrees correspond to the (Ca,Sr)CuO phase that co-exists in the Bi 2223 matrix without reacting or forming any other product phase. There is no significant change in the lattice parameters after adding (Ca,Sr)CuO phase. The lattice parameters for Bi 2223 phase are given in Table 6.2.

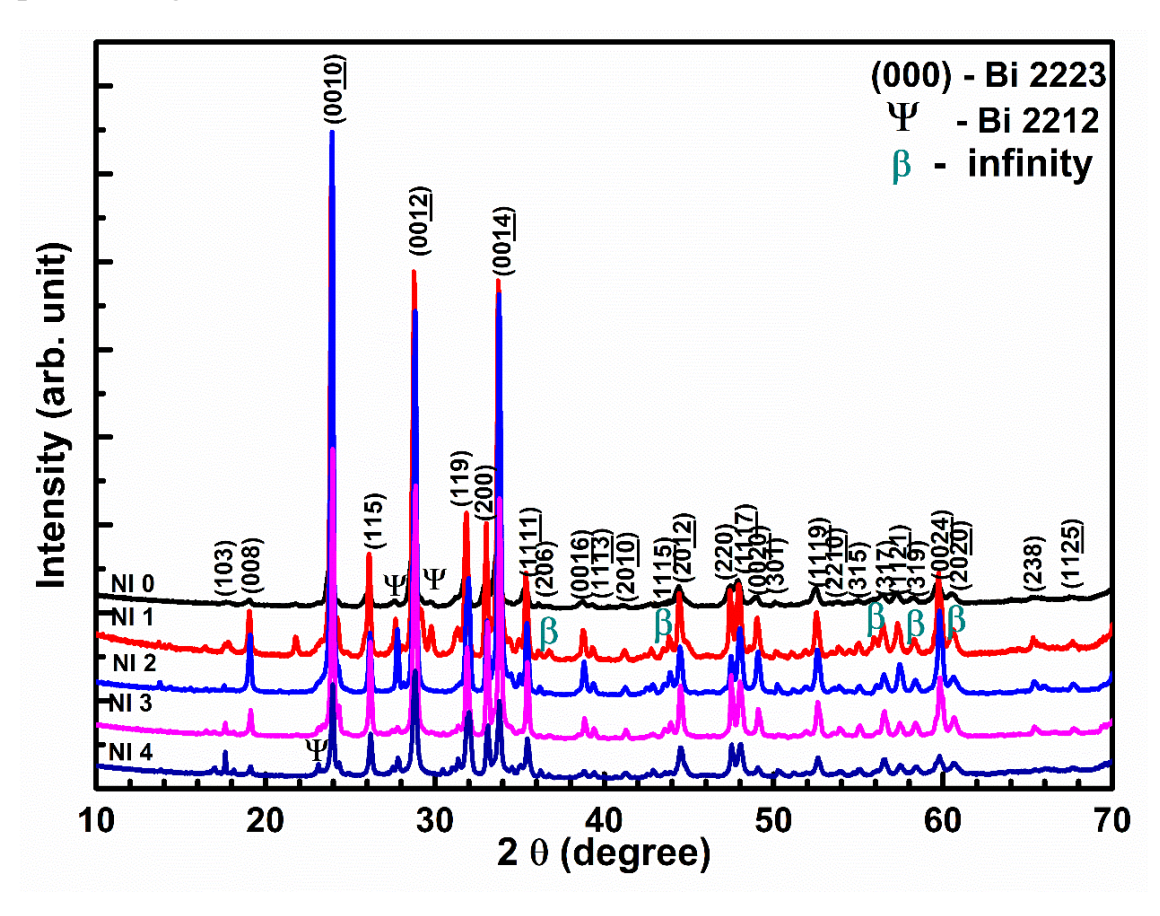


Figure 6.3: Indexed XRD patterns for NI 0 - NI 4 samples show peaks corresponding to Bi 2223 and other phases.

6.3.3 Microstructural analysis

In our earlier work, we added 20 mol of micron-sized Ca_{0.86}Sr_{0.14}CuO₂ phase particles to 100 mol of Bi 2223 composites and investigated the properties of the composite[14]. Our findings revealed that these micron-sized particles prove to be efficient in improving J_c and enhancing flux pinning, particularly at higher magnetic fields. Interestingly, these particles don't react with the Bi 2223 phase and are found to be present among Bi 2223 grains. An image of these particles distributed among Bi 2223 grains is shown in Fig. 6.4 (b).

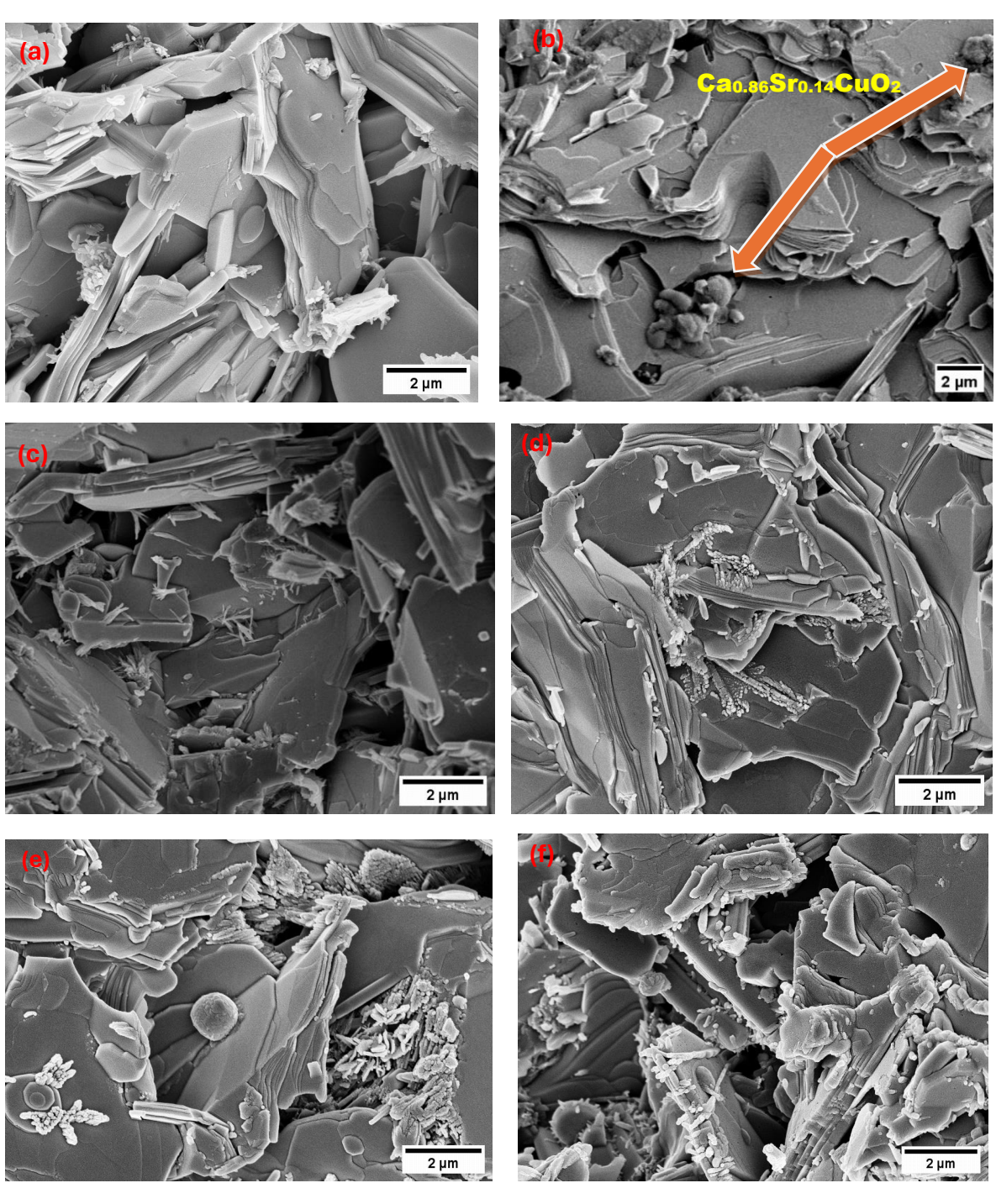


Figure 6.4: FESEM micrograph of samples, **(a)** for NI 0 sample, **(b)** micronsized Ca_{0.86}Sr_{0.14}CuO₂ phase particles added to Bi 2223 composites, from our previous study [14], **(c-f)** for NI 1-NI 4 samples showing platelet-like Bi 2223 grains and needle-shaped (Ca,Sr)CuO phase.

Large grains and platelet-like morphology observed in all the samples are typical of Bi 2223 microstructure, reported in the literature [11,21–25]. Platelet-like, randomly aligned grains belonging to the Bi 2223 phase are shown in Fig. 6.4. Needle-shaped secondary phase corresponding to the (Ca,Sr)CuO phase can also be seen for samples NI 1- NI 4 in Fig. 6.4(c-f). Sample NI 4 has the highest fraction of needle-like phase. After (Ca,Sr)CuO phase addition, a precise 2-phase YBCO superconductor like microstructure can be seen for samples NI 1- NI 4. The shape of Bi 2223 grains, after the (Ca,Sr)CuO phase addition was found to be unchanged.

Energy dispersive analysis of X-rays (EDAX) was used for compositional analysis and is shown in Fig. 6.5. The composition of the large platelets is nearly Bi 2223, and that of needle-like phase is nearly (Ca_{1.9}Sr_{0.1})CuO_{3+δ}. From Fig. 6.5, it is interesting to note that the (Ca,Sr)CuO phase after processing, transformed to needle-like phase having a diameter of around 40-80 nanometres for each needle. The composition for Bi 2223 and (Ca,Sr)CuO phase is given in Table 6.1. The composition for needle-shaped (Ca,Sr)CuO phase obtained from EDAX analysis is in agreement with that from XRD analysis, confirming that the (Ca,Sr)CuO phase coexists with Bi 2223 without reacting.



Table 6.1: Compositional analysis for sample NI 4, (Ca,Sr)CuO phase in needle shape and Bi 2223 phase grains

Elements	Bi 2223	(Ca,Sr)CuO		
	At.%	At.%		
Bi	6.9	0.9		
Sr	7.9	2.1		
Ca	9.5	22		
Cu	12.5	12.1		
0	63.2	62.9		

Figure 6.5: FESEM micrograph of samples NI 4, used for Edax analysis, showing platelet-like Bi 2223 grains and (Ca,Sr)CuO phase.

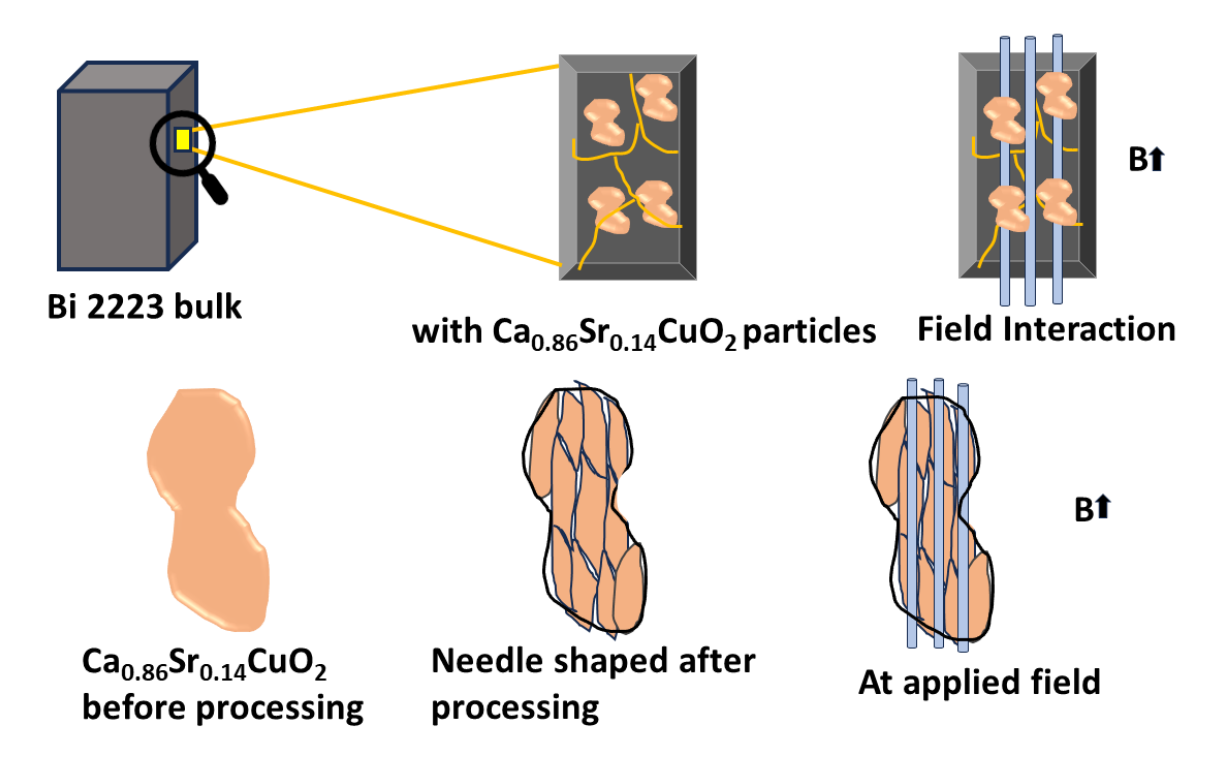


Figure 6.6: A schematic diagram showing a microstructural representation of Bi 2223 and (Ca,Sr)CuO phase particles and their field interaction

The (Ca,Sr)CuO phase breaks into a needle-like secondary phase lying among Bi 2223 grains without reacting with them; a pictorial representation of this is shown in Fig. 6.6. Such a microstructure in BSCCO superconductors, where needle-like secondary phase or modified 2-phase microstructures has not been reported in the literature for BSCCO superconductors, where their effect on J_c is studied.

6.3.4 Temperature dependence of magnetization

To determine the superconducting transition temperature, the temperature dependence of magnetization was measured in the 120- 20 K temperature range at a 5 mT applied DC field. As shown in Fig. 6.7, all samples show a sharp diamagnetic transition around 105 K, suggesting that all the samples are superconducting and Bi 2223 is the main phase present. No diamagnetic transition around 85 K corresponding to the Bi 2212 phase was observed. Nearly constant T_c (Onset) for all the samples suggests that the (Ca,Sr)CuO phase addition has not affected the Bi 2223 lattice. Transition width (ΔT_c), measured using criteria discussed in section 3.4.3 in chapter 3. ΔT_c is low for samples Ni 1 and NI 4. T_c and ΔT_c are given in Table 6.2.

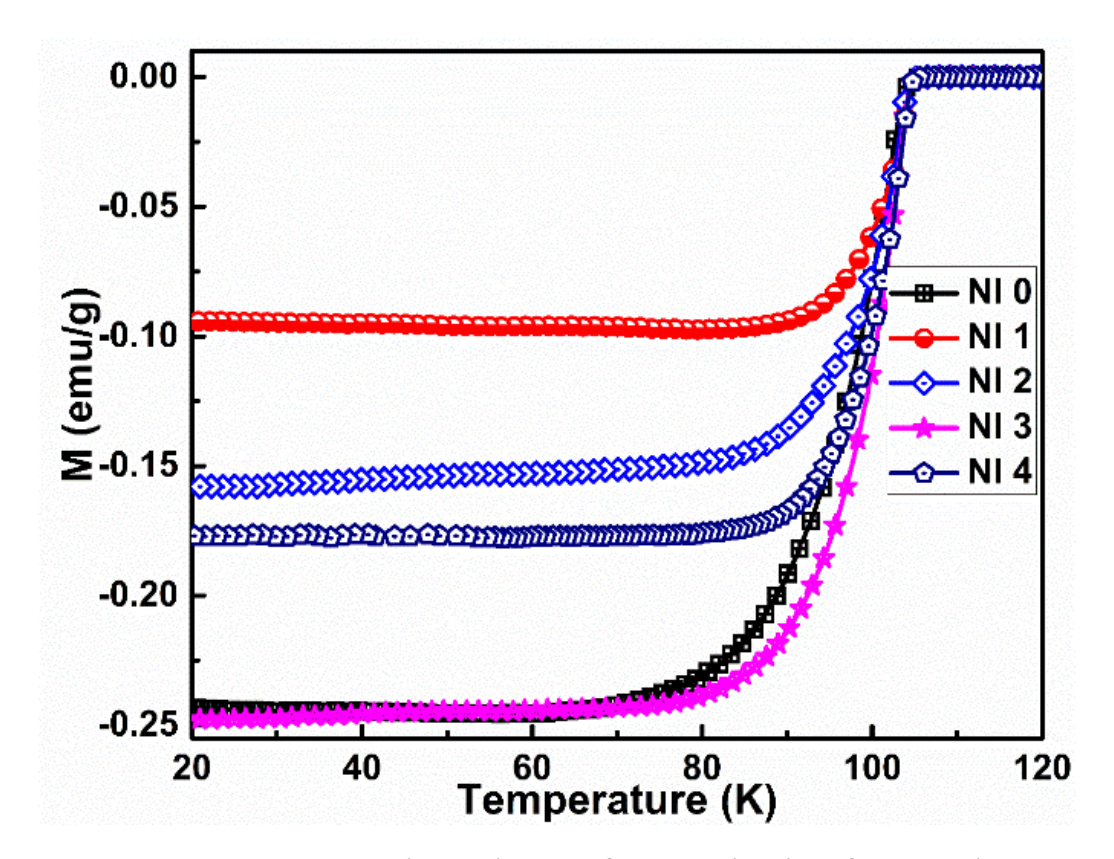


Figure 6.7: Temperature dependence of magnetization for samples NI 0- NI 4 showing a diamagnetic transition around 105 K

Samples NI 0 and NI 3 have higher Meissner fractions, whereas sample NI 1 has a lower Meissner fraction due to presence of small amount of Bi 2212 phase content, which was also confirmed by XRD analysis.

Table 6.2: Nano Ca_{0.86}Sr_{0.14}CuO₂ phase content added to Bi 2223, Transition temperature, transition width for all samples

Sample	Ca _{0.86} Sr _{0.14} CuO ₂ added	Lat	T _c , K	ΔT _c , K		
	to 100 mol of Bi 2223 (mol)	a, Å	b, Å	c, Å		
NI 0	0	5.413(7)	5.381(3)	37.067(8)	104.5	18.4
NI 1	1	5.406(8)	5.396(7)	37.075(3)	105	12.2
NI 2	5	5.403(5)	5.386(0)	37.050(2)	104.8	16.5
NI 3	10	5.407(3)	5.403(7)	37.063(2)	104.9	16.5
NI 4	50	5.409(5)	5.401(0)	37.092(5)	104.8	10.8

6.3.5 Critical current density and Flux pinning force density

Bean's extended critical state model [26] was employed to calculate the critical current densities for all samples at various temperatures.

The field dependence of J_c for all samples at 20 K - 77 K is shown in Fig. 6.8(a-d). The higher J_c observed at 20 K for samples NI 2- NI 4 is attributed to the presence of an adequate number of pinning centers provided by needle-shaped (Ca,Sr)CuO, effectively pinning the flux lines. In contrast, samples NI 0-NI 1 exhibit lower J_c values due to the insufficient availability of pinning centers.

At 30 K and 50 K, the J_c values increase systematically with (Ca,Sr)CuO phase content at low fields (till 2T) for all samples and at higher fields for all except for sample NI 3. The J_c- B behaviour for samples NI 2 and NI 4 is better at higher fields due to the availability of sufficient pinning centres. The (Ca,Sr)CuO phase, present in needle-shaped particles of a few nanometres in size, appears to be effective in contributing to flux pinning and help in sustaining J_c at higher fields. The poor performance of sample NI 3 is attributed to the larger size of its Bi 2223 grains that result in lower density of defects at the grain boundaries, unlike in other samples with smaller grains. Similar grain size-based poor performance for BSCCO superconductors was reported in the literature [13,27,28]. The J_c (0) values at 20 K and 30 K for all samples are given in Table 6.3.

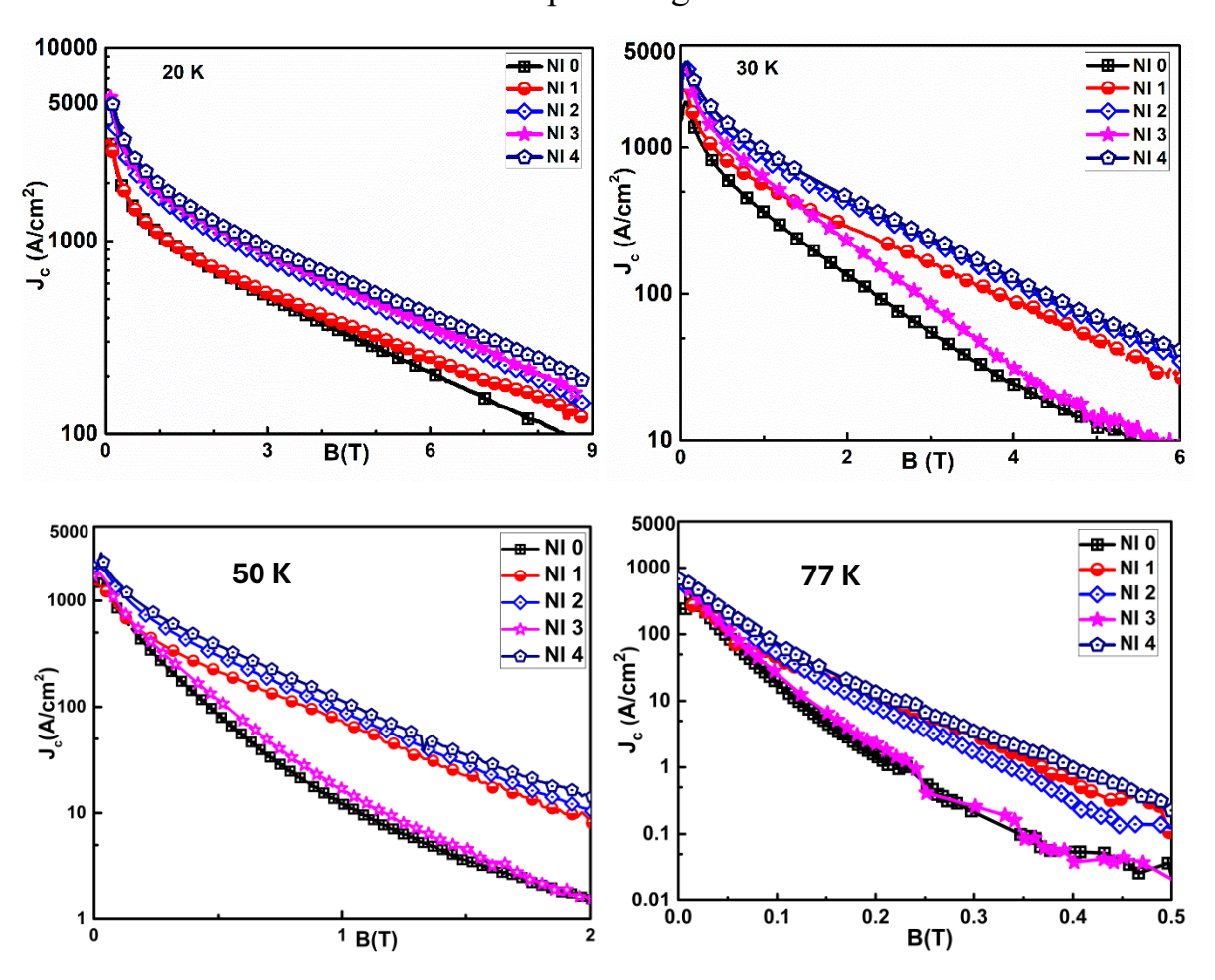


Figure 6.8 (a -d): Field dependence of critical current density for all samples at 20 K, 30 K, 50 K, and 77 K

In BSCCO superconductors, fluxons have enough activation energy to overcome the pinning effect far below the critical temperature (T_c), where thermal fluctuations can affect the flux motion [29]. To overcome this, nanoparticles are added to the superconducting matrix to act as efficient pinning centres. By varying the concentration and size of nanoparticles, the superconducting properties of BSCCO superconductors can be fine-tuned. The field dependence of F_p (= J_cXB) at various temperatures is shown in Fig. 6.9 (a-e), and the $F_{p \text{ max}}$ values at various temperatures are shown in Table 6.3. At 10 K, sample NI 3 has the highest F_p , and all samples have a steady increase in F_p with the field, suggesting that all samples have sufficient pinning to overcome the effect of Lorentz force at 10 K.

Table 6.3: Critical current densities at zero field and flux pinning force density maximum at 20 K, 30 K, and 50 K for all samples

Sample	20 K		30	K	50 K		
	J _c (0) kA/cm ²	$F_{p max}$ N/cm^3	$J_{c}(0)$ kA/cm^{2}	F _{p max} N/cm ³	$J_{c}(0)$ kA/cm ²	$F_{p max}$ N/cm^3	
NI 0	3.3	19.4	2	4.6	1.6	0.7	
NI 1	3.3	21	2.5	7.5	1.4	1.4	
NI 2	5	31	3.7	10.9	2.1	2	
NI 3	5.6	32.9	3.5	7.9	1.9	0.9	
NI 4	5.4	35.4	3.9	12.5	2.8	2.4	

With a rise in temperature, the thermal activation energy of fluxons increases and moves the flux lines; to arrest their movement, an adequate number of effective pinning centers, distributed uniformly in the superconducting matrix, are required to be created for pinning the flux lines. At 20 K, a systematic increase in F_p -B variation with an increase in the I-phase content can be seen. All samples have F_p maxima around 4 T field at 20 K. At 30, 50 K, and 77 K, F_p increases with (Ca,Sr)CuO phase content except for the sample NI 3. The relative drop in F_p after the corresponding F_p maxima is more rapid for sample NI 3 sample, while all others have a systematic variation with field. This behaviour is attributed to the lower extent of pinning by interfacial defects, generated at larger grains in NI 3, as observed from microstructures. As the temperature increases, F_p maxima shift to lower fields, due to a rise in the depinning energy, which is usually seen in HTSc. At temperatures above 10 K, sample NI 4 has shown the best performance and is attributed to large amount of nano (Ca,Sr)CuO phase needles,

deposited at platelet boundaries, providing sufficient pinning. At temperatures 30 K and 50 K, the full width half maximum (FWHM) values of $F_p(B)$ curves for NI 1, NI 2, and NI 4 exceed those of the other samples. The increased FWHM values in these samples imply that effective pinning occurs over broader field range due to the nano I-phase present.

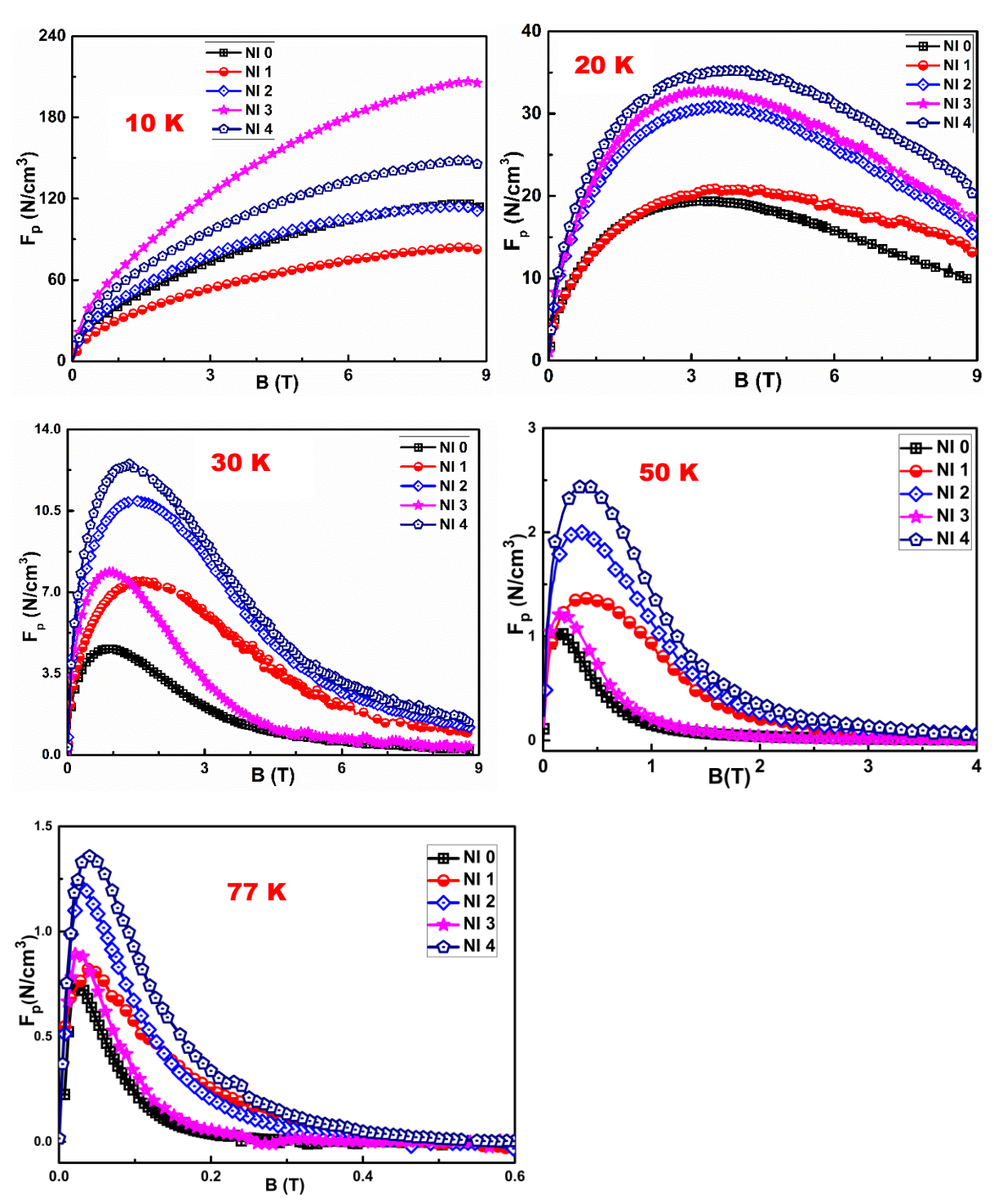


Figure 6.9 (a-e): Field dependence of pinning force density for all samples at 10 K, 20 K, 30 K, 50 K, and 77 K

Only a few reports are available in the literature where large amount of second phase (like nearly 50 mol in proportion to 100 mol of Bi 2223) is added and enhancement in J_c is sustained at higher content even at 77 K. In the case of ZnO addition to Bi 2223 reported for 0-50 wt%, J_c was found to fall even at 5 wt.% ZnO addition [35]. Similar results were obtained by adding nano ZrO₂ (0-50 mol) to Bi 2223 [12].

We believe that, like in YBCO where around 30 vol% of micron-sized Y 211 phase addition to Y 123 provides sufficient pinning, large amounts of the (Ca,Sr)CuO phase in Bi 2223 will be beneficial to suppress flux creep. It also offers adequate flux pinning in Bi 2223 without disturbing the Bi 2223 superconducting matrix.

The (Ca,Sr)CuO phase of ~500 nm particles added were seen after processing to break into a large number of needle-like secondary phase nanoparticles of 40-60 nm and get deposited at the boundary of Bi 2223 grains without reacting with them. A pictorial representation of this is shown in Fig. 6.6. (Ca,Sr)CuO phase locally disperses in the matrix without agglomerating or reacting with Bi 2223. This (Ca,Sr)CuO phase helps in sustaining the J_c by arresting the flux lines at higher temperatures and fields. This controlled the thermally assisted flux flow as observed for the sample NI 4, which has superior properties due to adequate addition of (Ca,Sr)CuO phase particles.

6.4 Conclusions

The introduction of (Ca,Sr)CuO phase particles systematically enhanced the superconducting properties of Bi 2223 composites. XRD analysis revealed that the (Ca,Sr)CuO phase does not react forming other phases, even up to 50 mol addition to Bi 2223 (100 mol). This is because (Ca,Sr)CuO phase is derived from the same phase diagram of the BSCCO system. The superconducting transition temperature T_c remained nearly constant at 105 K even with the addition of (Ca,Sr)CuO phase. Microstructural examination revealed that the (Ca,Sr)CuO phase transformed into needle-shaped precipitates and were distributed along the boundaries of platelet-like grains of Bi 2223 phase. It is observed that samples with smaller grains exhibit superior J_c-B behavior due to enhanced flux pinning by the increased interfacial defect density, J_c increased with (Ca,Sr)CuO phase content as seen for samples NI 1, NI 2 and NI 4, except for sample NI 3 with larger Bi 2223 grains. The unique evolution of nanosized (needle-shaped) (Ca,Sr)CuO phase in microstructure resulting in improved superconducting properties gains significance in designing Bi 2223 superconductors with adequate

non-superconducting inclusions as in the YBCO system. This study provides valuable insights for fabricating Bi 2223 composites/tapes with improved microstructure and enhanced superconducting and flux pinning properties.

References

- [1] X.L. Wang, A.H. Li, S. Yu, S. Ooi, K. Hirata, C.T. Lin, E.W. Collings, M.D. Sumption, M. Bhatia, S.Y. Ding, S.X. Dou, Thermally assisted flux flow and individual vortex pinning in Bi₂Sr₂Ca₂Cu₃O₁₀ single crystals grown by the traveling solvent floating zone technique, J. Appl. Phys. 97 (2005). https://doi.org/10.1063/1.1855531.
- [2] T. Haugan, P.N. Barnes, R. Wheeler, F. Melsenkothen, M. Sumption, Addition of nanoparticle dispersions to enhance flux pinning of the YBa₂Cu₃O_{7-x} superconductor, Nature. 430 (2004) 867–870. https://doi.org/10.1038/nature02792.
- [3] A. Gurevich, Challenges and opportunities for applications of unconventional superconductors, Annu. Rev. Condens. Matter Phys. 5 (2014) 35–56. https://doi.org/10.1146/annurev-conmatphys-031113-133822.
- [4] W. Wei, J. Schwartz, K.. Goretta, U. Balachandran, A. Bhargava, Effects of nanosize MgO additions to bulk Bi_{2.1}Sr_{1.7}CaCu₂O_x, Phys. C Supercond. 298 (1998) 279–288. https://doi.org/10.1016/S0921-4534(97)01889-3.
- [5] S. Zhang, C. Li, Q. Hao, J. Feng, T. Lu, P. Zhang, Optimized Intergrain Connection and Transport Properties of Bi-2212 High-Temperature Superconductors by Ag Nanoparticles Inclusions, J. Supercond. Nov. Magn. 28 (2015) 1729–1736. https://doi.org/10.1007/s10948-015-2981-1.
- [6] U. ÖZTORNACI, B. ÖZKURT, The effect of nano-sized metallic Au addition on structural and magnetic properties of Bi_{1.8}Sr₂Au_xCa_{1.1}Cu_{2.1}O_y (Bi-2212) ceramics, Ceram. Int. 43 (2017) 4545–4550. https://doi.org/10.1016/j.ceramint.2016.12.109.
- [7] M.E. Aytekin, B. Özkurt, The Influence of Nano-Sized SnO₂ Doping on Physical and Magnetic Properties of the Bi₂Sr_{2-x}(SnO₂)_xCa₁Cu_{1.75}Na_{0.25}O_y Superconductors, J. Supercond. Nov. Magn. 33 (2020) 965–970. https://doi.org/10.1007/s10948-019-05336-w.
- [8] K.C. Goretta, V.R. Todt, D.J. Miller, M.T. Lanagan, Y.L. Chen, U. Balachandran, J. Guo, J.A. Lewis, Engineered flux-pinning centers in Bi₂Sr₂CaCu₂O_x and TIBa₂Ca₂Cu₃O_x superconductors, J. Electron. Mater. 24 (1995) 1961–1966. https://doi.org/10.1007/BF02653017.
- [9] Z.Y. Jia, H. Tang, Z.Q. Yang, Y.T. Xing, Y.Z. Wang, G.W. Qiao, Effects of nano-ZrO₂ particles on the superconductivity of Pb-doped BSCCO, Phys. C Supercond. Its Appl. 337 (2000) 130–132. https://doi.org/10.1016/S0921-4534(00)00072-1.
- [10] M. Annabi, A. M'chirgui, F. Ben Azzouz, M. Zouaoui, M. Ben Salem, Addition of nanometer Al₂O₃ during the final processing of (Bi,Pb)-2223 superconductors, Phys. C Supercond. Its Appl. 405 (2004) 25–33. https://doi.org/10.1016/j.physc.2004.01.012.
- [11] R. Mawassi, S. Marhaba, M. Roumié, R. Awad, M. Korek, I. Hassan, Improvement of superconducting parameters of Bi_{1.8}Pb_{0.4}Sr₂Ca₂Cu₃O_{10+δ} added with nano-Ag, J. Supercond. Nov. Magn. 27 (2014) 1131–1142. https://doi.org/10.1007/s10948-013-

- [12] P.K. Verma, A. Kaipamangalath, M.R. Varma, V.S. Bai, Non-reactive Nano WO₃ Inclusions to Enhance Flux Pinning in Bi-2223 Superconductor Composites, IEEE Trans. Appl. Supercond. 34 (2023) 1–25. https://doi.org/10.1109/tasc.2023.3332750.
- [13] E. Guilmeau, B. Andrzejewski, J.G. Noudem, The effect of MgO addition on the formation and the superconducting properties of the Bi 2223 phase, Phys. C Supercond. Its Appl. 387 (2003) 382–390. https://doi.org/10.1016/S0921-4534(02)02360-2.
- [14] P.K. Verma, T. Rajasekharan, S.C. Das, K.P. Surendran, V. Seshu Bai, Effect of nano ZrO₂ addition on the properties of Ca_{0.86}Sr_{0.14}CuO₂ added Bi 2223 composites, J. Phys. Conf. Ser. 2545 (2023) 012014. https://doi.org/10.1088/1742-6596/2545/1/012014.
- [15] N. Devendra Kumar, T. Rajasekharan, K. Muraleedharan, A. Banerjee, V. Seshubai, Unprecedented current density to high fields in YBa₂Cu₃O_{7-δ} superconductor through nano-defects generated by preform optimization in infiltration growth process, Supercond. Sci. Technol. 23 (2010) 105020. https://doi.org/10.1088/0953-2048/23/10/105020.
- N. Devendra Kumar, P. Missak Swarup Raju, S. Pavan Kumar Naik, T. Rajasekharan, V. Seshubai, Effect of preform compaction pressure on the final microstructures and superconducting properties of YBa₂Cu₃O_{7-δ} superconductors fabricated by directionally solidified Preform optimized infiltration growth process, J. Low Temp. Phys. 174 (2014) 113–127. https://doi.org/10.1007/s10909-013-0955-x.
- [17] J.H. Greenberg, L. Ben-Dor, V. Beilin, D. Szafranek, Effect of fluorination on preparation of Bi(Pb)SCCO 2223 by the citrate precursor process, J. Mater. Sci. 30 (1995) 5103–5109. https://doi.org/10.1007/BF00356056.
- [18] N. Darsono, D.H. Yoon, K. Raju, Effects of the Sintering Conditions on the Structural Phase Evolution and T C of Bi_{1.6}Pb_{0.4}Sr₂Ca₂Cu₃O₇ Prepared Using the Citrate sol–gel Method, J. Supercond. Nov. Magn. 29 (2016) 1491–1497. https://doi.org/10.1007/s10948-016-3459-5.
- [19] P.M.S. Raju, V. Seshubai, T. Rajasekharan, A generic process to introduce nanoparticles into powder preforms and its application to Infiltration Growth processing of REBa₂Cu₃O₇ superconductor, Mater. Chem. Phys. 161 (2015) 59–64. https://doi.org/10.1016/j.matchemphys.2015.05.004.
- [20] P.K. Verma, B.V. Reddy, T. Rajasekharan, R. Revathy, M.R. Varma, V.S. Bai, Two-Phase Microstructure Generated by Reaction of Nano WO₃ Addition and its Effect on Flux Pinning in Bi 2212 Composites, J. Supercond. Nov. Magn. (2024). https://doi.org/10.1007/s10948-023-06675-5.
- [21] P.M. Sarun, R.P. Aloysius, U. Syamaprasad, Preparation of high performance (Bi,Pb)-2223 superconductor using a sol-gel synthesized amorphous precursor through controlled gelation, Mater. Lett. 60 (2006) 3797–3802. https://doi.org/10.1016/j.matlet.2006.03.152.
- [22] R.R. Kumar, R.P. Aloysius, R.J. Bose, P. Guruswamy, U. Syamaprasad, Preparation of dense, high J_c Bi-2223 superconductors by multistage cold pressing, Supercond. Sci. Technol. 18 (2005) 689–693. https://doi.org/10.1088/0953-2048/18/5/018.

- [23] R.P. Aloysius, P. Guruswamy, U. Syamaprasad, Enhanced flux pinning in (Bi, Pb)-2223 superconductor by Nd addition, Supercond. Sci. Technol. 18 (2005) 427–431. https://doi.org/10.1088/0953-2048/18/4/009.
- [24] M. Zouaoui, A. Ghattas, M. Annabi, F. Ben Azzouz, M. Ben Salem, Effect of nanosize ZrO₂ addition on the flux pinning properties of (Bi, Pb)-2223 superconductor, Supercond. Sci. Technol. 21 (2008). https://doi.org/10.1088/0953-2048/21/12/125005.
- [25] H. Fallah-Arani, A. Sedghi, S. Baghshahi, F. shahbaz tehrani, R.S. Moakhar, N. Riahi-Noori, N.J. Nodoushan, Bi-2223 superconductor ceramics added with cubic-shaped TiO₂ nanoparticles: Structural, microstructural, magnetic, and vortex pinning studies, J. Alloys Compd. 900 (2022) 163201. https://doi.org/10.1016/j.jallcom.2021.163201.
- [26] M.H. Gharahcheshmeh, E. Galstyan, A. Xu, J. Kukunuru, R. Katta, Y. Zhang, G. Majkic, X.-F. Li, V. Selvamanickam, Superconducting transition width (ΔT_c) characteristics of 25 mol% Zr-added (Gd, Y)Ba₂Cu₃O_{7-δ} superconductor tapes with high in-field critical current density at 30 K, Supercond. Sci. Technol. 30 (2017) 015016. https://doi.org/10.1088/0953-2048/30/1/015016.
- [27] A. Zelati, A. Amirabadizadeh, A. Kompany, H. Salamati, J.E. Sonier, Critical Current Density and Intergranular Coupling Study of the Dysprosium Oxide Nanoparticle Added Bi_{1.6}Pb_{0.4}Sr₂Ca₂Cu₃O_y Superconductor, J. Supercond. Nov. Magn. 27 (2014) 2185–2193. https://doi.org/10.1007/s10948-014-2588-y.
- [28] P.M. Sarun, S. Vinu, R. Shabna, A. Biju, U. Syamaprasad, Microstructural and superconducting properties of Yb-substituted (Bi,Pb) -2212 superconductor sintered at different temperatures, 472 (2009) 13–17. https://doi.org/10.1016/j.jallcom.2008.04.103.
- [29] M.A. Ali, S.S. Banerjee, Coexistence of different pinning mechanisms in Bi-2223 superconductor and its implications for using the material for high current applications, J. Appl. Phys. 131 (2022). https://doi.org/10.1063/5.0093741.

Chapter 7

Summary and Conclusions

The movement of flux lines, known as flux creep, leads to a gradual increase in the resistance of the superconductor over time, eventually causing it to lose its superconducting properties. This usually occurs at high temperatures or in the presence of strong magnetic fields, leading to a decrease in the critical current density of the material [1].

Controlling flux creep in HTS materials is essential for maximizing their performance for practical applications. Pinning centers are defects or impurities within the material that trap magnetic flux lines, preventing their movement. So, superconducting materials with suitable pinning centers are sought to reduce the impact of flux creep. Modifying superconducting material's microstructure using grain boundary engineering or nano-structuring can improve flux pinning capabilities and inhibit flux creep. Various methods can be employed to enhance the pinning properties of the superconductor, such as introducing nanoparticles, irradiation with high-energy particles, or creating artificial pinning centers through nano-structuring techniques [2].

At lower temperatures and fields, reports in the literature suggest that secondary phases are effective in enhancing J_c . However, at temperatures of 30 K and higher, the quest continues for an appropriate secondary phase to control the movement of flux lines and mitigate flux creep [3].

7.1 Problem addressed

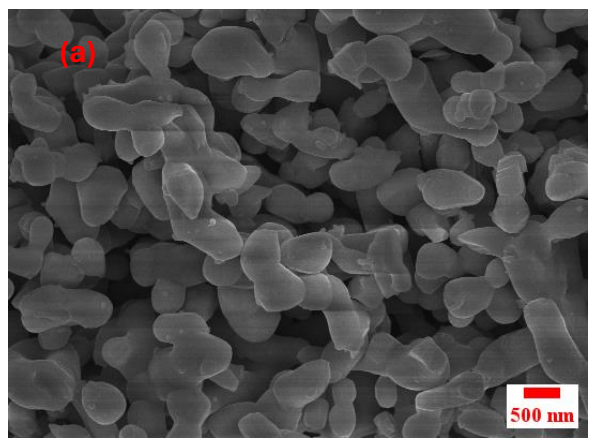
To prevent flux creep in HTSc, defects are introduced in the superconducting matrix by introducing secondary phases, applying high-energy ion radiation, or refining processing techniques. Several efforts have been made to introduce secondary phases into BSCCO superconductors. Still, challenges have been encountered that include secondary phase agglomeration, interaction with the matrix phase, or substitution to the lattice site. The realization of an optimized two-phase microstructure in BSCCO superconductors featuring a uniformly distributed secondary phase of sufficient quantity in the superconducting matrix still needs to be discovered.

7.2 Important findings

- The J_c and flux pinning properties of Bi 2212 composites with WO₃ nanoparticle addition improved at low concentrations (0.1 wt.%) of WO₃. The sol-casting process enabled the uniform distribution of WO₃ nanoparticles in the Bi 2212 matrix. At higher concentrations of WO₃ nanoparticle addition, W reacts locally and forms a secondary phase (WSr₂CaO₆), having a spherical shape with a diameter in the 20-80 nm range. This local reaction results in a microstructure resembling that of a two-phase YBCO. The number density of these WSr₂CaO₆ phase particles increases with WO₃ content, and WSr₂CaO₆ phase particles are found to settle at grain boundaries. T_c (Onset) and Bi 2212 phase content decrease with WO₃ concentration. At high concentrations of WO₃ addition, W substitutes to the lattice, and WSr₂CaO₆ phase content increases, which subsequently results in a decrease in J_c and flux pinning properties.
- ➤ Unlike Bi 2212, WO₃ nanoparticles were added to once processed and ground Bi 2223 powder. This prevented the substitution of W into the lattice and reaction of WO₃ with matrix elements. T_c(Onset) was constant at around 105 K. J_c, and flux pinning improved at low concentrations (0.1 wt.%) of nano WO₃ addition. WO₃ nanoparticles were effective at moderate temperatures and applied fields. Microstructural analysis showed that unlike Bi 2212, there was no evidence of secondary phase formation. However, W-containing precipitates were detected at higher concentrations of nano WO₃ addition. The irreversibility field increases with an increase in W content, except for the sample containing 0.5 wt.% of WO₃, which has a lower density. Flux pinning analysis suggests that normal surface pinning is the dominant mechanism at low fields due to interfacial defects associated with grain/platelet boundaries, and addition of WO₃ nanoparticles has reduced the rapid decrease in J_c due to flux creep at higher fields.
- ➤ Larger amounts (10 wt.%) of nano ZrO₂ addition to the composite of (Ca,Sr)CuO₂ phase added to Bi 2223 in 20:100 mol proportion, have suppressed the formation of the Bi 2223 phase and promoted the formation of the Bi 2212 phase. Microstructural analysis revealed large platelet-like grains of Bi 2223 in composites till 1 wt.% of nano ZrO₂ addition. The addition of only (Ca,Sr)CuO₂ phase particles has enhanced J_c up to an applied field of 9 T at 20 K. (Ca,Sr)CuO₂ phase is located as non-reacting

spherical particles distributed among Bi 2223 grains, leading to enhanced flux pinning at higher magnetic fields, by creating a two-phase microstructure like that of Y 123 with Y 211 precipitates. The effective increase in J_c is attributed to the high density of small-sized structural defects that form at the interfaces of the second-phase particles and the matrix and facilitate effective pinning. The addition of ZrO₂ nanoparticles reacts with the (Ca,Sr)CuO₂ particles, forming SrZrO₃ as an impurity phase. This decreased the superconducting phase fraction and lowered the J_c(0) compared to the sample with only (Ca,Sr)CuO₂ phase addition but enhanced the field range in which flux pinning was effective in samples with ZrO₂ addition. Analysis of the flux pinning mechanism suggest that surface pinning is the dominant pinning mechanism at low fields. Examination of the data, fit the Hughes model, indicates that composite with 1 wt.% of nano ZrO₂ addition has better-pinning properties at fields close to B* than samples with lower ZrO₂ content. This is attributed to flux pinning caused by the defect density created by the reaction products after nano ZrO2 addition. Pinning from different mechanisms is thus observed to be operative at different field regimes. Irreversibility field increased after (Ca,Sr)CuO₂ and nano ZrO₂ additions.

➤ (Ca,Sr)CuO₂ phase particles, which remained unreacted among Bi 2223 grains, were discovered to improve Jc significantly at higher fields and temperatures. This prompted us to introduce submicron-sized (Ca,Sr)CuO₂ phase particles to the Bi 2223 matrix. Submicron (Ca,Sr)CuO₂ particles were synthesized via the citrate route and added in varying concentrations (0-50 mol) to 100 mol of Bi 2223. After processing, submicron (Ca,Sr)CuO₂ particles break into nanometre-sized needle-shaped precipitates and settle at grain boundaries, as shown in Fig. 7.1.



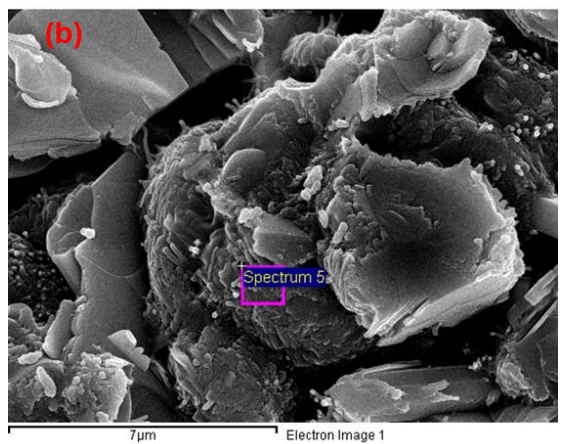


Figure 7.1(a &b): FESEM micrograph of (Ca,Sr)CuO₂ phase before and after processing showing transformation into nanometer-sized needle-shaped precipitates.

The superconducting transition temperature T_c remained nearly constant at 105 K even with the addition of (Ca,Sr)CuO₂ phase. Microstructural examination revealed that the (Ca,Sr)CuO₂ phase transformed into needle-shaped precipitates and were distributed along the boundaries of platelet-like grains of Bi 2223 phase. The J_c and flux pinning properties improve systematically with (Ca,Sr)CuO₂ phase content except for the sample with 10 mol of (Ca,Sr)CuO₂ phase addition as it has bigger sized Bi 2223 grains, and agglomeration of needles was also observed.

On comparing with WO₃ and ZrO₂ added Bi 2223 series, the (Ca,Sr)CuO₂ phase added series has better J_c and flux pinning at temperatures above 30 K up to 77 K, compared to pure Bi 2223. Fig. 7.2 summarizes the field dependence of J_c and F_p of best samples in each series.

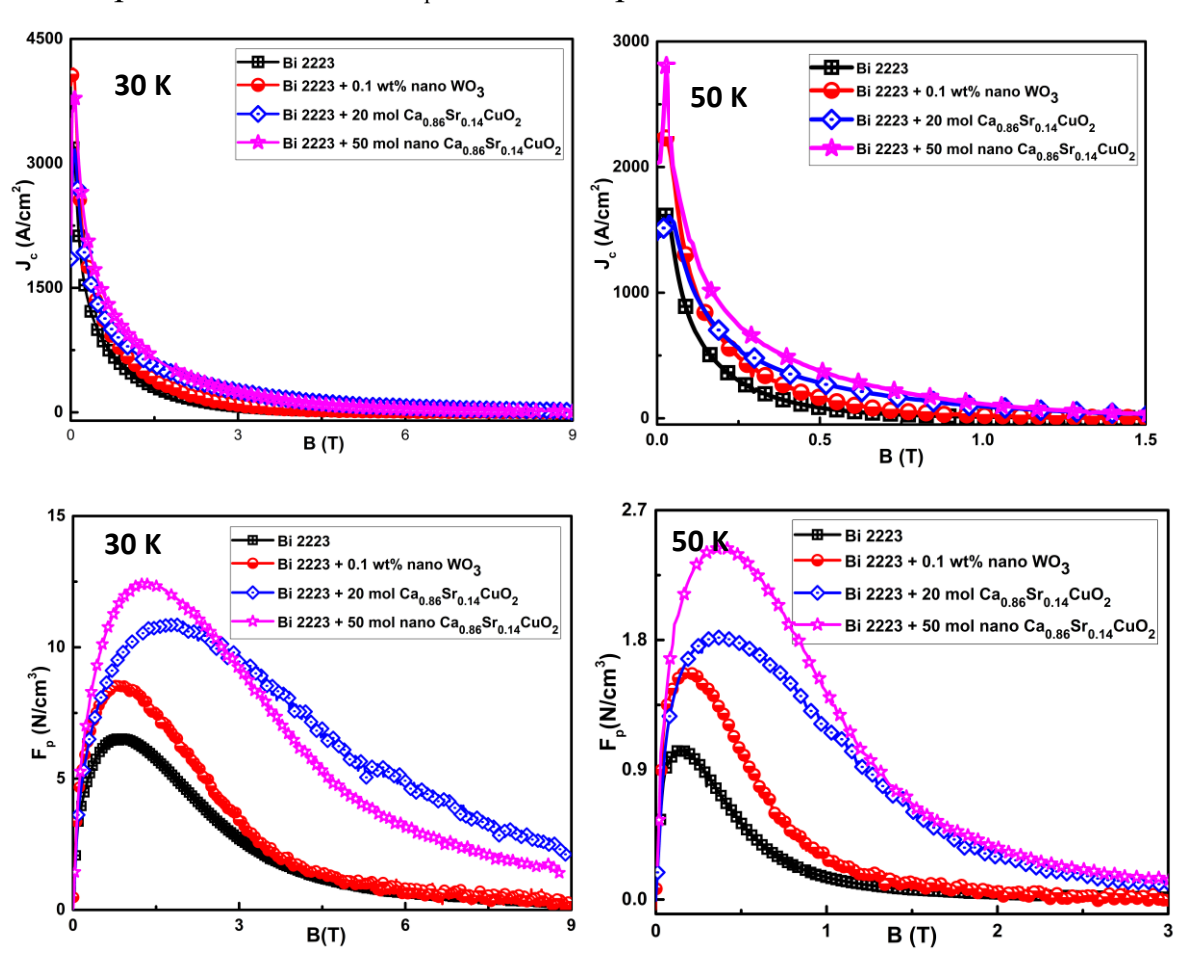


Figure 7.2(a-d): Field dependence of J_c and F_p at 50 K for Bi 2223 composites with nano WO_3 , 20 mol $(Ca,Sr)CuO_2$ and 50 mol nano $(Ca,Sr)CuO_2$ phase addition.

The (Ca,Sr)CuO₂ phase, which is derived from BSCCO phase diagram, effectively enhances J_c and flux pinning force density. The literature does not report a secondary phase added in high concentrations (50 mol) that can improve superconducting properties. (Ca,Sr)CuO₂ phase converts into needle-shaped secondary phase precipitates after processing and form a two-phase YBCO-like microstructure. The two-phase microstructure is helpful in controlling flux creep. As can be seen from Fig. 7.2, at higher temperatures of 50 K, where flux creep is higher, samples with 50 mol (Ca,Sr)CuO₂ phase have better J_c- B and F_p- B behaviour, suggesting its efficacy in suppressing flux creep, especially at higher temperatures.

Overall, Sol-casting enabled the uniform distribution of nanoparticles in the matrix. WO₃ nanoparticles are effective in improving J_c at low concentrations. (Ca,Sr)CuO₂ phase addition is helpful in creating a two-phase microstructure. ZrO₂ nanoparticles reacted with (Ca,Sr)CuO₂ phase and higher concentrations of ZrO₂ nanoparticle addition caused suppression in the Bi 2223 phase formation. Submicron-sized (Ca,Sr)CuO₂ phase particles convert to needle-shaped nanometre-sized secondary phase and form a two-phase microstructure. These needle-shaped precipitates settle at grain boundaries and help in arresting flux creep.

The outcome of our work projects the potential of fabricating Bi 2223 superconducting tapes containing submicron-sized (Ca,Sr)CuO₂ phase particles at 50 mol or higher (to be optimized) concentrations. This endeavor is aimed at achieving superior J_c, enhanced flux pinning, and suppressed flux creep in BSCCO superconductors.

References

- [1] M.R. Koblischka, Nanoengineering of flux pinning sites in high-T_c superconductors, Tsinghua Sci. Technol. 8 (2003) 280–291.
- [2] M. Koblischka, A. van Dalen, T. Higuchi, S. Yoo, M. Murakami, Analysis of pinning in superconductors, Phys. Rev. B Condens. Matter Mater. Phys. 58 (1998) 2863–2867. https://doi.org/10.1103/PhysRevB.58.2863.
- [3] A. Glatz, I.A. Sadovskyy, U. Welp, W.K. Kwok, G.W. Crabtree, The Quest for High Critical Current in Applied High-Temperature Superconductors, J. Supercond. Nov. Magn. 33 (2020) 127–141. https://doi.org/10.1007/s10948-019-05255-w.

Conference/ Schools attended

- 2018. Workshop on machine drawing and machining at University of Hyderabad, Hyderabad, India during 20° 26° August, 2018.
- 2019. 27th National Symposium on Cryogenics and Superconductivity at Indian Institute of Technology, Bombay, India during 16th 18th January, 2019.
 - 2019 Conference on Physics and Chemistry of Functional materials at GITAM University, Hyderabad, India from 21st August −22st February, 2019.
 - 2020 Online workshop on material characterization and techniques held online by Chitkara University, India during 20-21 July 2020.
 - 2020 Webinar on 'Recent Advances on Nanoscience and its Applications' held online by JNU- New Delhi, India during 27-28 July 2020.
 - 2020 Applied superconductivity conference (ASC-2020) held online during 24 October 07 November 2020
 - 2022 International Symposium on Superconductivity (ISS-2022) held in Nagoya, Japan, from November 29- December 01, 2022
 - 2023 Frontier in Physics (FIP- 2023) held at University of Hyderabad, Hyderabad, India, from March 03- 04, 2023.

Poster/Talk presented

- 2019 Presented a poster titled "Effect of isothermal hold on microstructure and growth of single grain YBCO superconductors in the Conference on Physics and Chemistry of Functional materials, held at GITAM University, Hyderabad, India during 21 August −22 February, 2019.
- 2020 Presented a poster titled "Enhancement of flux pinning in Bi₂Sr_{2.14}Ca_{0.86}Cu₂O_{8-d} superconductor composite in the "Applied Superconductivity Conference (ASC-2020)" held online from 24 October 07 November 2020.
- Delivered a talk entitled "Effect of nano ZrO₂ addition on the properties of Ca_{0.88}Sr_{0.14}CuO₂ added Bi-2223 composites" at 35th International Symposium on Superconductivity (ISS-2022) held in Nagoya, Japan, during November 29- December 01, 2022.
- Delivered a talk entitled "Enhancement of flux pinning in BSCCO superconductors by nanoparticles addition" at Frontier in Physics (FIP- 2023) held at University of Hyderabad, Hyderabad, India, from March 03- 04, 2023.

Research Publications

- 1]. **Pawan Kumar Verma**, A. Kaipamangalath, M. R. Varma and V. Seshu Bai, Non-reactive nano WO₃ inclusions to enhance flux pinning in Bi 2223 superconductor composites, *IEEE Transactions on Applied Superconductivity, vol. 34, no. 1, pp. 1-12, Jan. 2024, Art no.* 8000112, DOI: 10.1109/TASC.2023.3332750
- 2] **Pawan Kumar Verma,** B. V. Reddy, T. Rajasekharan, R. Revathy, M. R. Varma and V. Seshu Bai, Two-phase microstructure generated by reaction of nano WO₃ addition and its effect on flux pinning in Bi 2212 composites, **J Supercond Nov Magn 37, 1–14 (2024)** https://doi.org/10.1007/s10948-023-06675-5
- 3] **Pawan K Verma,** T. Rajasekharan, S.C. Das, K.P. Surendran and V. Seshu Bai, Effect of nano ZrO₂ addition on the properties of Ca_{0.86}Sr_{0.14}CuO₂ added Bi-2223 composites, **Journal of Physics:** Conference Series 2545 (2023) 012014, doi:10.1088/1742-6596/2545/1/012014.

4] P. Jeevan Kumar, Poly Rose, **Pawan Kumar Verma**, T. Rajasekharan and V. Seshu Bai, BSTO components using rapid prototyping and different gelcasitng systems, **Open Ceramics**, **17**, **100512**. https://doi.org/10.1016/j.oceram.2023.100512

Patents filed

- 1] V. Seshu Bai, T. Rajasekharan, **Pawan Kumar Verma**, S. Srinath, A method for producing Bi-2223 superconductor supporting high current density, **Patent filed, application no.-**202441037158
- 2] V. Seshu Bai, T. Rajasekharan, P. Jeevan Kumar, Poly Rose, **Pawan Kumar Verma**, A. Rajnikant, A method for fabricating a component with complex geometry, **Patent filed, application no.- 202441032541**

Studies on the role of nano additives on the microstructure and Flux pinning in Bi₂Sr₂(Ca_{0.86}Sr_{0.14})_{n-1}Cu_nO_{2n+4} superconductor composites

by Pawan Kumar Verma

Submission date: 20-May-2024 02:38PM (UTC+0530)

Submission ID: 2383901352

File name: Pawan_Kumar_Verma_BSCCO_Thesis_for_Plagiariasm_check.pdf (9M)

Word count: 32398 Character count: 161466 Studies on the role of nano additives on the microstructure and Flux pinning in Bi2Sr2(Ca0.86Sr0.14)n-1CunO2n+4 superconductor composites

ORIGINALITY REPORT

SIMILARITY INDEX

INTERNET SOURCES

PUBLICATIONS

STUDENT PAPERS

PRIMARY SOURCES

Seshu Bai. " Non-reactive Nano WO Inclusions to Enhance Flux Pinning in Bi-2223
Superconductor Composites ", IEEF Pawan Kumar Verma, Aswathi The school of Physics School of Physics Ayderabad Transactions on Applied Superconductivity, 2023

Publication

Pawan Kumar Verma, B. Venkatesulu Reddy, T. Rajasekharan, Ramany Revathy, Manoj Raama Varma, V. Seshu Bai. "Two-Phase Microstructure Generated by Reaction of Nano WO3 Addition and its Effect on Flux Pinning in Bi 2212 Composites", Journal of Superconductivity and Novel Magnetism, 2024

Publication

Pawan Kumar Verma, Aswathi Kaipamangalath, Manoj Raama Varma, V. Seshu Bai. " Nonreactive Nano WO Inclusions Dr. V. Scohu Bai

to Enhance Flux Pinning in Bi-2223 Superconductor Composites ", IEEE Transactions on Applied Superconductivity, 2024 Publication

4	Pawan K Verma, T. Rajasekharan, Shamili C Das, K P Surendran, V Seshu Bai. " Effect of nano ZrO addition on the properties of Ca Sr CuO added Bi 2223 composites ", Journal of Physics: Conference Series, 2023	3% N. Seshu Bai School of Physics School of Hyderabad Iniversity of Hyderabad
5	ir.niist.res.in:8080 Internet Source	1 %
6	Submitted to University of Hyderabad, Hyderabad Student Paper	1%
7	shibaura.repo.nii.ac.jp Internet Source	<1%
8	Advances in Superconductivity XI, 1999.	<1 _%
9	r.o.uow.edu.au Internet Source	<1%
10	etheses.bham.ac.uk Internet Source	<1%
11	Advances in Superconductivity X, 1998.	<1%

Prof. V. Seshu Bai School of Physics



UNIVERSITY OF HYDERABAD

CENTRAL UNIVERSITY P.O. GACHIBOWLI, HYDERABAD – 500 046

Plagiarism-free statement

This is to certify that the thesis entitled "Studies on the role of nano additives on the microstructure and Flux pinning in $Bi_2Sr_2(Ca_{0.86}Sr_{0.14})_{n-1}Cu_nO_{2n+4}$ superconductor composites" authored by Pawan Kumar Verma has been screened by the Turnitin software at the Indira Gandhi Memorial Library of the University of Hyderabad. The software shows 38% similarity index, out of which 31% came from candidate's own three research articles related to this thesis, which are already published and available online. The effective similarity index excluding his research articles is 38% -31% = 7%, which is in accordance with university guidelines. Hence the thesis is free from plagiarism.

V. Seshu Bai

V. Seshu Bai V. Seshu Bai School of Physics University of Hyderabad

Date :21st May 2024